REPORT DOCUMENTATION PAGE

AFRL-SR-BL-TR-99-

0301

1. AGENCY USE ONLY *(Leave blank)*	2. REPORT DATE	3. REPORT TYPE AND DATES COVERED
	AUGUST 18, 1999	WORKSHOP PROCEEDINGS

4. TITLE AND SUBTITLE
CONTRACTORS' MEETING IN TURBULENCE AND ROTATING FLOWS

5. FUNDING NUMBERS

F49620-97-1-05?9

6. AUTHOR(S)
DR THOMAS BEUTNER

7. PERFORMING ORGANIZATION NAME(S) AND ADDRESS(ES)
AIR FORCE OFFICE OF SCIENTIFIC RESEARCH
801 N. RANDOLPH STREET, ROOM 732
ARLINGTON, VA 22203-1977

8. PERFORMING ORGANIZATION REPORT NUMBER

9. SPONSORING/MONITORING AGENCY NAME(S) AND ADDRESS(ES)
AIR FORCE OFFICE OF SCIENTIFIC RESEARCH
801 N. RANDOLPH STREET, ROOM 732
ARLINGTON, va 22203-1977

10. SPONSORING/MONITORING AGENCY REPORT NUMBER

11. SUPPLEMENTARY NOTES

12a. DISTRIBUTION AVAILABILITY STATEMENT
APPROVED FOR PUBLIC RELEASE, DISTRIBUTION IS UNLIMITED

12b. DISTRIBUTION CODE

13. ABSTRACT *(Maximum 200 words)*

This report documents annual progress reports and final reports from grants and contracts in the Air Force Office of Scientific Research program in Turbulence and Rotating Flows. Major topical areas covered by these reports include turbulence measurements and modeling, flow control theory and demonstrations, turbomachinery flow fields, heat transfer in turbomachinery, reduced order modeling of complex flows, and microelectromechanical systems (MEMS) sensors and actuators.

20000121 002

14. SUBJECT TERMS			15. NUMBER OF PAGES
			288
			16. PRICE CODE

17. SECURITY CLASSIFICATION OF REPORT	18. SECURITY CLASSIFICATION OF THIS PAGE	19. SECURITY CLASSIFICATION OF ABSTRACT	20. LIMITATION OF ABSTRACT
U	U	U	

Standard Form 298 (Rev. 2-89) (EG)
Prescribed by ANSI Std. 239.18
Designed using Perform Pro, WHS/DIOR, Oct 94

DTIC QUALITY INSPECTED 1

AIR FORCE OFFICE OF SCIENTIFIC RESEARCH

CONTRACTORS' MEETING IN TURBULENCE AND ROTATING FLOWS

Air Force Office Of Scientific Research Contractors' Meeting in Turbulence & Rotating Flows
Albuquerque, NM ♦ August 18-19, 1999

TABLE OF CONTENTS

DEMONSTRATION OF ROBUST MICROMACHINED JET TECHNOLOGY AND ITS APPLICATION TO REALISTIC FLOW CONTROL PROBLEMS

AFOSR GRANT F49620-97-1-0519

Mark G. Allen and Ari Glezer
School of Electrical and Computer Engineering &
School of Mechanical Engineering,
Georgia Institute of Technology, Atlanta, GA

Abstract

In this work, we are investigating the use of microfabrication technology to create a micromachined fluidic control system (consisting of micromachined actuators, sensors, and control/drive circuitry) with a goal of application in practical fluids problems, such as UAV-scale aerodynamic control. Our approaches include: (1) the development of suitable micromachined synthetic jets (*microjets*) as actuators, which obviate the need to physically extend micromachined structures into an external flow; and (2) a non-silicon alternative micromachining fabrication technology based on metallic substrates and lamination (in addition to traditional MEMS technologies) which will allow the realization of larger scale, more robust structures and larger array active areas for fluidic systems. As an initial study, an array of MEMS pressure sensors and an array of MEMS modulators for orifice-based control of microjets have been fabricated, and characterized. Both pressure sensors and modulators have been built using stainless steel as a substrate and a combination of lamination and traditional micromachining processes as fabrication technologies.

Introduction

Micromachined devices have been primarily realized using silicon substrates [1]. In many applications, the use of traditional silicon-substrate micromachined devices may be limited, for example by the lack of ability of the surrounding silicon substrate to absorb large mechanical shocks. In this work, we have investigated the use of more robust substrates as suitable starting points for both bulk and surface micromachined structures, as well as investigated the possibility of the substrate forming essential structural components of the device package. Alternative fabrication techniques, such as techniques more commonly used in either conventional machining as well as electronic packaging fabrication (e.g., lamination), are combined with more traditional integrated-circuit-based microelectronics processing techniques to create micromachined devices on these robust substrates.

One of the advantages of the use of robust substrates is the possibility of co-fabrication of the micromachined devices and their packages using, e.g., the robust substrate itself as an integral part of the sensor package. Another advantage is that due to substrate robustness, these co-packaged devices may be able to be used in mechanically harsh environments, such as aerodynamic applications. Finally, it is envisioned that the larger-scale devices (especially actuators) producible by this fabrication technology will have increased control authority over their silicon counterparts.

The use of synthetic jets [2] as fluidic actuators enables the possibility of altering the apparent aerodynamic shape of an airfoil by creating a closed recirculation region without extending any mechanical parts into the crossflow of the airfoil. This approach is very suitable for a MEMS-based flow control scheme, since (1) such devices have already been demonstrated as being compatible with micromachining technology [3]; and (2) the relatively 'delicate' MEMS devices do not need to be exposed to the flow; in fact, the devices can be recessed under an orifice plate, safely out of reach of the flow. A microjet, pressure sensor, and provision for integrated circuitry can also be combined together to form a module suitable for repetition into an array. Such a module contains a modulator to switch the synthetic jets on and off at each orifice hole, a pressure sensor to sense the local pressure, and some local electronics to perform readout, signal linearization, and/or local control.

In the previous report we concentrated on sensor development, and have recently published a paper on the pressure sensor technology (Ref. 4). This report covers progress from July 1998 to July 1999, and is divided into three sections: progress in robust micromachining technology, specifically for the robust

microjet modulator and the robust pressure sensor; and progress in synthetic jet technology, specifically, vortex generation for aerodynamic control using synthetic jets. By incorporating conventional machining technology with lamination and surface micromachining, robust actuators were achieved. The Kapton diaphragm used for the first generation of pressure sensors was replaced by a stainless steel diaphragm.

1. Progress in robust microjet modulator technology

The actuator concept being pursued is shown in Fig. 1. Sheets of material are laminated onto a stainless steel substrate, lithographically patterned, and surface micromachined to form standoffs and flow channels. The flow channels permit airflow through an orifice conventionally machined in the substrate when the actuators are in the 'off' position. When the actuators are energized, the flexible sheet is deflected toward the surface, constricting the airflow and ultimately blocking the orifice. Currently, the actuators are

Figure 1. Schematic cross-section of robust microjet modulator

driven electrostatically, by application of a voltage between the flexible sheet and the substrate. Synthetic jets are formed by addition of a piezoelectric driver attached to the actuator side of the substrate orifice. Centerline velocities on the order of 3 m/s have been measured through the three types of actuators as will be described later.

Actuator Fabrication

The devices (Fig. 2) are fabricated using lamination technology, and are made from stainless steel (SS) substrates and diaphragms, and polyimide standoffs. The process begins with a 0.05 inch milled stainless steel substrate, Kapton polyimide film, and 12.5 μm SS 302 foil. The milled substrate is 2" x 2" with 25 milled holes 2 mm in diameter. The Kapton is Type 200 HN from Dupont, and the SS302 thin film is a prefabricated, over-the-counter shim stock. To fabricate the actuators, the Kapton is first laminated to the milled substrate, and the SS foil is laminated to the Kapton. This is done in two steps for improved adhesion between each layer. Next, photolithography is used to mask the stainless steel sheet for wet

Figure 2. Photograph of modulator

etching. The stainless steel is formed into three different types of actuator geometries using a wet etch. Finally, the Kapton is removed using an isotropic dry etch, in which the stainless steel film serves as the mask for surface micromachining of the underlying Kapton. By sizing the geometries of the modulator appropriately, patterning of the Kapton sacrificial layer to form anchor points is avoided. A photograph of a two inch substrate bearing stainless steel modulators is shown below. Some of the modulators have been removed to show the underlying orifice holes.

Actuator geometry and performance

The actuating diaphragms consist of a central 'pad' region, which acts to cover up the orifice holes, and support beams of a variety of geometries shown in Fig. 3. For all actuators, the pad is 3.6 mm in diameter, and is designed to deflect 50 μm (the standoff height) to block the 2 mm orifice hole on the milled substrate. Each actuator has four beams extending normally outward at angles of 0°, 90°, 180°, and 270°. Also, all beam widths on the actuators are 200 μm. Geometric representations of the designed actuators are shown in the figure below. The first actuator tested has beams 1.5 mm long extending outward from the center actuator pad. This actuator had an actuation voltage of 157 V and a first resonant frequency of 384 Hz. The second type of actuator has an "S-shaped" arm with a total length of 1.4 mm. It had an actuation voltage of 550 V and a first resonant frequency of 1.145 kHz. The third actuator had an "S-shaped" beam with a total length of 2.75 mm. It had an actuation voltage of 320 V and a first resonant frequency of 409 Hz.
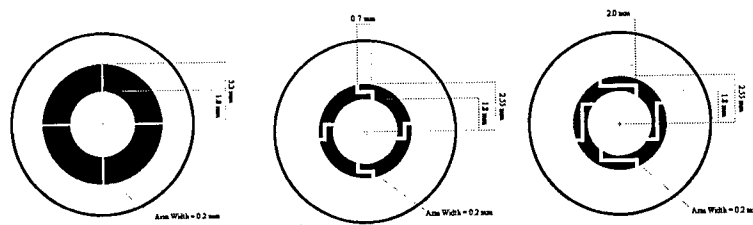
Figure 3. Three different shapes of modulators

Verification of operation using PIV

Particle image velocimetry (PIV) tests were performed on the modulator actuators, both to demonstrate that synthetic jet flow could pass through the modulators, as well as to demonstrate modulator-based control of the synthetic jet flow. Both a single modulator test (in which one isolated modulator was turned 'on'), and a dual modulator test (in which one of two adjacent modulators was turned 'on') were performed.

For the single valve PIV test, the third modulator type (2.75 mm total length) described above was used, and the piezo-driver was driven at 900 kHz. Centerline velocity from the orifice was measured at 3 m/s before electrostatic actuation (i.e., before the pad was drawn down to cover the orifice hole; figure left) and ~0 m/s once actuated (figure right). This experiment demonstrates that the modulator can physically stop a flow by controlled actuation.

The dual valve PIV tested the actuation of one valve when two valves were open, and this test used the second modulator described above (1.4mm total beam length). In this test, the centerline velocities were once again measured to be ~3 m/s when open (figure left). When one valve was actuated, the centerline velocity through the second hole remained constant and no additional vectoring was experienced (figure right).
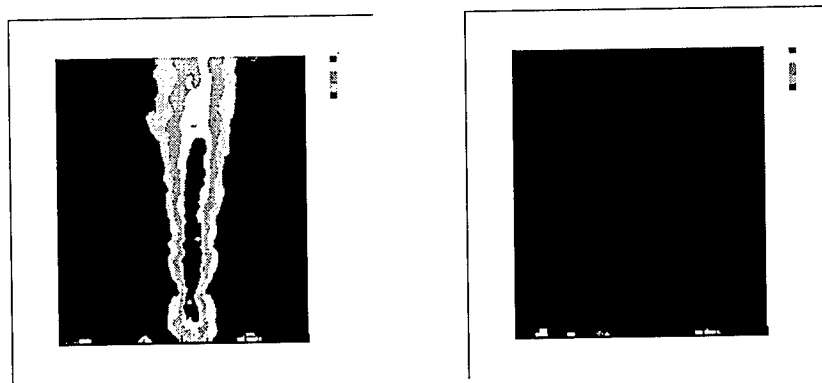
Figure 4. Single and dual modulator test using PIV.

2. Progress in robust pressure sensor technology

In the last report, a robust capacitive pressure sensor array was demonstrated. It used stainless steel as a substrate, Kapton film as a pressure-sensitive flexible plate, and electroplated nickel as a back electrode. By sensing the capacitance change of the capacitor formed between the flexible diaphragm and the rigid backplate (Figure 5), and by knowing the mechanical properties of the diaphragm, the pressure can be determined. An important attribute of this design is that only the steel substrate and the pressure sensor inlet is exposed to the flow; i.e., the sensor is self-packaged [4]. A critical point in this design was that Kapton was exposed to the flow. We report an improved fabrication technology, which uses a stainless steel diaphragm, thus ensuring that only stainless steel is exposed to the flow.

3
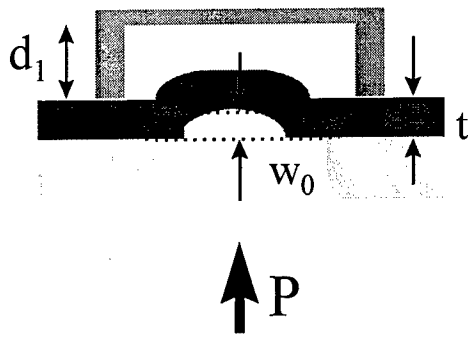
Figure 5. A schematic diagram of the side-view of the capacitive pressure sensor.

Figure 5 shows a schematic diagram of the side-view of the device, where d_1 is an initial gap distance between the fixed back electrode and the flexible plate electrode, w_o is the deflection at the center of the plate, t is the thickness of the plate, and P is the applied uniform pressure. An analytical model is shown in [4].

Fabrication of robust pressure sensor

The fabrication sequence of the robust pressure sensor starts on a square stainless steel substrate. Its side length and thickness are 5.7 cm (2 inch) and 0.5 mm (20 mil.), respectively. An array of 8x8 pressure inlet holes with a diameter of 2 mm, with 5 mm center-to-center distances, are milled through the substrate. A Kapton film (Dupont, Kapton HN200, 50μm [2 mil.] thick) and a stainless steel film are laminated onto the milled substrate using a hot press. The pressure sensitive flexible plates will be the stainless steel film in the regions suspended over the milled pressure inlet holes. Next a polyimide (PI) isolation layer is deposited with a thickness of 3μm. To create bottom electrodes, electroplating seed layers, and bonding pads (Figure 6), a triple metallic layer of Ti/Cu/Ti is deposited with a thickness of 250/6000/250 Å and patterned. Two layers of AZ4620 photoresist are spun onto the patterned layer, yielding a final thickness of photoresist of approximately 40~45 μm. The photoresist is patterned to create electroplating molds and nickel supports are electroplated through the molds. To fabricate the backplate, a Ti/Cu/Ti metallic triple layer is deposited to act as a seed layer. Thick photoresist (AZ 4620) is spun on the seed layer (approximately 20μm thick) and patterned to act as electroplating molds. Nickel is electroplated through the molds to create the backplates. Finally, the photoresist sacrificial layers and the seed layer in between them are etched using Acetone to create an air gap between the fixed backplate and the pressure sensitive stainless steel diaphragm (Figure 5). Finally the Kapton underneath the stainless steel diaphragm is removed by dry etch using RIE.
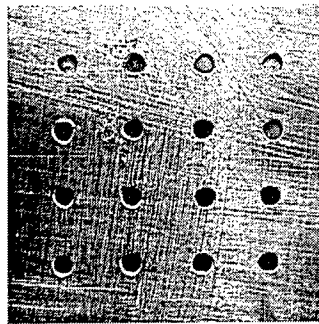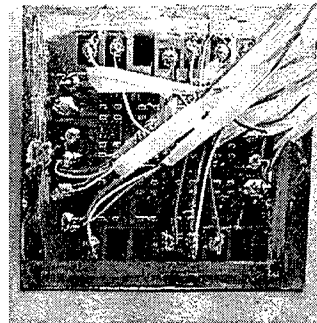
(a)   (b)

Figure 6. Photomicrographs of fabricated pressure sensors. (a) side exposed to flow. (b) sensor view.

Measurement

The capacitance of individual pressure sensors has been measured using a Keithley 3322 LCZ meter. Measured capacitances for undeflected pressure sensors were in the range 59pF to 95pF depending on the length of interconnections between bonding pads and sensors. The electronics chosen to read out the pressure sensors is an astable multivibrator, the frequency of which depends on the capacitance of the sensor. We have achieved this integration by using surface mount components; both operational amplifiers and surface-mount external resistors for the multivibrator circuit.

4
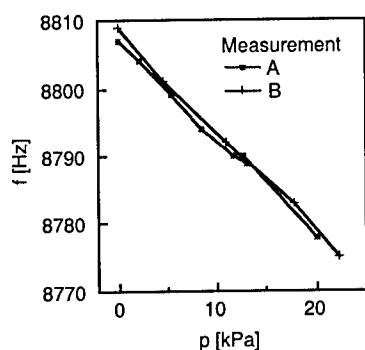
Figure 7: Theoretical and measured values of net capacitance change.
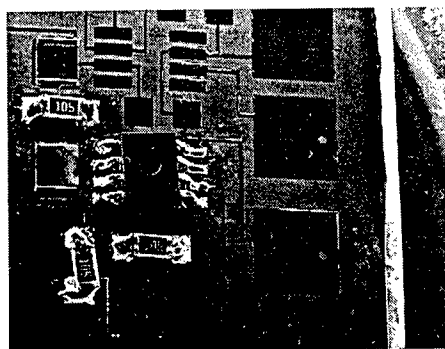
Figure 8. A photomicrograph of the surface-mount chip integrated on laminated Kapton film.

Specific improvements since the last report are:

1. The wiring paths have been reconfigured to minimize the parasitic capacitances.

2. Surface-mount passive components have been integrated in the system (in the previous reporting period, the passive components were external). The sensitivity of the pressure sensor is typically -1.48 Hz kPa^{-1}.

The values of capacitance and/or corresponding frequency change produced by the sensors are easily measurable in their current form. However, in order to achieve higher sensitivity, reduction of the parasitic capacitance is desirable. Furthermore, a multiplexing scheme to address larger numbers of sensors using a control bus has to be developed. We are currently investigating feasibility of flip-chip bonding as well as wire-bonding of the silicon circuitry.

3. Progress in synthetic-jet-based vortex generation for aerodynamic control

The operational range of fixed vortex generators and of vortex generator jets can be substantially extended by using synthetic jet actuators of the type achievable using robust substrate micromachining. An important attribute of these jets is that when they are operated in close proximity in phased arrays (which can be achieved using MEMS technology), they can be cooperatively vectored simply by adjusting the relative phase of their individual control signals. A non-zero phase angle between adjacent jets results in a combined jet that vectors toward the jet that is leading in phase, thus leading to the formation of either clockwise or counterclockwise vorticity.

In the present work, each vortex generator module is comprised of a pair of adjacent jets emanating out of rectangular (300 μm wide) orifices that are parallel along their long (streamwise) dimension and are 1.25 mm apart. The interaction of three jet pairs in the absence of a cross flow is shown in PIV (particle image velocimetry) images in Fig. 9. These images are color raster plots of the velocity magnitude (ranging from 0-3.5 m/s) in the spanwise cross flow (y-z) plane. In the figure below left, all three jet pairs are driven in phase and are nominally normal to the surface. In the figure below right, the right hand side jet in each pair
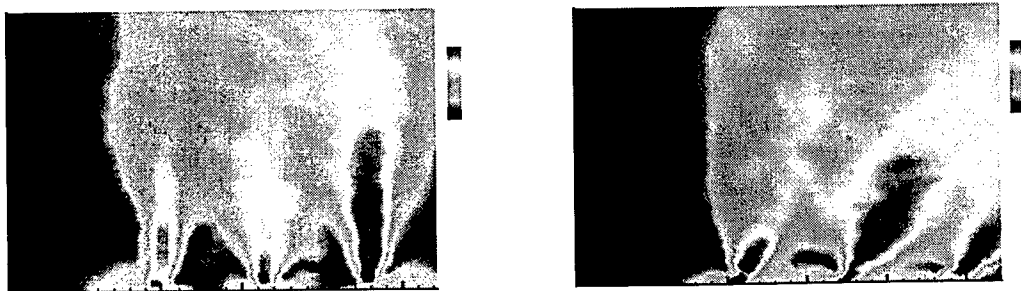
Figure 9: Velocity magnitude plot of vectored microjets

is leading in phase (by 80°) and the resultant jets are all vectored to the right. Other spanwise jet interactions are easily software-programmed by altering the relative phase angle of each pair.

An investigation of the evolution of vectored synthetic jets in a cross-flow is conducted in a small-scale wind tunnel where the jet array module is integrated into the test section floor. In the spanwise (x-y) view, the vertical and spanwise velocity components are captured and thus it is possible to compute directly the sense and strength of the streamwise vorticity. Data is taken at a number of streamwise stations. Figure 10 show superposed images of the velocity vectors in the y-z plane and color raster plots of the streamwise vorticity for a single jet pair taken at x/L = 3 (L is the streamise length of the jet orifice). In the center figure, the phase angle is 0 and the data shows almost no traces of streamwise vorticity. In the right figure the right hand side jet is leading in phase by 130° and the vectoring is to the right leading to the formation of a strong counter-clockwise vortex. When the phase angle is reversed (left) the sense of the streamwise vortex is reversed (i.e., clockwise). Note the appearance of vorticity of the opposire sense in each image next to the tunnel wall owing to the induced boundary layer.
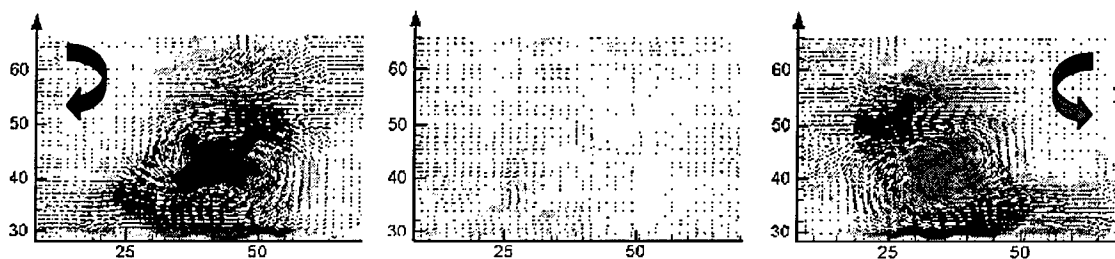
Figure 10: Vectored synthetic jets in a cross-flow

Conclusions

Robust materials have been studied as suitable substrates for micromachined devices. Lamination combined with traditional micromachining processes, has been investigated as a suitable fabrication process for the robust substrates.

A capacitive pressure sensor array using a robust stainless steel shim stock, stainless steel diaphragm, and lamination processing has been designed, fabricated, and characterized. Read-out circuitry has been designed and integrated with the pressure sensors, providing a frequency-modulated output. Surface-mount chips were directly integrated on robust micromachined devices to make high sensitivity devices.

A robust modulator array using a robust stainless steel shim stock, Kapton film as an insulator, stainless steel metal foil as a modulator body has been designed, fabricated, and characterized. The PIV tests for parts of robust modulator arrays show that microjets as high as 6 m/s can be modulated using this device.

Acknowledgement/Disclaimer

References

[1] H. Baltes, "CMOS micro electro mechanical systems," *Sensors and Materials*, vol. 9, pp.331-346, 1997.
[2] R. D. James, J. W. Jacob, and A. Glezer, "A round turbulent jet produced by an oscillating diaphragm," *Journal of Physics of Fluids*, vol. 8, no. 9, pp. 2482-2495, 1996.
[3] D. J. Coe, M.G. Allen, M.A. Trautman, and A. Glezer, "Micromachined jets for manipulation of macro flows" in *Proceedings 1994 Solid-State Sensors and Actuators Workshop*, 1994, pp.243-247.
[4] Chang, S.P., Lee, J.B., and Allen, M.G., "A Robust 8x8 Capacitive Pressure Sensor Array," proceedings of the 1998 Annual Meeting of the ASME, 1998.

TURBULENT SPOT CHARACTERIZATION AND THE MODELING OF TRANSITIONAL HEAT TRANSFER IN TURBINES

Grant Number F49620-97-1-0524

Richard J. Anthony
Dept. Engineering Science
University of Oxford, U.K

Terry V. Jones
Dept. Engineering Science
University of Oxford, U.K.

Tara Chaidez
M.A.M.E. Department
Syracuse University, NY

John E. LaGraff
M.A.M.E. Department
Syracuse University, NY

Abstract
Accurate predictions for boundary layer transition are important to the turbine blade designer since nearly half of the blade chord length may be transitional. Unsteady values for local heat flux and skin friction within this region are dictated by the generation, propagation, and coalescence of turbulent spots within an otherwise laminar boundary layer. Formation of an accurate transition model, which can be used to significantly improve CFD codes, requires experimental measurement of actual turbulent spot characteristics, and how they are affected by parameters such as freestream turbulence, pressure gradient, etc.

A large amount of this experimental work has been carried out using the unique facilities at the University of Oxford under previously supported AFOSR grants. The
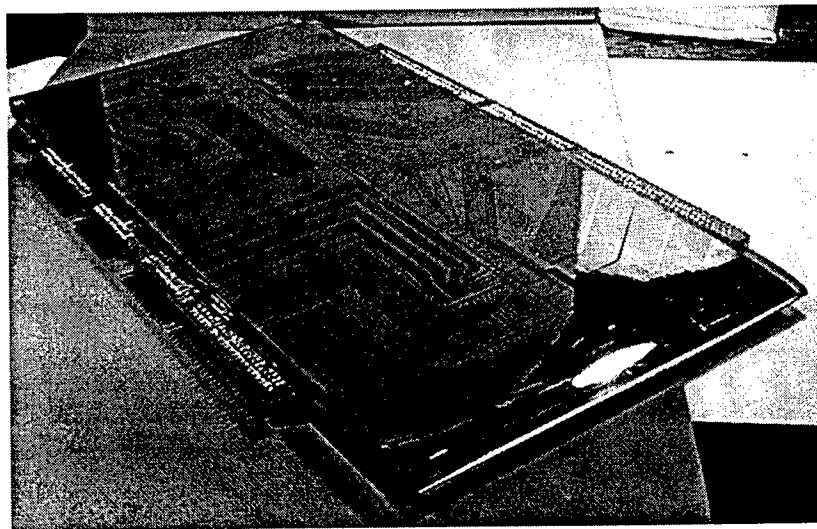
Figure 1. 332mm x 150mm x 10mm Plexi-glass flat plate model covered with a flexible, 50μm thick sheet of polyimide. 233 platinum sensors are sputtered onto the surface for high resolution turbulent spot measurements.
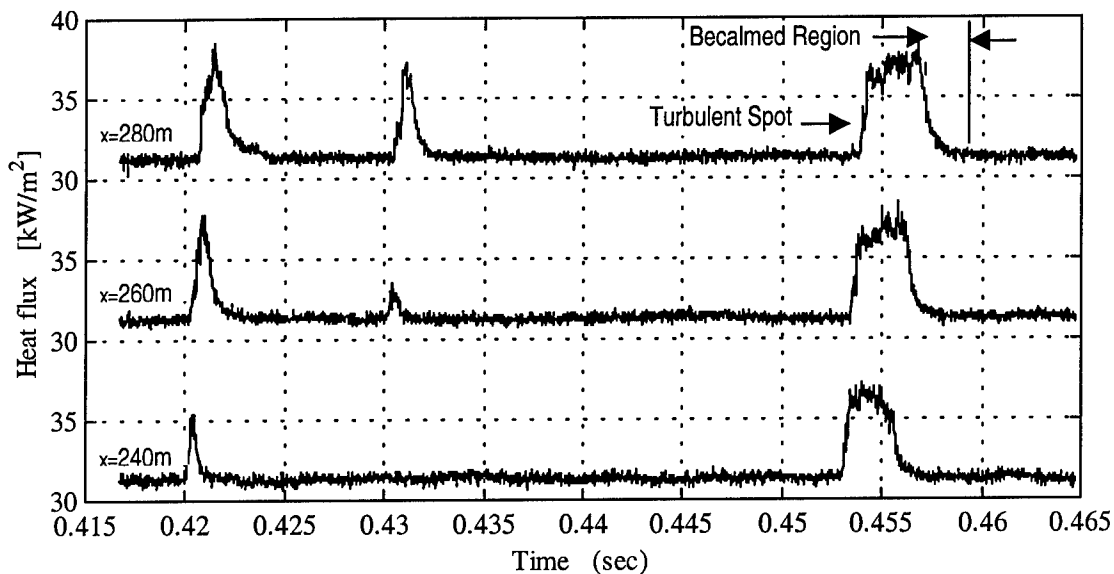
Figure 2. Turbulent spot heat flux signals at three streamwise locations. Turbulent spots develop, grow and convect down the surface, causing a step rise in the local heat flux as is passes.

experimental work has continued this year[1] using new high-density thin film heat transfer gauge arrays, which have been developed specifically for high resolution, high frequency turbulent spot measurements. Parallel to this work, the development was undertaken of a CFD code for transitional heat transfer based on the formation of turbulent spots using actual existing experimental data[2]. Once completed, this code may be incorporated into current CFD codes, thus providing designers with a better tool for predicting transitional heat transfer in turbines.

The experimental work at Oxford has made use of new high density thin film heat transfer gauge arrays and signal processing techniques to capture detail that was previously unobtainable. Details of the new instrumentation are given in Anthony et. al. (1999). High spatial resolution is important for accurate measurement of key transition parameters, especially turbulent spot generation rate. The platinum high density thin film arrays are sputtered onto a flexible, 50μm thick, insulating sheet of polyimide. This sheet of sensors is then glued onto the surface of a Plexi-glass flat plate model. Completed construction of the wind tunnel model is shown in **Figure 1**. The platinum layout consists of 233 heat flux sensors on a single model surface.

The model is installed in a high speed subsonic wind tunnel at Oxford where experiments are run over a range of Reynolds number and Mach number (0.1-0.4). Heat flux is driven by a temperature difference between the model and freestream airflow. The transient run time is very short (~0.3 sec) allowing a 1-D semi-infinite heat conduction analysis to be used (Schultz and Jones 1973). Typical heat flux traces from three consecutive streamwise sensors are shown in **Figure 2**. A passing turbulent spot causes a brief jump in heat flux from the laminar level to the turbulent level. This example of streamwise

---

[1] Second year D.Phil. study done at The University of Oxford by Richard J. Anthony
[2] First year Master's study done at Syracuse University by Tara Chaidez
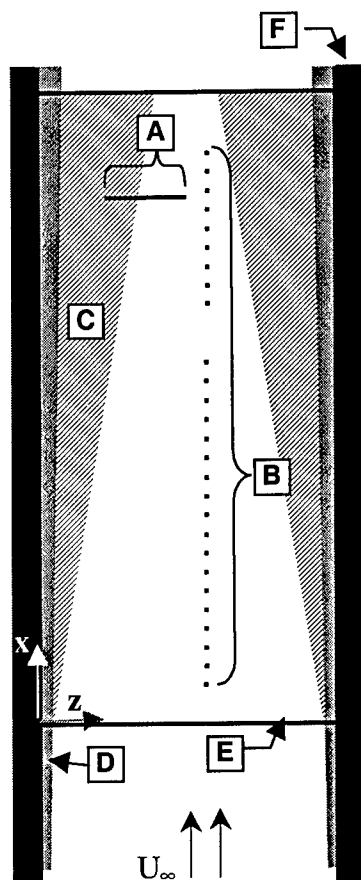
Figure 3. Sensor arrays located on flat plate with multi-moded transition; natural and sidewall induced.

Light – High Heat Flux (Turbulent Boundary Layer)

Dark – Low Heat Flux (Laminar Boundary Layer)

(a) $Rex = 0.78 \times 10^6$

(b) $Rex = 1.1 \times 10^6$

(c) $Rex = 1.61 \times 10^6$

Figure 4. 2-D heat flux history in the z-t plane measured from spanwise array (3-A) over 8 ms at three different Reynolds numbers above Mach 0.2.. Turbulent heat flux is light, laminar is dark.

data shows how spots appear, grow, and convect down the model surface. From this data, the different convection velocities of the spot leading edge, trailing edge, and becalmed region are obtained, and the streamwise growth of the spot can be measured. This data agrees with similar results collected by Clark (1993) and Hofeldt (1997) using traditional thin film gauges.

Data on the propagation and growth of turbulent spots have been well documented. One parameter that has been difficult to measure directly however, is turbulent spot generation rate. This requires high-frequency, high-spatial resolution measurements that traditional thin film gauges could not obtain.

The new high density thin film arrays are unique in that they allow higher spatial resolution to capture greater detail than before. Many sensors may be grouped close enough together that "images" of transitional heat transfer events crossing a spanwise array may be generated. A result of the surface heat flux imaging technique is shown n **Figures 3 and 4**.

This example describes an experiment measuring multi-moded transition across the model. The plate is held at both sides at mid-height of the test section, with air flowing over both top and bottom. While a relatively low turbulence freestream meets nearly all of the leading edge (**3-E**), turbulent endwall boundary layers (**3-D**) growing along the tunnel sidewalls (**3-F**) induce a "bypass" transition near the front corners where the plate meets the wall. The geometry of the test section is crudely similar to a turbine blade lying perpendicular and between its base and the endwall. The induced turbulent spots on the plate grow and convect across the plate at a constant spreading angle of nearly 11° (**3-C**). The effects of the turbulent endwall boundary layer on the plate, which were nearly insignificant at the front of the model, go on to *dominate* the plate's surface towards the rear.

At a distance further down the plate is a spanwise array of 19 closely spaced thin film sensors, which lay partly inside the bypass transition zone and partly outside in the undisturbed boundary layer. Data from this array for three different local Reynolds numbers is shown in **Figure 4**. **Figure 4a** shows what the sidewall induced transition looks like in the z-t plane. A chain of individual turbulent spots is evident near the wall. As we increase the Reynolds number (**Figure 4b**) we begin to see *both* bypass transition in the lower half near the wall, and naturally-occurring turbulent spots in the outside region towards the center of the plate. Note that the detail shown in this image is taken across a 36mm spanwise length in less than 8 ms, in a flow having a freestream Mach number just over 0.2. As we increase Reynolds number once more (**Figure 4c**), the natural transition down the center of the plate has progressed further, with spots merging into one another forming a mostly turbulent boundary layer.

Experiments have been run to quantify turbulent spot generation rate using the "heat flux imaging" capability of the new instrumentation. These experiments will go on to study the effects of freestream turbulence, along with the effects of favorable and adverse pressure gradients. Freestream turbulence will be generated using bar grids placed upstream from the model. Adjustable pressure gradient liners have been manufactured for the test section allowing a range of both favorable and adverse pressure gradients to be tested. Results from these experiments will be added to an intermittency model, which may be patched into CFD code to better model the transition zone.

CFD study:

A parallel study has begun at Syracuse University as part of a two-year Master's thesis. Further investigation of the transition zone will be performed using both analytical and computational techniques. An improved intermittency model will be developed using acquired experimental boundary layer transition data, which accounts for varying pressure gradient and freestream turbulence conditions. A 2-D laminar and turbulent Navier-Stokes time-marching code will be developed, and its output will be compared to experimental results.

Intermittency (γ) is defined as the fraction of time a given point in the boundary layer is turbulent (i.e covered by turbulent spots). Its value ranges from 0, meaning always laminar, to 1.0 meaning always turbulent. Statistical intermittency models provide good

to excellent predictions for parameters within the transition region, thus providing a valuable tool for the turbine blade designer. The idea of modeling transition parameters based on intermittency was first proposed by Emmons (1951). Since then several researchers have refined or expanded upon the so-called universal intermittency model (Narasimha 1985). This study will review existing models in hope of developing an improved model that accurately includes the effects of freestream turbulence and pressure gradient in its prediction.

A 2-D laminar and turbulent time marching Navier-Stokes code is also currently being developed for data comparison of the new model with experimental results. For the laminar viscous flow calculations, the governing Navier-Stokes equations are represented in conservative form, and the equation of state is used to solve for the pressure and to close the equations.

The unsteady equations are advanced to a steady state solution by use of the Jameson four-stage Runge-Kutta scheme. This scheme is second-order accurate for non-linear equations and includes artificial viscosity to the solution to prevent odd-even point decoupling and oscillations near shock waves or stagnation points. This is especially important for the numerical stability when there is not enough natural viscosity present in the solution. This scheme will be further enhanced by use of acceleration techniques as given by Arnone and Swanson (1993) and residual smoothing techniques as given by Jameson (1984).

The effect of turbulence in the flow field will be taken into account by using the eddy viscosity hypothesis. This states that the effective molecular viscosity μ and the effective thermal conductivity k are replaced with a linear combination of the fluid properties in both a laminar and turbulent state. The turbulent quantities will be computed by use of the 2-equation, k-ω turbulence model. This model is chosen over the k-ε model because it offers a better prediction for boundary-layer flows subjected to various adverse pressure gradients (Wilcox 1998).

Figure 5. Planned flowchart of time-marching CFD routine for transition modeling.

Finally, linear combination models will be used to account for the effects of intermittent variations in flow parameters within the

transition region. In this case, the mean flow in the transition zone is a linear combination in the proportion $(1-\gamma){:}\gamma$ of the mean flow in the laminar boundary layer starting from the stagnation point and the turbulent boundary layer beginning from the onset of transition.

Acknowledgement/Disclaimer

References

Anthony, R.J., 1999, "Development of High-Density Arrays of Thin Film Heat Transfer Gauges", *Proc.of the 5ᵗʰ ASME/JSME Thermal Engineering Joint Conference*, San Diego, CA. AJTE99-6159.

Arnone, Swanson, 1993 "A Navier-Stokes Solver for Turbomachinery Applications", Journal of Turbomachinery, April 1993, Vol. 115.

Clark, J.P., Jones, T.V., and LaGraff, J.E., 1993, 'On the Propagation of Naturally-Occurring Turbulent Spots," *Journal of Engineering Mathematics*, special issue on turbulent spots, ed. F.T. Smith.

Dang, 1999 *Monograph in Computational Fluid Dynamics*, Lecture Notes, Department of Mechanical, Aerospace, and Manufacturing Engineering, Syracuse University

Emmons, H.W., 1951, "The Laminar-Turbulent Transition in a Boundary Layer – Part 1," *Journal of the Aeronautical Sciences*, Vol. 18, pp. 490-498.

Hofeldt, A., 1997, *The Investigation of Naturally-Occurring Turbulent Spots Using Thin-Film Gauges*, D.Phil. Thesis, Department of Engineering Science, Oxford University, U.K.

Jameson 1984, *Transonic Flow Calculations*, Princeton University Report MAE 1651

Narasimha, R., 1985, "The Laminar-Turbulent Transition Zone in the Boundary Layer," *Progress in Aerospace Sciences*, Vol. 22, pp. 29-80.

Schultz, D.L. and Jones, T.V., 1973, "Heat Transfer Measurements in Short-Duration Hypersonic Facilities," AGARD AG-165.

Wilcox 1998, *Turbulence Modelling for CFD*, DCW Industries, Inc., © 1998

EXPERIMENTAL INVESTIGATION OF HIGH-SPEED BOUNDARY LAYERS WITH WALL ROUGHNESS

F49620-98-1-0038

Dr. Rodney D. W. Bowersox
Department of Aerospace Engineering and Mechanics
The University of Alabama

Abstract

Analysis of the supersonic mean and turbulent rough-wall boundary layer data was finalized this year. In addition, the numerical simulations of the supersonic case, using simple turbulence models, was also completed. The subsonic (Mach 0.25 and 0.65) blow-down facility construction was completed and testing has begun. This abstract presents an overview of the Mach 2.8 experimental and numerical results and a brief description of the subsonic facility with preliminary data.

Introduction

Compressibility and surface roughness produce complex turbulent boundary layers, which have important practical Air Force applications. For example, *New World Vistas*[1] has identified viscous drag reduction and increased engine efficiency as enabling technologies for future Air Force war fighting capabilities. A key technological challenge that is important to all of the components of vehicle propulsion and aerodynamic systems is the quantification of the of effect surface roughness on turbulent boundary layer characteristics (e.g., skin friction, heat transfer, Reynolds shear stresses, boundary layer growth, etc.). A second Air Force applications is access to space, where for example research for the Space Shuttle program indicated that vehicle control effectiveness was significantly influenced by roughness on the control surface and the forebody ahead of the control panel.[2]

Current predictions of high-speed flow over surfaces with roughness are founded in crude heuristic extrapolations of the incompressible low-speed database, and the development of engineering prediction methods and turbulence models suitable for high-speed flow over rough surfaces is hindered by a scarcity of experimental data.

Objective

The principal objective of this research program is to experimentally investigate the combined influence of compressibility and surface roughness on the mean and turbulent flow characteristics of high-speed high Reynolds number turbulent boundary layer flow to further understanding and predictability.

Approach

A comprehensive experimental program that uses both traditional and laser diagnostic techniques is currently being performed. To provide information that will be useful to a broad range of applications and to quantify compressibility effects, three high Reynolds

13

number flow conditions are being tested: incompressible (M = 0.25), compressible subsonic (M = 0.65), and supersonic (M = 2.8). To better isolate compressibility effects, for each flow condition, the Reynolds number is matched and the same six flow models (described in the next paragraph) are being tested.

Five rough wall models and a smooth wall case, for comparison purposes, are being tested to examine roughness height and blockage effects. The roughened wall models consist of three random sand-grain and two uniformly distributed roughness topologies. The 2-D distributed roughness model has rectangular elements (0.56 x 0.56-mm^2) that span the width of the test section with a wavelength of 2.18-mm. The 3-D distributed plate has cubic pillars (0.56 x 0.56 x 0.56-mm^3) also with a wavelength of 2.18-mm. The surface topology of each model was accurately (to within 4.0%) documented with a confocal laser scan microscope. All of the roughness elements are in the fully rough regime. The topologies coupled with the detailed experimental data will prove useful for developing and validating future turbulence models including LES and DNS methods. Table 1 summarizes the topological statistics for each of the six test plates.

Along with the detailed experimental studies, a companion numerical investigation is being performed primarily to quantify the strengths and weaknesses of current turbulence models. In-house boundary layer and parabolized Navier-Stokes solvers with a variety of popular algebraic models are being used. van Driest first established a simple modification of his near wall damping function for rough-wall flow.[3] Since then, numerous other formulae based on the mixing length method followed. The two additional models investigated here, namely those of Cebeci-Chang[4] and Kragstad[5], also involve modifying the van Driest damping function. These models were compared to supersonic experimental data acquired in this study.[6]

Table 1: Roughness Parameters

Model	Mean height (mm)	Std. Dev. (mm)	Blockage (mm^2/mm)	K_s^2 (μm)	k_s^{+2}
Smooth[1]	0.007	0.005	0.00	N/A	N/A
80 Grit	0.53	0.17	0.53	0.44	104
36 Grit	0.90	0.34	0.90	1.42	395
20 Grit	0.83	0.50	0.82	1.98	572
3D Distrib.	0.56	0.024	0.14	0.91	241
2D Distrib.	0.56	0.024	0.56	1.09	289

[1]For k = 0.007mm, k$^+$ = 1.1 (aerodynamically smooth).
[2]Equivalent sand grain calculated with the method of Schlichting[1] for the Mach 2.8 data plotted with van Driest scaling.

Progress
The supersonic experimental and numerical work was finalized this year. The subsonic blow-down facility construction was completed and testing has begun. Table 2 lists the subsonic tunnel flow conditions.

Table 2: Subsonic Test Conditions

Mach	P (MPa)	T (K)	Re/m (x10^6)
0.25	0.21	292	23
0.65	0.21	273	23

Results

The influence of roughness on a long list of important flow properties has been extensively described in Ref. [7-9]. Due to space limitations, those detailed discussions are not repeated here. A brief qualitative overview of the salient findings, which stemmed from an assimilation of the acquired data, was described in the 1998 Abstract.[10] Hence, only the results from the numerical comparisons are highlighted here. A detailed description of the methods, numerical validation, and results can be found in Fan and Bowersox.[6]

Shown in Fig. 1a are the velocity profiles for all six plates plotted with defect law [4-6] scaling. The collapsing of the defect law profiles was the expected result based on the low-speed database and the high-speed data (also shown on Fig 1a). The agreement between the present predictions and the experimental data was considered very good. Representative Law of the Wall plots for the smooth and 20 grit plate (roughest plate), with van Driest scaling, are shown in Fig. 1b. The predicted profile for the smooth plate is in excellent agreement with both flat plate theory and the experimental data. The predicted velocity profiles agreed very well with the experimental data in the outer region. The differences between the three models became more significant in the inner region ($y^+ < 100$). However, experimental data were not available in this region for comparison. Representative mean density profiles are shown in Fig. 1c. For the smooth and rough plates, the calculations were all in good agreement with experimental data.

Representative turbulence shear stress profiles for the smooth and 20 grit plate, normalized by the local mean velocity, are plotted in Fig. 2. The predicted Reynolds shear stresses from all three turbulence models for all six plates matched the LDV data very well, demonstrating that the Reynolds shear stress was well modeled by each formulation. As was the case for the experimental data, the numerical shear stress profiles in the outer region were all independent of the roughness Reynolds number for the outer scaling used in Fig. 2. For the roughest case, the van Driest model produced slightly better agreement with the experimental data, when compared to the other two.

For the rough-wall predictions, each of the three models performed well on a different integral parameter. For example, the Kragstad model produced the largest skin friction coefficients, which were still less than the experimental data by nominally 6.0%. The van Driest model produced better boundary layer thickness predictions (within 6.5%), and the Cebeci-Chang formulation produced better momentum thickness predictions (within 4.0%). However, the differences between the three models were significant, where some predicted quantities were 25% apart.
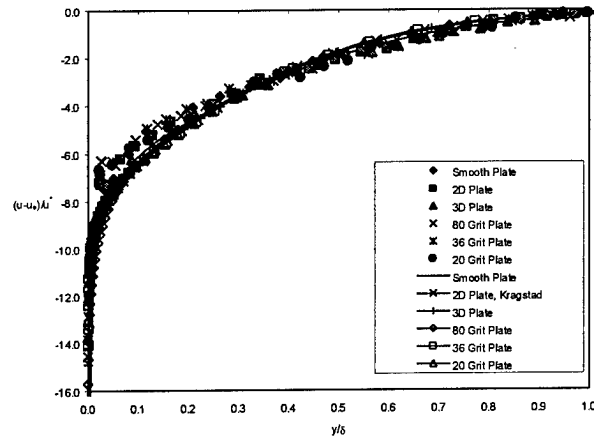
(a) Defect Law Plot.
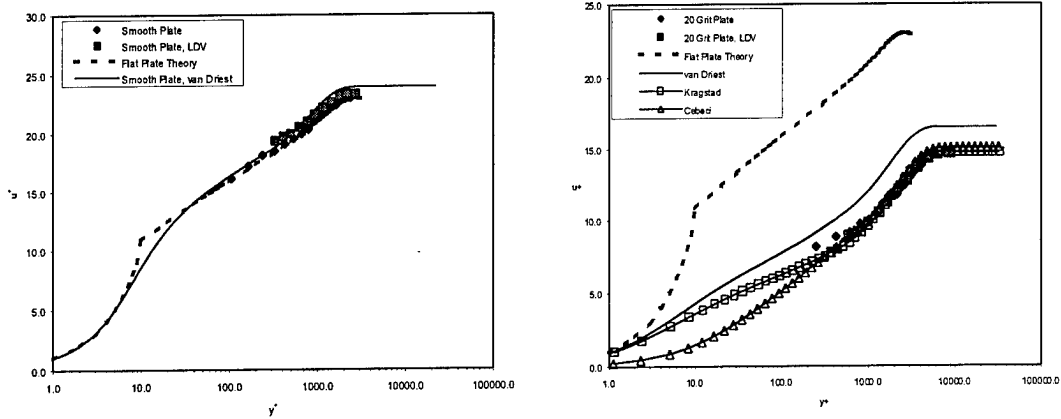
(b) Representative Law of the Wall plots (left: smooth plate, right: 20 grit plate).
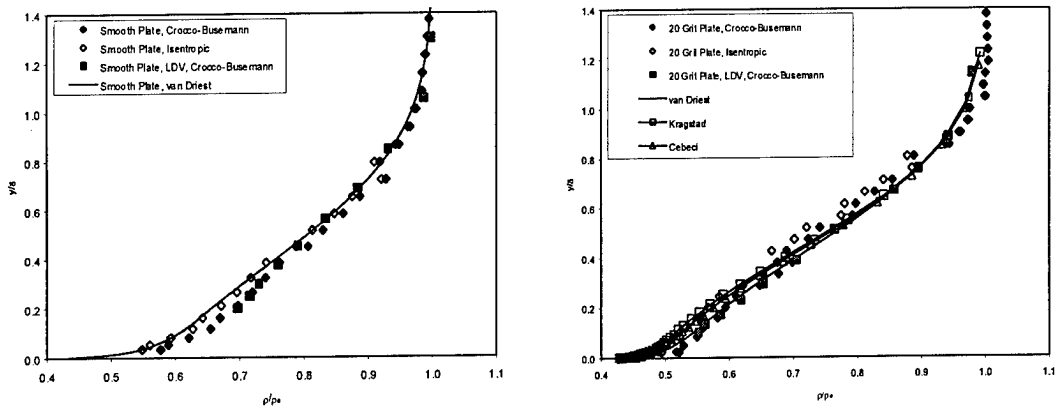
(c) Representative density plots (left: smooth plate, right: 20 grit plate).
Fig. 1 Comparison of mean flow results to experimental data (Mach 2.8).
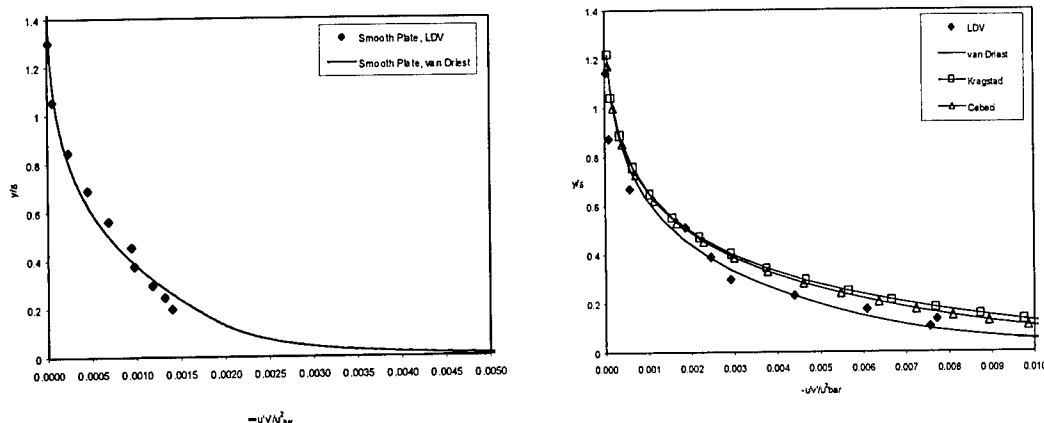
Fig. 2 Comparison of Reynolds shear stress to experimental data for the smooth (left) and 20 grit plates (right).

Future Work
The future plans for this project parallel the original research proposal. The subsonic experimental testing and numerical calculations will continue through 2000. Also during 1999, the supersonic rough wall wall shear stresses will be reaccomplished using direct measurement floating element sensors.

Personnel
Rodney Bowersox is the lead PI. Student support has/is provided by Capt. Robert M. Latin (PhD student, completed 6/98), Mr. Huaiguo Fan (MS student, completed 9/98), and Victor Pritchett (PhD student, in-progress).

FY98 Publications
Latin, R., *Influence of Surface Roughness on Supersonic High Reynolds Number Turbulent Boundary Layer Flow*, Air Force Institute of Technology PhD Dissertation AFIT/DS/ENY/98M-02, March, 1998.

Latin, R. and Bowersox, R., "Influence of Surface Roughness on the Mean and Turbulent Flow Properties of Supersonic Boundary Layer," AIAA-99-1017, AIAA 37th Aerospace Sciences Meeting, Reno, NV, Jan. 1999. In-review *AIAA J.*

Fan, H., *Numerical Analysis and Turbulence Modeling Of High-Speed Turbulent Flow Over Rough Surfaces*, The University of Alabama MS Thesis, September 1998.

Fan, H. and Bowersox, "Numerical Analysis of High-Speed Flow over Rough Surfaces," AIAA-99-2381, 35th AIAA/ASME/SAE/ASEE Joint Propulsion Conference, Los Angeles CA, June 1999.

Technology Transitions
This work is closely coordinated with the AFRL/PRSS high-speed propulsion effort (monitor: Dr. D. Glawe). In addition, this work is directly related to many of the goals

listed in the *New World Vistas* [e.g., drag reduction and improved engine efficiency (IHPTET) for hypersonic missiles, global reach aircraft and access to space].

Acknowledgement/Disclaimer

References

1. USAF Advisory Board, *Aircraft and Propulsion Technologies, New World Vistas Air and Space Power for the 21st Century*, USAF, 1995.
2. Christoph, G. H., "Prediction of Rough-Wall Skin Friction and Heat Transfer," *AIAA Journal*, Vol. 21, No.4, 1983, pp. 509-515.
3. van Driest, E.R., "On Turbulent Flow Near a Wall," *Journal of Aerospace Science*, Vol.23, Nov.1956, pp. 1007-1011.
4. Cebeci, T. and Chang, K.C. "Calculation of Incompressible Rough-Wall Boundary-Layer Flows," AIAA Journal Vol. 16, No.7, 1978, pp. 730-735.
5. Kragstad, P., " Modification of the van Driest Damping Function to Include the Effects of Surface Roughness," *AIAA Journal* Vol.29, No. 6, 1990, pp. 888-894.
6. Fan and Bowersox
7. Latin, R., *The Influence of Surface Roughness on Supersonic High Reynolds Number Turbulent Boundary Layer Flow*, PhD Dissertation, AFIT/DS/ENY/98M-02, March 1998.
8. Latin, R. and Bowersox, R., "Influence of Surface Roughness on the Mean and Turbulent Flow Properties of Supersonic Boundary Layer," AIAA-99-1017, AIAA 37th Aerospace Sciences Meeting, Reno, NV, Jan. 1999.
9. Latin, R. and Bowersox, R., "Influence of Surface Roughness on Supersonic Boundary Layer Turbulent Flow Structure," *14th International Symposium on Airbreathing Engines (XIV ISABE)*, Florence, Italy, Sept. 5-10, 1999.
10. Bowersox, R., "Experimental Investigation Of High-Speed Boundary Layers with Wall Roughness," Proceedings from the 1998 AFOSR Turbulence and Internal Flows/Unsteady Aerodynamics and Hypersonics Conference, Annapolis MD, August 1998, pp. 31-36.

MEMS-BASED CONTROL OF AIR-BREATHING PROPULSION

AFOSR/DARPA Grant No F49620-97-1-0526

Kenneth Breuer
Department of Aeronautics and Astronautics
Massachusetts Institute of Technology
Cambridge, MA 02139

Choon Tan
Department of Aeronautics and Astronautics
Massachusetts Institute of Technology
Cambridge, MA 02139

Abstract

Two methods for controlling tip leakage flows in axial compressors are discussed. The first method reduces the effective tip gap while the second method forces enhanced mixing of the tip gap shear layer. Preliminary results indicate that both methods work, but further measurements and exploration of the large parameter space need to be conducted in order to further quantify and optimize these phenomena. MEMS devices in support of the program have also been developed successfully.

1 Program Objectives

The objectives of the research program are to demonstrate effective and efficient flow control methods to alleviate problems associated with tip leakage flows in axial compressors. Benefits of successful control include improved stage performance and efficiency as well as increased stall margin.

2 Flow Control Strategies

Two approaches are being investigated. The first is to use a synthetic jet, located on the compressor casing, to create a virtual wall and to reduce the leakage flow through the tip gap. This is termed a "steady" control strategy since the control is effected through a steady modification of the flow field. The second approach is an unsteady flow control strategy, in which the leakage jet (which has the characteristics of a wall jet) is forced at an appropriate frequency and amplitude in order to enhance the jet spreading and subsequent fluid mixing. Both of these approaches are illustrated schematically in Figure 1, and preliminary results are presented in the current research update.
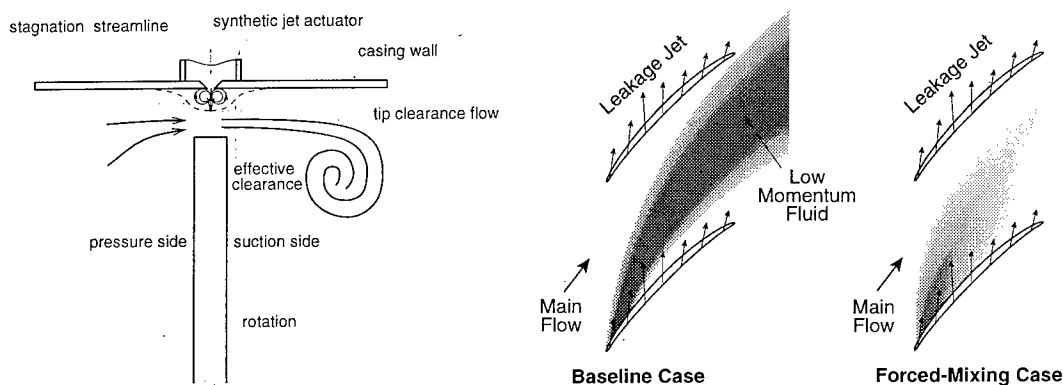
Figure 1   Schematics of control strategies. The left panel shows the "steady" control in which the effective tip gap is reduced by the introduction of a momentum source at the casing wall. The right two panels shows the "unsteady" control in which the leakage jet is forced at its natural frequency, resulting in enhanced mixing, and thus improved pressure recovery.

3   Experimental Results

Two experiments have been designed to test the concept and particulars of active control of tip leakage flows. The first is a very simple experiment in which a tip flow is generated without the complication of the axial core flow. This is to demonstrate that control of the tip flow can be achieved and to assess the effects of actuator amplitude and frequency as functions of the tip leakage velocity and driving pressure. The second experiment is a more complete model of the compressor flow and consists of a five-bladed cascade experiment with a variable tip clearance.

Figure 2. Schematic of experimental setup for actuated tip flow. Both the gap height and the location of the actuator with respect to the gap can be varied.

3.1   Actuated Tip Flow Experiment

As mentioned above, this experiment was designed to confirm that the concept of active flow control using actuators is indeed valid and can produce a significant effect on the flow. The apparatus consists of a pressurized box that sits on above the actuator. (Figure 2). The pressure box has an adjustable faceplate so as to allow for variation in the height of the gap, which simulates the tip clearance of the compressor blade. The baseplate sits above the actuator, which in this case is a large compression driver.   An adjustable gap provides the actuator exit orifice. Flow visualization is achieved with a smoke wand placed inside the box, which then bleeds through the gap. By varying the box pressure and tip gap, one can control the velocity and mass flow through the gap. In addition, the frequency and amplitude of the actuator can be varied as well as its position with respect to the gap

Figure 3. Photographs of tip flow visualized using smoke particles. The left frame shows the flow paths without control. The right frame shows the flow patterns with the actuator aligned with the leading edge of the tip and operating.

Qualitative visual results are illustrated in Figure 3 which shows photographs of the tip flow before and during the use of actuation. With the actuator turned off, the smoke flows freely from left to right through the gap, and the tip vortex rollup is clearly visible to the right of the wall. However, upon turning on the actuator, the tip flow is clearly blocked and very little smoke leaks through the tip. By varying the location of the actuator relative to the tip, it was found that the control was more effective when the actuator jet was situated at the leading edge of the "blade". Behavior based on varying other parameters was as expected. A reduction in the amplitude of the actuator resulted in a lessened effect on the flow. An increase in flow rate or a decrease in the gap height, both of which increased the flow velocity across the gap (for a given pressure difference across the gap), also resulted in a reduction in actuator effectiveness. Quantitative data is currently being obtained using hot wire measurements to map out the reduction of mass flow through the gap as functions of the gap dimensions (height, length) and the actuator amplitude, frequency, geometric design and placement in the gap.

3.2 Cascade Wind Tunnel Experiment

The cascade test section has been designed and has been fabricated in a low-speed wind tunnel at MIT. The cascade consists of five blades, three of which are cantilevered to provide a variable tip gap. The baseline performance (with no control) shows good agreement with similar experiments, indicating a loss coefficient that increases linearly with increasing tip gap. Three actuators are placed above the center blade located approximately near the 10, 30 and 50% chord locations. The actuators are voice-coil driven synthetic jets. The resonant frequency of the devices was low (around 50 Hz) and they were operated above this frequency, but below the Helmholz frequency of the cavity (about 1200 Hz). Peak actuator velocities ranging from 10 – 40 m/s were typical, depending on the voltage and frequency of operation.

The control experiments were performed at the relatively low Reynolds number of 0.8×10^5. This was due to limitations in the current actuator operation. The total pressure loss coefficients measured for two cases (actuator off and on) at 3%C downstream of the trailing edge of the blades are shown in Figure 4. The tip clearance was set to 3%C. Two effects of control can be observed. Firstly, there is a clear effect on the tip vortex region which is almost completely eliminated in the controlled flow. However, a secondary loss region is observed away from the wall and closer to the blade. The exact nature of this needs to be determined using full measurements. A second, less obvious, effect of control is that the loss in the wake of the blades appears to be reduced. This is probably a slightly spurious result due the low Reynolds number of the test in which case, the forcing "cleans up" the two dimensional wake losses which might be due to a low-Reynolds number separation. This effect will also be examined more carefully during the coming year.

Figure 4. Contours of total pressure loss coefficient, ω measured in axial plane 3%C downstream of the cascade exit. Top: with actuator off. Bottom: actuator on.

4 MEMS Device Development

The MEMS component of the program is not intended to be a limiting feature of the research, but rather is aimed at providing sensors and actuators that can be used in the active control programs outlined above. To this end, the program's efforts have focused on the development of shear stress and temperature sensors, as well as glow-discharge actuators. The shear and temperature sensors are based on standard thermal sensor designs that utilize the temperature coefficient of resistivity of a sensor metal, in this case Platinum.

The goal of the sensor design is to minimize the thermal mass of the sensor to maintain a high frequency response. This requires that the sensor element be small and (more importantly) that the sensor be thermally isolated from the substrate. These goals are accomplished by depositing the Platinum sensor film on a very thin (1500 A) Silicon nitride membrane suspended over a deep (20 micron) evacuated cavity. The temperature sensors are effectively the same sensors, but are operated in a four-point manner in which a small current (not enough for Ohmic heating) is passed through the sensor through a first set of leads. The voltage drop across the sensor (which will vary with temperature) is read off via a second pair of leads.

Figure 5. Optical micrograph, showing second-generation shear-stress and temperature sensors. The thin white line is the exposed platinum of the sensing resistor exposed by etching the over-deposited gold. The light blue circle is the 1500A nitride membrane covering the vacuum cavity. The left frame shows a single sensor while the center frame shows an array of three two-dimensional sensors, each of which enable a directional measurement of shear. The right frame shows a temperature sensor with a four-wire excitation and readout.

In testing, the sensors show excellent performance with good sensitivity and frequency response (square-wave response test was limited by the anemometer circuitry which rolled off at 40 kHz). Further testing is planned during the coming year.

4.1 Glow Discharge Actuators

Recent developments in flow actuators have resulted in the increased interest in glow discharge actuators which offer the possibility of effective actuation through the generation of an RF discharge. The chief attraction of such devices are ease of fabrication and that they have no moving parts. Macroscopic Glow discharge devices typically require very high voltages (1000 – 5000 V) and frequencies in the 1-5 kHz range. These voltages are not very convenient for many experiments or applications, and it is thought that if the dielectric layer can be reduced in thickness, then similar field strengths can be achieved with lower voltages, albeit at higher frequencies. With this in mind, a first generation glow discharge actuator was fabricated using a Silicon wafer as the

Figure 6: Optical Photograph of second-generation glow discharge actuators. The interdigitated fingers are separated by a transparent polyimide layer, 1 micron thick.

ground plane, a thin (1 micron) silicon dioxide film as the dielectric and gold film deposited on top of the oxide layer as the drive electrodes. Moderate voltages were required (200V) to operate this device, but the insulating layer (silicon oxide) broke down rather quickly. For this reason, second generation device have been fabricated with a

more robust design (shown in Figure 6). The new design has two layers of patterned electrodes, separated by a polyimide layer. These devices and will be tested in the coming months.

5 Summary of Recent Accomplishments

In the past period, the following milestones have been accomplished:

- Experimental
  - Design and fabrication of experimental facilities, baseline performance measurements
  - Successful preliminary control of tip vortex flow in cascade
  - Successful demonstration of mass flow control in prototypical tip leakage flow

- MEMS Sensors
  - Design and fabrication of second-generation thermal sensors
  - Successful testing of flow sensors
  - Benchtop testing of first-generation glow-discharge actuators
  - Design, fabrication of second-generation glow discharge actuators

6 Goals for Coming Year

- Experimental
  - Parametric characterization of tip leakage control
  - Demonstration of effective tip leakage control in prototype and cascade experiments
  - Design of larger-scale rotating rig experiment
  - Design of control system needed for full-up active control

- MEMS Sensor/Actuators
  - Full testing of Glow discharge actuators
  - Integration of sensors/actuators into cascade/tip leakage experiment

Acknowledgement/Disclaimer

REAL-TIME FEEDBACK CONTROL OF MIXING IN A HEATED JET

CONTRACT NUMBER: F49620-97-C0021

A. Cain, Y. Ikeda
Phantom Works
The Boeing Company

P. Moin
Mechanical Engineering Department
Stanford University

J. Freund
Department of Mechanical and Aerospace Engineering
University of California, Los Angles

D. Parekh
Georgia Tech Research Institute

Objectives

The primary objectives of this program are to investigate methods for real-time feedback control of mixing in heated jets and to demonstrate the resulting techniques in a laboratory environment.

Status of Effort

Much of the effort in this investigation concerns the choice of a systems model. The model must be of sufficient fidelity that the essential aspects of mixing in a heated jet are captured but at the same time the approach must be simple enough that the calculations enable a real-time capability. The reference direct simulation calculations provide a check on simpler approaches. In the past year several approaches have been examined. Reduced resolution direct simulations at low Reynolds numbers have shown promise. Even time-accurate Reynolds averaged calculations look useful. Among the more interesting approaches examined include the use of discrete vortex methods and a model based on eigenmodes of the linear equations applied to an evolution equation at finite amplitude. The accomplishments section of the report will summarize these efforts.

In the controller design effort, we have finished evaluation of candidate techniques and downselected a technique for laboratory demonstration. The technique we selected was proposed by Calise at Georgia Institute of Technology, and uses neural networks (NN) to perform system identification and feedback linearization. The data for system identification are being generated by means of computational fluid dynamics (CFD) simulation. WIND code, which is the Boeing in-house Navier-Stokes solver that has been released into the public domain under the NPARC Alliance, has been employed to

perform the simulation. As soon as the controller design is completed, it will be implemented into the scaled nozzle system, and the performance will be demonstrated.

Accomplishments/New Findings
It is desirable in many circumstances to enhance mixing in the exhaust from aircraft engines. Applications include lift enhancement, signature reduction, and temperature reduction on blown flaps. This work focuses on the latter case. The blown flap on a C-17 is currently made out of titanium to avoid melting. If mixing can be significantly enhanced so that the plume temperature is reduced, the flap could be constructed from aluminum, a much lighter and less expensive alternative.

Recently, acutuators have been developed and tested on a full-scale engine which have the control authority to accomplish this objective. The goal of this work is to optimize their parameters to maximize their effectiveness. This is being undertaken as a joint experimental, numerical, and control theory effort.

The past 25 years have seen many examples of open-loop control of the flows with significant practical importance. During the same time, there have been tremendous developments in the area of closed-loop feedback control strategies for linear and nonlinear systems. It has been seen in many applications that coordination of control application with state measurements in the closed-loop setting is essential for optimum system performance. Thus, the possibility of feedback control of flow systems such as turbulent jets should be carefully examined. However, such control problems also pose technical difficulties as turbulent flow systems are multi-scale and difficult to compute with a high degree of fidelity. Thus, the present work explores the development of low-order system models for use in the feedback control framework for the jet control problem. The present work is part of a collaboration involving Georgia Tech, Stanford University, UCLA, and The Boeing Company.

1. Simulation based efforts

Simulations were used in two different ways to study and improve jet mixing and its control. In the first, a direct numerical simulation database was probed to examine the relation and reliability of different metrics (or, in control theory terminology, "cost functions") for mixing; in the second, relatively inexpensive simulations were used in a "proof-of-concept" demonstration to evaluate the utility of evolution strategies for optimizing jet mixing controls. Both efforts are ongoing, with particular focus on the application of evolution strategies to optimize jet actuation. These efforts are summarized in this section.

To provide a realistic simulation database to analyze, large-scale direct numerical simulations were conducted of jets forced with a flapping type excitation at Strouhal numbers of 0.2 and 0.4. The jet Reynolds numbers was 3600, which might seem low if compared to corresponding experiments, but all essential aspects of the experiments were reproduced in these simulations. A baseline, unforced case was also simulated. These databases were probed to evaluate the utility of metrics for mixing that might be

incorporated into a feedback control law. Of particular interest was a planar integral of jet fluid mixture fraction raised to the fourth power as might be measured optically. A comparison between an instantaneous profile, a one forcing period average, and a long-time average is shown in Fig. 1. The most notable result is that the long-time and single-period averages are extremely close, which indicates that the one period average gives a reliable measure of the long-time mean of a periodically forced jet in a measurement time of one forcing period. This result is not at all obvious given the apparent chaotic behavior of the jet turbulence (Fig. 2).
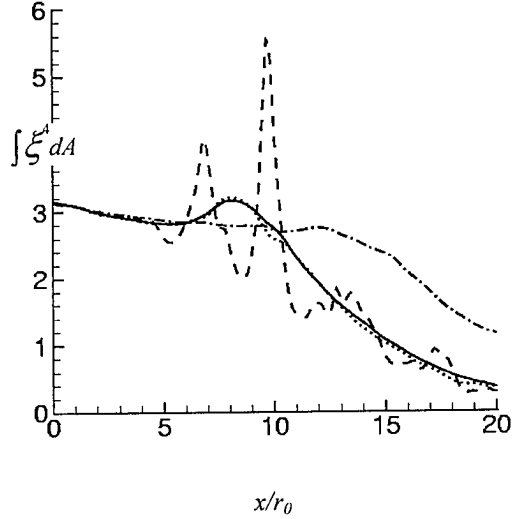
Fig. 1. Instantaneous (-------), one forcing period (·············), and long time average (———) of ξ^4 integrated over planes normal to the jet axis. ξ is the jet fluid mixture fraction. Also shown is the same metric for an unexcited jet (--·--·--).
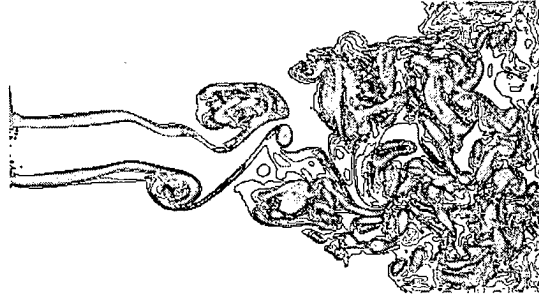
Fig. 2. Turbulence in the jet forced with $St = 0.2$ visualized with vorticity magnitude.

Our second approach is to use evolution strategies for jet mixing. These strategies are based on the basic principles of evolution: a reproduction cycle, natural selection and diversity of variation. They are robust and highly parallel. In the context of jet optimization, an individual of the evolution process is defined as a vector of the jet parameters for n modes of excitation, $(St_1, A_1, \phi_1;...;St_n, A_n, \phi_n)$, where St is the Strouhal number, A the amplitude of the actuation, and ϕ the phase relative to the other modes.

The suitability of a vector of parameters for jet optimization is evaluated with a metric or fitness function. An initial population of vectors is subjected to repeated mutation and selection until a sufficiently good individual is found.

Low Reynolds number simulations were used to test the applicability of evolution strategies to the jet control problem. Here the forcing from a fluidic actuator (Fig. 3) was optimized for maximum excitation of the jet. These particular actuators were based on those used in experiments and on full scale engines. In these tests, a superposition of three harmonic modes constituted the blowing from the actuators. Each of these modes had an amplitude U_a, a phase ϕ (relative to the other modes), and a Strouhal number St_D that were varied by the optimization algorithm. Initial values for the parameters are shown in Table 1 and an instantaneous picture of the jet's response to this excitation is given in Fig. 4(a). The jet is seen to be perturbed, but there is little gross excitation of the large-scale flapping mode that has been found to be effective for enhancing mixing. After 200 iterations, the evolution algorithm arrived at parameters that did excite the jet in this way (Fig. 4b) and these parameters are shown in Table 2. It is interesting that the optimization procedure significantly reduced the amplitude of two of the signals leaving only a single high amplitude mode with Strouhal number of approximately 0.2 forcing the jet. This same single mode was discovered by ad hoc experimentation to be very effective at exciting the jet in experiments (D. E. Parekh *et al.*, AIAA 96-0308,1996).
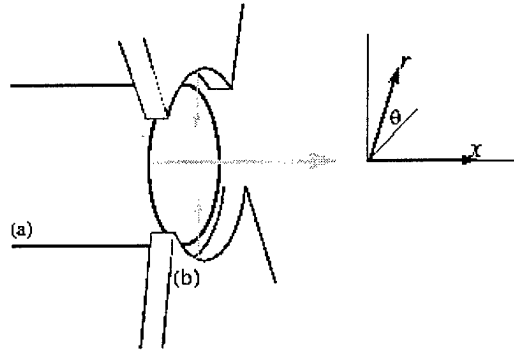
Fig. 3. Geometry schematic showing the jet nozzle (a) and the actuators (b).

Signal #	U_a/U_j	St_D	ϕ
1	0.45	0.30	0.00
2	0.40	0.20	0.70
3	0.35	0.50	1.00

Table 1: Initial forcing parameters.

Signal #	U_a/U_j	St_D	ϕ
1	0.04	0.33	0.54
2	0.42	0.17	0.31
3	0.07	0.45	1.57

Table 2: Forcing parameters after 200 iterations.

For this application, the modeled actuators were very similar to those implemented in corresponding experiments. Given the success of these simulations, further optimization will be carried out in collaborative experiments which have the advantage that many iterations can be performed in a short period of time. In future work the simulations will be used to optimize the actuators themselves and work proceeds in this direction. Such an optimization is difficult to undertake in the laboratory because it is impossible to construct a single device that generates fluidic actuation with a completely arbitrary blowing profile, frequency, and amplitude. However, such a general actuator is straightforward to implement in a simulation. The only constraint placed on the actuators will be that they are realizable in hardware, so, once they are optimized, they can be built, tested, and applied.

Evolutionary optimization techniques are robust, but they require large numbers of iterations in order to achieve the optimization goal. In order to minimize the computational cost required for each optimization cycle, Direct Numerical Simulations of an incompressible jet at a Reynolds number 1200 have been performed. This allowed us to further enhance the type and parameters of the evolution strategy and analyze the metric for the optimization. The jet has been perturbed by modifying the initial velocity profile. In order to reduce the computational cost, the DNS has been performed on a rather coarse grid, and a fitness function has been chosen which allows estimation of the long-term response of the jet from the early stages of the simulation. One possible choice is based on the volume integral of the squared radial velocity, which is a measure for the spreading of the jet and hence a suitable metric for turbulent mixing. The integral has been calculated within the subdomain between 5 and 10 jet diameters from the nozzle. It is necessary to investigate how the fitness value changes as a function of the time in the DNS. Fig. 4 shows the integrated radial velocity as a function of time for different Strouhal numbers. While a definite decision about the best solution is only possible at large times, an estimate of the Strouhal numbers that lead to large spreading angles of the jet can already be made at t=1.8, and the fitness value has been determined at that time. The optimization identified St_D=0.22 as one effective control mechanism, which corresponds to an actuation at almost the same frequency as that shown in Table 2. For this excitation large jet spreading angles are observed. Another suitable excitation is achieved for approximately the double frequency St_D =0.45.
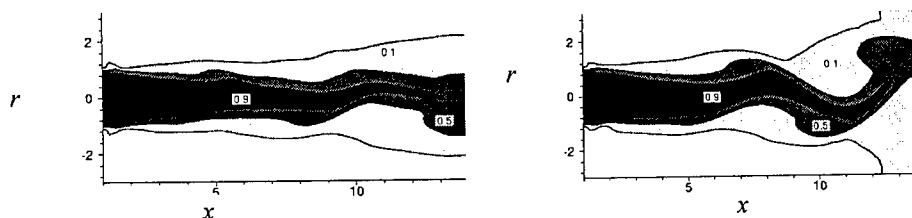
Fig. 4. Jet mixture fraction for the first guess parameters (a) and after the best case parameters after 200 iterations (b).

If we choose as a fitness function the integrated value of the radial velocity over the whole computational domain (0 to 10 diameters from the orifice), the best solution is found for another Strouhal number, St_D =0.38 (see Fig. 5). Since the best solution depends on the fitness function that is chosen for optimization, it must be chosen and tested carefully for each application. An instantaneous picture of the flapping jet, obtained for St_D =0.38 and amplitude U_a/U_j =0.05, is shown in Fig. 6. For comparison, the vorticity magnitude of the compressible jet at St_D =0.2 is shown in Fig. 2. A passive scalar has been used to visualize the spreading of the jet. The amount of spreading is very large when compared with the small amplitude of the actuation. Present efforts are directed toward the improvement of the convergence rate of the evolution strategies and the incorporation of a penalty for large amplitudes of actuation in the fitness function.
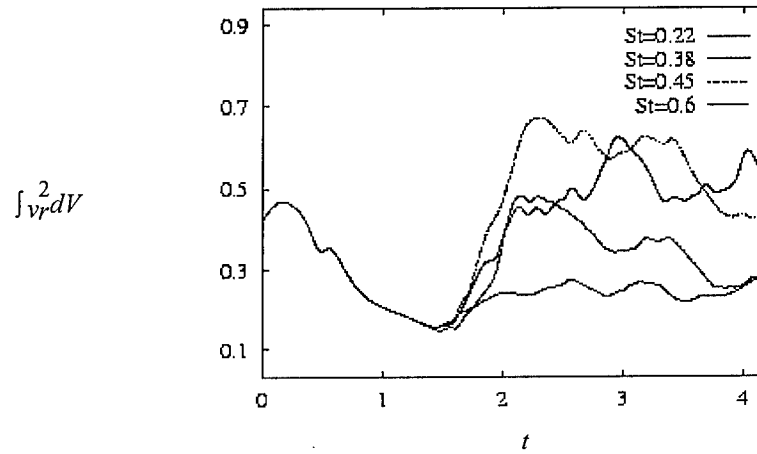
Fig. 5. Fitness value as a function of time for different Strouhal numbers.
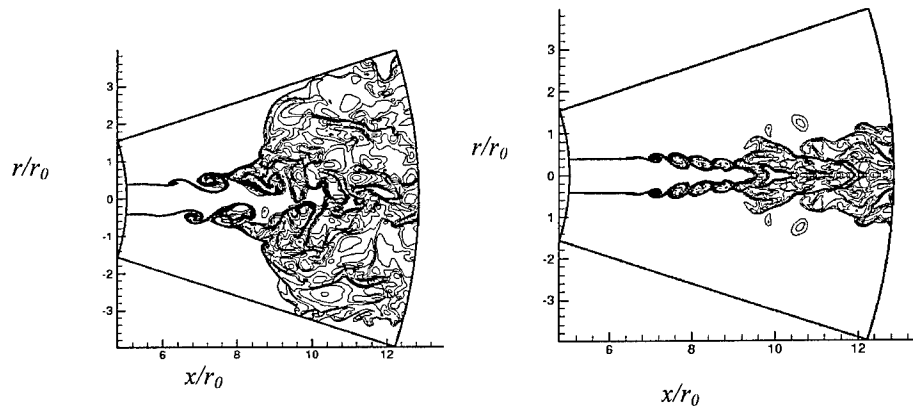
Fig. 6. Contours of the passive scalar field in the $\theta = \pi/2$ and $\theta = 0$ plane for an incompressible Reynolds number 1200 jet excited at Strouhal number 0.38.

30

2. Vortex model of bifurcating and blooming jets

We model a circular jet by the combination of discrete vortex filaments and a semi-infinite cylindrical sheet of vorticity. The cylindrical sheet models the nozzle source flow whereas the ring filaments model the vortex rings generated by the axial excitation of the shear layer. The interaction of the vortex sheet with the filaments is assumed to be such that the sheet influences the motion of the filaments but the filaments do not influence the sheet. The Strouhal number sets the time between creation of new ring filaments at the origin. This model can simulate the experimental observations as shown in Figs. 7 and 8.

For the optimization, several metrics for jet spreading angle were considered, including the average radial displacement of the vortex elements, jet spreading angle, and ring trajectory angles. We also considered amplitude normalized formulations of these metrics to account for the cost of excitation. The metrics were evaluated over a broad range of test cases to check if they would be robust enough to provide the proper relative rating over the parameter space considered. Some metrics are artificially biased by the initial displacement of the rings or by normalization with very small excitation amplitudes. One metric that is both simple and effective for this simulation is the average angle of the nominal ring trajectories. For each case, this metric is evaluated after the same number of periods (typically, eleven) of axial excitation. The nominal ring trajectory angle, θ, is defined as the angle between the jet centerline and the line that connects the center of the jet exit to the centroid of the vortex ring nodes.

Starting with an initial guess for each of these parameters and constraints on the range of values allowable for each parameter, the genetic algorithm searches the range of values allowable for each parameter, the genetic algorithm searches to optimize jet spreading. The scope of this work did not allow for an exhaustive investigation of the parameter space and convergence characteristics, but even these preliminary simulations yielded promising results. With all four parameters varied simultaneously, the genetic algorithm selects a blooming jet similar to what has been observed in experiments.

Figure 7 Blooming jets: Experiments
of Lee and Reynolds (1985)
$\beta = 1.7, A_\eta = 0.04, St_a = 0.46, \mathrm{Re} = 4300.$
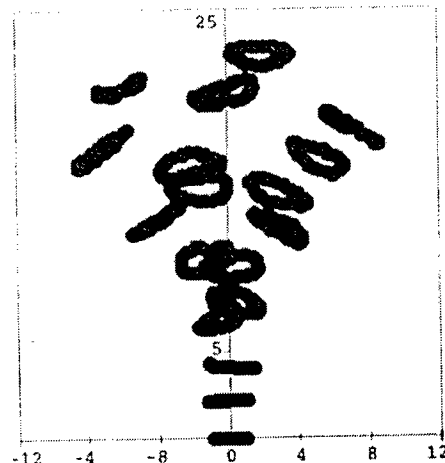
Figure 8 Blooming Jets: Simulations
$\beta = 1.7, A_\eta = 0.05, St_a = 0.55$

31

Initially we expected the algorithm to select a bifurcating jet similar to Fig. 8 with values St and Ah that maximize the spreading angle. Instead, a unique jet flow (Figs. 9and 10) was found that had never been observed in previous experiments or calculations. This jet flow initially resembles a bifurcating jet. Several diameters downstream, however, the two branches of the jet exhibit a secondary bifurcation in which the rings change direction along a path with an azimuthal angle about π/4 different from their original trajectory. This results in a wide spreading angle as seen in Fig. 10.
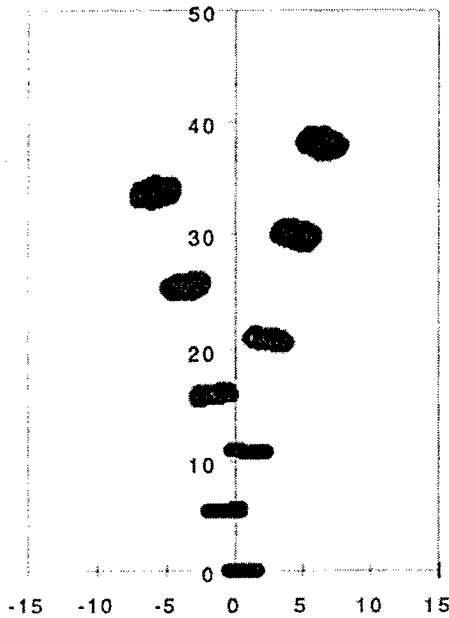
Figure 9 Hybrid bifurcating jet with
$St_a = 0.28, A_\eta = 0.63, \beta = 2,$ and
$\phi = 0$ (side view).
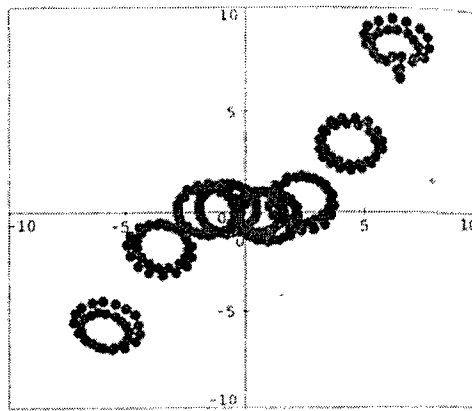
Figure 10 End view. Each ring's 32 nodes are plotted as solid circle.

These preliminary results from the application of evolution strategies to the problem of flow control suggest that stochastic optimization can be a valuable tool that can complement physical understanding and deterministic optimization techniques.

3.   Simplified systems models
To design feedback control algorithms, it is very useful to have a simple model that accurately captures the relevant physics of the phenomena under consideration. Such a model, which should have sufficient simplicity to enable real-time state estimation, is developed in the present work using linear stability theory to model the initial development of the instabilities leading to the turbulent breakdown of a jet. Direct numerical simulations of turbulent jets carried out by Freund et al. (1998) will be used as validation for these models; when performed properly, such simulations can capture the relevant flow physics "exactly", albeit at a very large computational expense.

System identification techniques may also be used (instead of linear stability theory) to develop input-output system models of jets for use in the feedback control setting, as explored by Ikeda (1998). Such models may be constructed without any reference to the equations which govern or approximate the flow physics. The present work is an intermediate-level approach that uses inviscid linear stability theory to approximate the jet system. A key feature of the present work is a piecewise quadratic approximation of the mean flow that permits rapid solution of the equations. The authors acknowledge the careful work of Pal (1998) in deriving the stability equations used.

The formulation of Viswanathan and Morris (1992) was implemented using the piecewise quadratic stability formulation for obtaining the eigenvalues. An example of the predicted evolution of the shear layer edges using only the n=0 axisymmetric disturbance is shown in Fig. 11. Figure 12 shows the locally dominant wavenumber versus downstream distance in jet radii. It is assumed that, when a distrubances saturates (due to the thickening of the shear layer), the sub-harmonic will become dominant and evolve until saturation, and so on. The results shown in Figs. 11 and 12 are for an initial shear layer thickness of 1% of the jet radius.

Systems modeling for control of jet flows
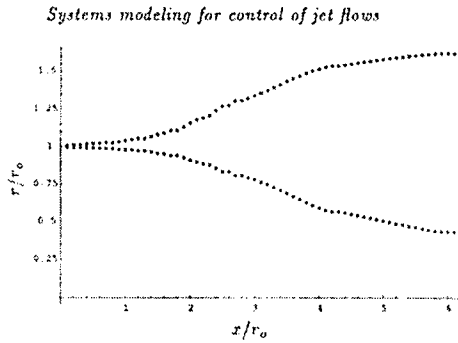
Figure 11 Inner and outer shear layer edges.   Figure 12 Locally dominant instability wave number
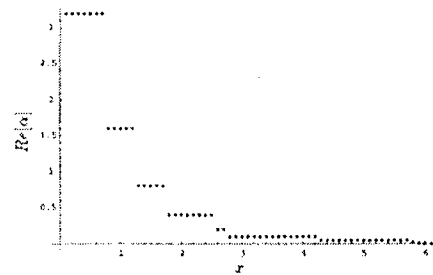
An approximate analytic solution to the appropriate incompressible linear stability problem, and the role of this solution in the evolution of the round jet, has been investigated. When fully implemented, such a formulation may model the physical behavior of the jet with sufficient accuracy to be used as a state model in a feedback control setting. Once programmed in an efficient manner, the computational expense of this model should be manageable. The use of such a model as a state estimator in a feedback control framework thus appears promising though the "real" problem prediction must include at least the n=+/-1 modes in addition to the n=0 mode given here. In the case of a thin shear layer, the n=+/-1 modes grow similarly to the n=0. However, the solution for n=+/-1 is required as the shear layer thickness becomes significant relative to the jet radius. For the mixing problem it is likely that the solution near the end of the potential core will need to be calculated. A transformation analogous to the Squire reformulation (of the three-dimensional planar stability problem into an equivalent two-dimensional problem in the transformed variables) will be pursued in the round jet problem.

Controller Design for Real-Time Feedback Control

We have selected a technique viable for real-time control for nonlinear flow systems. The technique uses neural networks to perform inverted system identification and feedback linearization. The system identification is done by off-line neural networks while the feedback linearization is done by on-line neural networks.

A. System Identification - We consider a system depicted in Fig. 3 The system input consists of a paired pulsed jets which excite the jet coming out of the nozzle, and the system output consists of the spatially averaged downstream temperature.

Let the system be described by $\dot{T} = f(T, A, \omega)$ where T, A, and ω respectively denote the temperature, excitation amplitude, and excitation frequency. Assuming that f^{-1} exists, if we let $u = f(T, A, \omega)$, then $[A, \omega]^T = g(T, u) = f^{-1}(T, u)$. By Taylor series expansion, it follows that $A = \sum_i w^A_i \cdot u^i$ and $\omega = \sum_i w^\omega_i \cdot u^i$ where w^A_i and w^ω_i are weights to be determined by applying off-line neural networks to CFD data.

B. Feedback Linearization – Due to the model inversion error, the actual system may have an error term Δ such that $\dot{T} = u + \Delta(T, u)$ where $\Delta(T, u) = f(T, \hat{A}, \hat{\omega}) - f(T, A, \omega)$, and $\hat{A}$ and $\hat{\omega}$ are estimated excitation amplitude and frequency, respectively. By setting the control system configuration as shown in Fig. 13, we have an equation for the tracking error $E = T_{cmd} - T$ such that $\dot{E} = -K \cdot E + v - \Delta(T, u)$. Our goal here is to determine v such that v cancels the error $\Delta(T, u)$, and to derive the error states to zero asymptotically. Calise showed that this can be done by assuming the existence of v which cancels the modeling error Δ, and that the weights w_i in $v = \sum_i w_i \cdot \beta_i(T, u)$ can be determined by applying Lyapunov stability theory, which results in $\dot{w_i} = -\gamma \cdot E \cdot \beta_i(t, u) / 2 \cdot K$, where $\beta_i(T, u)$ and γ denote radial basis functions and learning rate, respectively.
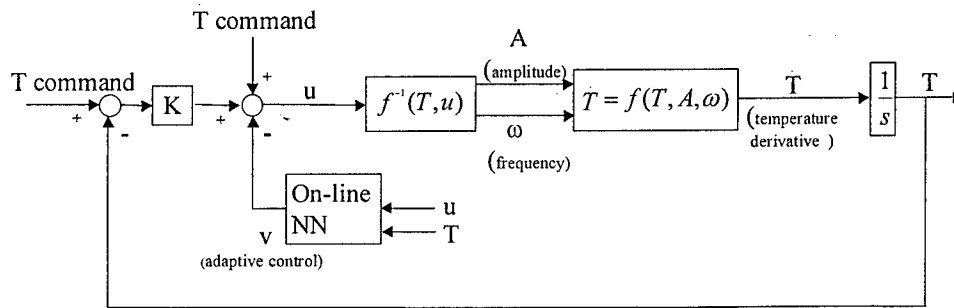
Fig 13. Adaptive Control Mechanism

Personnel Supported

The Boeing Company – Dr. Alan Cain, Dr. Yutaka Ikeda

Stanford University – Dr. Parviz Moin

University of California – Dr. Jonathan Freund

Georgia Tech Research Institute – Dr. David Parekh

Interactions/Transitions

Yutaka Ikeda accepted an invitation from Dr. Mezic at University of California, Santa Barbara (UCSB) to participate the workshop held at UCSB on October 29, 1998, and had discussions with some of their faculty members on possible collaboration towards technology transition.

Alan Cain gave a presentation on active flow control and participated in the United Technology Research Laboratory hosted workshop 11-12 November 1998.

Honors/Awards

Publications

Ikeda, Y., "Real-Time Active Flow Control Based on Modern Control Theory", 29th AIAA Fluid Dynamics Conference, AIAA 98-2911, 1998.

P. Koumoutsakos, J. B. Freund, and D. Parekh, ``Evolution strategies for parameter optimization in jet flow control", Proceedings of the 1998 Summer Program, Center For Turbulence Research (1998).

A. B. Cain, T. Bewley, J. B. Freund, and T. Colonius, ``An Approach to Systems Modeling for Real-Time Control of Jet Flows", Proceedings of the 1998 Summer Program, Center For Turbulence Research (1998).

J. B. Freund and P. Moin. ``Mixing Enhancement Using Fluidic Actuators: Direct Numerical Simulations", ASME Fluids Eng.Division, FEDSM98-5235 (1998).

Bewley T., J. B. Freund, P. Moin, A. Cain, and D. Parekh. ``Optimization of Forcing Profiles for Turbulent Jets", Bull. of the Am. Physical Soc. 43 (1998)

D. Parekh, P. Koumoutsakos, J.B. Freund, T. Bewley.``Optimization of Jet Control Parameters via Genetic Algorithms"Bull. of the Am. Physical Soc.}, 43 (1998)

ROTATING MINIATURE HEAT PIPES FOR TURBINE BLADE COOLING APPLICATIONS

AFOSR-F49620-96-1-0315

Yiding Cao
Department of Mechanical Engineering
Florida International University
Miami, Florida 33199

Objectives

Turbine blade cooling is crucial to protecting metal surfaces from hostile thermal environments and achieving a higher engine thermal efficiency. The application of micro/miniature heat pipes in turbine blades has been proposed for the reduction of turbine blade temperature. The heat pipe is considered to be an advanced technique that could push the turbine inlet temperature to a higher level. The main objective of this research project is to study the fundamental transport phenomena of radially rotating miniature heat pipes under turbine cooling conditions. The research results can be used for the design and fabrication of miniature heat pipes in turbine blades. The knowledge gained in this study can also be used for employing miniature heat pipes in other engine components such as turbine disks.

Status of Effort

- A data acquisition/power supply system for the rotating experimental apparatus was established. The rotating experimental apparatus with the data acquisition and power supply system can work successfully under designed working conditions and extensive experimental data have been taken using this system with a good accuracy.
- Two high-temperature miniature heat pipes were filled with a small amount of sodium as the working fluid. The heater used to supply the heat to the evaporator of the heat pipe was successfully fabricated. All experimental tests have been successfully completed.
- A set of closed-form analytical solutions for the temperature distribution along the heat pipe length was derived. Experiments for the heat pipe startup, steady state operation, and effects of various parameters on the heat pipe performance were conducted. The comparisons were made between the experimental data and closed-form analytical solutions with good agreement. The research project under the contract AFOSR-F49620-96-1-0315 has been successfully completed. The research results prove that the radially rotating miniature heat pipe has a very large heat

transfer capability and a very high effective thermal conductance. At the same time, the heat pipe structure is simple and its manufacturing cost is low. It can also withstand strong vibrations and work in a high-temperature environment. Therefore, the combination of the traditional air-cooling technology with the radially rotating miniature heat pipe is a feasible and effective cooling means for high-temperature turbine blades.

Accomplishments

1. **Construction of the data acquisition and power supply system for the experimental apparatus.** The apparatus with the data acquisition and power supply system was completed and is schematically shown in Fig. 1. The apparatus can operate at revolutions up to 3,600 rpm. The maximum working temperature of the miniature heat pipe was 900 °C. The electrical power input to the heater was adjusted using a transformer from 0 to 110 V. All experimental data, such as heat inputs and temperatures at various locations of the heat pipe, were scanned and recorded by the data acquisition system and saved in a computer subsequently.

2. **Fill of high-temperature heat pipes.** Two stainless-steel miniature heat pipes had been filled with a small amount of sodium as the working fluid. One heat pipe has a diameter of 1.5 mm and approximately 0.06 g of sodium charge, and the other has a diameter of 2 mm and approximately 0.08 g of sodium charge. The heat pipes are schematically shown in Fig. 2. Tests on these two heat pipes have been completed on the constructed experimental apparatus as shown in Fig. 1.

3. **Closed-form analytical solutions and comparisons with experimental data.** Based on the assumption of one-dimensional laminar and incompressible vapor flow under a steady-state operating condition and employing force and energy balances over differential control volumes, a closed-form analytical solution for the vapor temperature distribution along the heat pipe length was derived:

$$T_{v,z} = T_{v,z_0} + \Delta T_{v,z} =$$

$$T_{v,L} - \begin{cases} \{\dfrac{T_v F_v Q_c}{h_{fg}\rho_v \sin\phi}(L_{eff} - \dfrac{z^2}{2L_c}) + \dfrac{T_v \sin\phi}{h_{fg}}\omega^2[(z_0 + \dfrac{1}{2}L)L - (z_0 + \dfrac{1}{2}z)z]\} & 0 \le z \le L_c \\ \\ \{\dfrac{T_v F_v Q_c}{h_{fg}\rho_v \sin\phi}[L_{eff} - \dfrac{1}{2}(L - \dfrac{(L-z)^2}{L-L_c})] + \dfrac{T_v \sin\phi}{h_{fg}}\omega^2[(z_0 + \dfrac{1}{2}L)L - (z_0 + \dfrac{1}{2}z)z]\} & L_c \le z \le L \end{cases}$$

$$(1)$$

The above analytical solution excludes the diffusion effects of non-condensable gases and only the friction and centrifugal force effects are taken into account. After incorporating the diffusion effects of non-condensable gases, a more general closed-form analytical solution for the vapor temperature distributions along the heat pipe length was found:
Evaporator section:

$$T_{v,z} = T_{v,L} - \frac{T_v F_v Q_c}{h_{fg} \rho_v \sin\phi} \{L_{eff} - [L - \frac{(L-z)^2}{L-L_c}]\} - \frac{T_v \omega^2 \sin\phi}{h_{fg}}[(z_0 + \frac{1}{2}L)L - (z_0 + \frac{1}{2}z)z]$$

$$L_c \leq z \leq L \qquad (2)$$

Condenser section:

$$T_{v,z} = T_{v,L} - T_{L_c} + T_s + a - \Delta T_v + \Delta T_{v,z} + \Delta T_{n,z}$$

$$= \begin{cases} \Delta T_{v,z} - \Delta T_v + T_{v,L} - c[\exp(m(2L_c - z)) - \exp(mz)] & L_{c,n} \leq z \leq L_c \\[2ex] T_{v,L} - T_{L_c} + T_s + a - \Delta T_v + a[\exp(mz) - 1] & 0 \leq z \leq L_{c,n} \end{cases} \qquad (3)$$

Some representative experimental results for the temperature distributions along the heat pipe length are presented in Figs. 3-6, along with some comparisons with the analytical solutions. Fig. 3 illustrates typical temperature distributions during the heat pipe startup. The startup behavior of the current rotating heat pipe is frontal in nature with a sharp drop off in temperature across the vapor front and no pressure recovery in the condenser. Fig. 4 shows the comparisons between the temperature distributions along the heat pipe length and those along a heat pipe container (the heat pipe shells without charging any working fluid) with the same flow rate of cooling air, dimensionless centrifugal forces, and geometrical dimensions. The effective heat conductance of the heat pipes is 60-100 times higher than the thermal conductivity of copper or about 1,000–1,700 times higher than that of the stainless steel used as the shell in the current study. These comparisons from Fig. 4 prove that radially rotating miniature high-temperature heat pipes can work very effectively and reliably. Their heat transfer capacities are much higher than any metals available. Because the condenser end was mounted onto the outer cylinder of the high-speed rotating test apparatus with a screw thread, a large extra heat sink was thus formed at the condenser end, and some heat from the condenser end was directly transferred into this heat sink. As a result, the heat pipe temperature near the condenser end was forced to stay at a low level. Without this heat sink, the effective conductance of the heat pipes could be much higher. Fig. 5 shows the steady-state temperature distributions along the heat pipe length with different heat inputs for both heat pipes. In Eq. (1), the temperature drops along the heat pipe length are caused only by the friction and centrifugal force of the vapor flow. Therefore, the temperature drops along the dimensionless heat pipe length are very small, and the temperature distributions are nearly straight lines, as shown in Fig. 6. Eqs. (2) and (3) give the temperature distributions along the dimensionless heat pipe length with a flat front of vapor-gas interface when a portion of the condenser length, $L_{c,n}$ = 4 mm, is occupied by non-condensable gases. Comparing the closed-form analytical solutions with the experimental data in Fig. 6, it is evident that the closed-form analytical solutions from Eqs. (2) and (3) are more realistic than the analytical solutions from Eq. (1) and are closer to the experimental results. Due to the existence of the heat sink at the condenser end, however, a relatively large deviation from the experimental data occurs close to the condenser end. The theoretical and experimental studies have proven that the radially rotating miniature heat pipe studied in this research project is a feasible and effective cooling means for high-temperature turbine blades.

Personnel Supported

Yiding Cao (Principal investigator), Jian Ling (Ph.D. candidate, part-time), Songphol Chattuchai (Graduate student), and Alejandro Lopez (Graduate student).

List of Publications

1. Cao, Y. and Chang, W.S., 1997, "Analyses of Heat Transfer Limitations of Radially Rotating Heat Pipes for Turbomachinery Applications," AIAA Paper No. 97-2542, *AIAA 32nd Thermophysics Conference*, June 23 – 25, Atlanta, GA.

2. Cao, Y., Ling, J., and Chang, W.S., 1998, "Analyses of Liquid and Vapor Flow in a Miniature Radially Rotating Heat Pipe for Turbine Blade Cooling Applications," 11th International Heat Transfer Conference, Kyongju, Korea.

3. Ling, J., Cao, Y., and Chang, W.S., 1999, "Analyses of Radially Rotating High-Temperature Heat Pipes for Turbomachinery Applications," *ASME J. of Engineering for Gas Turbines and Power*, Vol.121, pp.306-312.

4. Ling, J., Cao, Y., and Lopez, A., 1999, "Experimental Investigations of High-Temperature Rotating Miniature Heat Pipes," Submitted for publication, *ASME Journal of Heat Transfer*.

5. Ling, J. and Cao, Y., 1999, "Closed-Form Analytical Solutions for Radially Rotating High-Temperature Heat Pipes Including Non-Condensable Gas Effects," Submitted for publication, *Int. J. Heat and Mass Transfer*.

Transitions

The principal investigator is currently working with Turbine Engine Division, Air Force Research Laboratory for turbine disk cooling employing rotating heat pipes. The fundamental knowledge gained under the present program from AFOSR regarding the operating characteristics of the rotating heat pipe is being used for the disk cooling problem at Wright-Patterson AFB.

Acknowledgement
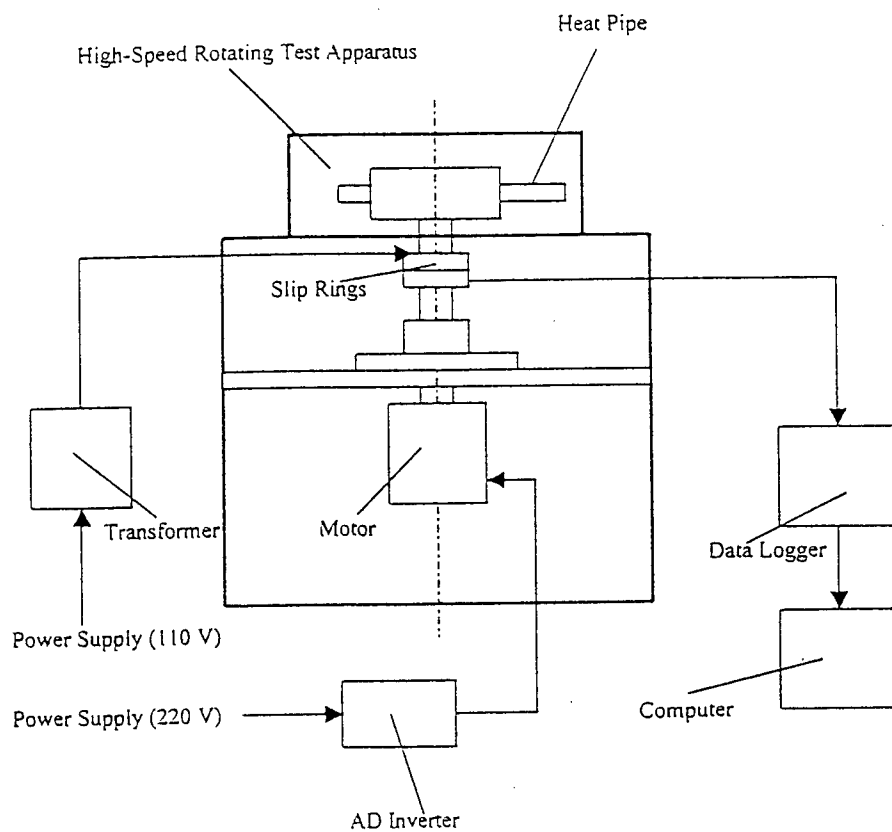
Fig. 1 Schematic of a high-speed rotating test apparatus with a data acquisition and power supply system.
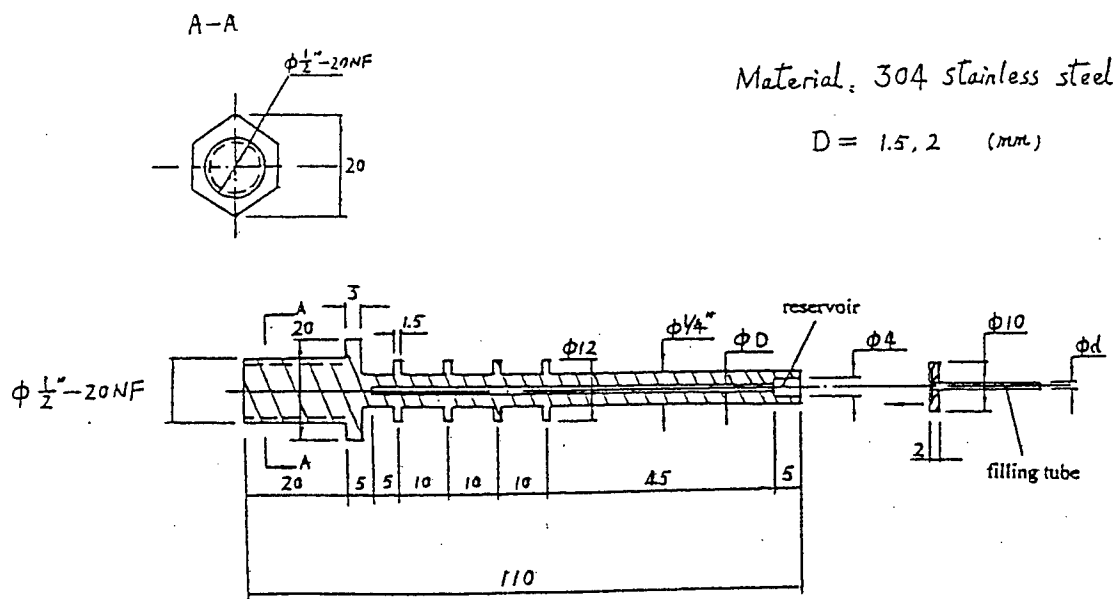
Fig. 2 Configuration of a designed sodium heat pipe
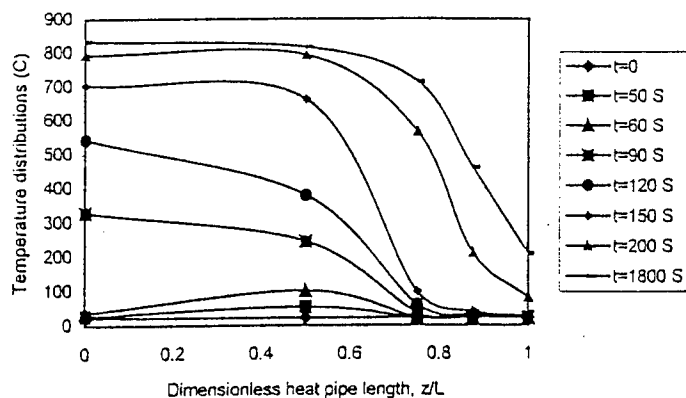
Fig. 3 Axial temperature distributions with diffuse effects of non-condensable gases during the heat pipe startup process ($\omega^2 \overline{Z}_a / g = 470$, $d_i = 1.5$ mm, $Q=176$ W).
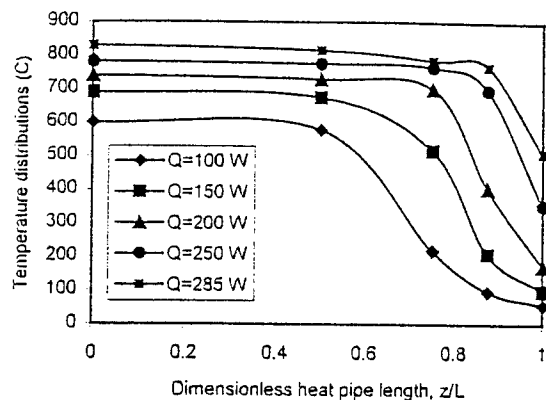
Fig. 5 Axial temperature distributions with different heat inputs ($\omega^2 \overline{Z}_a / g = 470$, $d_i = 1.5$ mm, $W = 6.7 \times 10^{-3} m^3 / s$).
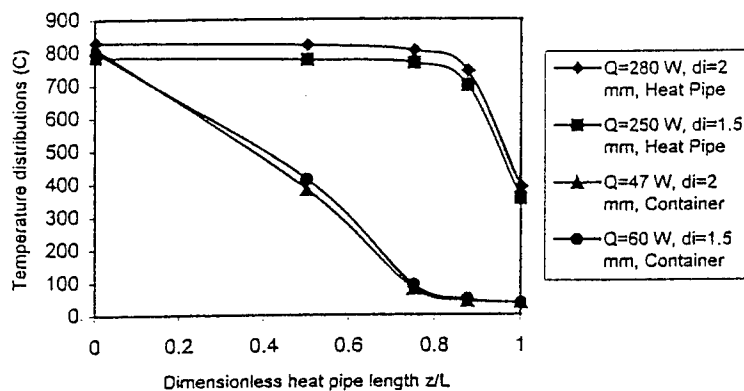
Fig. 4 Comparisons of the temperature distributions between the heat pipes and heat pipe containers ($\omega^2 \overline{Z}_a / g = 470$, and $W = 6.7 \times 10^{-3}$ m^3/s).
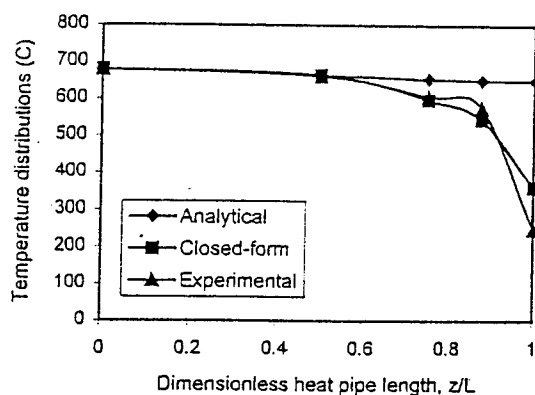
Fig. 6 Comparisons of the analytical solutions and experimental results for the temperature distributions ($L_{c,r} = 4$ mm, $\omega^2 \overline{Z}_a / g = 1881$, $d_i = 2$ mm, $Q=275$ W).

42

USE OF MEMS FOR MICRO AIR VEHICLES

Bruce Carroll, Norman Fitz-Coy, Andrew Kurdila, Mark Sheplak, and Wei Shyy
Department of Aerospace Engineering, Mechanics & Engineering Science
University of Florida

Toshikazu Nishida
Department of Electrical and Computer Engineering
University of Florida

Abstract

This is a three-year, multidisciplinary effort to investigate the application of MEMS to the control of low Reynolds number flows about Micro Air Vehicles (MAVs). The specific goals of this investigation are to develop a quantitative and qualitative understanding of microelectromechanical systems (MEMS) based sensor and actuator interactions with low Reynolds number flows found on MAVs, resulting in improved aerodynamic performance and mechanisms for active and passive flight control.

Approach

A dominant aerodynamic feature of MAVs is the lower lift-to-drag ratio and much reduced stall margin, which leads to a precipitous decline in aerodynamic efficiency as Reynolds number is lowered. The amplification of small-scale MEMS control inputs into large-scale effects via fluid dynamic instability and growth mechanism are being investigated. Figure 1 shows a low Reynolds number (Re < 100,000), laminar separation followed by transition of the separated shear layer and reattachment. Mild actuation of the boundary layer near the separation location is expected to trigger a quicker transition of the separated shear layer, providing a mechanism for control of the reattachment location. We are also considering MEMS induced and controlled vortical structures, originating with small perturbations at the leading edge of the MAV wing to enhance the lift. A third possible mechanism is to utilize flexible membrane wing panels as an additional amplification mechanism for the MEMS actuation. While Figure 1 describes our ultimate goal for an improved MAV airfoil, simpler geometries are being
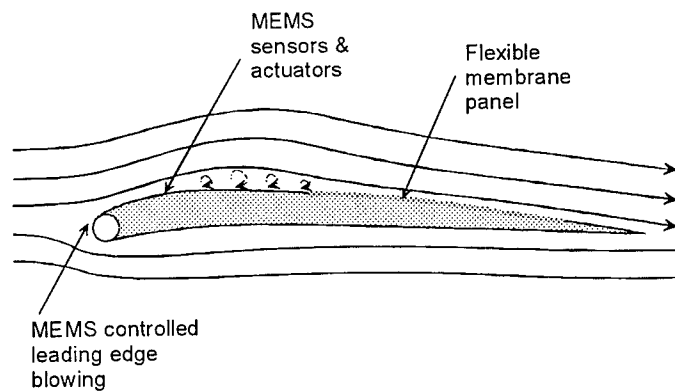
Figure 1. Illustration of actuation and sensing strategies

employed to study the fluid/MEMS interactions from both a fundamental fluid dynamics perspective and from a control theory viewpoint. Our test configuration is shown in Figure 2. This configuration consists of a "macro" scale vibrating piezo flap for actuation and a MEMS based shear sensor array for reattachment detection. As discussed below, we are using this configuration to quantify the MEMS actuation requirements, to develop our MEMS sensing capabilities and to provide a test case for development of model based and neural network control strategies for the non-linear system.
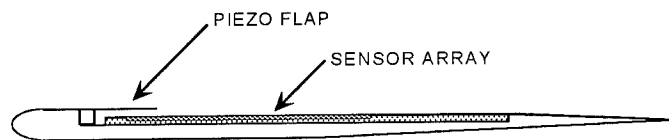
Figure 2. Test Geometry for quantitative determination of actuation requirements.

Progress

Results for several aspects of this project have been reported in the literature and will only be summarized here for brevity. Our computational algorithms were checked against experimental results and shown to yield sufficient accuracy.[1] The CFD results were then used to develop neural network control. Using radial basis functions, we have successfully trained neural networks to map the flow characteristics (i.e., C_L/C_D as a function of angle of attack and Reynolds number) for viscous flow around a two dimensional airfoil.[2] Building on the success of these studies, inverse plant models based on neural network mappings are being developed and will be used in

Figure 3. SEM image of MEMS shear sensing element.

feedforward compensators. The impact of leading edge blowing on the low Reynolds number flow field was also investigated numerically.[3] These computational techniques are currently being applied to the test geometry of Figure 2 as a complement to the experimental results presented below.

Our main experimental investigation for this reporting period has made use of the test geometry in Figure 2. An elliptical leading edge profile was used to ensure the laminar boundary layer remains attached until separation at the at the trailing edge of the piezo flap. The piezo flap actuator was built by High Technology Inc. The current design was based on a similar design by Dr. Louis Cattafesta.[4] A linear array of MEMS shear sensors is being used to detect the reattachment location on the upper surface. Figure 3 shows a SEM image of a single shear stress sensor that was fabricated using a wafer bond/etch-back process at MIT. The sensing element is a platinum thin film deposited on a 1500Å-

thick silicon nitride diaphragm over a 10μm-deep sealed vacuum cavity. The sensor is packaged on a milled printed circuit board flush mounted on the surface of the airfoil.

A series of preliminary experiments with a low speed impinging jet verified the operation of the shear sensor array. Before useful measurements on the current test geometry can be performed, we deemed it necessary to obtain a detailed characterization of the shear sensor array.[5] Multiple resistance vs. temperature experiments have been performed to determine Temperature Coefficient of Resistance (TCR) for platinum thin film sensing element of the shear stress sensor. The results indicated a TCR = .0027 °C^{-1} with 2.7% nonlinearity in resistance over a range of 25-300 °C. Extensive current-voltage testing of multiple sensors has been performed. Coupled with the experimentally determined TCR, the Sensor Overheat can be determined for any electrical biasing conditions. Mean shear calibrations in constant current (CC) mode have been performed at overheats of .4, .6, .8, and 1 in laminar flow for shears up to .08 Pa and in turbulent flow for shears of .15 – 2 Pa. Details of the characterization will be presented at the upcoming Aerospace Sciences Meeting.[5] The sensor array is currently being reinstalled in the airfoil upper surface for a new series of experiments.

Concurrently with the shear sensor characterization, a series of flow field measurements were performed using PIV and mean surface pressure measurements. Mean surface pressure distributions are shown in Figure 4 for zero angle of attack and a chord Reynolds number of 79,000. The actuators were driven with a sinusoidal input of fixed amplitude and a range of frequencies from zero to 500 Hz. The minimum pressure location, which corresponds roughly to the mean reattachment location, is seen to move forward as
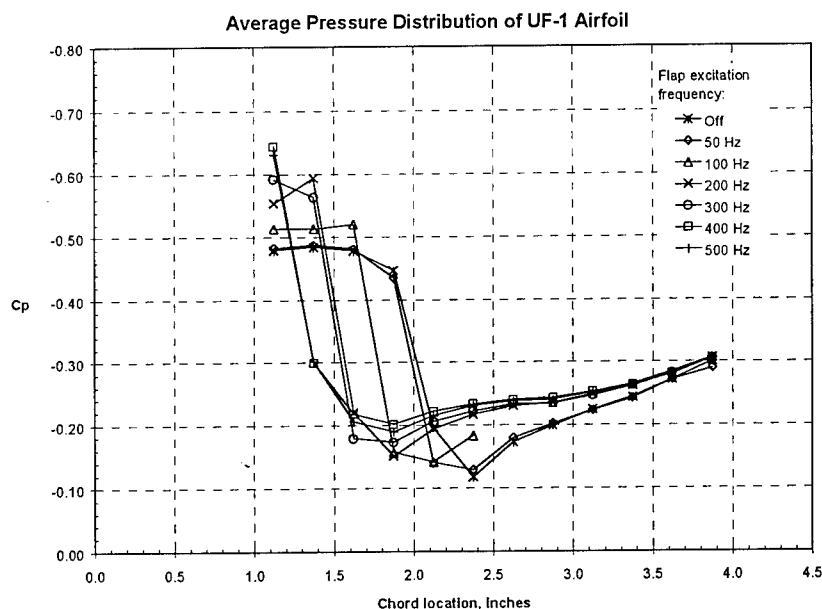
Figure 4. Time averaged surface pressure measurements for various actuation frequencies.

actuation frequency is increased. (The flap trailing edge is located at 1.125 inches.) PIV images were acquired for these same operating conditions with selected instantaneous visualizations shown in Figure 5. For an actuation frequency of zero the laminar boundary layer separates from the trailing edge and undergoes a "natural" transition and reattachment process. Actuation is seen to induce a vortex structure in the shear layer with the vortex spacing decreasing as actuation frequency increases. Mean vector plots for 100 Hz and 300 Hz are shown in Figure 6 and demonstrate the correlation of time average reattachment location to actuation.

Future Work

During the next reporting period we will extend the work presented here. Phase locked PIV imaging will be implemented so that the time resolved evolution of the shear layer transition process can be studied and correlated to the actuation characteristics and surface measurements. This data will then be
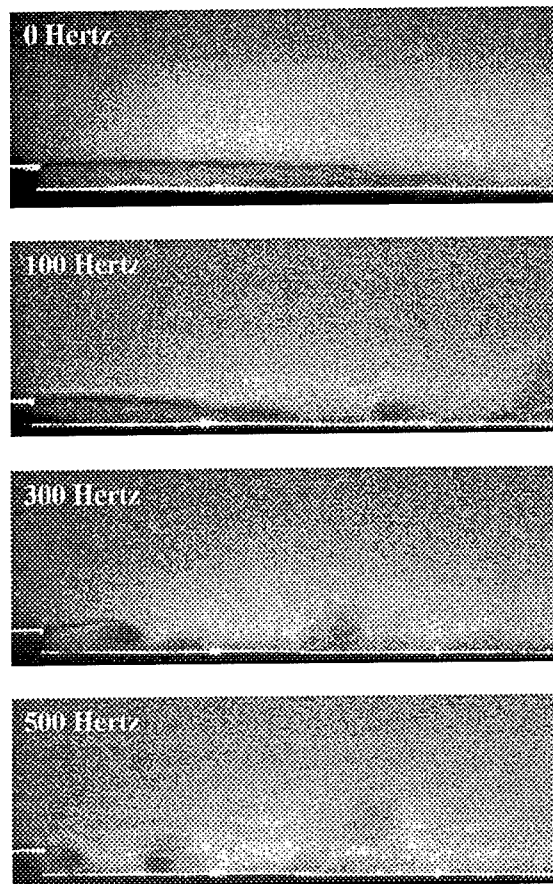
Figure 5. Instantaneous PIV images for increasing actuation frequency.
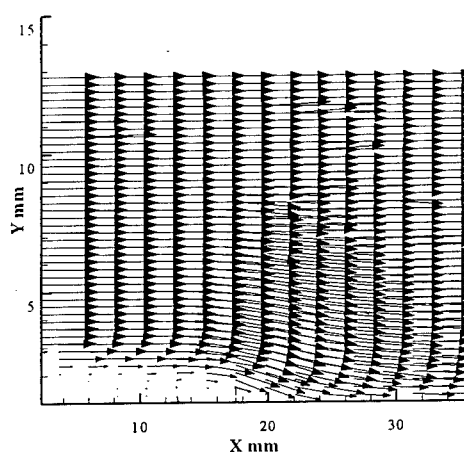
(a) 100 Hz
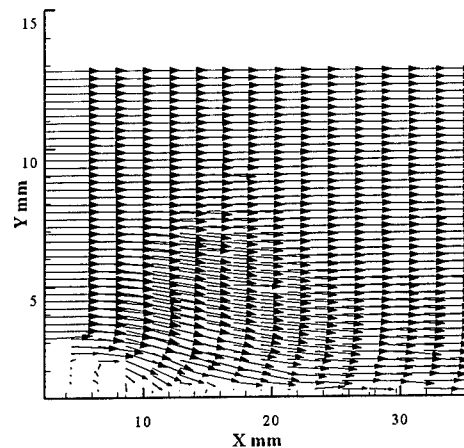
(b) 300 Hz

Figure 6. Mean velocity vector maps for actuation frequencies of 100 and 300 Hz.

used to refine the computational algorithms, especially the transition model. A scanning vibrometer is being acquired and will be used to perform a 3-D characterization of actuators under load. This information is critical to provide accurate boundary conditions to the numerical simulations and to provide specifications of actuation requirements for future MEMS actuator development. As a complement to the MEMS shear sensor array we are developing a microphone array based on commercially available electret sensors. This will provide quantitative specifications for MEMS based separation/reattachment detection using microphone arrays. Control algorithms are being developed and implemented to selectively position the mean reattachment location for arbitrary free stream conditions.[6] Closed loop control will be based on measurements of mean surface pressure, fluctuating surface pressure and fluctuating surface shear stress with actuation waveform being the controlled parameter.

Personnel

Faculty and graduate assistants from two departments are collaborating on this research effort. The work is subdivided into three main subject areas: Aerodynamics, MEMS, and Controls, although considerable overlap and coordination between areas exists. The personnel in each subject area are listed in the following table:

Subject Area	Faculty	Graduate Assistants
Aerodynamics	Bruce Carroll (AeMES) Wei Shyy (AeMES)	Carlos Fuentes Xiong He
MEMS	Toshikazu Nishida (ECE) Mark Sheplak* (AeMES)	Anthony Cain
Controls	Norman Fitz-Coy (AeMES) Andrew Kurdila* (AeMES)	Nilay Papila Jing Li

*Drs. Sheplak and Kurdila are new members of our faculty and were not listed on the original proposal. However, they have been making substantial contributions to the project and are now listed as Co-PI's.

References

1.* Shyy, W., Klevebring, F., Nilsson, M., Sloan, J., Carroll, B. and Fuentes, C. "A Study of Rigid and Flexible Low Reynolds Number Airfoils," Journal of Aircraft, Vol. 36, (1999) pp.523-529.

2.* Papila, N., Shyy, W., Fitz-Coy, N. and Haftka, R.T., "Assessment of Neural Net and Polynomial-Based Techniques for Aerodynamic Applications," AIAA 17th Applied Aerodynamics Conference, Paper No. 99-3167 (1999).

3.* Shyy, W., He, X. and Thakur, S. "Jets and Free Stream Interaction Around a Low-Reynolds Number Airfoil Leading Edge," Numerical Heat Transfer, Part A, Vol. 35, (1999) pp.891-902.

4. Cattafesta, L. N., III, Garg, S., and Washburn, A. E., "Piezoelectric Actuators for Fluid-Flow Control," Proceedings of the SPIE, Vol. 3044, pp. 147-157, March, 1997.

5.* V. Chandrasekaran, A. Cain, T. Nishida, M. Sheplak, "Dynamic Calibration Technique for Thermal Shear Stress Sensors with Variable Mean Flow," To be presented at the AIAA Winter Annul Meeting, Jan. 10-13, 2000, Reno Nevada.

6.* A. J. Kurdila, B. F. Carroll "Reduced Order Modeling for Low Reynolds Number Flow Control," Smart Structures and Materials Conference, Technical Conference 3667 Mathematics and Control in Smart Structures, SPIE Paper no. 3667-07, Proceedings of SPIE Vol. 3667, Newport Beach, CA, Mon.-Thurs. 1-4 March 1999.

*Indicates a publication resulting from this grant.

ACTIVE CONTROL OF SELF-SUSTAINED OSCILLATIONS IN THE FLOW PAST A CAVITY

Tim Colonius

Division of Engineering and Applied Science

California Institute of Technology

Pasadena, CA 91125

Abstract

Direct Numerical Simulations of the flow past an open cavity are used to investigate and characterize self-sustained flow/acoustic oscillations and their radiated acoustic field. In addition, modeling efforts are directed at providing low-order flow models for use in active control laws. Open cavities on aircraft are subject to intense pressure fluctuations due to a flow/acoustic resonance involving shear layer instability waves, acoustic feedback, and scattering and receptivity problems at cavity edges. Resulting internal acoustic loads with sound pressure levels (SPL) in excess of 160 dB have been measured and these can damage stores, fatigue nearby surfaces and components, and lead to intense noise radiation.

This report describes recent progress in simulating and characterizing the resonant instabilities for two-dimensional cavities with laminar boundary layers upstream. The results show an interesting transition from a shear layer mode, for shorter cavities and lower Mach numbers, to a wake mode for longer cavities and higher Mach numbers. The shear layer mode is well characterized by the process described by Rossiter [1]. The wake mode is characterized instead by a large-scale vortex shedding with Strouhal number independent of the Mach number, and the boundary layer periodically separates upstream of the cavity. Both drag and acoustic radiation are significantly increased in wake mode. The wake mode oscillation is similar to that reported by Gharib and Roshko [2] for incompressible flow with a laminar upstream boundary layer.

Approach

The fully compressible, unsteady, Navier-Stokes equations are solved for two and three dimensional flows using 6th-order-accurate compact finite-difference schemes [3]. A 4th-order Runge-Kutta scheme is used to advance the equations in time. Non-reflecting boundary conditions are applied at all open boundaries, and are presently based on buffer zone techniques (e.g. [4]) together with the one-dimensional boundary conditions of Poinsot and Lele [5].

Figure 1 shows a schematic diagram of the computational domain. A Cartesian grid is used, with clustering of nodes near all the walls. The code is parallelized using a domain decomposition method. Typical grids contain about half a million grid points. The code has been run on 8 to 32 processors of an IBM SP2. The wall is assumed to be isothermal at the same temperature as the freestream. The simulations are initiated by spanning the cavity with a Blasius flat plate boundary layer. The following parameters may be independently varied: the length of the cavity relative to the initial boundary layer thickness at the cavity leading edge, L/θ ; the Reynolds

number, Re_θ, based on the freestream velocity, U, the boundary layer thickness and the kinematic viscosity in the ambient; the Mach number of the freestream, M; and the cavity length to depth ratio, L/D .
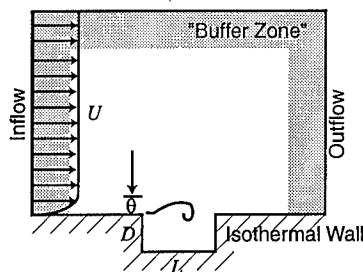
Figure 1: Schematic diagram of cavity configuration and computational domain.

It is of critically important that instabilities are independent of the location of the boundaries, and the boundary conditions. This is because repeated spurious reflections of waves can lead to self-forcing of the flow, in a process indistinguishable from the physical instability (e.g.[4]). We have run several cases with variable boundary location and grid spacing, in order to find appropriate boundary locations, as well as demonstrate grid convergence [6]

Results

The computations reveal a transition between two fundamentally different modes of cavity oscillations. These modes are termed, following Gharib and Roshko [2], as shear layer mode and wake mode. The runs performed show that transition from shear layer to wake mode occurs as the length of the cavity is increased relative to the upstream boundary layer thickness (for constant L/θ and Re_θ), and as M is increased with other parameters constant. The shear layer mode is characterized by the roll-up of vorticity in the shear layer and impingement on the downstream cavity edge. The frequencies are in reasonable agreement with those predicted by the Rossiter equation, and consist primarily of Rossiter modes 1 and 2 [1]. Spectra and frequencies of oscillation are discussed in more detail below. The iso-contours of vorticity depicted in figure 2 are representative of the shear layer mode of oscillation. The cavity is relatively quiescent, with a weak vortex occupying the latter half of the cavity. Vorticity of the opposite sign (to boundary layer vorticity) is generated along the walls of the cavity. Note that at two different instants in time, while the phase of the disturbances in the shear layer has shifted, the vorticity contours in the cavity are nearly the same. Animations of the contours confirm that the interaction of the flow in the cavity with the shear layer is relatively weak.

The wake mode is characterized by a large scale shedding from the cavity leading edge, in a manner similar to bluff bodies. The shed vortex has dimensions of nearly the cavity size, and as it is forming, boundary layer fluid is directed into the cavity. The vortex is shed from the leading edge and ejected from the cavity in a violent event. The pressure fluctuations large enough to cause flow separation upstream of the cavity, and the shed vortex induces separation in the boundary layer downstream
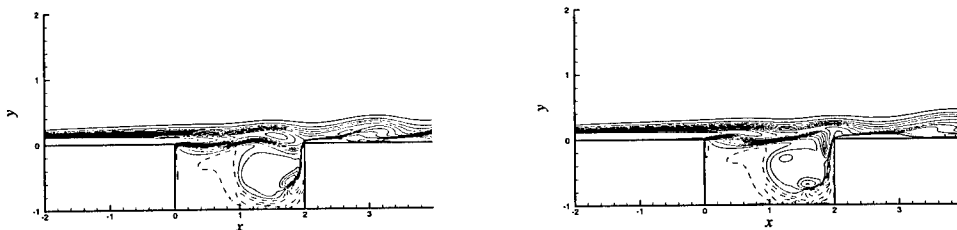
Figure 2: Instantaneous vorticity contours in shear layer mode at two different instants during the oscillation cycle with $M = 0.6$, $L/D = 2$, $L/\theta = 52.8$, and $\mathrm{Re}_\theta = 56.8$. 15 contours between $\frac{\omega D}{U} = $ -5 and 1.67. Positive contours are dashed. Only a small portion of the computational domain near the cavity is shown.

of the cavity as it convects away. We believe the upstream separation is a key feature of the transition to wake mode, and is discussed further below. Figure 3 shows two snapshots of the vorticity field in wake mode. The radiated acoustic field was examined [6] and shows substantial differences between wake mode and shear layer mode.
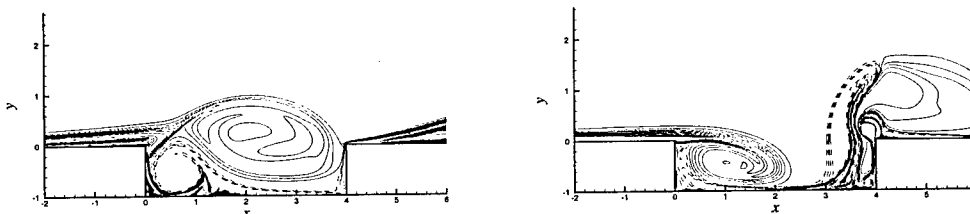
Figure 3: Instantaneous vorticity contours in wake mode at two different times during the oscillation cycle for $M = 0.6$, $L/D = 4$, $L/\theta = 102.1$, and $\mathrm{Re}_\theta = 58.8$. Same contour levels as previous figure.

Gharib and Roshko [2] performed experiments on incompressible cavities (an annular gap in an axisymmetric body in water), where the upstream boundary layer was also laminar. Transition between non-oscillatory, shear layer, and wake modes occurred at $L/\theta = 80$ and $L/\theta = 160$. Our data show that the change from wake mode to shear layer mode depends also on the Mach number. As in the experiments, the computed drag is significantly higher in wake mode [6].

The spectra of the oscillations are also substantially different in wake and shear layer mode. In figure 4, distinct peaks from spectra for runs in shear layer mode are compared to predictions from the modified Rossiter formula (e.g. [7]). The agreement is relatively good and within the scatter of experimental data (e.g.[8]). It needs also to be noted that the spectra were computed from computational data over relatively low numbers of periods (compared to experiments). Short time series, with necessary windowing techniques, can lead to significant leakage among the low frequencies.

Nevertheless, the figure provides evidence that the instability mechanism in shear layer mode is the one envisioned by Rossiter.
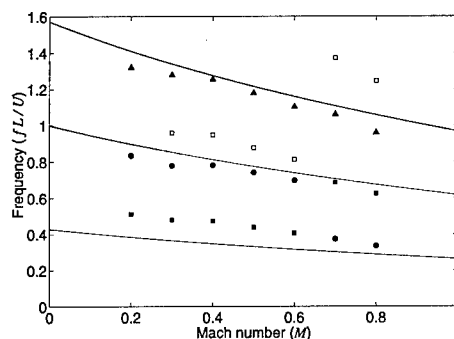
Figure 4: Strouhal numbers for peaks in spectra for a series of runs in shear layer mode with $L/D =2$, $L/\theta =52.8$, and $\mathrm{Re}_\theta = 58.8$. The square symbols indicate the highest amplitude mode, circles the second highest, and triangles, the third highest. The open squares are peaks in the spectra at the first harmonic of the highest amplitude Rossiter mode. The lines are the modified Rossiter formula for modes $m = 1$, 2 and 3.

The spectra in wake mode are very different. After an initial transient, which at early times is similar to shear layer mode, the flow becomes nearly periodic in time, with the fundamental period corresponding to the vortex shedding from the leading edge. After a transient, the fundamental mode oscillates at a Strouhal number of 0.25, which is lower than Rossiter mode one (0.31), and additional peaks in the spectrum are all harmonics of the fundamental. In addition, there is very little variation of the fundamental frequency with M. For $M = 0.4$ to $M = 0.8$ the fundamental frequency varied less than 4%, compared to the expected variation of about 20% for Rossiter mode one. The 4% variation is, in fact, within the uncertainty in frequency associated with the total sampling period. The lack of variation with M indicates that the mode is not acoustically driven, and it appears that the feedback in this case is provided by the complicated recirculating flow in the cavity.

It should be noted that the transition from shear layer to wake mode, detected in incompressible experiments and the present compressible computations, appears not to have been noted in previous compressible experiments. The very low Reynolds number of the calculations, and the laminar state of the upstream boundary layer could be the cause of wake mode. For the computations, Re_θ is on the order of 100, which is of the same order as in the incompressible experiments [2], but much lower than any compressible experiments. While it is unlikely that the shear layer dynamics are highly dependent on Reynolds number, even for Re_θ as low as 100, the impact of the oscillations on an upstream laminar boundary layer could be very different than for a turbulent one.

The computations show that in wake mode, the boundary layer alternately separates and reattaches well upstream of the cavity edge, due to the oscillating adverse pressure gradient caused by the vortex shedding. We hypothesize that the transition to wake mode occurs because pressure fluctuations from the cavity grow to sufficient

size to cause separation in the laminar boundary layer upstream. At present, we have detected the transition, holding D/θ constant and increasing L/D (and therefore also L/θ) and increasing M holding other parameters constant. This result suggests that in order to be relevant to typical compressible cavity experiments, numerical simulations with laminar upstream boundary layers should avoid parameter regimes where wake mode can be expected. It is not clear, at present, what role L/θ plays in the transition, although a previous study by Sarohia [9], which had a laminar boundary layer upstream, suggested that the shear-layer mode instability characteristics were independent of D/θ. Further numerical experiments are planned to explore different trajectories through parameter space to further characterize the transition.

A turbulent boundary layer would be much more resistant to such separation and may preclude the emergence of wake mode. We speculate that this is the reason why wake mode has not been detected in previous compressible cavity experiments. Of course, it is impossible at present to rule out that other Reynolds number and three-dimensional effects do not also act to preclude the wake mode.

Future Work

As noted above, further two-dimensional computations are underway to establish the relation between unsteady separation upstream of the boundary layer and the transition to wake mode. Modifications to the code have been made to allow for blowing and suction from the wall upstream of the cavity. In a first test, we are attempting to prevent transition to wake mode by sucking off the boundary layer upstream of the cavity.

Also underway are efforts directed at the development of low-order flow models to be used in conjunction with active control laws. The Proper Orthogonal Decomposition (method of snapshots) is being used with data from the two-dimensional cavity runs to derive a low-dimensional system of ODE's governing the oscillations. Active control will be directly implemented in the computations to validate the efficacy of this approach.

Future work also includes the investigation of three dimensional instabilities in the shear layer and modes of self-sustained oscillation. An efficient three-dimensional parallel version of the code is complete.

Additional Information

The following personnel at the California Institute of Technology have been supported in part under this grant:

1. Dr. Tim Colonius, Principal Investigator, Asst. Prof. of Mechanical Engineering,

2. Dr. Amit Basu, Visiting Associate

3. Dr. Greg Hernandez, Postdoctoral Scholar

4. Mr. Clarence W. Rowley, Graduate Research Assistant,

The following publications resulted from this grant (1/1/98-7/1/99):

1. Colonius, T. and Basu, A.J. and Rowley, C.W., "Numerical Investigation of the Flow Past a Cavity", *AIAA Paper 99-1912*, 1999.

2. Colonius, T. and Basu, A.J. and Rowley, C.W., "Computation of Sound Generation and Flow/Acoustic Instabilities in the Flow Past an Open Cavity.", *ASME FEDSM99-7228 (Invited)*. To be presented at the 3rd ASME/JSME Joint Fluids Engineering Conference, July 18-23, 1999, San Francisco, CA.

3. Rowley, C.W. and Colonius, T., "Numerically Nonreflecting Boundary Conditions for Multidimensional Aeroacoustic Computations", *AIAA Paper 98-2220*, 1998.

4. Rowley, C.W. and Colonius, T., "Discretely Nonreflecting Boundary Conditions for Linear Hyperbolic Systems", *submitted to J. Comput. Phys.*, 1999.

References

[1] J. E. Rossiter. Wind-tunnel experiments on the flow over rectangular cavities at subsonic and transonic speeds. Technical Report 3438, Aeronautical Research Council Reports and Memoranda, October 1964.

[2] M. Gharib and A. Roshko. The effect of flow oscillations on cavity drag. *J. Fluid Mech.*, 177:501–530, 1987.

[3] Sanjiva K. Lele. Compact finite difference schemes with spectral-like resolution. *J. Comput. Phys.*, 103(1):16–42, November 1992.

[4] T. Colonius, S. K. Lele, and P. Moin. Boundary conditions for direct computation of aerodynamic sound generation. *AIAA J.*, 31(9):1574–1582, September 1993.

[5] T. Poinsot and S. K. Lele. Boundary conditions for direct simulation of compressible viscous flows. *J. Comput. Phys.*, 101:104–129, 1992.

[6] T. Colonius, A. J. Basu, and C. W. Rowley. Numerical investigation of the flow past a cavity. *AIAA Paper 99-1912*, 1999.

[7] C. K. W. Tam and P. J. W. Block. On the tones and pressure oscillations induced by flow over rectangular cavities. *J. Fluid Mech.*, 89:373–399, 1978.

[8] L. N. III Cattafesta, M. S. Kegerise, and G. S. Jones. Experiments on compressible flow-induced cavity oscillations. *AIAA Paper 98-2912*, 1998.

[9] V. Sarohia. Experimental and analytical investigation of oscillations in flows over cavities. *AIAA J.*, 15:984–991, 1977.

TURBOMACHINERY FLUID MECHANICS
(Unsteady Blade Row Interactions in Transonic Flows)

LRIR:92WL034

William W. Copenhaver
AFRL/PRTF
Wright Patterson AFB OH

Abstract
Future advanced military aircraft missions require that air breathing engines operate at double the current thrust-to-weight ratio capabilities. The turbomachinery components of the air breathing engine establishes the engines ability to generate thrust and also account for the greatest percentage of weight in the engine. To meet the thrust-to-weight goals, turbomachinery weight must be reduced and performance increased by the use of thin wide-chord blades with increased loading levels and tip speeds (flow Mach #) while decreasing blade-row spacing. Each of these factors individually results in increases in flow field unsteadiness and together creates significant design challenges. Conditions within the turbomachinery components have become highly unsteady as a result of complex inlet aerodynamic distortions, separated flows, shocks, strong wakes, and passage voticies.

Turbomachinery performance is governed by unsteady fluid flows yet steady design methods are currently used to develop turbomachinery by compensating for the lack of basic knowledge with extensive empirical correlations. The development process is lengthy and expensive, particularly when extrapolations are made to existing correlations as the significance of unsteadiness increases. The need for obtaining further understanding and better design methods related to unsteady turbomachinery flows is key to future advances in compression system performance. Conventional design approaches are steady in nature and do not account for strong unsteady interactions. The magnitude and nature of the unsteady influence between closely spaced transonic blade-rows is not fully understood and therefore cannot be modeled during design.

Results from a research program to investigate blade-row interactions between closely-spaced highly-loaded blade-rows in a transonic compressor are provided in this abstract. Three specific topics, related to unsteady blade-row forcing, blade-row spacing effects on efficiency, and flow swallowing capabilities of imbedded stages are investigated through experimental and computational methods in this study. The results show strong upstream blade-row forcing due to potential fields from a downstream transonic blade-row. High levels of unsteady surface loading were measured and it was determined that spacing between blade-rows had a significant influence on unsteady loading. The studies presented here also indicate significant drops in aerodynamic efficiency due to increased interaction loss. Finally, results from this study demonstrated that for closely spaced blade-rows the choke flow capacity of the rotor does not equal the capacity when tested in isolation. The findings from these studies suggest that unsteady influences are significant when blade-row spacing is reduced.

Research Goals

A joint Air Force Research Lab, Propulsion Directorate (AFRL/PR) / Air Force Office of Scientific Research (AFOSR) initiative is currently underway to establish quantitative evidence of the unsteady effects on the blade passage scale, identify the relative importance of length and time scales of unsteady flow phenomena in turbomachinery and provide for future improvements in technology based on the recognition of unsteady phenomena. The initiative will investigate the effect of unsteady flow fields on blade loading, blade structural response, loss production, wake transport, and wake attenuation.

The specific research goals that will be addressed in this effort are as follows:

1. Investigate and quantify the fundamental vane/blade interaction phenomena relevant to the upstream bow shock forcing function of a downstream rotor in a transonic compression system.

2. Investigate and identify the relevant interaction mechanisms that produce significant increases in aerodynamic loss between adjacent transonic blade-rows.

3. Investigate the effects of stator/rotor axial spacing and stator solidity on overall transonic stage (rotor/stator) performance, with a focus on mass flow capacity.

Experiment

The experiments presented here were performed in the Air Force Research Laboratory Propulsion Directorate Compressor Aero Research Laboratory. (CARL) at Wright-Patterson Air Force Base. The experimental hardware was designed so that the wake generator-to-rotor (where the wake generator models a stator) axial spacing can be set to three values denoted as "close," "mid," and "far" as shown in Fig. 1. The spacings normalized by the wake generator chord are 12%, 26% and 56% respectively.
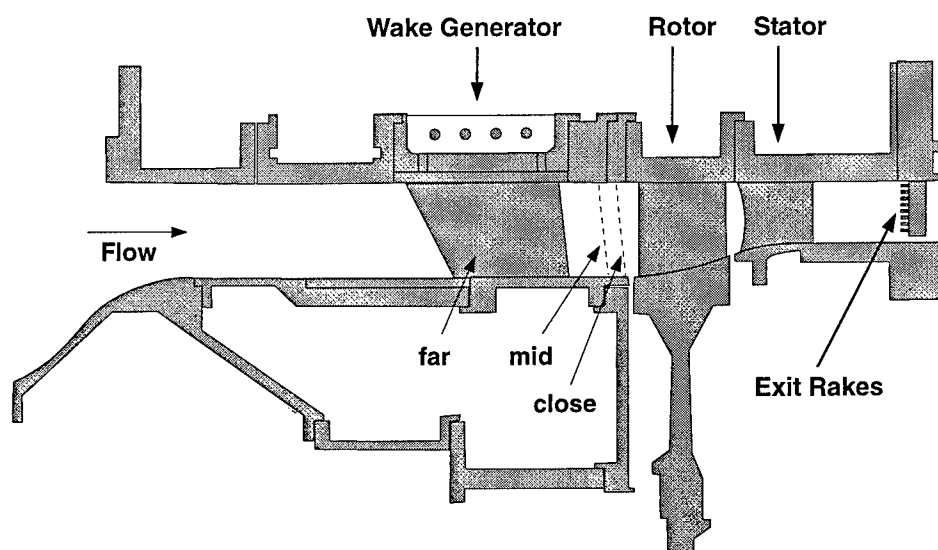
Figure 1. Stage Matching Investigation rig cross-section.

Blade-row Spacing Influence on Unsteady IGV Loading

A series of experiments were performed to investigate the IGV unsteady surface pressure response due to the upstream traveling pressure field generated by the downstream rotor. The influence of blade-row spacing on the time resolved IGV surface pressure fields were established. The data is non-dimensionalized based on the inlet static pressure and then differenced across the IGV surface. Two radial span locations of 50% and 75% at 70%, 83%, 89% and 95% chordwise locations, respectively, were analyzed. The axial spacings compared are 12%, 26% and 56% of the rotor chord. Figure 2. demonstrates the level of peak unsteady loading seen on the upstream blade row due to the bow shock. The figures also indicate that a non-linear relationship exists when this interaction is strong at 75% span.
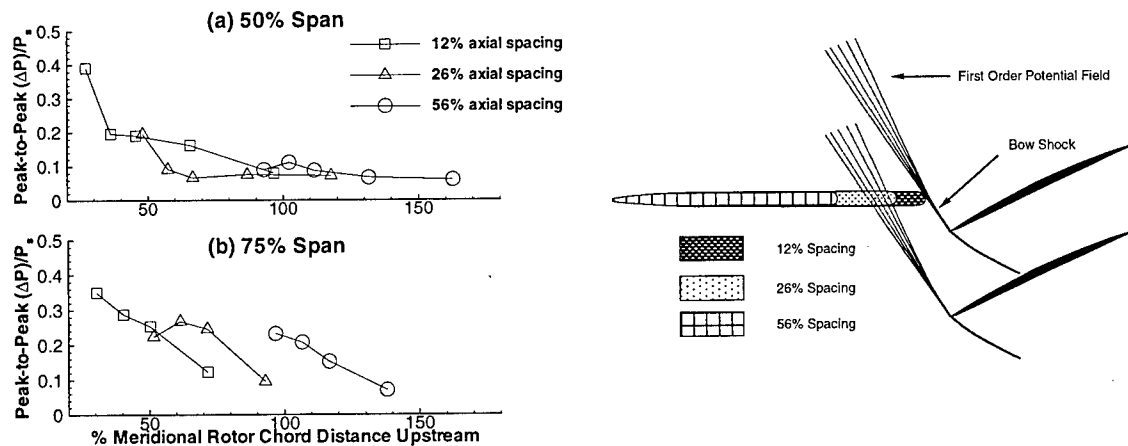
Figure 2. Influence of Spacing and Span on IGV Loading

This research has demonstrated significant unsteady potential pressure variations up to 70% chord on an upstream blade-row due to a downstream rotor bow shock. In addition changes in spacing between these blade-rows has a significant influence on the magnitude and character of the forcing function. Also, variations in spanwise shock strength produce a change in the loading level of the IGV with spanwise location. These upstream influences can have a significant impact on forced response studies for closely spaced blade-rows. These results also demonstrate the potential for significant wake modifications and subsequent loss generation due to this strong bow shock potential field.

The possibility for generation of additional aerodynamic loss and blockage due to this interaction is further studied in the next sections. The influence of blade-row spacing on measured efficiency will be considered first followed by a study of the influence of blade-row spacing on mass flow swallowing capability.

Influence of Spacing on Aerodynamic Efficiency

The research compressor was converted to a two-blade-row configuration by removing the downstream stator. A circumferential total pressure and total temperature traverse mechanism was positioned approximately 1 rotor chord-length downstream of the rotor. Data were obtained for rotor operation between peak efficiency and stall with 40 wake generators installed at the three axial spacings defined previously

The area averaged performance results from the exit plane survey are presented in Figure 3. The bars on the figure indicate the measurement errors. The results in Figure 3 suggest that for a common flow rate, reduced axial spacing has a significant effect on both pressure rise and efficiency. The results show a 1 point drop in efficiency as the spacing is reduced from 56% of upstream blade-row chord (Far Spacing) to 12% chord (Close Spacing). Figure 3 also indicates that the overall pressure ratio is reduced by approximately 3% as the spacing is reduced. These findings are contrary to the experimental results for subsonic flows showing that reducing the axial gap between blade rows in subsonic multistage compressors increased the pressure ratio and efficiency for a given flow coefficient. The pitchwise distributions of pressure ratio for both the close and far spacing at similar flow rates are also shown in Figure 3. For the close axial spacing configuration the wakes from the upstream wake generator can clearly be seen as 4 high gradient regions of reduced pressure ratio. While for the far axial spacing the wakes are nearly non-existent; only identified by the weak gradients. This supports the findings, from the flow capacity study to be addressed next, that for the 56% axial spacing the wakes are nearly mixed out. However, for the close axial spacing the wakes do not have time to mix before encountering the rotor potential field and therefore can clearly be seen downstream of the rotor. The pressure loss encountered by these wakes is far greater than that of simple wake mixing. This suggests that perhaps some other mechanism to create loss occurs while the unmixed wake fluid is under the influence of the rotor.
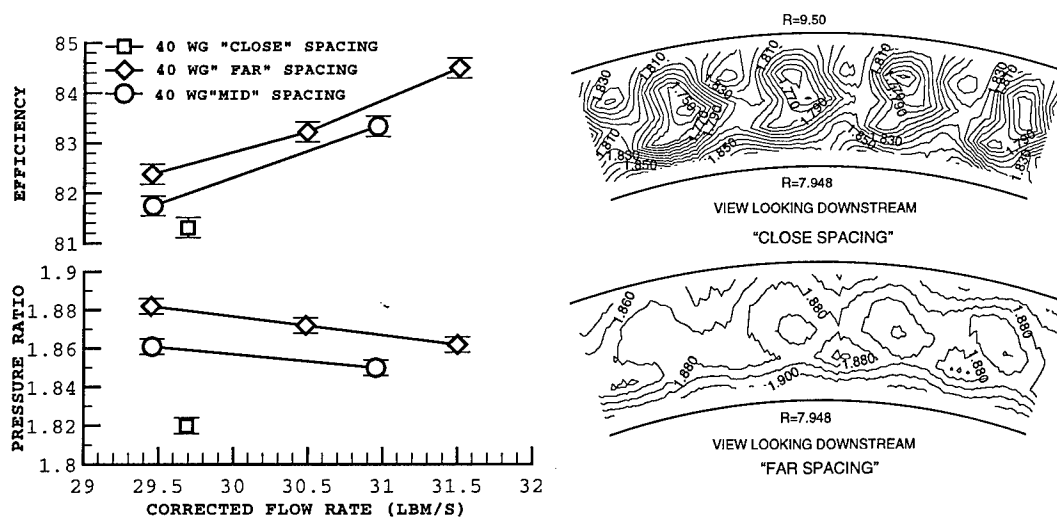
Figure 3. Influence of axial spacing on pressure rise and efficiency of the wake generator and rotor configuration.

Influence of Blade-Row Spacing on Flow Capacity

The choking flow capacity (which for this stage is set in the rotor) results, at the design corrected rotational speed, for the 40 and 24 wake generator cases are shown in Figure 4. Both the three-blade-row choking flow rate as well as the two-blade-row (i.e., the three-blade-row corrected) choking flow rate, are shown in the figures. As seen in the figures, the actual three-blade-row flow rate drop from the "without wake generator case" is significant for both the 40 and 24 wake generator count cases. These results, when corrected for mass averaged total pressure loss at the rotor face indicate no overflowing of the embedded stage as was originally expected when the experiment was designed. Instead, an apparent underflow of 2% for the 40 wake generator close spacing case exists. However, at 56% or "far" spacing no evidence of this drop in flow can be seen.

The flow rate correction is based on isolated wake generator calibration results and so does not include any blade row interaction or shock/wake interaction losses. These losses, if they exist at all, would tend to increase the computed corrected flow rate, i.e., the embedded flow rate. In addition to this, the upstream wakes may effect the blockage development within the rotor and this would directly effect its choking flow capacity. Small blockage changes within a rotor are difficult to sort out even with results from numerical simulations.
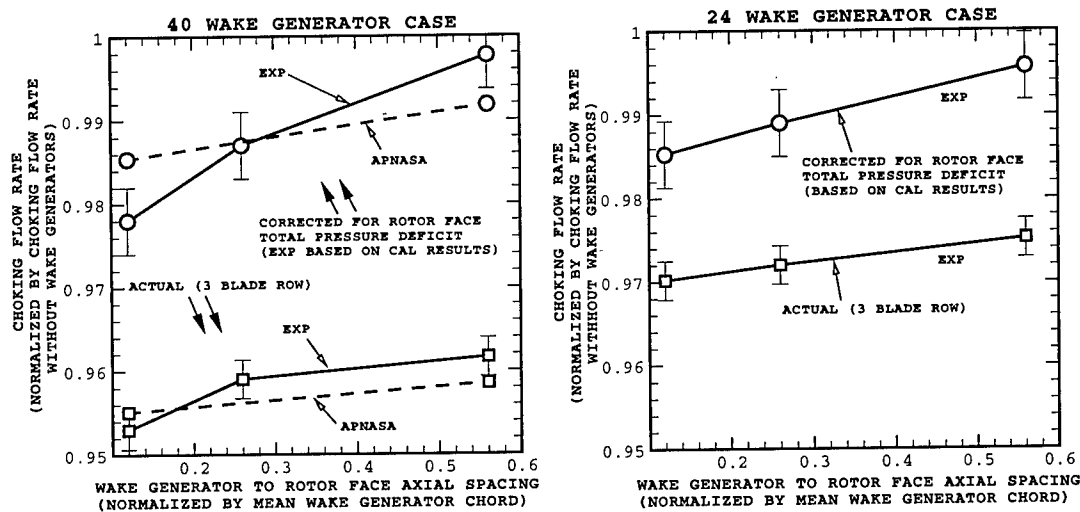
Figure 4. Choking flow rate as a function blade row spacing for the 40 wake and 24 wake generator configurations at the design rotational speed.

Clearly, at some wake generator-to-rotor axial spacing the wake mixing will be complete and any effects from blade row interaction or rotor blockage phenomena will diminish to zero. For this stage, this point is apparently reached (within the uncertainty) near the "far" spacing for both wake generator vane counts. At spacings closer than this other mechanisms, such as those just mentioned, are at work. These effects, having been detected far down the choke line, would only be expected to increase, as the stage is backpressured.

Summary

The present work was an attempt to address the long-standing question regarding the overflow of embedded transonic compressor stages, to establish the influence of axial spacing on performance and quantify the unsteady forcing on upstream blade row. The experiment was designed to isolate and investigate the effects of upstream two-dimensional wakes on downstream stage flow capacity and performance as well as quantify upstream forcing. An individual summary for each investigation is provided below

Flow Capacity: The results show that for axial spacings beyond 50% of the upstream blade chord, simple wake mixing alone fully accounts for the flow losses and a simple correction based on the rotor face mass averaged total pressure deficit is sufficient. At spacings closer than this, other effects or loss mechanisms exist. These may include: 1) Shock/wake or other two-dimensional blade row interaction loss sources not accounted for in the calibration procedure; 2) Increased blockage development in the rotor due to the upstream wakes or secondary flows; and 3) Three-dimensional or other effects not accounted for in the experiment.

Aerodynamic Losses: The experiment with the wake generator and rotor alone (without the exit stator assembly) demonstrated that additional losses above those of conventional mixing do exist for the close axial spacing configuration. These losses resulted in a 1% drop in overall efficiency and a 3% reduction in pressure rise capability.

Aeromechanical Forced Response: This investigation reveals several significant fundamental flow physics phenomena: (1) upstream traveling unsteady pressure fluctuations are significant; (2) the rotor bow shock dominates the pressure variations; (3) changes in axial spacing effects the magnitude and character of the unsteady pressure loading.

The influences of axial spacing on imbedded transonic rotor performance (flow swallowing pressure rise, efficiency and forced response) seen in this study are significant and must be further understood if designs continue to trend toward higher blade loading and reduced spacing. Research is ongoing that will attempt to identify and clarify the relevant aerothermodynamic flow details associated with these close blade row spacings.

MEMS-BASED CONTROL FOR AIR BREATHING PROPULSION: EXTERNAL JET FLOW

Thomas C. Corke

Illinois Institute of Technology[1]
Mechanical, Materials & Aerospace Department
Fluid Dynamics Research Center
Chicago, Il

Background

This work is aimed at the use of an azimuthal array of plasma actuators placed inside the nozzle of a high Mach number axisymmetric jet in order to control the unsteady initial condition of instability modes which affect jet spreading and radiated acoustic tones. The use of plasma actuators is based on concepts developed in our earlier work (Corke & Cavalieri (1995, 1997); Corke, Cavalieri & Matlis, 1998). The present work requires new designs which can produce a stable plasma over large areas (scale up to full-scale jet applications), operate efficiently at atmospheric pressure, and be capable of being easily implemented on thin-skin nozzles used in full-scale jets.

The jet control is designed to couple the shear layer instability modes with the jet column mode. The shear layer modes include both axisymmetric and helical modes in different combinations. This is motivated by our previous work (Corke & Kusek, 1993) where the combination of an axisymmetric mode at the fundamental frequency and helical modes at the subharmonic frequency leads to the double-exponential growth of the helical modes and significant enhanced spreading of the jet shear layer. Closed-loop control will utilize arrays of MEM sensors (provided by MIT) which will be placed at locations in the flow where they will sense velocity and/or temperature (for heated jets) fluctuations associated with the shear layer and core instabilities. Instantaneous time series are constructed and used as input to the actuators to produce an electronic feed-back. With positive feed-back, this results in a steady limit cycle. The frequency is determined by the stability characteristics and a feed-back constraint which requires an integer number of wave lengths from the feed-back sensor to the actuator (or point of receptivity). This methodology is based on the previous work of Ahn (1994), and implemented in the first year of this research program by Chang (1998).

The second year of research has primarily focused on the further development of the plasma actuator arrays, and the documenting of their use in the open-loop excitation of different helical instability of core modes in a round jet. The mile-stones have included:

1. The development of more stable dielectric/insulator materials which allow essentially infinite operation times for the plasma actuators.

2. The development of a new concept of electrode placement and control time series which allows for the first time, phase shifting between neighbor electrodes. This concept is

---

[1]New address: University of Notre Dame, Aerospace & Mechanical Engineering Department, Notre Dame, IN 46556

essential towards increasing the excitation amplitudes of the plasma actuators, and in exciting helical modes in round jets.

3. The quantifying of the unsteady control coefficient, C_μ, for the plasma actuators. This provides a scaling relation between the input voltage and unsteady excitation amplitudes which can be used to design actuators for high-speed applications.

4. The use of the phased actuators to excite the jet column mode for a range of helical mode azimuthal mode numbers from $0 \le m \le 8$ in a jet with $U_j = 30.6 m/s$ and $Re_D = 1.05 \times 10^5$.

The following gives a more detailed summary of the results in these four areas.

Flat-array Phased Plasma Actuators

An extensive effort has been made on the development of actuators which are based on the concept of producing a plasma in a localized region to generate unsteady vortical disturbances. The plasma is produced over electrodes which are located on a surface, where it can excite a boundary layer or separated shear layer. This type of actuator has been used by us in the past to excite instability modes in Mach 3.5 laminar boundary layers (Cavalieri, 1995; Corke et al., 1997, 1998), and to excite shear layers in incompressible to transonic Mach number jets. In a recently completed DARPA Phase I project with UTRC, these actuators showed the potential for producing large control coefficients needed for separation control applications on helicopters. The advantages of the plasma actuators are (1) that they are fully electronic, with no moving parts which can fatigue or limit the frequency band width, (2) they have a high energy density, and (3) they are fully scalable in size, with MEMs scales providing some advantages in their operation.

The plasma flow-actuator concepts are illustrated in Figure 1. For this, an a.c. voltage is supplied to a pair(s) of electrodes. The electrodes are separated by a dielectric-insulator material. In our first application (Cavalieri, 1995), an air gap was used between the electrodes. Presently, we use materials which have better properties than air. When the a.c. potential across the electrodes exceeds a threshold value (inversely proportional to the electrode spacing and a function of the dielectric properties) the air forms a plasma. The plasma produces a body force on the ambient air, $F_B \propto \mathrm{grad}(E^2)$. This amounts to a low pressure region which induces a flow towards the plasma. The no-penetration boundary condition at the wall results in a secondary flow away from the wall, which is represented in the bottom part of Figure 1. With electrodes which are aligned with the flow direction, the secondary motion produces counter-rotating streamwise vortices.

If an electrode pattern which produces an asymmetric plasma strength distribution is used, it is possible to induce a mean velocity. This was used by Roth et al. (1998) to produce a steady thrust component of approximately 3f/s on the wall in a turbulent boundary layer.

The magnitude of a mean flow component produced by plasma actuators, or the magnitude of unsteady disturbances, can be greatly enhanced by phase-shifting the a.c. input to neighbor electrodes. The object here is to cause the plasma to translate in space. In theory, this has the potential to produce velocities of $\mathcal{O}200f/s$ (Roth, 1995) with moderate voltages and low power.

Previous attempts by others (Roth et al., 1998) to supply phase-shifted a.c. voltages, capable of producing a plasma, to individual electrodes which were exposed to air, had
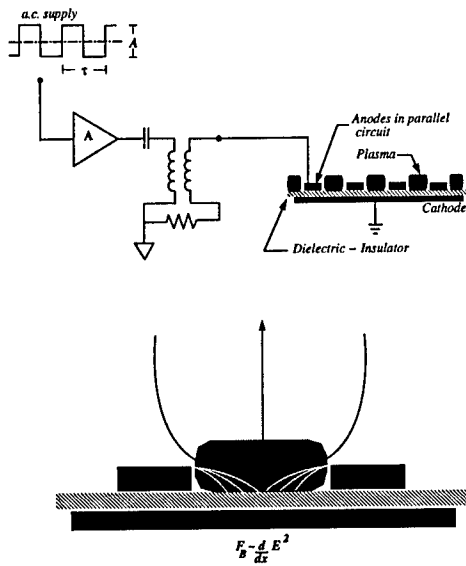
Figure 1. Schematic showing plasma flow-actuator concepts.
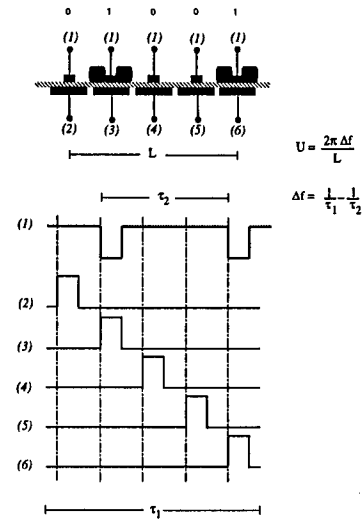
Figure 2. Schematic of two-frequency phased excitation to produce unidirectional plasma motion.

failed. The outcome was arcing between the exposed electrodes because the potential at certain phase increments exceeded the breakdown value for the air. Our approach, which is illustrated in Figure 2, solved that problem. In this case, the phased electrodes (labeled 2-6) are on the underside of the dielectric layer, where they can be isolated from each other by a high-voltage insulator. The electrodes which are exposed to the air (1) have a common a.c. supply. The time traces below the electrode pattern depict one complete cycle to each of the electrodes, where the number on the left refers to the particular electrode. For the lower electrodes, the time series is a short duty cycle pulse which is phase shifted by 72° with respect to its neighbor. These are operated at frequency f_1. The upper electrodes also operate with a short duty cycle time series, but at a frequency, f_2. The plasma forms on either side of the electrode on the upper surface where the potential is large enough. In Figure 2, this occurs where there is a conjunction of the high and low states at a particular electrode, such as (3) and (6). Because the frequencies are different between the time series to the upper and lower electrodes, the location of the plasma moves. The velocity at which it moves is equal to

$$U = 2\pi(f_2 - f_1)l$$

where l is the length of the electrodes corresponding to one period, τ_1.

We have applied this concept towards exciting helical modes in an axisymmetric jet. A schematic is shown in Figure 3. In this case the dielectric insulator was molded to fit along the inside wall of a straight nozzle extension. Eight (8) electrodes on the outside (labeled 2-9), have inputs with different phase shifts, to excite different helical mode numbers. The time series to excite an $m = 4$ mode is shown in the figure. The plasma forms on the flow-side of the dielectric, on either side of the electrodes labeled (1). The implementation of this concept in a straight extension on the exit of the jet nozzle is shown in the photographs in Figure 4.
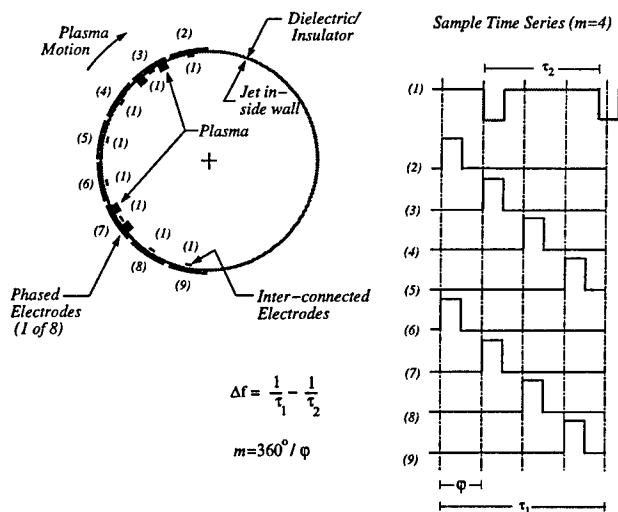
Figure 3. Schematic of two-frequency phased excitation to produce helical disturbances in a round nozzle.
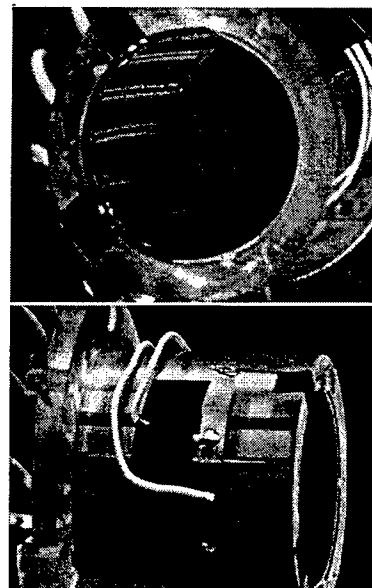
Figure 4. Photograph of nozzle extension showing internal and external electrodes.

The azimuthal position of the plasma travels around the nozzle based on the phase shift between neighbor electrodes, and the frequency difference between the time series supplied to the inner and outer electrodes. This is documented in Figure 5, which shows a movie frame sequence for conditions to excite a $m = 1$ helical mode. Time starts in the top-left frame, and increases in each successive frame going from left to right and continuing from the top to bottom rows. In this sequence, the plasma (bright line) is seen to move around the nozzle, starting from the bottom.

Column Mode Excitation

The plasma actuator was used to excite the jet column mode at different azimuthal mode numbers in the range $0 \leq m \leq 8$. This investigation is the next step towards the combined excitation which couples the shear layer and column modes, that was investigated last year using miniature speakers as the actuators (Chang, 1998). The excitation frequency was $f = 266\text{Hz}$, which corresponds to the most amplified $S_t = fD/U_j = 0.44$. The velocity time series were obtained from a constant-temperature hot-wire, which were digitally sampled. Discrete Fourier analysis of the time series was used to determine the amplitude of velocity fluctuations of the excited mode.

Figure 6 shows the streamwise development of the centerline velocity fluctuations at the excitation frequency for the different azimuthal mode numbers. The upward triangles corresponds to the natural (unforced) jet. The solid line indicates the linear growth rate based on the natural jet. In all cases, the amplitude increases as a result of the helical mode excitation. Further downstream, the largest amplitudes correspond to the $m = 0$ and $m = 4$ cases.

This effect of azimuthal mode number on the centerline velocity fluctuations is further
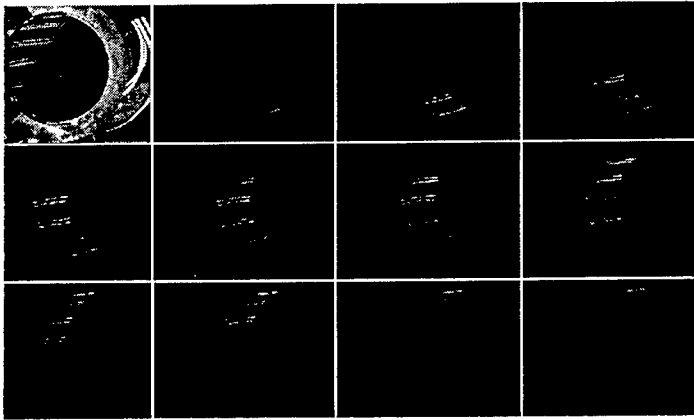
Figure 5. Sequential movie frames showing plasma motion to excite $m = 1$ helical mode.
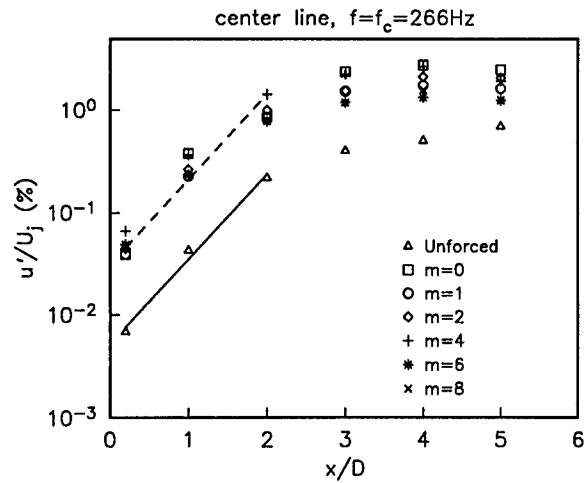
Figure 6. Streamwise development of centerline u'/U_j level at the column mode frequency for different azimuthal mode numbers.
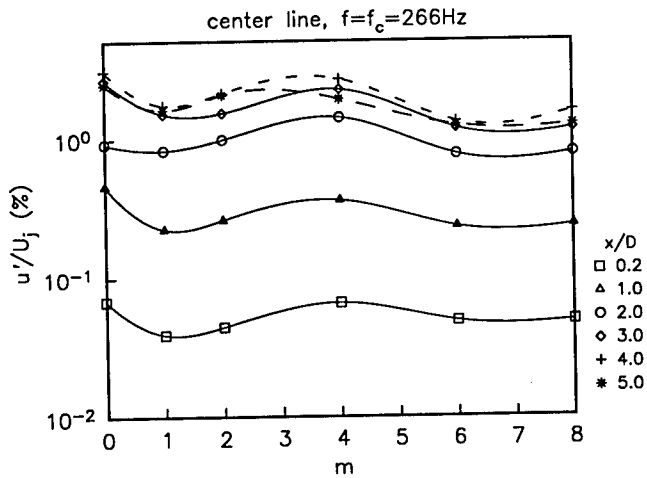
Figure 7. Centerline column mode u'/U_j levels as a function azimuthal mode number, at different x/D locations.
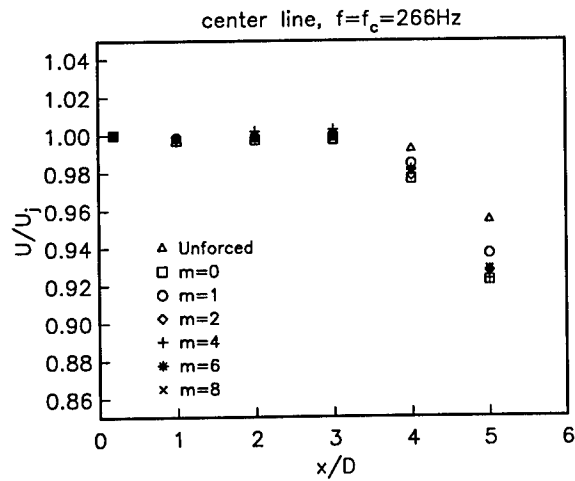
Figure 8. Streamwise development of centerline mean velocity for different azimuthal mode numbers.

demonstrated in Figure 7. This shows the u'/U_j level as a function of m at different x/D locations. Initially, $m = 0, 4$ & 8 produce higher centerline fluctuations. However, past amplitude saturation, $x/D \simeq 4$, the highest levels shift towards lower azimuthal mode numbers, $m = 0$ & 2.

The effect of the azimuthal mode number on the centerline mean velocity is shown in Figure 8. Further downstream, all of the excitation cases result in a faster centerline velocity decay. The largest decay occurs for the $m = 0$ & 4 modes, which is consistent with the fluctuation amplitude results in Figure 7.

Other Results and Future Direction

These results are a small part of an extensive study of the effect of azimuthal mode number on the development of the shear layer and column modes, which was conducted using the the phased plasma actuator. The next steps in this research will be:

1. to configure the phased plasma actuator for a thin-walled nozzle,

2. to investigate its ability to excite modes at higher jet Mach numbers ($\mathcal{O}$ 0.6-0.8) and Reynolds numbers ($Re_D \simeq 0.5 \times 10^6$),

3. operate the actuator with closed-loop feedback, similar to Chang (1998).

This work will be conducted in the high-speed jet facility in the Hessert Center for Aerospace Research at the University of Notre Dame.

Acknowledgment/Disclaimer

References

Ahn, S. 1994. Low dimensional dynamics of azimuthal modes in an axisymmetric jet with enhanced feedback. Ph.D. Ill. Inst. Tech.

Corke, T. C. and Kusek, S. M., 1993. Resonance in axisymmetric jets with controlled helical mode input. *J. Fluid Mech.*, **249**, pp. 307-336.

Corke, T. C. & Cavalieri, D. 1997. Controlled experiments on instabilities and transition to turbulence in supersonic boundary layers, AIAA 97-1817.

Corke, T. C., Cavalieri, D. & Matlis, E. 1998. Controlled experiments on instabilities and transition to turbulence in supersonic boundary layers, to appear *NASA CR*.

Chang, A. 1998. Mode-coupled feedback excitation in an axisymmetric jet. M.S. Thesis, Ill. Inst. Tech.

Roth, J. R., Sherman, D. & Wilkinson, S. 1998. Boundary layer flow control with one atmosphere uniform glow discharge surface plasma. AIAA-98-0328.

UNSTEADY AND THREE-DIMENSIONAL FLOWS IN TURBOMACHINES

AFOSR Grant F49620-96-1-0266

A.H. Epstein, E.M. Greitzer, G.R. Guenette, J.L. Kerrebrock, C.S. Tan,
R, Keogh, A. Khalak, D. Vo
Gas Turbine Laboratory
Massachusetts Institute of Technology

Abstract

1.0 Introduction

This document constitutes an annual progress report on a multi-investigator research program on unsteady and three-dimensional flow phenomena in turbomachines. The report covers the work conducted during the period June 1, 1998 to June 31, 1999. The unifying theme in the work described is the view that primary barriers to achieving increased overall performance of turbomachines are linked to local phenomena which are inherently three-dimensional and/or unsteady. The objectives of this multi-investigator program are as follows.

1) Elucidate the physical mechanisms associated with steady and unsteady interactions between turbine aerodynamics and rotor blade film cooling that debit turbine efficiency and blade life.

2) Identify parameters that characterize flutter in high performance compressor and develop methodology for compressor flutter clearance..

3) Quantify the impact of flow unsteadiness in multi-stage turbomachines on performance and develop effective strategies for managing these effects with the intent of performance enhancements.

Progress made in the past year toward accomplishing the above objectives is described in Section 2.0 entitled "Influence of Film Cooling on the Aerodynamic Performance of Film Cooled Turbines ", Section 3.0 entitled "Flutter Clearance Methodology", and Section 4.0 entitled "Unsteady Flow in Turbomachinery Endwall Flows: Role of Tip Leakage Vortex/Endwall Flow on Axial Compressor Rotating Stall Inception."

2.0 Influence of Film Cooling on the Aerodynamic Performance of Film Cooled Turbines

This is part of an effort to study the aerodynamic performance penalties due to film cooling on a fully-scaled transonic turbine stage. The test turbine has a design pressure ratio of 2.0 with a loading coefficient of 2.0. The cooling mass flow for the NGV, rotor and casing cooling account for 10% of the stage exit mass flow. The results from two series of experiments in MIT Blowdown Turbine Facility are compared:

Uncooled Turbine Performance – In order to measure the performance penalties due to film cooling, a test was conducted on the uncooled turbine in order to determine its aerodynamic performance. The results from this uncooled test form a baseline against which the performance of the cooled turbine can be compared. This test required

incorporating several new features into the Blowdown Turbine Facility. Actual turbine power was measured directly while ideal power was determined by measuring turbine mass flow, pressure ratio, and inlet total temperature. The turbine was tested over a range of operating conditions by varying its pressure ratio and corrected speed.

Cooled Turbine Performance – The film cooled turbine was fabricated by incorporating cooling channels into the uncooled turbine nozzle guide vanes and rotor blades using Electrical Discharge Machining. The film cooling holes were then machined by laser drilling holes from the airfoil surfaces to the cooling channels. Preliminary testing of the film cooled turbine has begun. The turbine will be tested over the same range of operating conditions as the uncooled turbine. A range of coolant to mainstream mass flow and temperature ratios will also be tested. A combination of analytical and computational tools will be used to determine if the differences between the uncooled and cooled performances can be explained using models developed using cascade tests.

3.0 Flutter Clearance Methodology
The objective of this task is the development of methodologies for assuring, by testing, that compressor and fan designs are free of self-excited aeroelastic instabilities (flutter) throughout their operating range. Such assurance requires understanding of the dependence of the flutter boundaries on all relevant (dimensionless) parameters that vary during operation, so that testing can be conducted over the full relevant parameter space. In current practice such testing is generally limited to two-parameter domains, defined by reduced velocity and incidence, or by location on the compressor performance map, which is expressed in terms of pressure ratio vs corrected weight flow and corrected speed. This program has focused on stall-flutter as a phenomenon that has been especially troublesome to the aircraft engine community.

Modeling conducted under this program has shown that a full definiton of the stall-flutter boundaries for high speed compressors and fans requires consideration of at least four dimensionless parameters: Mach number, reduced velocity, incidence, and the ratio of mechanical damping to relative air density. The modeling further defines the shape of the flutter boundaries in this four-space, in terms of a set of coefficients that must be determined empirically and by use of numerical models that embrace two of the parameters. The available flutter data base is currently being examined in the context of the model, to determine the coefficients and their level of generality. Data that has been embraced to date includes that from a family of core compressors and from two fans.

4.0 Unsteady Flow in Turbomachinery Endwall Flows: Role of Tip Leakage Vortex/Endwall Flow on Axial Compressor Rotating Stall Inception

4.1 Introduction
A key objective of this subtask is to establish the link between blade passage flow events (particularly the tip clearance flow and the casing boundary layer) and rotating stall inception to enable the quantitative delineation of the physical parameters that control rotating stall. Recently, three-dimensional single and multi-bladed computations of an isolated compressor rotor by Hoying [1] showed that the central feature of the flow associated with the development of short length-scale (spike) stall inception was the tip clearance vortex moving forward of the blade leading edge. Vortex kinematic arguments were used to provide a physical explanation of this motion and also to explain why the tip vortex trajectory at the leading edge of the compressor sets compressor stability. Further

detailed analysis of the multi-blade computational results showed that both tip vortex circulation and blockage increases with throttle closing prior to stall. At stall inception, the traveling disturbance causes the tip vortex trajectory and circulation in any particular blade passage to oscillate in time and to lead in phase of the blockage oscillation. Single-blade computations showed similar tip vortex behavior prior to stall and stall point compared to the multi-blade calculation. A criterion for compressor stall inception in terms of tip vortex position and the utility of single-blade computations for predicting stall point had been developed based on these results [2].

4.2 Progress in the Past Year

In the past year, the focus has been on examining the following issues:

(1) Adjacent stator blade rows can potentially affect the behavior of the tip vortex, and thus stall inception. How is the observed stall behavior different in a full-stage (rotor-stator) or multi-stage environment from isolated rotor situations ?

(2) Hoying's simulation was based on inviscid casing assumption. However, a casing boundary layer implies a decrease in upstream velocity seen by the tip vortex and an increase in blade tip loading and blockage. What impact would the presence of the casing boundary layer have on the stall inception behavior?

(3) What is the mechanism of stall disturbance propagation with respect to the blade row?

To address the first two issues, we repeated Hoying's computations with the addition of a stator blade row and with or without a large shear layer at the casing (i.e. to model viscous versus inviscid casing wall situation). Single blade passage rotor-stator calculations showed that the only effect of the casing shear layer is, as expected, to cause the tip vortex trajectory to move to the leading edge at a higher mass flow due to the lower incoming velocity in the tip region.

However, the multi-bladed calculations show a difference in the stall inception process in the presence of a stator and/or casing shear layer. First, simply adding a stator caused the compressor to exhibit long length-scale (modal) stall inception. It is likely that the addition of the stator changed the system to stall by modes. This effect of adjacent blade row(s) on stall is in agreement with the work by Gong [3] on modeling multi-stage compressor instability.

With a casing shear layer representative of the incoming boundary layer seen by an embedded stage, short length-scale disturbances do appear in the tip region, as in Hoying's single rotor computations, but do not grow. On a preliminary basis, we may thus deduced that the casing boundary layer can affect the rotor-stator stage stalling behavior.

To complement the analytical/computational effort, we have also examined data from several organizations. Specifically experimental data from a low speed multistage compressor at Whittle laboratory [4] appear not to indicate the tip vortex trajectory at the rotor leading edge for spike stall inception while data from an axial pump [5] with a high rotor stagger angle and a large casing boundary layer showed the tip vortex trajectory at the leading edge prior to stall. Numerical simulations by Van Zante [6] for NASA Compressor Stage 35 also showed that tip vortex trajectory moves to the rotor leading edge as compressor is throttled toward stall.

We infer from the above that: (i) there can be blade events other than the tip vortex

trajectory position (relative to rotor leading edge) that can set compressor stall, and (ii) flow event that set spike stall inception depends on compressor design parameters and casing boundary layer.

4.3 <u>Current and Future Work</u>

Based on results obtained in the past year as described in the above, the following questions need to be addressed for an adequate parameterization of compressor stall inception:

(1) What determine the flow event(s) on the blade passage level that set compressor stall inception?

(2) If compressor tip clearance/endwall flow limit compressor stability, what specific aspects of (e.g. tip vortex trajectory vs blockage associated with) the casing endwall/clearance flow play the role of initiating compressor stall?

(3) What sets short-length scale (spike) versus long-length scale (modal) stall inception?

Resolution of the these questions would enable the delineation of conditions for a specific route to compressor stall, and the development of effective methodologies to manage compressor stability margin.

<u>References</u>

1. Hoying, D.A., C.S. Tan, H.D. Vo and E.M. Greitzer, 1998, "Role of Blade Passage Flow Structures in Axial Compressor Rotating Stall Inception," ASME Paper 98-GT-588.
2. 1997 AFOSR Annual Contractor Meeting
3. Gong,Y., C.S. Tan, K.A. Gordon and E.M. Greitzer, 1998, "A Computational Model for Short Wavelength Stall Inception and Development in Multi-Stage Compressors," ASME Paper 98-GT-476.
4. Seitz, P., N. Cumpsty, Private Communications, Whittle Laboratory, U.K., 1999.
5. Bross, S., S. Brodersen, H. Saathoff and U. Stark., 1997, "Experimental and Theoretical Investigation of the Tip Clearance Flow in an axial Flow Pump," 2nd European Conference on Turbomachinery –Fluid Dynamics and Thermodynamics, Antwerpen, Belgium, 1997
6. Van Zante, D.E., Strazisar, A., Wood, J., Hathaway, M., Okiishi, T., "Recommendations for Achieving Accurate Numerical Simulation of Tip Clearance Flows in Transonic Compressor Rotors," ASME 99-GT-390.

CONTROL OF SEPARATION USING PULSED WALL JETS:
NUMERICAL INVESTIGATIONS USING DNS AND LES

AFOSR Grant Number F49620-97-1-0274

Abstract

by

Hermann F. Fasel
Department of Aerospace and Mechanical Engineering
The University of Arizona
Tucson, AZ 85721

CONTROL OF SEPARATION USING PULSED WALL JETS: NUMERICAL INVESTIGATIONS USING DNS AND LES

Hermann F. Fasel

Department of Aerospace and Mechanical Engineering

The University of Arizona, Tucson

Abstract

In a numerical/theoretical effort, we are investigating the dynamical behavior of coherent structures in unforced, and periodically forced, turbulent wall jets. Experimental research by Wygnanski and co-workers (Wygnanski 1997) has provided considerable evidence that periodically forced wall jets (tangential oscillatory blowing) may be an effective method for the control of separation of flows over single-element or segmented airfoils (including flaps). However, many of the fundamental mechanisms that are responsible for the often striking effect of oscillatory blowing are not yet understood. Therefore, in close collaboration with the experimental effort, direct numerical simulations (DNS), large-eddy simulations (LES), and stability investigations are being carried out for typical wall jet configurations. These configurations arise when periodic forcing is applied for separation control in practical applications, e.g., separation control for flows over airfoil/flaps. To this end, we are performing numerical simulations for weak wall jets, that is, for wall jets that are embedded in a strong external stream. Future simulations are also planned for wall jets over curved surfaces. The work described is a continuation of a research effort funded previously by AFOSR, where the major emphasis has been on strong wall jets (no external stream or a weak external stream) and for flat plate surfaces only. Most of the necessary numerical tools required for the present and future numerical simulations were developed during this previous research effort (e.g. Navier-Stokes codes for DNS and LES). The goal of the present research effort is, with the joint experimental/numerical approach, to uncover the governing physical mechanisms responsible for the striking effect of oscillatory blowing on separation, and thus provide the physical understanding required to further develop this technique for practical use. Towards this end we are performing simulations using simplified model geometries that allow a reliable investigation of the relevant mechanisms and prevent contamination by effects that are not relevant.

Over the past decade, a great amount of experimental work has been performed by Wygnanski and coworkers (Wygnanski 1997) which clearly demonstrates the effectiveness of using pulsed wall jets for delaying separation. The setup of one such experiment (Seifert et al. 1993) is illustrated in Figure 1a. As an ultimate goal of our computational research we plan to investigate the flow over actual slotted flaps (Figure 1b). However, this geometry is very complex since effects of adverse pressure gradient and curvature are present simultaneously. Therefore, we have focussed first on flat surface geometries (Figure 1c) in order to isolate the influence of the adverse pressure gradient on weak wall jets.

a) NACA 0015 airfoil with slotted flap used in experiments by Seifert et al. (1993).

b) future computational flow geometry:
curved surface, adverse pressure gradient

c) current computational flow geometry:
flat surface, adverse pressure gradient
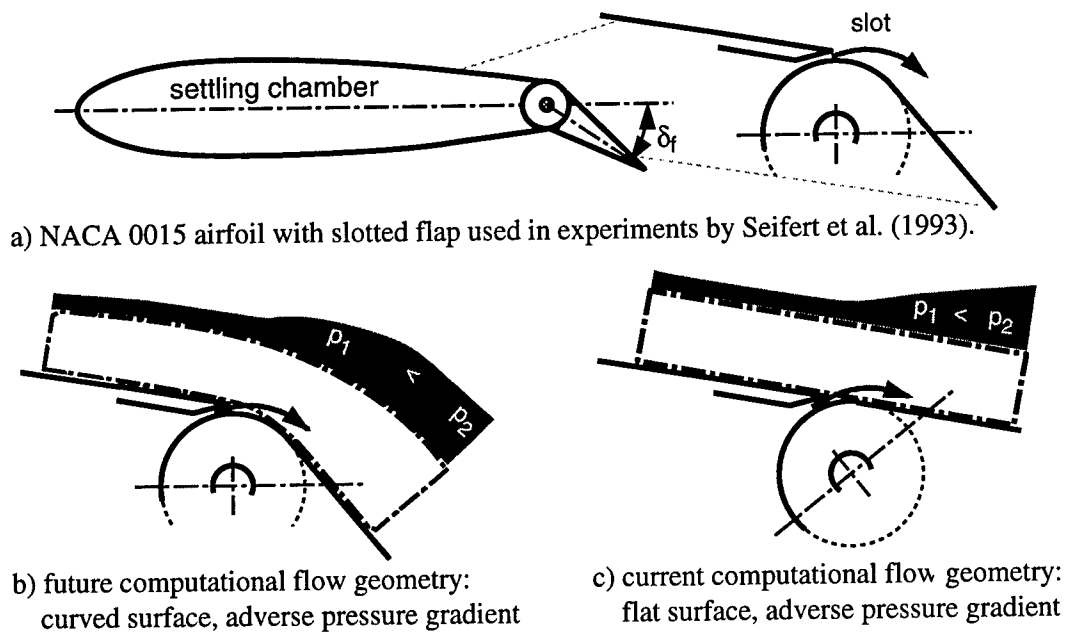
Figure 1: Flow over a slotted flap with oscillatory forcing.

The Navier-Stokes codes employed for our numerical investigations were originally developed in our research group for boundary layer transition and have since been adapted to the wall jet flow geometry. In these codes, the complete incompressible Navier-Stokes equations are solved in vorticity-velocity formulation. For the time integration, a fourth-order Runge-Kutta method is employed. For the spatial discretization in the streamwise and the wall-normal directions, fourth-order accurate compact differences are used, while the spanwise direction is treated pseudo-spectrally. For the LES of turbulent wall jets, as a first step, a basic Smagorinsky-type subgrid-scale model (suggested by Speziale 1995) was implemented into the Navier-Stokes code using a constant Smagorinsky coefficients. As we have reported in the AFOSR contractor meeting last year, this baseline eddy-viscosity model performs reasonably well for LES of zero-pressure gradient weak wall jets. However, from preliminary calculations we know that this baseline model cannot properly estimate the subgrid-scale stress for more complex flows (such as wall jet flows with strong adverse pressure gradients) which may be close to separation (Figure 1c). Therefore, we are currently implementing a new subgrid-scale model into the wall jet codes. This model has been developed in cooperation with C. Speziale of Boston University (Speziale 1998). The new subgrid-scale model is based on the algebraic stress model (ASM), developed originally by Gatski and Speziale (1993), that allows for a misalignment between the stress and strain rate tensor as it occurs in non-equilibrium flows. A key feature of the new LES model is that it is consistent with DNS for fine grid resolution and with Reynolds Averaged Navier-Stokes (RANS) calculations for coarse grid resolution. The performance of the LES code with the new model has been evaluated in the RANS limit for a turbulent boundary layer and for a turbulent strong wall jet. For both types of flows very good agreement with the published literature was achieved.

a) wall jet velocity
maximum and minimum
versus
streamwise direction

(dotted line represents
free stream velocity)

b) wall jet velocity profiles
at three streamwise
locations

(dotted profiles
represent
undisturbed
boundary layer)
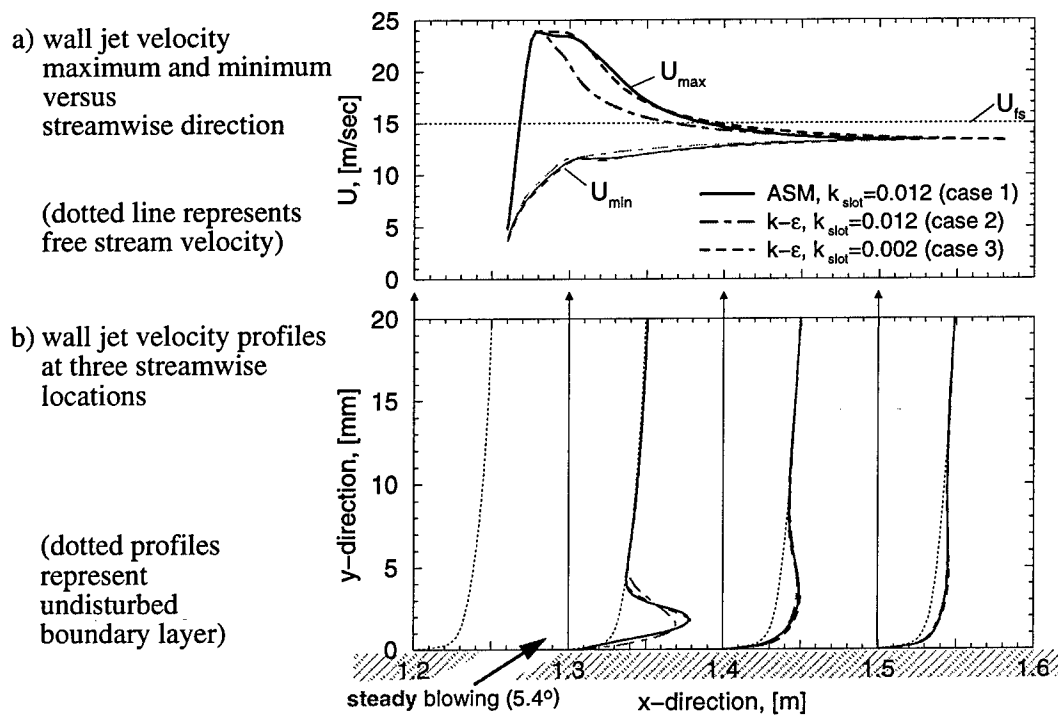
Figure 2: Test case for the new LES methodology: RANS calculation of a weak wall jet blown into a turbulent boundary layer through a slot at a shallow angle (5.4°). Comparison of the streamwise velocity components computed with ASM and with a standard $k - \epsilon$ model.

For further testing of the model we performed RANS calculations of a turbulent weak wall jet which was generated by blowing into a turbulent boundary layer through a slot at a shallow angle (geometry in Figure 1c). Over the blowing slot, streamwise and wall-normal velocity profiles are specified. This simple approach for modeling the blowing slot, while allowing for some flow adjustment close to the slot, produces the correct downstream development of the wall jet, as was demonstrated in earlier simulations (DNS of laminar wall jets, LES of turbulent wall jets using the Smagorinsky baseline model). For the new LES, a Dirichlet boundary condition is also imposed for the turbulent kinetic energy ($k_{slot} > 0$). k_{slot} provides a measure for the turbulence level within the injected fluid. We have verified that the choice of k_{slot} only influences the flow close to the blowing slot and is not crucial for the development of the weak wall jet further downstream. This is illustrated in Figure 2, where the streamwise development of the wall jet velocity is compared for three different RANS calculations: ASM with $k_{slot} = 0.012$ (case 1), standard $k - \epsilon$ model with $k_{slot} = 0.012$ (case 2), standard $k - \epsilon$ model with $k_{slot} = 0.002$ (case 3). While the three cases differ close to the blowing slot, they are all in good agreement further downstream. Over the blowing slot, the standard $k - \epsilon$ model is certainly not well calibrated, and, as a result, it is very dissipative (case 2). Consequently, the weak wall jet initially decays more rapidly than for the ASM (case 1). This can be offset by reducing k_{slot}. The $k - \epsilon$ model (case 3) then matches the ASM result (case 1) even close to the slot.

74

a) ASM, k$_{slot}$=0.012   b) ASM, k$_{slot}$=0.005
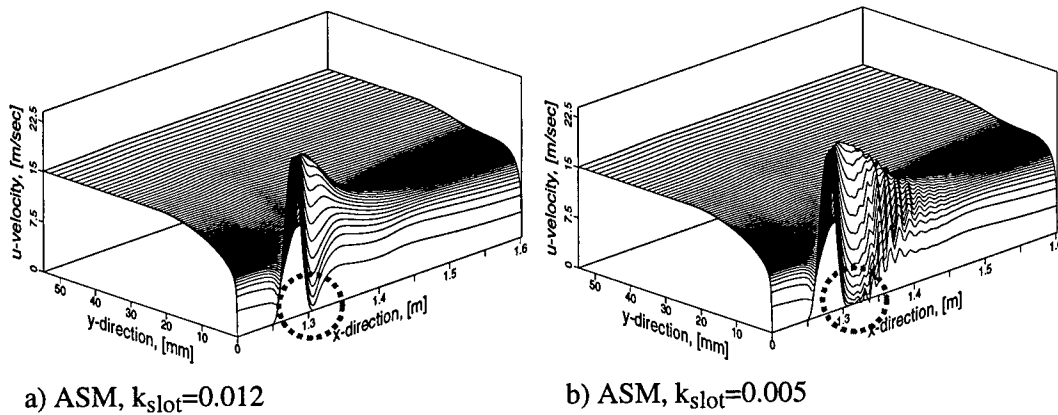
Figure 3: Unsteady RANS calculation of weak wall jet using ASM. Shown are perspective plots of the streamwise velocity for two different levels of turbulent kinetic energy that are specified over the blowing slot (k_{slot}).

An important feature of the new LES methodology is the fact that it allows for unsteady calculations even in the RANS limit. This is accomplished by the use of a time-accurate Navier-Stokes code and the use of the self-adjusting turbulence model (ASM). An example is provided in Figure 3 which shows perspective plots of the streamwise velocity for two RANS calculation using ASM with different levels of k_{slot}. While in the case of k_{slot} = 0.012 (Figure 3a) the flow converges to a steady state, in the the case of k_{slot} = 0.002 (Figure 3b), downstream traveling, unsteady structures are observed. These structures originate in a small separation bubble which has formed right downstream of the blowing slot. Note, that for smaller k_{slot} the jet has less turbulent intensity, and, as a consequence, turbulent mixing is decreased. Therefore, locally the jet can separate from the surface. When the standard $k - \epsilon$ is used instead of the ASM, a separation bubble occurs only for a much smaller k_{slot}, and even when vortical structures are eventually generated, they decay very rapidly.

In parallel with the development of our code employing the new LES methodology, we have investigated turbulent weak wall jets using LES with the Smagorinsky baseline model. Towards the goal of investigating tangential blowing as a tool for separation prevention on an airfoil geometry, we have studied the effect of tangential blowing into a turbulent boundary layer with an adverse pressure gradient. A typical case of such investigations is presented in Figure 4. In the absence of blowing, the turbulent boundary layer separates due to the strong adverse pressure gradient, as illustrated in Figure 4a. When steady blowing is employed (not shown), the flow remains attached, although it gets close to separation. With additional periodic forcing (Figure 4b) the flow does not come close to separation. This can be seen most clearly from the skin friction coefficient plotted in Figure 5 for the three cases. While forcing the weak wall jet clearly produces two-dimensional coherent structures (Figure 4b), their growth rate is lower than could be expected from experimental findings (Zhou, personal communication). It is suspected that the baseline Smagorinsky model which was employed in this LES provided too much dissipation.
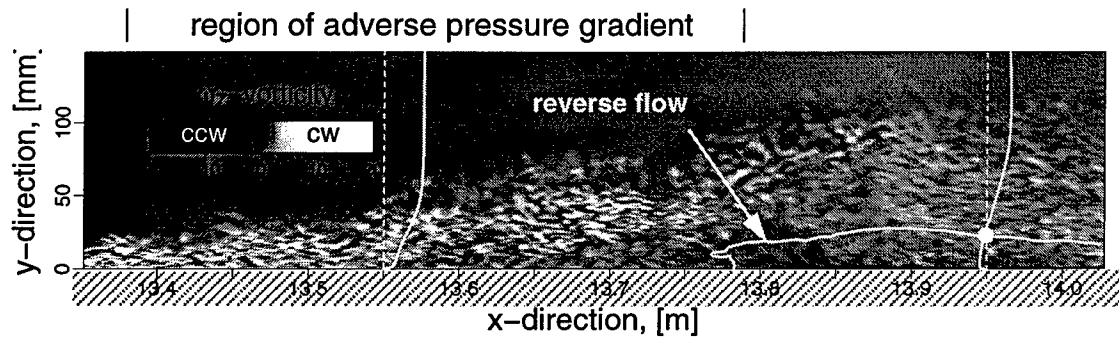
a) turbulent boundary layer without wall jet
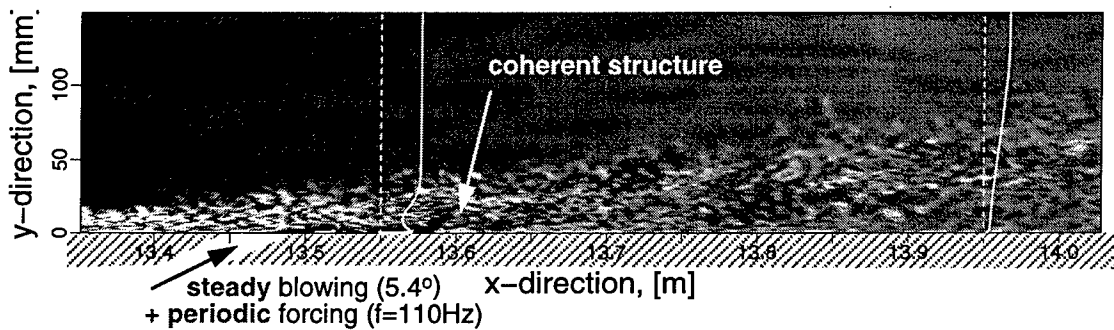
b) turbulent boundary layer with forced wall jet

Figure 4: Turbulent flat-plate boundary layer subjected to strong adverse pressure gradient. Separation prevention using a weak wall jet. Shown are color-contours for the 2-D Fourier component of the instantaneous spanwise vorticity.

a) streamwise velocity at the free stream and wall jet velocity maximum

b) skin friction coefficient versus streamwise direction
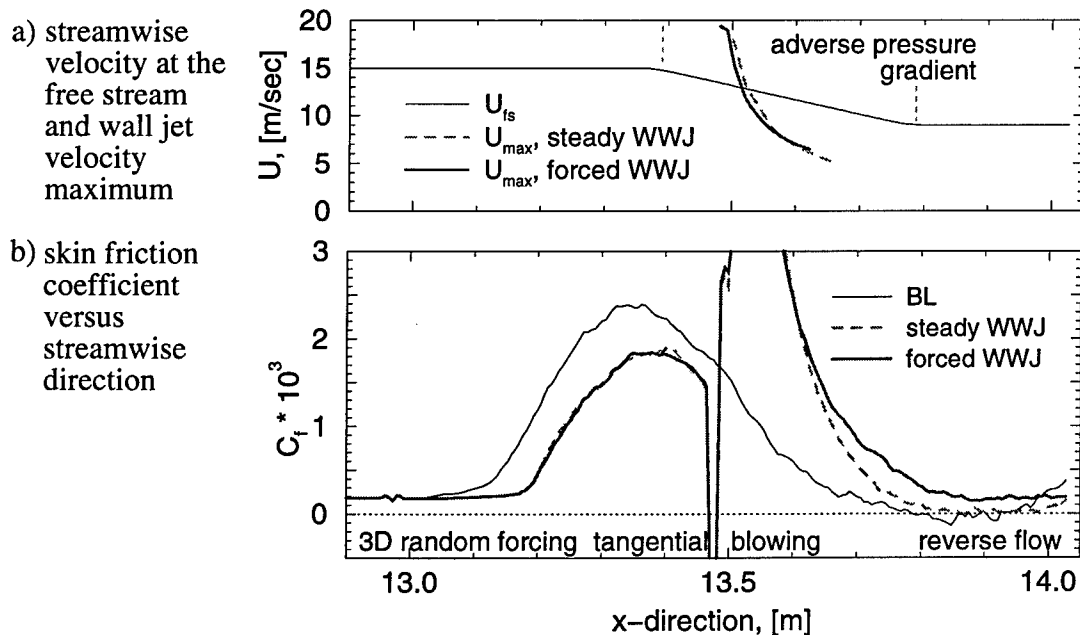
Figure 5: Streamwise development of time-averaged flow quantities for the calculations shown in Figure 4.

Future Work

For the remainder of the present research project, we will further test the new LES methodology for computing unforced and forced turbulent weak wall jets. The new LES methodology will then be employed for investigating turbulent weak wall jets used for separation prevention (Figure 4). We expect that with the new LES approach the development of coherent structures in the flow will better match experimental findings. As a next step, we plan to incorporate a curved grid geometry into our LES code. This will enable us to study the effect of curvature on weak wall jets (Figure 1b). A Navier-Stokes code for computing on curved wall geometries is already in use for DNS of the turbulent flow over a Stratford ramp (Zhang and Fasel 1999).

Acknowledgement/Disclaimer

References

Gatski, T. and Speziale, C., 1993, "On Explicit Algebraic Stress Models for Complex Turbulent Flows," *J. Fluid Mech.* **254**, 59-78.

Seifert, A., Bachar, T., Koss, D., Shepshelovich, M., and Wygnanski, I., 1993, "Oscillatory Blowing: A Tool to Delay Boundary-Layer Separation," *AIAA J.* **31**, 2052-2059.

Speziale, C., 1998, "Turbulence Modeling for Time-Dependent RANS and VLES: A Review", *AIAA J.* **36**, 173-184.

Wygnanski, I., 1997, " Boundary Layer and Flow Control by Periodic Addition of Momentum (invited)," AIAA Paper 97-2117.

Zhang, H.-L. and Fasel, H., 1999, "Direct Numerical Simulation of the Turbulent Flow over a Stratford Ramp", AIAA Paper 99-3359.

Personnel

Hermann F. Fasel, Professor, principal investigator
Stefan Wernz, graduate student

Presentations at Conferences

Wernz, S. and Fasel, H., 1997, "Numerical Investigation of Forced Strong and Weak Wall Jets," *APS*, 50th Annual Meeting of the Division of Fluid Mechanics, San Francisco, CA, November 23-25.

Wernz, S. and Fasel, H., 1999, "Numerical Investigation of Turbulent Weak Wall Jets Using LES and RANS," 15th Arizona Fluid Mechanics Conference, Tucson, AZ, April 23-24.

SHEAR FLOW CONTROL USING SYNTHETIC JET FLUIDIC ACTUATOR TECHNOLOGY

Ari Glezer
Woodruff School of Mechanical Engineering
Georgia Institute of Technology

I. Overview

The global aerodynamic forces on lifting surfaces are manipulated by dynamic control of flow reattachment and separation using fluidic actuators based on synthetic (zero net mass flux) jet technology that has been developed at Georgia Tech (Smith and Glezer, 1998). The efficiency of synthetic jets for modifying the aerodynamic characteristics of an unconventional airfoil has been demonstrated in a series of wind tunnel experiments (Smith et al., 1998 and Amitay et al., 1998, 1999) at moderate Reynolds numbers (up to 10^6) and resulted in a dramatic increase in lift coupled with a decrease in pressure drag. The jets are typically operated at frequencies that are an order of magnitude higher than the shedding frequency of the airfoil [$F^+ \sim O(1)$] and because they are zero net mass flux in nature, their interaction with the cross flow leads to local modification of the apparent shape of the flow surface. Full or partial reattachment including the controlled formation of a closed separation bubble, can be effected by the streamwise location and the strength of the jets. The excitation is effective over a broad streamwise domain that extends well upstream of where the flow separates in the absence of actuation and even downstream of the front stagnation point on the pressure side of the airfoil.

In the present experiments, the response of the flow to time-modulated control input is measured in the cross stream plane of the airfoil wake using jet frequencies that are either well above or of the same order as the natural shedding frequency [i.e., $F^+ \sim O(10)$ and $\sim O(1)$, respectively]. For both frequency ranges, the collapse of the separated flow region is associated with a strong momentary reduction in lift followed by a substantial increase in the mean lift. However, while at $F^+ \sim O(10)$ the shedding of organized vortical structures subsides following the initial transient, at $F^+ \sim O(1)$ actuation leads to a time-periodic shedding of a train of vortices (at the actuation frequency) that correspond to (peak to peak) lift coefficient fluctuations (at $F^+ = 0.95$) of up to 45% of the mean lift.

II. Experimental Setup

The experiments are conducted in an open return, low-speed wind tunnel (maximum speed of 32m/sec) having a square test section measuring 0.91m on the side. The airfoil model spans the entire test section and is comprised of a leading edge circular cylinder mounted within an aerodynamic fairing that is based on a uniformly stretched NACA four-digit series symmetric airfoil as shown schematically in Figure 1. The 62.2mm diameter cylinder can be rotated about its axis within the fairing and it is tangent to the surface of the fairing at the apexes of its cross-stream edges (i.e., +/-90^0) where the airfoil has its maximum thickness. The chord of the combined cylinder-fairing airfoil is 25.4cm, its thickness to chord ratio is 24% and its angle of attack, α, can be independently varied between -25^0 and 25^0. The center section of the cylinder houses a pair of adjacent synthetic jet actuators each having a flush mounted rectangular orifice (0.5mm wide and 140mm long), such that the orifices are colinear with respect to the axis of the cylinder along their long dimension, and separated by 2.5mm. The performance of each jet is

quantified in terms of the conventional momentum coefficient, C_μ. The center section of the cylinder and the fairing are instrumented with 92 pressure ports. Cross stream distributions of the streamwise and cross stream velocity components are measured in the wake of the airfoil using hot wire sensors having X-wire configuration that are mounted on a computer-controlled traversing mechanism.
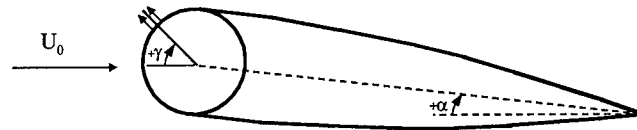
Figure 1. Airfoil model.

III. Results

The effect of the forcing frequency on the flow field around the airfoil is discussed in detail in an earlier paper by Amitay et al. (1999). The measurements are taken at an angle of attack of 17.5^0, a free stream velocity of 18.5 m/s, the actuator jets are at an angle $\gamma = 60^0$ relative to the oncoming flow and have a combined momentum coefficient of 1.8×10^{-3}. The transient response of the flow to pulsed excitation is measured in the wake of the airfoil at $x/c = 2$, phase-locked to the modulating pulse.

The transient effects of pulsed modulation are shown in gray scale raster plots of the phase-averaged cross-stream distributions of the spanwise vorticity (computed from the measured phase-averaged velocity field) for $F^+ = 10$ and $F^+ = 0.95$ (Figures 2a and 2b, respectively). Corresponding time-averaged cross-stream spanwise vorticity distributions of the unforced and forced flows are shown for reference on the right hand side of each phase plot (using open and solid symbols, respectively). The reattachment begins with the advection of a strong clockwise vortex past the measurement station indicating *a reduction in lift* that is followed closely by a stronger counter-clockwise vortex indicating the re-establishment of lift. For the high frequency forcing (Figure 2a) these vortices are followed by a series of smaller vortices of alternating signs and diminishing strength. The reduced wake of the attached flow ultimately reaches a quasi steady state of symmetric vorticity distribution as can be seen for $t/T > 300$ (T is the excitation period). In contrast to the reattachment at $F^+ \sim O(10)$, when the reduced actuation frequency is $O(1)$ (Figure 2b), the reattachment is followed by the coherent shedding of a train of strong vortices at the actuation frequency. When the (pulse modulation) control is turned off, the flow separates again and the airfoil loses its lift. This reduction in lift is accompanied by a decrease in circulation and the shedding of negative (clockwise) vorticity.

In order to further demonstrate the effect of the forcing frequency on the dynamics of the flow reattachment, the synthetic jets are driven at six frequencies corresponding to $F^+ = 0.95, 2.05, 3.4, 10, 14.7$ and 20. Actuation at low F^+ (0.95, 2.05 and 3.4) is effected using two pressure speakers mounted at the opposite ends of the cylinder, while the high frequency forcing is obtained using piezoelectric-based actuators described by Amitay et al. (1998) that are mounted within the cylinder cavity, directly below the jet orifice. The present experiments have shown that at $F^+ > 3.5$, the effectiveness of jets produced by the speakers is significantly diminished due to three-dimensional acoustic effects and the appearance of standing waves within the cavity of the cylinder. Hot wire measurements of the spanwise velocity distributions in the presence of tunnel flow (not shown) have revealed spanwise non-uniformities and phase reversal at high ($F^+ \sim O(10)$) frequencies. The velocity distributions of the piezoelectric-based drivers that are normally used at high reduced frequencies do no reveal any spanwise non-uniformities over their entire operating range.

Figure 3 shows a comparison between pressure coefficient distributions around the airfoil at F^+ = 10 when the actuation is effected using speakers (solid circles) and piezoelectric-based drivers (open symbols). Here, the airfoil is at α = 15°, control is applied at γ = 60°, C_μ = 1.8·10⁻³ and the chord Reynolds number is Re_c = 310,000. From the figure it is clear that the effectiveness of synthetic (zero net mass flux) jets at high reduced frequencies is greatly influenced by the actuator performance. While forcing with the piezoelectric-based drivers results in complete reattachment of the flow to the airfoil, forcing with speaker-based drivers (associated with a much larger internal cavity) results in a very small effect in the vicinity of the jets.

Figure 4a shows distributions of pressure coefficient around the airfoil at F^+ = 0.95 (circles), 2.05 (stars) and 3.4 (triangles), while Figure 4b shows the pressure distributions at F^+ =10 (circles), 14.7 (stars) and 20 (triangles). The pressure distribution for the unforced flow (solid line) is also shown in each figure for comparison. Forcing at low frequencies (Figure 4a) results in a very sharp suction peak at x/c = 0.075, which corresponds to the location of the separation in the unforced case with continuos pressure recovery towards the trailing edge. Although the magnitude of the suction peak appears to be independent of the excitation frequency (within the range tested here) it appears that the degree of pressure recovery towards the trailing edge decreases with increasing excitation frequency, and is accompanied by an increase in pressure drag. However, when the control input is applied at $F^+ \geq$ 10 (i.e., more than an order of magnitude higher than the shedding frequency, F^+ = 0.7), the pressure distribution on the airfoil (Figure 4b) exhibits larger and wider suction peak than the lower forcing frequencies, and consequently a larger increase in the lift coefficient. It is also noteworthy that downstream of the suction peak the pressure difference between the suction and pressure sides is smaller than at corresponding stations for the low frequency forcing resulting in a *lower* pressure drag. Moreover, while at the low forcing frequencies (Figure 4a) the pressure distribution varies with the forcing frequency, at high forcing frequencies (Figure 4b) the pressure distribution is virtually invariant.

Integration of the pressure distributions around the airfoil for the different reduced frequencies yields the coefficients of lift and pressure drag, as well as the lift-to-pressure drag ratio which is shown in Figure 5. Two distinct domains are immediately apparent. In the first domain (I), in which the forcing frequencies are of the same order of the shedding frequency (F^+ < 4) L/D_p decreases with increasing forcing frequency. While this trend might be expected based on the receptivity of the separated shear layer, it may also be, at least partially, attributed to degradation in the performance of the acoustic drivers at higher operating frequencies. In the second domain (marked as II in the figure), the forcing frequency is more than an order of magnitude higher than the shedding frequency ($F^+ \geq$ 10) and the lift-to-pressure drag is 1.3 times higher than at F^+ = 0.95 and appears to be independent of the forcing frequency.

To further explore the differences between the two frequency regimes, the flow response to pulse (hat shaped) amplitude modulation of the control input at the different forcing frequencies is investigated using the phase-averaged circulation about the airfoil, which is computed from the vorticity flux in the wake (Amitay and Glezer, 1999). (In what follows, a negative increment in the steady circulation corresponds to a positive increment in lift). Figures 6a-d show the time history of the (phase-averaged) incremental change in circulation with respect to the unforced flow for F^+ = 0.95, 2.05, 3.4 and 10, respectively. As is evident from these data, the transition from separated to attached flow is accompanied by large fluctuation in circulation and the organized shedding of vorticity concentration of alternating signs. In all cases, the time-averaged circulation (and consequently the lift coefficient) reaches the same magnitude following the transients. However, at F^+ = 0.95, 2.05 (Figures 6a and b, respectively) the circulation

oscillates at the forcing frequency with peak-to-peak fluctuations that decrease from 45% to 7%, respectively, of mean circulation of the attached flow. When the forcing frequency is increased to $F^+ = 3.4$ and 10 (Figures 6c and d), the oscillations at the driving frequency are immeasurable and, as shown in Figure 5, there is a nominal increase of approximately 35% in lift–to-pressure drag ratio compared to the low frequency.
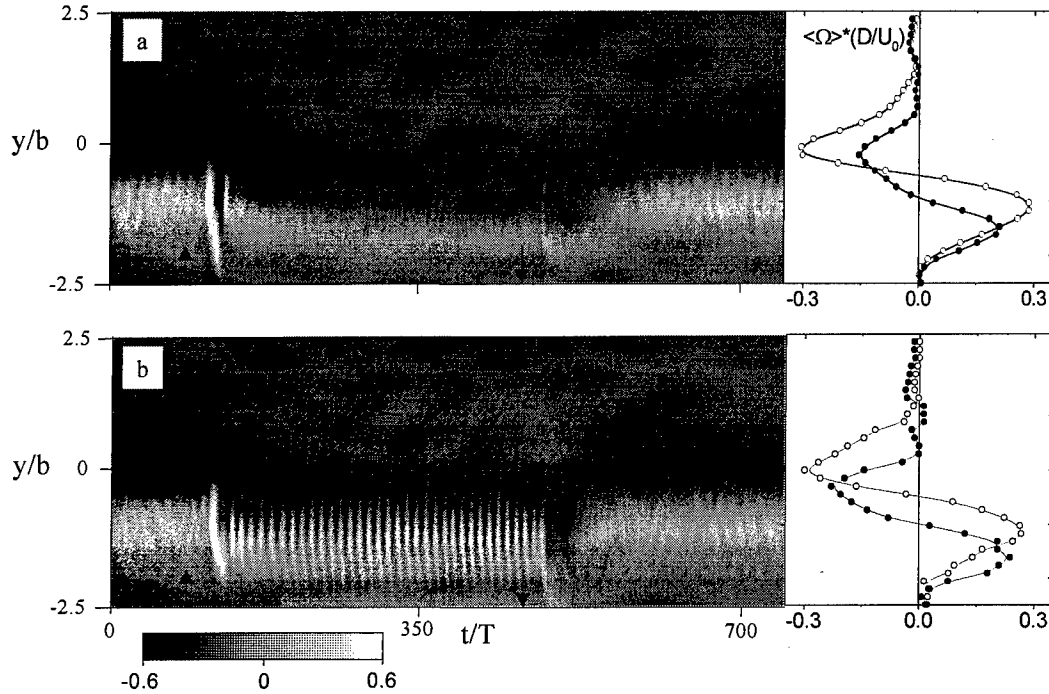
Figure 2. Phase-averaged grayscale raster plot of the cross-stream distribution of the spanwise vorticity along with the corresponding time-averaged spanwise vorticity on the right; $F^+=10$ (a) and 0.95 (b).
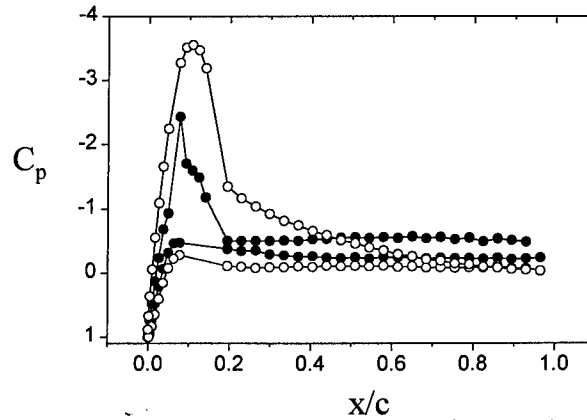
Figure 3. Effect of non-uniform spanwise forcing on the C_p distribution.

Immediately following the termination of the modulated control and before the circulation decreases to its level for the separated flow, there is an increase in the (negative) circulation that is associated with *a momentary increase in lift*. This phenomenon which appears to be similar to the variation of the circulation (and lift) during dynamic stall is the subject of our recent work (Amitay and Glezer, 1999) which focuses on pulse width modulation of vorticity concentrations for lift enhancement in a reattaching separated flows.
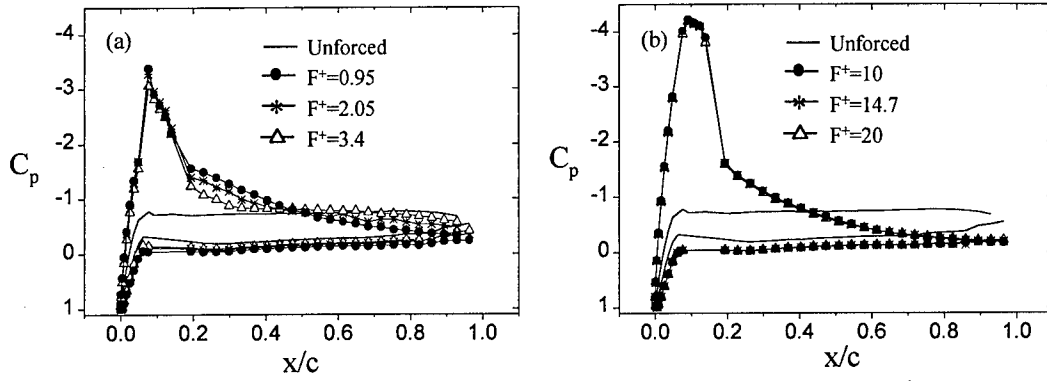
Figure 4. C_p distributions at $\alpha = 17.5°$ and $\gamma = 60°$. $F^+ \sim O(1)$ (a) and $F^+ \sim O(10)$ (b).
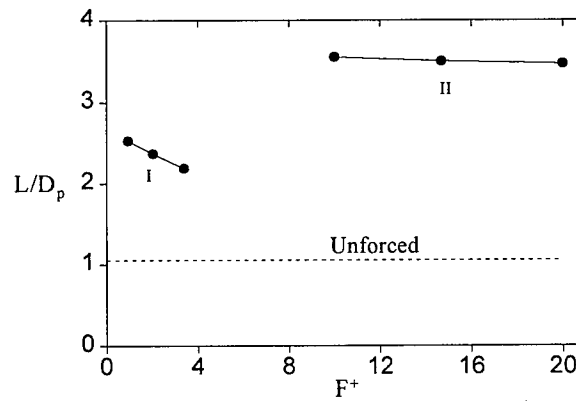
Figure 5. The effect of the forcing frequency on the lift-to-pressure drag ratio.
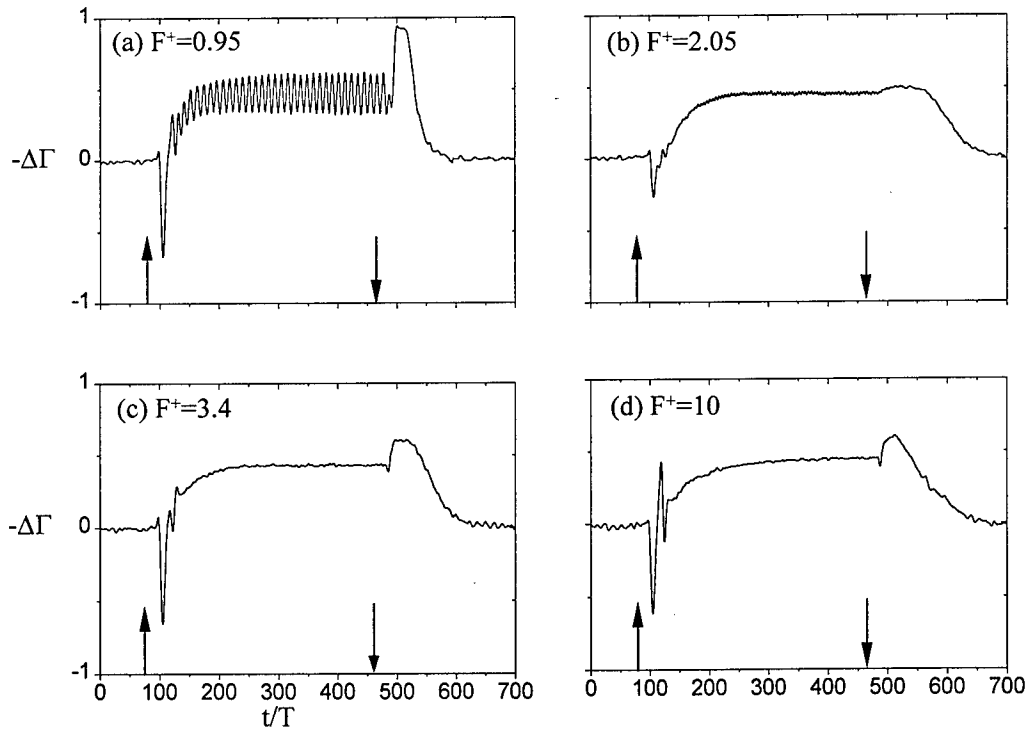
Figure 6. Phase-averaged circulation increment for $\alpha = 17.5°$ and $\gamma = 60°$ at different F^+.

The flow associated with low- and high-forcing frequencies are demonstrated in a sequence of smoke visualization images in Figures 7a-c (the separated flow, in the absence of control, is shown for reference in Figure 7a). The smoke is injected in a sheet at center span and is illuminated using a YAG laser. The field of view is restricted to $0.1 < x/c < 0.5$ above the airfoil (shown schematically in the insert in Figure 7a). When the control jets are operated at $F^+ = 10$ (Figure 7b), the flow is attached to the airfoil and the visualization shows a train of coherent vortical structures at the operating frequency of the jets. Spectral measurements along the surface of the airfoil (not shown) indicate that these vortices quickly lose their identity and vanish well before they reach the trailing edge of the airfoil. When the actuation frequency is $F^+ = 1.4$ (Figure 7c), the reattachment is characterized by the formation of larger vortical structures that scale with the chord of the airfoil and persist well beyond the trailing edge of the airfoil and into its wake (Amitay et al., 1999). It appears that because the formation frequency of these vortices couples with the natural shedding frequency of the airfoil, they are actually enhanced with downstream distance as might be predicted by stability theory. It is the formation and shedding of these vortical structures that leads to time-periodic variations in lift.

Figure 7. Smoke flow visualization. Unforced (a), $F^+ = 10$ (b) and $F^+ = 1.4$ (c).

References
1. Smith, B. L. and Glezer, A. (1998), "The Formation and Evolution of Synthetic Jets", *Phys. Fluids*, 10, pp. 2281-2297.
2. Smith, D. R., Amitay, M., Kibens, K., Parekh, D. E. and Glezer, A., 1998, "Modification of lifting body aerodynamics using synthetic jet actuators", AIAA Paper 98-0209.
3. Amitay, M., Smith, B. L. and Glezer, A., 1998, "Aerodynamic flow control using synthetic jet technology", AIAA Paper 98-0208.
4. Amitay, M., Kibens, V., Parekh, D. E. and Glezer, A., 1999, "Flow Reattachment Dynamics over a Thick Airfoil Controlled by Synthetic Jet Actuators", AIAA Paper 99-1001.
5. Amitay, M. and Glezer, A., 1999, "Aerodynamic flow control using synthetic jet actuators". Proceedings of the 3rd ASME/JSME Joint Fluids Engineering Conference, San Francisco, California.

A COMPUTATIONAL INVESTIGATION OF MEMS

David B. Goldstein
Center for Aeromechanics Research
Department of Aerospace Engineering and Engineering Mechanics
The University of Texas at Austin

Abstract

We are applying a recently developed direct numerical simulation approach to the development of MEMS incorporating both active and passive elements for turbulent boundary layer control. We have already carried out simulations of synthetic jets and textured surfaces and will model concepts involving hybrid active/passive elements as well as other surface textures related to riblets. We have completed a flow and geometric parameter study of synthetic jets and have gained valuable insight into the detailed physics of the actuators. We here present the results from simulations of periodic arrays of 2-D pulsed synthetic jets into an initially quiescent flow and, separately, preliminary simulations of turbulent flow over arrays of chevrons. While the synthetic jet simulations are at much higher Reynolds numbers than needed for MEMS drag reduction in a turbulent boundary layer, they do provide a basis for comparisons with experiments and with simulations of others.

Background

Recent advances have made it possible to directly simulate turbulent flow within modestly complex boundary geometries using the full Navier-Stokes equations. Such direct numerical simulation (DNS) may be used to explore the effects of fine scale surface textures and active flow controllers on a fully turbulent boundary layer. Surface modifications can have several applications but of present interest is the potential for drag reduction. Passive surface textures have been found experimentally to reduce drag by five to ten percent, as reviewed in [1] and [2]. Consequently, there is much interest in the potential of arrays of active flow manipulators for much greater drag reduction. MEMS elements have been manufactured with photolithographic techniques akin to those used to make computer chips. Such devices have been used to measure surface shear stress distributions in synthetic and fully turbulent boundary layers [3] and have been integrated with actuators in a feed-forward control approach [4].

Objectives

The objectives of the present study are to use our CFD approach to investigate boundary layer control devices, to expand on our initial investigations of MEMS, to explore a range of new surface textures, and to develop a fundamental understanding of the resulting boundary layer structure. In particular we aim to (1) model arrays of actuators for

comparison to experiment, (2) model a pulse jet's impact on boundary layer coherent structures, (3) examine the usefulness of combining actuators and sensors with passive surface texturing, and (4) determine the usefulness of a few new surface texture concepts. We report here on results from work on items (1) and (4).

Force Field Model in a Spectral Method

We use a spectral-DNS method initially developed to examine turbulent channel flow [5]. This method expands the spatial variables with Fourier and Chebyshev polynomials. Efficient transform methods are used to switch between real and spectral representations making this method attractive for its low computational cost and accuracy in simply-shaped domains. We use a localized force field to simulate stationary and moving surfaces. Such technique allows us to utilize the fast transform methods in fairly complex geometries. This approach, detailed in [6], was used by us to successfully simulate a number of active and passive devices in fully turbulent flow [7,8]. Our results for flow over flat plates and riblets [6,9] have been validated against both experiments and other numerical simulations.

Modeling an Array of Actuators

Our work is distinct from other synthetic jet simulations [10,11] in both the simulation method and the problem description. In [10], a turbulence model is used to model high Reynolds number flow and the simulation concentrates mainly in the far field. In [11], the cavity is defined with a moving boundary modeling the motion of a flexible diaphragm and the internal and external flows are calculated on separate grids simultaneously. As seen in the schematic drawing of figure 1, our approach simulates a piston motion by imposing a sinusoidal-varying streamwise velocity in a region 3 cells thick with the force field method. No-slip conditions are similarly used to define the slit plane. In addition, we impose a shear-free condition along the top and bottom boundaries to simulate the effect of a 2-D array of jets. We have completed parametric studies involving flow and geometric parameters and compared the results to both numerical [10,11] and experimental [12] data whenever possible.

We first examine the effect of flow parameters by varying the Reynolds and Strouhal numbers. The Reynolds numbers is defined with the half-slit width ($Re = U_{max}(H/2)/\nu$ where U_{max} is the mean peak velocity across the slit, H is the slit width and ν the kinematic viscosity) and the Strouhal number is defined according to the piston motion ($St = \omega(H/2)/U_{max}$ where $\omega = 2\pi f$ is the angular velocity). The external flow is characterized by separation at the sharp lip and roll-up of fluid into a pair of counter-rotating vortices. The ensuing jet has no net mass flux but entrains fluid from the surrounding flow near the slit. This entrained fluid must be drawn from the right-hand side of the domain along the sides of the jet. At moderate and high Re, two distinct types of vortex pairing are observed. The first type occurs at moderate Re and consists of pairing of the first, leading vortex pair with subsequent vortices into a larger vortical structure. Once this structure propagates far downstream, the simulation

reaches a steady-state in which subsequent ejected vortices dissipate before pairing can occur (figure 2). The second type of pairing occurs at high Re and consists of occasional pairing of vortices. Apparently this is a result of the complexity of the plenum flow which occasionally causes internal vorticity to be ejected through the slit, affecting the translational speed or celerity of the ejected vortices (figure 3). Variations in St substantially affects the jet formation. At low St, the piston has an effectively longer stroke with a longer actuation time. The longer stroke causes both an increase in mass ejected per cycle and impulse per unit width. Consequently, for low St, the large vortices formed remain coherent far downstream and are spaced far apart so that no pairing occurs. Conversely, at high St, the ejected vortices generated by each pulse continually merge upon exiting the cavity to form vortex sheets instead of a sequence of distinct vortices.

Inside the plenum there is a similar process of jet formation but the jet is strongly influenced by the close proximity of the piston face. The entering jet is deflected into a cavity-filling swirling motion. As noted in [11], the cavity flow becomes fairly periodic for all ranges of Re and St explored. However, unlike [11], the steady-state conditions are not reached within a few cycles, but rather after as many as 35 cycles. The complexity of the internal flow increases with Re so that for high Re, some vorticity occasionally is ejected during a cycle.

We have parametrically examined the effect of lip thickness and shape and the domain dimensions. Thickening the lip around the jet aperture allows a boundary layer to develop so that the effective slit width is reduced (figure 4). As a result, the vortices form with a higher celerity and pairing, if it occurs at all, is delayed downstream. A rounded lip produces a result intermediate between the sharp lip and a flat thick lip. A cusped lip has little effect since separation occurs at the sharp tip and is very similar to the sharp lip case. Increasing or decreasing the size of the external domain does not affect the near field appreciably: vortices do not "feel" the presence of the right-hand side wall until they are very close except due to the mean backflow feeding the entrainment.

Unlike the external flow, the internal plenum flow is not strongly affected by lip thickness or shape. However reducing the size of the cavity does cause substantial changes in the circulation cell. As the cavity becomes shallower, the primary circulation cell flattens out and allows secondary vortices to form at the edges of the cavity. For very shallow cavities, most if not all of the main circulation cell is ejected during each cycle.

Experimental results in [11] differ from ours in that an isolated real jet breaks down into smaller turbulent eddies in the vicinity of the slit. This breakdown is believed to be a consequence of 3-D instabilities not present in our 2-D simulation. In addition, spectral studies of the experimental data indicate that the jet breaks down without any pairing interactions. Aside from these differences attributable to the fact that we model 2-D periodic arrays of jets, agreement is pretty good. Our mean computational streamwise and centerline velocities, at several stations from the jet slit, match experimental data. Moreover, the vortices' trajectories also scale with the mean stroke length and period

of oscillation. Also the jet centerline velocity and growth matches theoretical scaling factors near the slit. We have also modeled paired synthetic jets as in the experiments of [13] and simulations of [14]. As observed in [12], pulsing the jets in phase produces counter-rotating vortices and a jet similar to the single jet case (figure 5). Preliminary studies from pulsing the jets out of phase show vortex jet steering but the results are dominated by the narrowness of the domain in the vertical y-direction (figure 6).

Modeling New Surface Textures

Results in [15] indicate that surface textures resembling randomly aligned rows of chevrons of height $O(7l^*)$ could produce dramatic drag reduction in turbulent channel flow. We have now completed several DNS runs of similar configurations. We have explored different random and regular orientations and a couple of different chevron shapes but so far we have been unable to obtain reduction in drag. We have sponsored a simplified version of the work in [15] as an undergraduate project to measure drag on a chevron-coated-flat-plate with a pitot rake [16]. However, preliminary results have also not found any substantial drag reduction. We are continuing to work on these simulations and expect to present results in the near future.

Future Work

In the immediate future, we expect to present detailed results on the jet simulations at the Reno 2000 AIAA Meeting and thus complete our work on high Re synthetic jet modeling. In the Fall, we plan to begin the analysis of existing turbulent DNS data over riblet-like textures to examine the correlations between those elements and coherent structures in the flow. We will then integrate low Re pulsing jet manipulators with the textured surface in an attempt to more efficiently reduce viscous drag.

The computational runs done to date were performed on our DEC Alpha 3000/700 workstations or on a Cray J90 supercomputer and usually completed in several hours.

References

[1] M. J. Walsh, 1990, "Riblets." In *Viscous Drag Reduction in Boundary Layers*, ed. D. Bushnell and J. Hefner, Progress in Astronautics and Aeronautics, v. 123, p. 203-259, AIAA Washington, DC.

[2] E. Coustols and A. M. Savill, 1992,"Turbulent skin-friction drag reduction by active and passive means: parts 1 and 2," Special course on skin-friction drag reduction, p. 8-1 to 8-55, March 2-6, in AGARD Report 768.

[3] C. M. Ho, S. Tung, G. B. Lee, Y-C Tai, F. Juang, and T. Tsao, 1997, "MEMS - A technology for advancements in aerospace engineering," AIAA paper 97-0545, *35th Aerospace Sci. Meet.*, Reno, NV, January 1997.

[4] K. S. Breuer and K. Amonlirdviman, 1999, "Advances in Feed-Forward Control of Turbulent Boundary Layers," AIAA Paper 99-3401, *30th AIAA FLuid Dyn. Conf.*, Norfolk, VA, June 1999.

[5] J. Kim, P. Moin, and R. Moser, 1987, "Turbulence statistics in fully developed channel flow at low Reynolds number," *J. Fluid Mech.*, **177**, 133.

[6] D. B. Goldstein, R. Handler, and L. Sirovich, 1995, "Direct numerical simulation of turbulent flow over a modeled riblet covered surface," *J. Fluid Mech.*, **302**, Nov. 10, 333-376.

[7] D. B. Goldstein and T.-C. Tuan, 1998, "Secondary flow induced by riblets," *J. Fluid Mech.*, **363**, pp. 115-151.

[8] T.-C. Tuan and D. B. Goldstein, 1996, "Direct numerical simulation of arrays of microjets to manipulate near wall turbulence," U. T. Austin Center for Aeromechanics Research Report CAR-96-3

[9] D. B. Goldstein, R. Handler, and L. Sirovich, 1993, "Modeling a no-slip flow boundary with an external force field," *J. Comp. Phys.*, **105**, pp. 354-366.

[10] L. Kral, J. Donovan, A. Cain and A. Cary, 1997, "Numerical simulations of synthetic jet actuators," AIAA Paper 97-1824 *28th AIAA Fluid Dyn. Conf.*, Snowmass CO, AIAA paper 97-1824.

[11] D. P. Rizzetta, M. R. Visbal, and M. J. Stanek, 1998, "Numerical investigation of synthetic jet flowfields," AIAA paper 98-2910, *29th Fluid Dyn. Conf*, Albuquerque, NM, June 1998.

[12] B. L. Smith and A. Glezer, 1998, "The Formation and Evolution of Synthetic Jets," *Physics of Fluids*, **Vol. 10, No. 9**, pp. 2281-2297.

[13] B. L. Smith, M. A. Trautman and A. Glezer, 1999, "Controlled Interactions of Adjascent Synthetic Jets," AIAA Paper No. 99-0669, *37th AIAA Aerospace Sciences Meeting*, Reno, NV, January 1999.

[14] L. Kral, D. Guo, 1999, "Characterization of Jet Actuators for Active Flow Control," AIAA Paper 99-3573, *30th AIAA Fluid Dyn. Conf.*, Norfolk, VA, June 1999.

[15] L. Sirovich and S. Karlsson, 1997, "Turbulent Drag Reduction by Passive Mechanisms," *Nature*, Vol. 388, pp. 753-755.

[16] A. Braun and T. Fitzgerald, "The Effects of Passive Mechanisms on the Turbulent Drag of a Flat Plate," Presented at the 1999 AIAA Southwest Regional Student Paper Competition, Albuquerque, NM, April 1999.
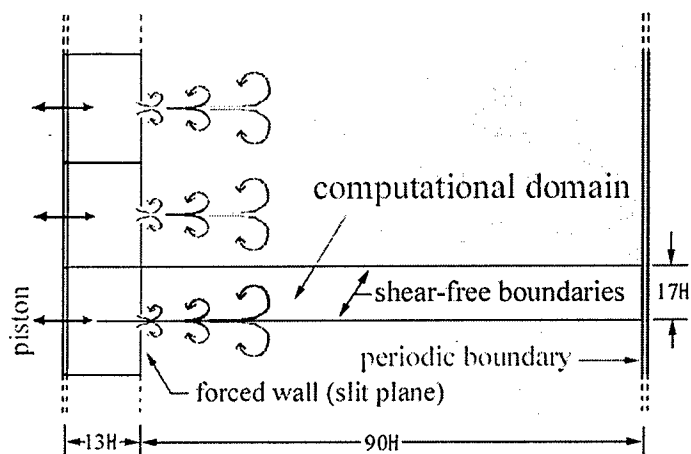
Figure 1: Schematic of array of synthetic jets and computatutional domain
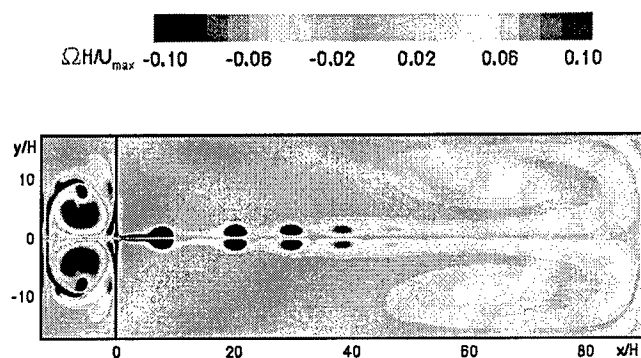
Figure 2: Vorticity countours after 30.5 cycles (Re = 104.2, St = 0.0628)
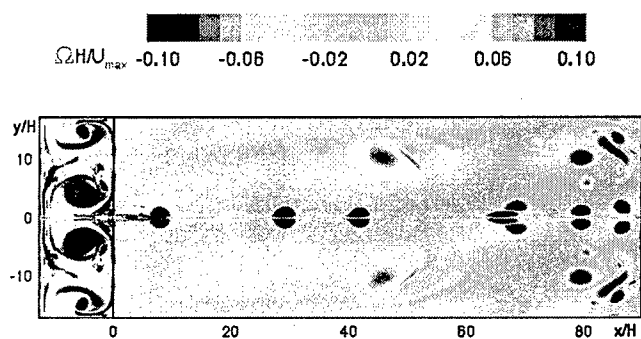
Figure 3: Vorticity countours after 37.75 cycles (Re = 416.6, St = 0.628)
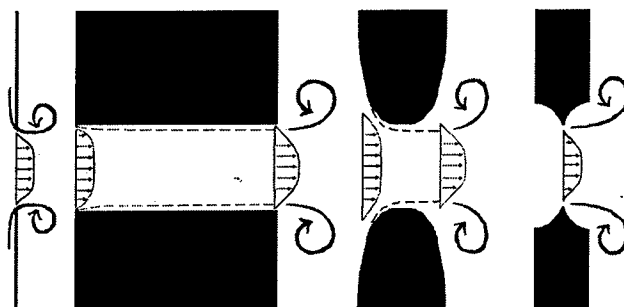
Figure 4: Schematic of lip shapes (thin sharp, flat, rounded and cusped)
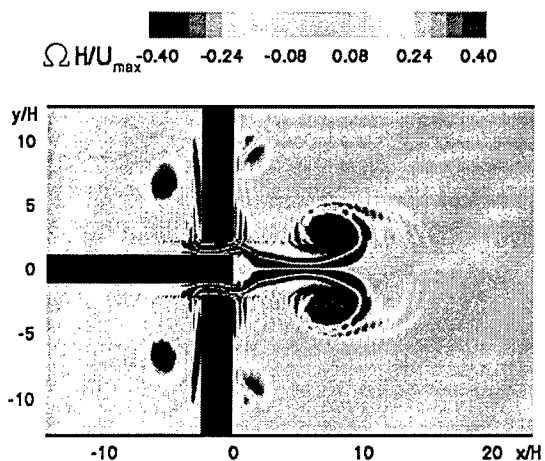
Figure 5: Vorticity countors after 3.5 cycles for paired jets at same phase angle (Re = 104.2, St = 0.0628)
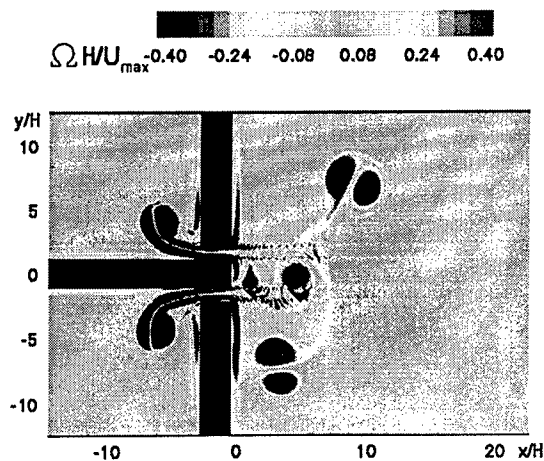
Figure 6: Vorticity countours after .75 cycle for paired jets at 60 deg phase (Re = 104.2, St = 0.0628)

90

VORTEX DYNAMICS AND AEROACOUSTICS OF LOW ASPECT-RATIO RECTANGULAR JETS

MIPR No. 995203130

Fernando F. Grinstein
Laboratory for Computational Physics & Fluid Dynamics
Code 6410, US Naval Research Laboratory
Washington DC 20375-5344

Abstract

The successful development of the next generation of advanced aircraft engines is contingent on the accurate prediction and reduction of the noise generated by the jet exhaust to environmentally acceptable levels. In order to be able to predict and reduce jet noise it is necessary to recognize the critical aeroacoustic sources and understand the generating mechanisms. The present models for jet noise produced by advanced engines are not adequate. Improved analytical and conceptual models based on sound theoretical understanding of the relevant mechanisms need to be developed to assist in devising efficient control strategies of far-field jet noise. Properly developed unsteady jet aeroacoustic simulations are ideally suited to provide insights on these mechanisms and suggest potentially useful innovative approaches for noise reduction.

Simulations performed under previous ONR support provided the basic database used in the present work. New analysis performed during FY98-FY99 under AFOSR support focused on aspect ratio effects and dependence on jet initial conditions, and was included in a paper submitted for publication. An overview of the recent studies of compressible, rectangular, free jets was presented at the Berlin99 Conference, with special focus on understanding the dynamics and topology of coherent vortical structures controlling the jet development, and identifying major near-jet noise generation mechanisms. Relevant issues of subgrid and supergrid modeling in free-jet numerical simulations were addressed in this context. The vortex dynamics underlying axis-switching and vortex bifurcation phenomena were examined, including: the roles of self-induced vortex-ring deformation, reconnection, braid vortices, aspect ratio (AR), and the transition to turbulence from laminar initial jet conditions. Qualitatively different vorticity geometries characterizing the near field of low-AR, M<2, ideally-expanded, rectangular jets were demonstrated, involving: i) self-deforming and ii) bifurcating vortex rings; interacting ring and rib (braid) vortices -- including, iii) single ribs aligned with corner regions (AR>1), and iv) rib pairs aligned with the corners (AR=1); v) smaller-scale, elongated, "worm" vortices in the turbulent jet regime. The near field entrainment of low-AR rectangular jets were shown to be largely determined by the characteristic geometry of the ring-rib interactions; progress in the study of noise generation mechanisms in low-AR jets was reported.

Invited Presentation

Vortex Dynamics and Aeroacoustics in Rectangular Free Jets, Invited Lecture, BERLIN99, Joint Conference of the Acoustical Society of America and the European Acoustics Association, Berlin, Germany, March 16, 1999; J. Acoust. Soc. Am. **105**, Nr. 2, Pt. 2, p.1007 (1999).

Journal Paper

F.F. Grinstein, Vortex Dynamics and Transition to Turbulence in Rectangular Free Jets, submitted to *Journal of Fluid Mechanics*.

Acknowledgement/ Disclaimer

FLOWFIELD MIXING ENHANCEMENT AND NOISE CONTROL USING FLEXIBLE FILAMENTS

AFOSR GRANT No. F49620-96-1-0378

Ephraim Gutmark
Department of Mechanical Engineering
2508 CEBA Bldg.
Louisiana State University
Baton Rouge, LA 70803
(504) – 388 - 5792

Abstract
The subject research program seeks to explore a novel method for achieving passive flow field control, with applications to mixing enhancement and noise reduction, through the interaction of the flow with flexible filaments. Figure 1 illustrates the manner in which this concept is implemented by aligning the filament with the flow at the exit plane of the nozzle.
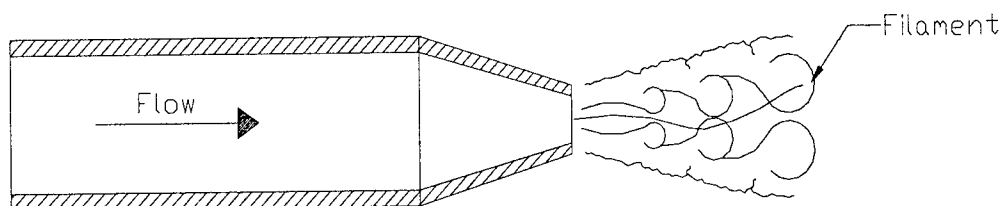
Figure 1: Filament in Jet Exit Plane

The primary purpose of the filament is to modify the large-scale structures within the flow. These structures consist of the vortex formation in subsonic flow and the shock structure in supersonic flow. This flow control can result in improved mixing, lower noise, and a more stable flow. Preliminary measurements using this arrangement have shown that it can significantly reduce the acoustical emissions (up to 30 dB) from both subsonic and supersonic jet flows, especially at screech conditions[1]. Additionally, the preliminary experiments show that significant mixing enhancement and flow control can be obtained using this configuration. The primary objective of this research program is to expand on these preliminary results to fully develop this unique approach to flow field modification.

Objective
The main goal of the subject research program is to thoroughly investigate the use of flexible filaments for flow control applications. Specifically, the program seeks to achieve the following objectives:

1) *Understand the physical mechanisms governing the filament/flow interaction.* Developing an understanding of the mechanisms responsible for the filament induced flow modifications is crucial for exploiting the full potential of this concept.

2) *Determine the optimal filament configuration(s) for achieving the desired flow control.* There are numerous parameters associated with the filament including its material properties, geometry, size, attachment location, and the number of filaments used. Each of these parameters may influence the extent of flow field modifications. The impact of these parameters will be investigated as part of the project.

3) *Quantify the attainable flow enhancements/modifications.* The potential benefits of the filaments for noise control and mixing enhancement will be investigated to document the extent of the enhancements achievable.

4) *Identify additional applications for this concept.* During the course of the research program, efforts will be made to identify additional applications for this concept.

Approach
To execute the subject research program, a jet flow facility capable of producing both subsonic and supersonic flows has been constructed. The facility has a coaxial flow arrangement with a primary flow capable of Mach numbers up to approximately 2.0 and secondary flow capable of approximately Mach 0.86. Also, the primary flow may be heated to a stagnation temperature of 500°F. In order to facilitate accurate acoustical measurements, an anechoic chamber has also been constructed. Noise measurements will be made in the near and far field by an array of high frequency response microphones to quantify the effect of the filament over a range of operating conditions. Data will be acquired using a National Instrument A/D board and a pair of Stanford Research spectrum analyzers. In addition to these acoustical measurements, quantitative flow field measurements and flow visualizations will be made. These measurements will help to develop an understanding of the physical mechanisms responsible for the noise suppression and to quantify the mixing enhancements and flow field alterations produced by the filament.

Progress
During the past year, fabrication of the jet flow facility, connection of the control system, and installation of instrumentation has been completed and preliminary testing begun. Figure 2 shows the completed jet flow facility with the secondary flow nozzle section removed. Preliminary tests completed include calibration of the primary jet control system, baseline sound intensity and cross spectra measurements. Additionally, acoustical measurements were made over a range of filament length and thickness for an unheated primary flow. These measurements were made at a stagnation pressure of 16.0 psig, which corresponds to an overexpanded Mach number of 1.1. Additional tests were also performed at the Boeing Interior Noise Test Facility (INTF) to evaluate the filament effect in a high subsonic cold jet.
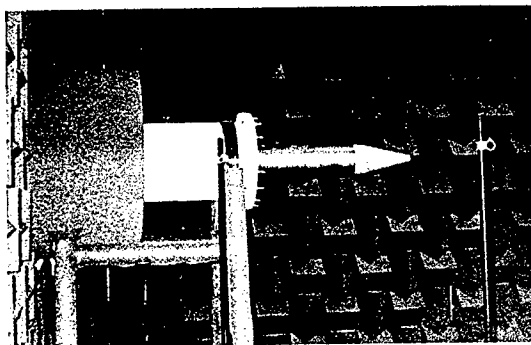
Figure 2: Louisiana State University Anechoic Jet Facility

Results

The baseline acoustical measurements exhibit the form expected for an underexpanded supersonic jet[2]. The turbulent mixing noise, screech tones, and shock associated noise are all clearly discernable in Figure 3. The fundamental screech tone occurs at approximately 3500 Hz, corresponding to a Strouhal number of 0.4. In addition, the noise components display the expected directional behavior[2]. The lower frequency turbulent mixing noise can be seen to the dominant noise generation mechanism in the downstream direction while much stronger screech intensities are seen at inlet angles of 90°. By comparison of the spectra obtained with the 90° microphones, the axisymmetric behavior of the jet can be verified. Figure 4 shows a comparison of baseline cross spectra measurements between these two microphones with the noise spectra obtained at 90°. The screech tones can be seen to exhibit a flapping mode as phase shifts of approximately 120° are clearly seen corresponding to the fundamental screech tone and the first harmonic.
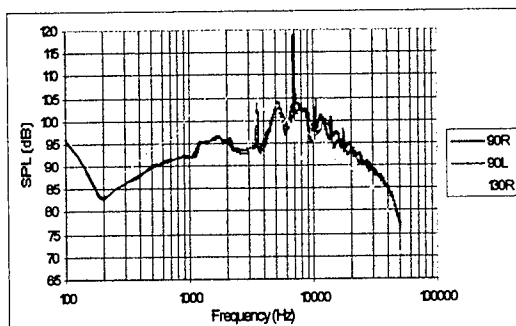
Figure 3: Baseline Acoustical Spectra Po=16psig
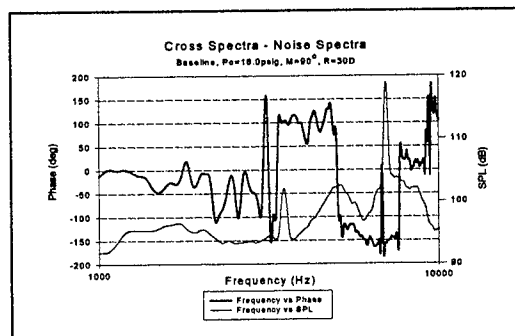
Figure 4: Baseline Cross Spectra Po=16psig

Next, baseline acoustical measurements were taken with the centerbody device, which is used to attach the filament in the flow centerline, in two different positions in order to quantify its effect on the acoustical spectra. The centerbody may be positioned where its tip is 2" upstream of the nozzle exit plane or where the centerbody tip coincides with the nozzle exit plane. These cases are referenced as short and long centerbody respectively. Figure 5 shows that the short centerbody has no effect on the acoustical spectra of the jet. However, the long centerbody is seen to have significant effect. The sound intensity level in the turbulent mixing range is reduced by approximately 5 decibels and the screech tones by as much as 10 decibels. These results indicate that the presence of the

centerbody tip at the nozzle exit plane may serve to stabilize the flow exiting the nozzle. As the figure shows, the long centerbody has no effect on the higher frequency shock associated noise. This would not be expected since the centerbody does not extend out of the nozzle and therefore cannot interact with the shock structure. Finally, the long centerbody is seen to increase the frequency of the screech tones. This is expected since the centerbody tip at the exit plane effectively decreases the nozzle diameter and therefore will increase the frequency for constant Strouhal number.
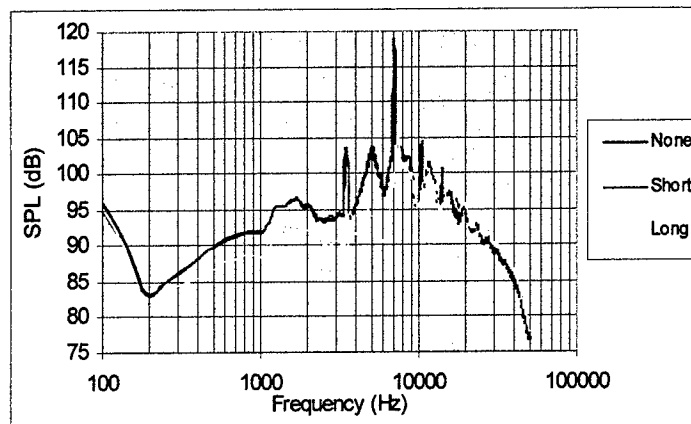
Figure 5: Acoustic Spectra for Various Centerbody Configurations

A full range of tests was performed with various filament lengths for both the long and short centerbody configurations. After an optimal filament length was determined the filament thickness was varied in an attempt to determine an optimal thickness. Selected results of these tests are presented in Figures 6-9 in order to illustrate the effect of varying these two filament parameters. Figures 6 and 7 show the noise spectra, at inlet angles of 90° and 130° respectively, obtained for various filament lengths using the short centerbody configuration. For both inlet angles, the 6 diameter and 5.3 diameter length filaments give almost identical results with the 5.3 diameter filament being marginally more effective. As the filament length decreases, its noise suppression ability can be seen to diminish. This is particularly apparent for the 90° case. Figures 8 and 9 show the effect of varying filament thickness with the jet in the long centerbody configuration. As the figures indicate, the noise suppression effect of the filament does not seem to be as sensitive to thickness as it is to length with a peak sound intensity difference of only about 1 decibel between the most and the least effective thickness. In Figures 6-9, the baseline spectra shown are those with the appropriately configured centerbody present (short in Figs. 6 & 7, and long in Figs. 8 & 9). In order to compare the overall noise reduction effect of the filament, a comparison between the optimally configured filament and the baseline noise spectra with no centerbody present is shown in Figure 10. The optimal filament arrangement for this operating condition proved to be an 8 strand thick, 5.3 diameter long filament attached to the long centerbody. The effect is quite dramatic as the filament reduces the peak noise level of the jet by approximately 20% (120dB to 95 dB peak) at an inlet angle of 90° and by approximately 8% (108 dB to 100 dB peak) at an inlet angle of 130°. Note that in all of the results presented, the noise spectra retain their expected form except that the screech tones are eliminated and the sound intensity is reduced over a wide frequency range.
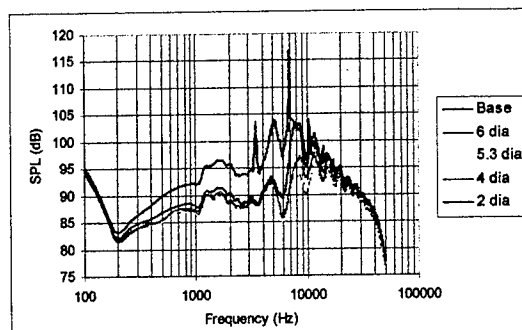
Figure 6: Length Effect, Mic 90°, Short Centerbody
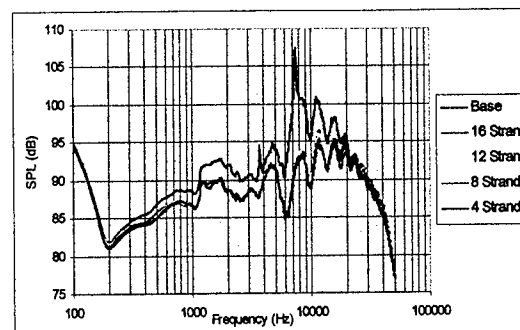
Figure 8: Thickness Effect, Mic 90°, Long Centerbody
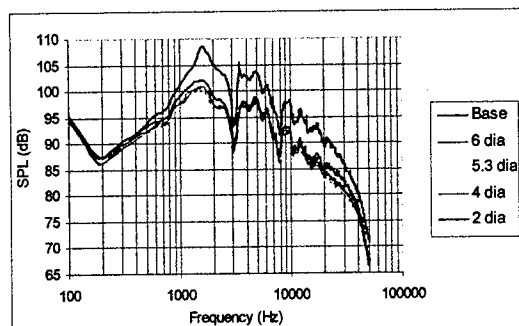
Figure 7: Length Effect, Mic130°, Short Centerbody
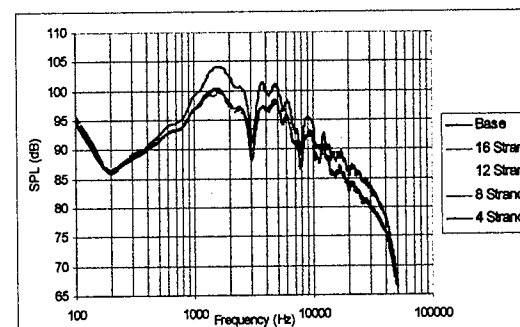
Figure 9: Thickness Effect, Mic 130°, Long Centerbody
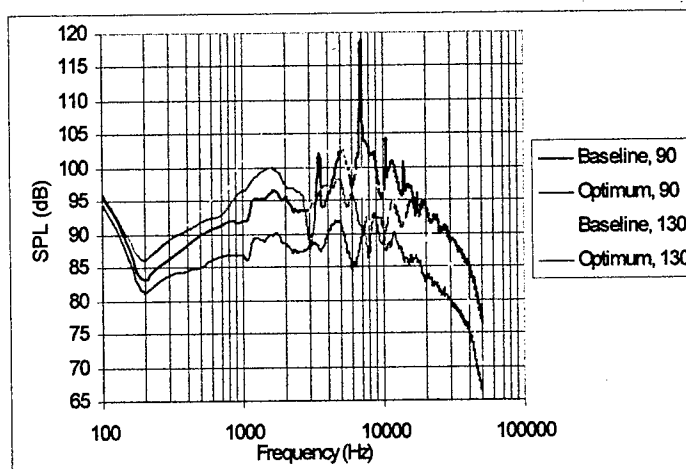
Figure 10: Comparison of Optimum Filament Spectra with Baseline Spectra

Technology Transfer

In addition to the results obtained at Louisiana State University, experiments were also conducted at the Boeing INTF to evaluate the ability of the filament to suppress noise. These tests focused primarily on the filament effect on high subsonic cold flow jets. While not as dramatic as for the supersonic case, the results indicate that the filament still produces substantial noise reduction (3-6 dB) over the entire frequency range[1].

Future Plans

With the jet flow facility fully operational, future work will focus on expanding on the preliminary results. Specifically, the filament effect will be investigated over a wide range of operating conditions. The primary jet will be operated at higher Mach numbers and coaxial flow, with secondary Mach numbers up to 0.86, will be investigated. The primary jet temperature will be varied from ambient to 500° F in order to study the effect of temperature gradients as well as velocity gradients. Complete sound intensity mapping, using a three dimensional traverse system, of the near field will be completed to expand on the acoustical data obtained thus far. In addition to continuing acoustical measurements, mean, coherent, and turbulent flow field measurements using hot wire anemometry, LDV, and PIV will be obtained. To facilitate understanding of the mechanism(s) responsible for the flow/ acoustic field modification, qualitative flow field information will be obtained using a Schlieren system and a laser sheet. These extensive measurements will help to allow the effect of the filament to be optimized for a range of realistic operating conditions. Finally, additional tests will continue to be run in larger facilities with higher temperatures and Mach numbers at Boeing and NASA Langley to study scaling effects.

References

1) Anderson, B., Wygnanski, I., Gutmark, E., "Noise Reduction by Interaction of Flexible Filaments with an Underexpanded Supersonic Jet", AIAA 99-0080, January 1999.

2) Tam, C.K.W. "Supersonic Jet Noise". Annual Review of Fluid Mechanics Vol 27, pp.17-43, 1995

Distributed Turbulent Flow Control by Neural-Networked MEMS

F49620-93-1-0332

Principal Investigator

C. M. Ho
Mechanical and Aerospace Engineering Department
University of California, Los Angeles
Los Angeles, California 90095

Phone: 310-825-9993   Fax: 310-206-2302
E-mail: chihming@seas.ucla.edu

Co-Principal Investigators

R. Goodman   J. Kim   Y. C. Tai

Abstract
An M^3 chip containing the necessary components to apply turbulence control has been successfully fabricated. This chip comprises of shear stress sensors and microflap actuators and their respective driving circuitry and is shown in Figure 1. Much work has been done to ascertain the functionality of the components, i.e. sensors and actuators, and to characterize these components. Improvements were made to both sensor design and fabrication process to attain better performance. Hardware implementation of a neuronet control logic is underway, to be included in the next generation of chips. The interaction between the microflap actuator and the turbulent boundary layer is being studied. Both experimental and numerical studies are ongoing to further refine the neuronet logic.
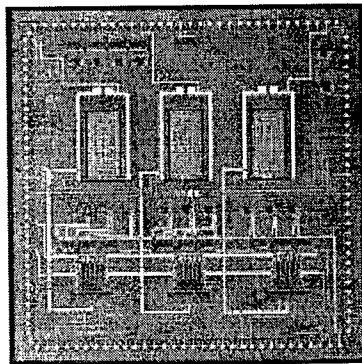
Figure 1: M^3 Chip

CFD

Validation of our microflap simulation techniques has continued to be an issue. Appropriate results with which our simulation results can be compared are not plentiful. Our knowledge concerning flow around a moving flap is also limited. Experimental measurement is difficult to perform accurately, and little literature deals with flow at the low Reynolds numbers in question. One useful work, already used, is In et al. (1995), which gives the steady lift and drag forces for flat plates at various angles of attack. Lighthill (1973) gives an analysis of hovering insect flight which has much similarity to our present situation. This is presently being used to provide validation of our ability to simulate transient effects of moving flaps.

Since our last report an improvement was made in the formulation of the body force method we use to simulate flaps. A novel numerical method for representing the internal boundary of the microflap has been incorporated into our computer simulation code. Previously neglected pressure gradient terms were included. Without them, our simulations of inclined flat plates were accurate up to 30 degrees. With the pressure gradient accounted for, the simulations are accurate up to 60 degrees. It would be possible to simulate completely vertical plates accurately, as well, but the geometry in the code would need to be modified. It is still expected that flaps will rise from the wall only small angles so as to minimize form drag. Figure 2 shows the simulation of a flat plate at a 45 degree angle of attack. Reynolds number is 20, based on free stream velocity and plate length. Velocity vectors show stagnation on the windward side of the plate, flow separation at the leading and trailing edges, and a wake region in the plate's lee.
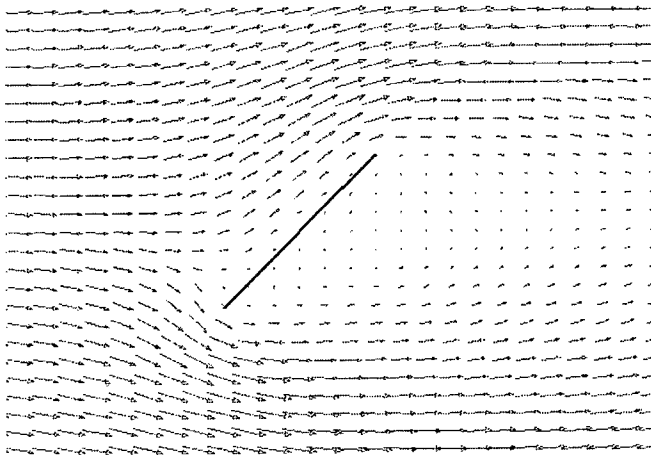
Figure 2: Simulation of flat plate at 45 deg. AOA, Re = 20

Experimental

After the successful fabrication of the M^3 chip, much work was done to characterize the components of the chip, i.e., the shear stress sensors and their driving circuitry and the microflap actuators. Figure 3 shows the response of a microflap actuator on a M^3 chip due to a continuous and a discrete pulse train driving signals. The flaps are designed to be actuated at their natural frequencies, about 3.5 kHz, in most instances. The particular

one shown in the figure was actuated at 3.78 kHz. Previously, it was reported that the response of the control system was limited by the 35 Hz response rate of the old actuator. The performance of the new microflaps has, in essence, eliminated this limitation and allows the control system to operate close to the maximum speed at which the system is capable of calculating an output response. Studies are also being done on the interaction between microflap actuation and the turbulent boundary layer. Sensor performance will be discussed in a later section.
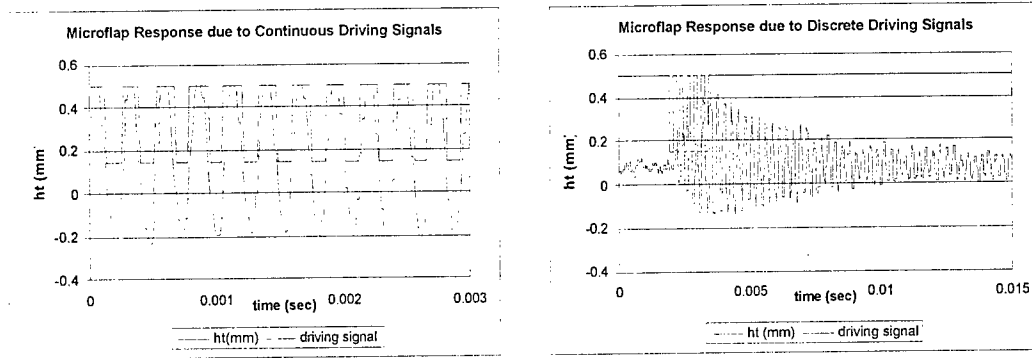
Figure 3: Microflap response due to continuous and discreet driving signals

It was also reported previously that a real-time control system has been successfully set up. This allows for the refinement of the neuronet logic, and possibly the development of new logic, as data collection can be done under the same both with and without actuator motion. Currently, the neuronet logic is taken directly from work done by J. Kim, et al, where the output signal is proportional to the sum of the weighted spanwise shear stress output from seven different sensors and is of the form:

$$\upsilon_{jk} = C \sum_{i=-3}^{3} W_i \frac{\partial w}{\partial y}\bigg|_{j,k+i} \quad , \quad C = \frac{K}{\sum_j \upsilon_j^2}$$

Where υ_{jk} are velocity outputs, the W_i are fixed weights, and C is a proportionality constant chosen such that the root-mean-squared value of the actuation is kept at $0.15u_\tau$. The weights for the different sensors had been generated from a CFD simulation and do not precisely reflect the current experimental conditions. Keeping the same basic structure for the neuronet, attempts were made to confirm these weights or establish new ones using experimental data and various training algorithms. As of yet, no consistent weights were found despite having found good error convergence and consistent C values during the training phase. Investigations are on going to determine whether a change in the setup or a modification of the logic is needed.

Control Circuits
In hardware, the aforementioned neuronet logic developed by J. Kim, et al is being implemented. We implement a single row of $\partial w/\partial y$ sensors that trigger a single row of actuators. The first thing that must be accomplished by the circuits is the summing and weighting of the sensor output voltages for $\partial w/\partial y$.

101

The weight pattern was implemented by choosing the capacitor ratios of a multiple input floating gate differential amplifier to match the weights obtained during network training. The lines are the ideal and the symbols represent the data. Four weights were implemented, ¼, -¼, ¾, and -¾. The other three weights had a value near 0 and thus do not need to be implemented. Test results for the circuit that performs the weighted summation are shown in Figure 4. The lines represent the ideal and the symbols are the actual data. The plot shows all single and pairwise inputs. For the single inputs a signal was applied to one input while all other inputs were grounded. For the pairwise inputs the same test signal was applied to two inputs and all others grounded. The test results for the RMS normalization circuit are shown in Figure Figure 45 where again the lines represent the ideal and the symbols are the data. Both circuits show very good performance.

The above circuits form the core of the signal processing circuitry for the control law implementation. Circuits also exist and are currently being worked on for the sensor and actuator driver. Furthermore, circuits which can implement a neural network on chip are also being investigated to allow for on-line training to adjust to the difference between real sensors and actuators and the ideal CFD results.

$$I_{out} = I_k \cdot \tanh\left(K\left(\sum_i \frac{C_i V_i}{C_{total}}\right)\right)$$

$$I_{out} = \frac{I_{ref} I_1}{\sqrt{I_{in1}^2 + I_{in2}^2}}$$
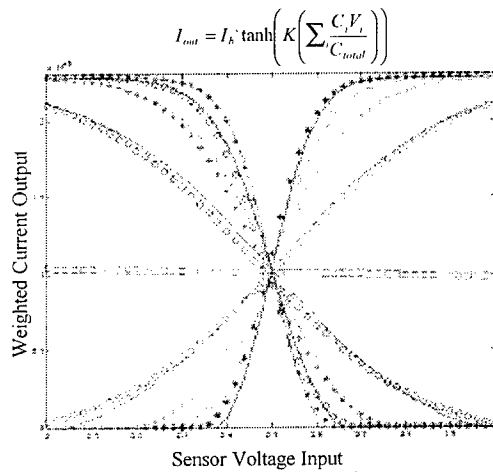
Figure 4: Summing and weighting circuit test results   Figure 5: RMS norm. circuit test results
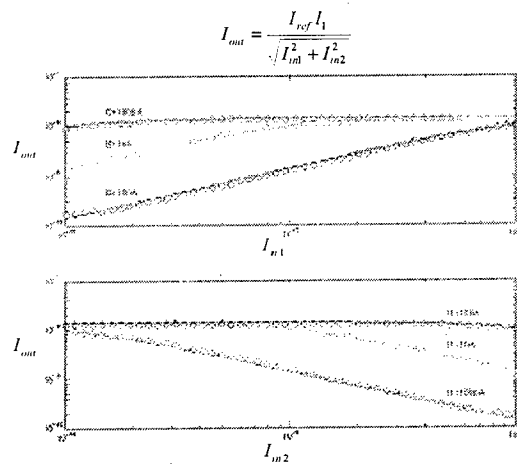
MEMS

Previously, we have demonstrated the advantages of a new shear stress sensor fabrication approach for integration with actuators and electronics. A fully integrated shear-stress sensor has been developed using a post-IC process that is added onto 4″ foundry-processed CMOS wafers. The shear-stress sensor uses a gate-polysilicon hot-wire as the sensing element that sits on a freestanding Parylene diaphragm suspended over a cavity.

In the past six-months, we modified the sensor design and processes to improve performance. Specifically, a special Parylene vacuum sealing and etchback process is developed for the purposes of achieving better thermal isolation (i.e. lower power consumption) and overall sensitivity.

CMOS

(a) Etching Hole Opening and BrF$_3$ Etching

(b) 3 μm Parylene-N Deposition

(c) Oxygen Plasma Etching Back
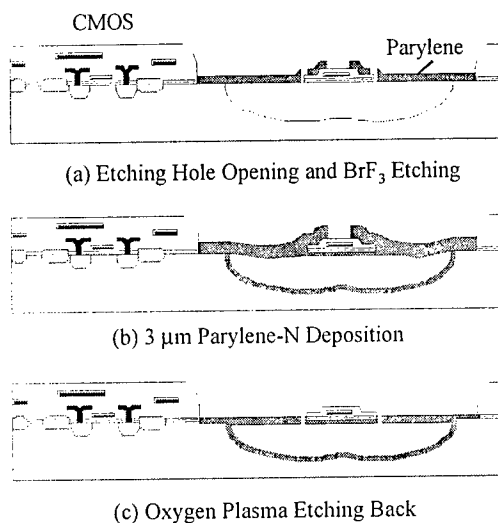
Figure 5: Modified process flow

Parylene Diaphragm

Poly Sensor
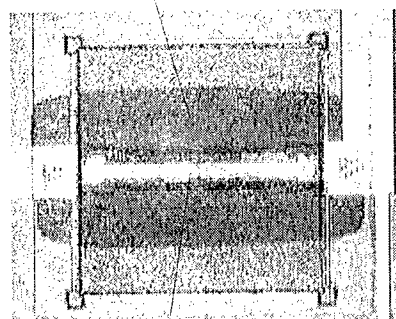
Figure 6: Picture of new shear stress sensor

Parylene Sensor

~ 55 mV/ Pa
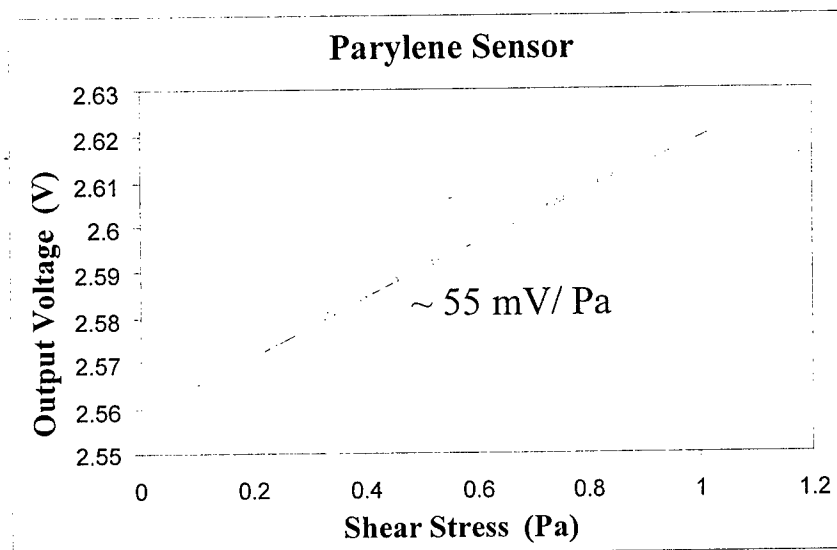
Figure 7: Windtunnel Test Result

In the old design, we fabricated etching holes on the center of the Parylene diaphragm. Currently, however, we open 4 μm wide slots overlapping the edge of the sensor bridge. In this manner, the actual etching slot has a width of 2 μm (Figure 5(a)). The obvious advantages of this modification are the ease of cavity etching, ease of slot sealing, and less flow interference. After the BrF$_3$ silicon etching to create the cavity underneath the parylene diaphragm, a second layer of Parylene (3 μm) is then deposited. Due to the comformal nature of this deposition, a thin film of Parylene is deposited inside the cavity as well as on the backside of the sensor diaphragm, eventually sealing the etching slots (Figure 5(b)). Finally, an oxygen plasma etchback is done with a timed etch. By using

this sealing and etchback process, an almost fully exposed sensor element and an 0.7 um thick Parylene diaphragm (Figure 5(c)) is realized. The fabricated sensor is shown in Figure 6. The sensitivity of output voltage to shear stress is 45~55 mV/Pa Figure 7 shows the windtunnel test results), while each sensor has a 6 mW power consumption at an overheat ratio of 10%.

References

K.M. In, D.H. Choi, and M.-U. Kim, ``Two-dimensional viscous flow past a flat plate," Fluid Dynamics Research, vol. 15, pp. 13-24 (1995).

M.J. Lighthill, ``On the Weis-Fogh mechanism of lift generation, "Journal of Fluid Mechanics, vol. 60, pp. 1-17 (1973).

DRAG REDUCTION VIA CONTROL OF STREAK INSTABILITY IN TURBULENT BOUNDARY LAYERS

Fazle Hussain & Wade Schoppa
Department of Mechanical Engineering, University of Houston

Abstract

Using direct numerical simulations of turbulent channel flow, we analyze the viability of skin friction reduction by prevention of streak instability near the wall. Based on our prior findings that streak instability directly generates the prominent near-wall streamwise vortices observed, we demonstrate and explain a unique, *very large-scale* drag reduction strategy. As proof-of-principle, significant (20-50%) drag reduction is revealed for imposed control with the following key advantages for practical implementation: (i) streamwise- and time-independent flow forcing, (ii) a spanwise wavelength of at least 4-6 streak widths (i.e. large-scale control), (iii) no requirement of sensors or control logic. The drag reduction results from weakened longitudinal vortices near the wall, due to forcing-induced suppression of the underlying streak instability. To further quantify the role of streak instability in vortex generation, conditional statistics of streak vorticity are extracted from fully-developed near-wall turbulence using a streak eduction procedure. Coupled with linear stability analysis of streaks with variable strength, results indicate that approximately 25% of lifted streaks are sufficiently strong to be unstable. A particularly attractive control approach (identified here) is to suppress these marginally unstable streaks via accelerated viscous annihilation of streak vorticity by large-scale straining motions.

Objectives

It is now well-established that near-wall vortical *coherent structures* (CS) in turbulent boundary layers are responsible for (i) increased drag on aircraft and marine vessels and (ii) enhanced wall heat transfer, hence higher blade temperatures, within gas turbines. Unfortunately, despite dedicated and massive efforts, viable boundary layer control techniques for these important applications remain essentially elusive. The principal practical limitation of popular microscale control approaches is that they are tuned to the sub-millimeter scale of near-wall CS. Consequently, tiny (hence fragile) actuators and/or sensors, such as micro-electro-mechanical devices (MEMS), are required. For engineering applications, durability limitations will obviously pose a formidable challenge for MEMS-based boundary layer control.

As an alternative, the focus of our AFOSR-supported research is to develop new bulk control approaches using very large-scale, time-independent control strategies (*e.g.* devices whose spacing is orders of magnitude larger than the natural streak spacing), without any sensors or control logic. In this way, more durable control is permitted, with each device providing drag reduction over an extended spatial domain containing dozens

(perhaps hundreds) of streamwise vortices. For additional details of our drag reduction approach, see Ref. [1].

In essence, we pursue large-scale control via manipulation of an underlying streak instability, shown in Ref. [2] to generate the near-wall streamwise vortices commonly observed. A detailed review of recent streak instability-based mechanisms of turbulence generation (ours and others) appears in Ref. [3]. Our primary ongoing objective is to identify and optimize robust drag reduction strategies which stabilize streak instability over a large spatial domain, with initial exploratory analysis (*e.g.* "numerical experiments") based on direct numerical simulations (DNS), to be followed by experimental verification, refinement and, hopefully, eventual implementation in practical systems.

Computational Approach

In the following, we address vortex regeneration and its control using direct numerical simulations of the Navier-Stokes equations. Periodic boundary conditions are used in x (streamwise) and z (spanwise), and the no-slip condition is applied on the two walls normal to y (normal); see Ref. [4] for the simulation algorithm details. The control simulations are initialized with full-domain channel flow turbulence at $Re=1800$ and 3200, with 48x65x48 and 192x129x192 dealiased Fourier modes respectively. Actuation is represented by an applied control flow, either maintained at a constant amplitude or allowed to freely evolve, superimposed onto the turbulence.

Results & Discussion

To summarize our recent findings[1], we have discovered (via DNS) significant drag reduction by: (i) a spanwise row of counter-rotating, x-independent streamwise vortices, and (ii) x-independent, z-directed colliding wall jets (region *WJ* in Fig. 1a). To demonstrate proof-of-principle for large-scale forcing, the z wavelength of the control flow is four times the characteristic streak spacing of approximately 100 wall units; even much larger-scale control (although computationally prohibitive) may be possible in practice. As illustrated in Fig. 1(a), the control flow (1) has a much larger scale than local minima of $u(y,z)$ near the wall, representing lifted low-speed streaks.

Significantly, we find substantial drag reduction is attainable via large-scale control – 20% for vortex control and 50% for wall jet control. In essence, both vortex and wall jet control prevent near-wall vortex generation by annihilating the naturally occurring (unstable) normal vorticity ω_y on streak flanks. The significance of this attenuation of streaks' ω_y lies in the fact that sufficient ω_y flanking streaks is required for vortex generation via streak instability[3]. The numerous preexisting lifted streaks (Fig. 1a) are flattened by splatting where the vertical control flow V_{con} pushes fluid toward the wall and the spanwise flow W_{con} spreads it in z (outside of *WJ*). Within the wall jet control region *WJ*, V_{con} is directed away from the wall and W_{con} converges in z, causing cross-diffusion of compressed streaks and hence weakening ω_y. Along the entire wall, control drastically decreases the ω_y originally flanking streaks in the uncontrolled flow (cf. Figs. 1a,c). As a consequence of this reduction of streak ω_y by control, ω_x and hence vortex

generation are significantly suppressed in the controlled flow (Fig. 1d), with no compact vortices present near the wall; in contrast, numerous drag-producing vortices with strong ω_x are present immediately above the wall without control (Fig. 1b).
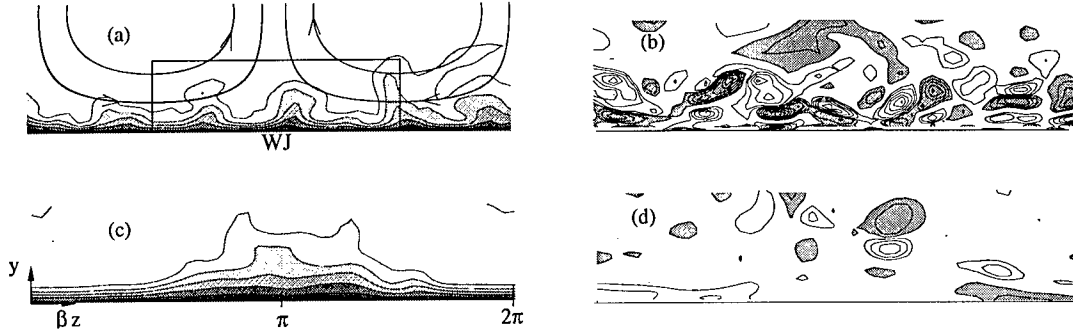
Figure 1. Distributions of $u(y,z)$ in (a,c) and $\omega_x(y,z)$ in (b,d) near one wall of turbulent channel flow at $Re=1800$, without (a,b) and with (c,d) an imposed large-scale control flow. The controlled flows, shown at $t_0^+=500$ (after control starts), have a frozen forcing amplitude of 6%. Note the disruption of streaks and the attenuation of streamwise vortices near the wall by control.

The current phase of our research involves detailed analysis of the streak instability-induced vortex generation mechanism[5], to permit development of robust control strategies based on these preliminary drag reduction results. In particular, we have undertaken a detailed linear stability analysis of near-wall streaks, based on conditional statistics of streaks educed from fully-developed near-wall turbulence. To isolate the three-dimensional dynamics of lifted streaks, in a "clean" environment free from existing structures and incoherent turbulence (including perturbations presumably induced by larger-scale outer vortices), we analyze a z-periodic row of parallel (x-independent) low-speed streaks, initially containing no vortices or ω_x whatsoever (*i.e.* $U(y,z)$ only). As a representation of vortex-free, lifted low-speed streaks of variable strength, we consider a base flow family of the form

$$U(y,z)=U_0(y)+(\Delta u/2)\cos(\beta_s z)\,g(y)$$
$$V=W=0,\tag{1}$$

where $U_0(y)$ is the mean velocity and $g(y)$ is an amplitude function which satisfies the no-slip condition at $y=0$ and localizes the streaks' velocity defect to a single near-wall region (*i.e.* $y^+<60$).

For illustrative purposes, it is useful to represent the "strength" of lifted streaks in terms of the maximum inclination angle θ of vortex lines on the streak flank, given locally by $\theta=\tan^{-1}(|\omega_y|/|\omega_z|)$. In this way, the strength of the base flow streaks (1) may be characterized conveniently as the maximum vortex line lift angle, *e.g.* defined at $y^+=20$ as $\theta_{20}=\tan^{-1}[\omega_y|_{max}/(dU_0/dy(y^+=20))]$ with $\omega_y|_{max}=\beta_s\Delta u/2$. Note that this provides a visual representation of the relative magnitude of the spanwise shear $\partial u/\partial z$ on the streak flank. Having shown linear instability of a $U(y,z)$ distribution visually representative of instantaneous lifted streaks in near-wall turbulence[2], we now quantify the growth rate

variation with streak strength, defined in terms of the lift angle θ_{20}. Note that for a fixed streak spacing, θ_{20} determines both the height and flank-slope of lifted U contours. Significantly, sinuous streak instability requires a threshold streak lift angle of approximately 50° (corresponding to a streak vorticity of $\omega_y|_{max}$=0.27), reflected by the region of positive growth rate σ in Fig. 2. Thus, lifted streaks may be either passive (stable) or dynamically active (unstable) to small-amplitude sinuous perturbations, depending upon rather slight (*i.e.* virtually indistinguishable visually) differences in streak vorticity. For instance, streaks with a lift angle of 45° are well within the stability regime, while 60° streaks exhibit a significant instability growth rate. Furthermore, this instability threshold indicates that well-defined lifted streaks, even those extending past the buffer layer, are not necessarily unstable. Past the instability cutoff, the growth rate increases approximately linearly with the streak vorticity $\omega_y|_{max}$ (nearly linearly with θ_{20} for this angle range), suggesting a dominant influence of $U(z)$ shear in driving sinuous instability. Nevertheless, the sinuous mode is shown to be inherently three-dimensional, and its growth mechanism is distinct from that of a one-dimensional $U(z)$ wake profile.
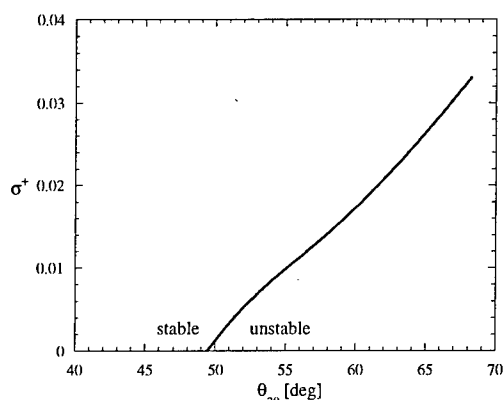
Figure 2. Dependence of sinuous mode growth rate on streak vortex line angle θ_{20} (z-maximum measured at y^+=20), illustrating threshold of streak lifting required for streak instability growth.
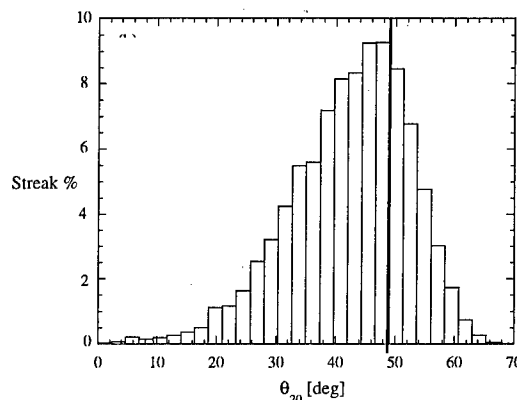
Figure 3. Histograms of conditional streak vorticity statistics, for streaks educed at y^+=20, from fully developed channel flow turbulence. The bold line denotes the instability cutoff in Fig. 2.

Owing to the threshold behavior in Fig. 2, the role of (linear) streak instability in fully developed near-wall turbulence relies critically on the magnitudes of streak $\partial u/\partial z$ (hence streak lift angle) actually realized. To obtain conditional streak statistics, an eduction procedure is used to extract individual streak realizations from a fully developed turbulent channel flow database[4] at Re=1800. To obtain local, unsmeared vorticity statistics isolated to streaks, the following streak eduction procedure is defined:

(i) Regions of $u'<0$ are identified at y^+=20.

(ii) Within each $u'<0$ region, the (x_c,z_c) locations of local minima of u' are identified as streak centers.

(iii) The first local maxima of $|\partial u/\partial z|$ in z is identified on either side of each streak center (x_c,z_c). The larger of these two $|\partial u/\partial z|$ values is recorded as the maximum vorticity for each streak realization.

For 50 time realizations of full-domain turbulence ($L_x^+\sim 1400$; $L_z^+\sim 450$), spanning 500 wall time units, this eduction procedure performed at $y^+=20$ extracts approximately 11,300 streak (y,z) cross-sections.

Subject to the conditional streak sampling outlined above, histograms of streak lift angle statistics for fully-developed near-wall turbulence are shown in Fig. 3 at an eduction location of $y^+=20$. Comparison of lift angle statistics (Fig. 3) with the corresponding streak instability growth rate (Fig. 2) indicates that approximately 25% of near-wall streaks are strong enough (i.e. with sufficient $\partial u/\partial z$) to be linearly unstable. Based on the instability cutoff behavior in Fig. 2 (consistent also with the stability of the turbulent mean profile $U(y)$ for channel flow), the straightening of streak vortex lines by background ω_z is a strongly stabilizing effect for sinuous streak instability.

In summary, streaks of sufficient strength for linear instability are in fact realized in near-wall turbulence, being most prominent between $y^+=20$-30. Note that at larger y, similar strong streaks are observed, but are much less common. In contrast, streaks localized only to the sublayer (i.e. not lifted into the buffer layer) are common, yet do not exhibit sufficient lift angles to be linearly unstable and hence are dynamically passive with respect to streak instability. Finally, note that other possible mitigating factors of streak instability, particularly the influence of viscous annihilation of base flow streak vorticity, are also important. Additionally, the streak count declines sharply near the stability cutoff (e.g. Fig. 3), indicating that the number of unstable streaks decreases rapidly with the corresponding growth rate (cf. Figs. 2,3). Thus, fully-developed near-wall turbulence contains marginally unstable streaks which may be rather easily stabilized by properly designed control. As shown here, such streak stabilization via either large-scale vortex generators or spanwise wall jets yields substantial drag reduction over a large spatial domain, making this a particularly attractive new avenue for boundary layer control.

Future Plans
These promising preliminary results, coupled with the massive economic impact of successful drag reduction, clearly warrant additional research. In particular, additional analysis and simulations are needed to optimize our new control strategy and to assess potential implementation strategies. Most importantly, experiments are now critical to verify this drag reduction phenomenon (observed computationally), and to develop large-scale actuation techniques which are efficient and durable.

Pending future support, we plan to analyze the viscous annihilation of streaks (i.e. a type of planar reconnection) brought about by control, in order to optimize the streak-stabilization effect. In particular, a (linear) 2D advection-diffusion equation will be developed for a periodic array of lifted streaks, subjected to a forcing term representing control. In this way, a variational problem may be developed to maximize the viscous annihilation of streak ω_y with minimum control-induced drag, subject to the constraints of mass conservation and both no-slip and non-penetrable wall boundary conditions. Additionally, we propose a formal analysis of streak instability via triple decomposition of fully-developed near-wall turbulence into: (i) locally x-averaged streaks, (ii) ensemble-

averaged 3D vortices CS), and (iii) incoherent turbulence. Governing equations relating each element may be derived, to ascertain the roles of recurring streak instability and incoherent turbulence (including outer flow turbulence) in an ensemble-averaged sense. This analysis will certainly enable more effective control of streak instability, and may help identify other effective control strategies. Finally, alternative control implementations will be investigated, including spanwise wall jets and near-wall control vortices generated by wall boundary condition manipulation (to mimic near-wall slot injection), for comparison with our current results for superimposed volumetric control.

Regarding future experimental studies, we have performed several exploratory experiments (based on limited funding from other resources) of our large-scale drag reduction approach. To date, we have designed and tested several large-scale actuation schemes, one of which yields very promising results (due to proprietary issues with UH, these results cannot yet be revealed). Pending patent submission and additional support, we plan a comprehensive experimental study to verify our preliminary drag reduction results, and to develop effective actuation techniques. Experiments will be conducted in our in-house low-noise wind tunnel (1.1m X 1.6m), fabricated with a floating plate to permit both direct drag measurement (using strain gauges) and acquisition of the wall shear distribution using flush-mounted hot-film sensors. In parallel, the cross-stream flows induced by various actuator designs will be evaluated and optimized using flow visualization in our in-house water tank facility (via laser induced fluorescence). Specific experimental objectives include (i) determination of the ranges of actuator shape, size, and spacing which provide effective drag reduction, (ii) visualization of the actuator-induced control flow, to permit comparison with effective control identified computationally, and (iii) documentation of the control influence on relevant turbulence statistics in the vicinity of a given actuator.

Acknowledgment/Disclaimer

References

[1] Schoppa, W. & Hussain, F. 1998 A large-scale control strategy for drag reduction in turbulent boundary layers. *Phys. Fluids* **10**, 1049.

[2] Schoppa, W. & Hussain, F. 1999 Coherent structure dynamics in near-wall turbulence. *Fluid Dyn. Res.* (to appear)

[3] Moser, R. D. 1998 Summary and appraisal of self-sustaining mechanisms. *AIAA Paper* 98-3002.

[4] Kim, J., Moin, P. & Moser, R. D. 1987 Turbulence statistics in fully developed channel flow at low Reynolds number. *J. Fluid Mech.* **177**, 133.

[5] Schoppa, W. & Hussain, F. 1999 Dynamics of coherent structure generation in near-wall turbulence. (in preparation)

FLUID-OPTIC INTERACTIONS II

F49620-97-1-0489

Eric J. Jumper
Department of Aerospace and Mechanical Engineering
University of Notre Dame, Notre Dame, Indiana

Abstract

Background. The transmission of a collimated light beam through a turbulent flowfield with index-of-refraction variations leads to a time-varying distortion of the beam's previously-planar, optical wavefront. These fluid-optic interactions have direct relevance to USAF systems. Fluid-induced aberrations degrade the performance of airborne imaging systems, airborne energy transmission systems (Airborne Laser, for example), as well as optical target acquisition and tracking systems.

Over the last decade, progress has been made in both measuring the dynamics of wavefront aberrations caused by atmospheric turbulence and using this information for designing and applying adaptive-optic equipment and techniques to correct these aberrations and restore some of the system performance losses.[1] For aberrations due to propagation through boundary and shear layers (called "aero-optics"), on the other hand, progress in adaptive-optic correction has been nonexistent. This is because the required spatial and temporal frequencies associated with the aero-optic problem (even for relatively slow, laboratory flows) are at least an order of magnitude greater than those presently able to be adaptive-optically corrected for the atmospheric-propagation case.[2] Thus, until very recently, the main research thrust in aero-optics has been the attempt to quantify the time-averaged, statistical, near-field wavefront distortion (as phase variance or rms Optical Path Difference, OPD_{rms}) in order to estimate the time-averaged, far-field degradation that might be expected for an optical system whose optical signals must traverse the aberrating, turbulent flowfield.[3]

Due in large part to the results of this and our previous AFOSR grant effort, the study of the time-resolved nature of aero-optic aberrations is now essentially routine. In our work, a high-bandwidth wavefront sensor (the SABT) was developed. The SABT has been able to capture the instant-to-instant dynamic nature of aero-optic aberrations for slow-speed (7 m/s) laboratory turbulent flows[2] as well as high-speed (0.8 Mach) shear layers.[4] The wavefront data has even been used to study the design requirements for adaptive-optic systems to correct aero-optic distortions.[5]

Objectives. The specific objectives of the present grant are to: (a) extend some of the instrumentation development work of the last grant by developing a derivative, two-dimensional wavefront sensor to the one-dimensional Small-Aperture Beam Technique (SABT) sensor; (b) address certain scaling issues that came to light in studying the similarities between optical aberrations due to propagation through the

heated jet and propagation through the compressible shear layer; (c) investigate the possible use of control to develop a scheme for real-time sensing and correcting the wavefront for propagation through compressible shear layers; and (d) further explore the relationship between the wavefront aberrations and the concomitant aberrating structures.

Approach. We have now extended the SABT sensor concept to the cross-stream direction as Objective (a). In the first grant, we demonstrated a high-bandwidth (~ 100 kHz) sensor which took advantage of the fact that aberrating, turbulent flow structures "convect" across the viewing aperture.[6, 2, 4] This reliance on structure convection, however, limits the SABT to measurement of the streamwise component of the optical wavefront. In the derivative instrument, we still use the streamwise convection to unfold the wavefront in the streamwise direction. In addition, we impose a scan velocity in the cross-stream direction to unfold the remaining orthogonal component, thereby producing the full, two-dimensional wavefront. An improved scanner and upgraded optical bench components produced successful wavefront measurements in our heated shear layer (water tunnel) facility since our last report. The resulting wavefronts were a time-resolved, time series; individual wavefronts were obtained at 600 Hz (2 measurements per scanner cycle).[7] A series of these wavefronts (every 20th time step) is shown in Fig. 1. The bandwidth of this new wavefront sensor can be increased to 8 kHz by incorporating a faster scanner (already in hand). We plan to use the 8 kHz instrument for two-dimensional wavefront measurements in laboratory air flows.
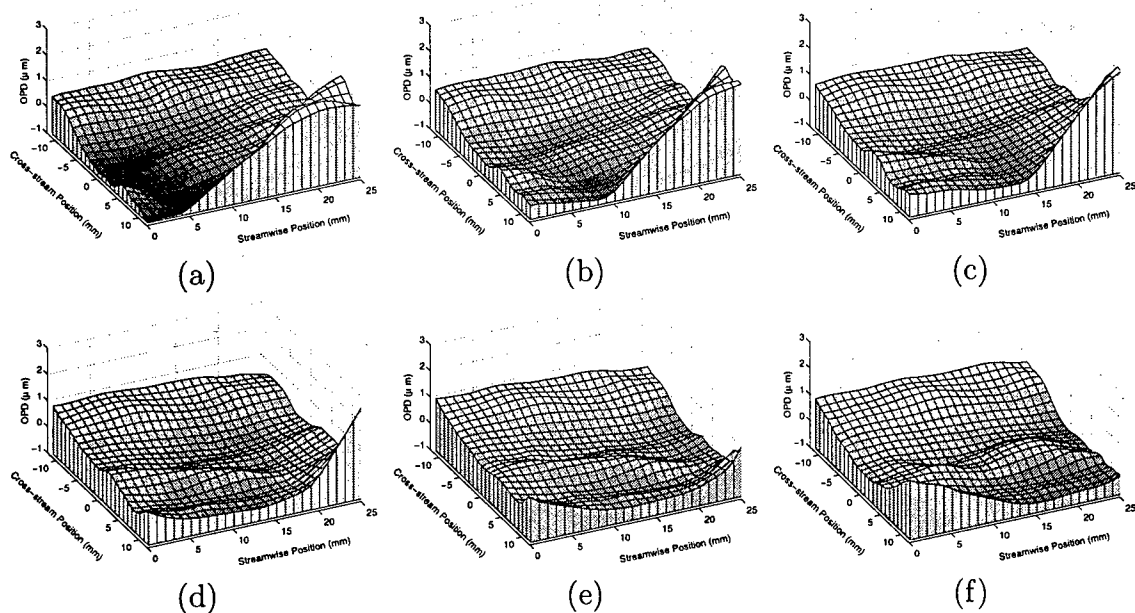

Figure 1: Experimental, two-dimensional, wavefront reconstructions: time steps = 924. (a) through 1024 (f). Between frames, $\Delta t = 0.0333$ sec; overall period (a)–(f) = 0.1667 sec.

Comparisons between the time series of wavefronts from propagation through our laboratory 7 m/s heated jet and a 0.8-Mach, compressible shear layer revealed a number of similarities and differences in the dynamic aberrations imposed on the wavefronts. In Objective (b), we are trying to better understand the compressibility mechanism that creates optical distortions. To do this, we are using a discrete-vortex method (DVM) to model the shear layer's velocity field. Given this velocity field, the pressure and concomitant density fields can be found by (iteratively) integrating the unsteady Euler equations as detailed in Ref. [8]. Unlike the case of a compressible boundary layer,[9] the pressure variations in a compressible shear layer are significant, as shown in Fig. 2. Fig. 2 also shows the schlierens and wavefronts produced by the computed density fields. As described in Ref. [8], our simulation reasonably models the large-scale distortions measured by Hugo *et al.* in the compressible shear layer[4] as shown in Fig. 3. We believe the smaller-scale measured aberrations were caused by temperature variations in the tunnel's splitter-plate boundary layer. Evidence of this is shown in the Station 1 wavefronts measured immediately downstream of the splitter plate (Fig. 3). Superpositioning the Station 1 experimental data on our Station 2 simulation produces wavefronts of similar character to those measured at Station 2 as shown in Fig. 3. With our simulation, we plan to explore suitable scaling laws for use in optical system design estimates and wind tunnel test data scaling.

The use of control for heated-jet experiments greatly enhanced certain areas of investigation in our previous work (see, for example, Refs. [10] and [11]). The coupling of control with the SABT sensor suggests the possibility of not only real-time sensing of wavefront aberrations but also for adaptive-optic correction. In Objective (c), we still plan to explore this possibility for propagation through either our heated shear layer water tunnel facility (mentioned above and in Ref. [7]) or in one of two available heated-air facilities. This will be a focus of our newest research assistant.

Finally, some preliminary investigations into inferring fluid-mechanic information from the distorted wavefronts were undertaken in our first grant (see, for example, Refs. [12] and [13]); however, in Objective (d) we have begun to investigate this relationship more formally by employing wavelet transforms and/or proper orthogonal decomposition methods to decompose the SABT signals and in so doing attempt to develop algorithms for extracting the velocities for each of the aberration-causing flow structures. This is the primary focus of our newest researcher.

Personnel. Three researchers have worked on this project over the past year. Dr. Eric J. Jumper has been the Principal Investigator. Edward J. Fitzgerald, graduate research assistant, has worked primarily on Objectives (a) and (b). James Cicchiello, graduate research assistant, has worked on Objectives (c) and (d).

Publications. Two meeting papers, Refs. [7] and [8], have been produced during the current reporting period. Versions of both of these meeting papers are being submitted as journal articles to *Optical Engineering* and *Journal of Fluid Mechanics*, respectively. In addition, a tentative arrangement has been reached with the editor
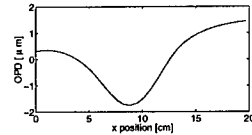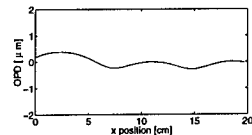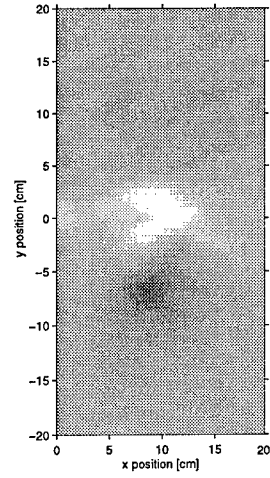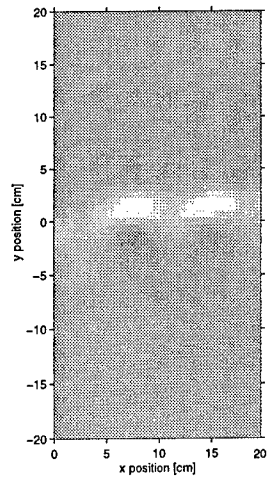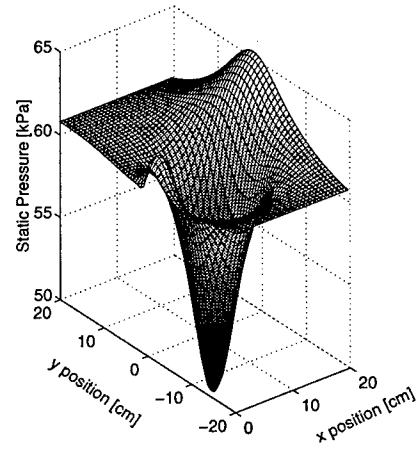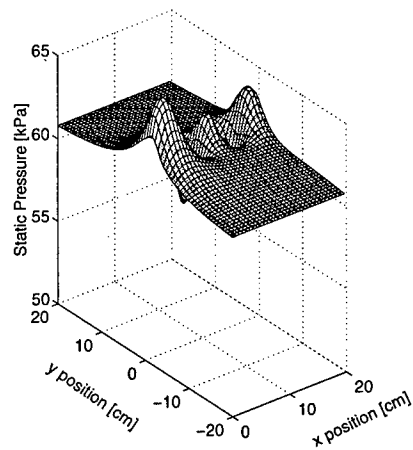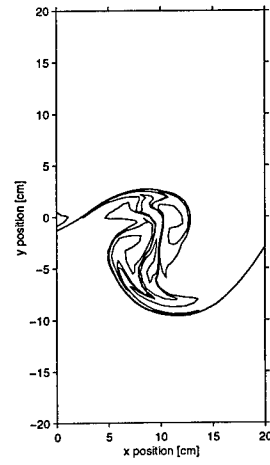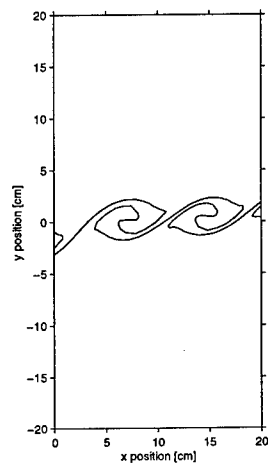
Figure 2: Compressible shear layer simulation at two time steps, one prior to pairing (left) and following multiple pairings (right).

Station 2 Numerical Simulation

Station 1 Experimental Data

High–Pass Filter: 750 Hz
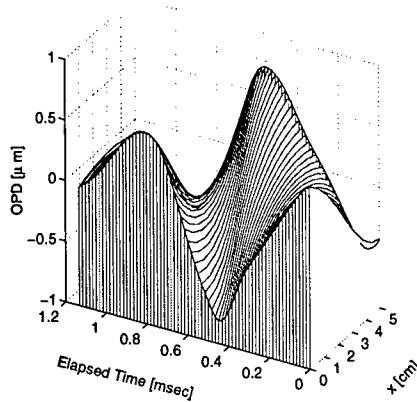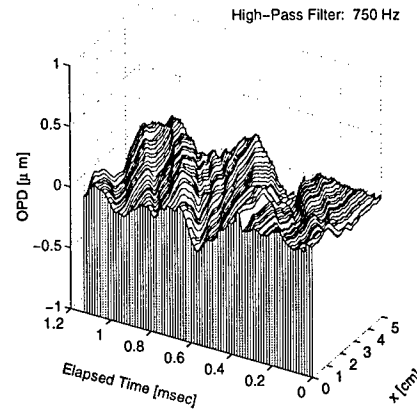
Simulation + Station 1 Experimental Data
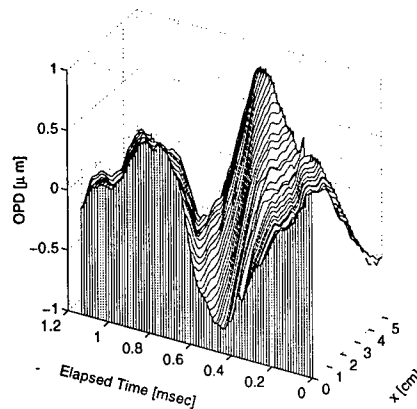
Station 2 Experimental Data

High–Pass Filter: 750 Hz
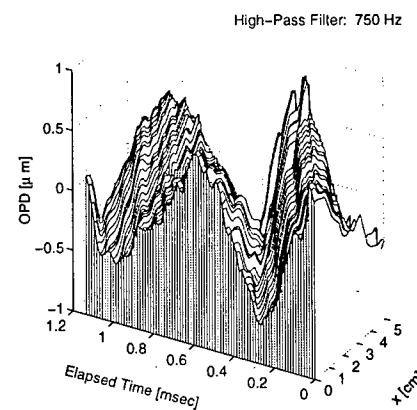
Figure 3: Comparison of wavefronts from discrete vortex simulation with superpositioned station 1 (experimental) wavefront to reconstructed experimental wavefronts for Acoustic Research Tunnel station 2.

of *Progress in Aerospace Sciences* to publish an updated version of the "AIAA Plasmadynamics and Lasers Best Paper Award (1997)"-winning review paper (Ref. [12]) funded under this grant.

References

[1] R. K. Tyson, "The status of astronomical adaptive optics systems," *O. E. Reports* **121**, pp. 11,13, Jan 1994.

[2] R. J. Hugo and E. J. Jumper, "Experimental measurement of a time-varying optical path difference by the small-aperture beam technique," *Applied Optics* **35**, pp. 4436–4447, August 1996.

[3] A. Verhoff, "Prediction of optical propagation losses through turbulent boundary/shear layers," in *Aero-Optical Phenomena*, K. G. Gilbert and L. J. Otten, eds., *Progress in Astronautics and Aeronautics Series* **80**, pp. 40–77, American Institute of Aeronautics and Astronautics, Inc., (New York), 1982.

[4] R. J. Hugo, E. J. Jumper, G. Havener, and C. Stepanek, "Time-resolved wave front measurements through a compressible free shear layer," *AIAA Journal* **35**(4), pp. 671–677, 1997.

[5] J. M. Cicchiello and E. J. Jumper, "Far-field optical degradation due to near-field transmission through a turbulent heated jet," *Applied Optics* **36**, pp. 6441–6452, Sep 1997.

[6] E. J. Jumper and R. J. Hugo, "Quantification of aero-optical phase distortion using the small-aperture beam technique," *AIAA Journal* **33**(11), pp. 2151–2157, 1995.

[7] E. J. Fitzgerald and E. J. Jumper, "Two-dimensional, optical wavefront measurements using a small-aperture beam technique-derivative instrument," in *Proceedings of the International Conference on Optical Technology and Image Processing in Fluid, Thermal, and Combustion Flow, (VSJ-SPIE 98)*, Dec 1998.

[8] E. J. Fitzgerald and E. J. Jumper, "Further consideration of compressibility effects on shear-layer optical distortion." AIAA Paper 99-3617, Jun 1999.

[9] A. J. Smits and J.-P. Dussauge, *Turbulent Shear Layers in Supersonic Flow*, American Institute of Physics, Woodbury, New York, 1996.

[10] R. J. Hugo and E. J. Jumper, "Constant current anemometry and its impact on aero-optical measurements." AIAA Paper 95-1986, Jun 1995.

[11] R. J. Hugo and E. J. Jumper, "Implications of the homogeneous turbulence assumption on the aero-optic linking equation," in *Optics, Imaging and Instrumentation, SPIE - International Society of Optical Engineering* **2546**, 1995.

[12] E. J. Jumper, "Recent advances in the measurement and analysis of dynamic aero-optic interactions (review paper)." AIAA Paper 97-2350, Jun 1997.

[13] R. J. Hugo and E. J. Jumper, "Experimental measurement of a time-varying optical path difference using the small-aperture beam technique," in *Optical Diagnostics in Fluid and Thermal Flow*, S. S. Cha and J. D. Trollinger, eds., *SPIE - International Society of Optical Engineering* **2005**, pp. 116–128, 1993.

PROPAGATING POTENTIAL DISTURBANCES IN TURBOMACHINERY

Eric J. Jumper
Department of Aerospace and Mechanical Engineering
University of Notre Dame, Notre Dame, Indiana

Paul I. King
Department of Aeronautics and Astronautics
Air Force Institute of Technology, Wright-Patterson AFB, Ohio

Abstract
Background. This joint project between the University of Notre Dame and the Air Force Institute of Technology will investigate the unsteady forced response of vanes in compressible-flow cascades, where the vanes are forced by unsteady, upstream-propagating potential disturbances. The investigation is geared toward providing a better understanding for predicting High Cycle Fatigue (HCF) failures in turbomachinery. This work will take a more fundamental look at phenomena already identified in joint studies between Notre Dame and the Air Force Academy, performed under the aegis of the Science and Technology (S&T) HCF program. These S&T studies have been directed toward characterizing unsteady aerodynamic forcing and unsteady pressure response in the inlet and fan section of an AlliedSignal F109 Turbofan.

Initially, the S&T project began as a cascade study in the Notre Dame, unsteady transonic cascade, which was specifically designed for the research. The Notre Dame cascade forms the test section of a transonic in-draft tunnel located in the Hessert Center for Aerospace Research. The tunnel is driven by up to three, 3,310-cubic-feet-per-minute, Allis-Chalmer vacuum pumps. A top-view schematic of the cascade-section geometry used in the S&T studies is shown in Fig. 1, along with the new unloaded cascade that will be referred to below. For the S&T studies, the cascade turning vanes were production-hardware stator vanes from the single, axial-flow compression stage of an AlliedSignal F109 turbofan engine. The cascade was formed by four midstream vanes and two wall vanes, creating five flow passages. In the cascade, the chord of these vanes was 1.28 in. and the blade spacing was 0.84 in. In the engine, the stators are swept aft from the hub to tip; however, in the cascade the vanes were mounted vertically to form a nominal, two-dimensional linear cascade. The cross-sectional inlet and outlet dimensions of the cascade were 4 in. × 4 in. Note that a variety of tests were run to verify that the cascade flow was two-dimensional over the instrumented region of the vanes.[1,2,3]

Unsteady forcing of the cascade vanes was established through vortex shedding from a row of five circular cylinders, aligned parallel with the span direction of the vanes and located, as shown in Fig. 1, 0.8 vane-chords downstream of the vane row. No active control of the cylinder shedding is needed in either cascade shown in Fig. 1, as all cylinders shed in phase. In either cascade, the cylinder shedding frequency may be varied by changing the cylinder diameter as, over the range of Reynolds numbers of interest, the Strouhal number is constant at approximately 0.2. Thus, the reduced frequency for the von Karman shedding may be set by selecting the cylinder diameter. All results referred to here are for forcing produced off of 3/16 in. diameter cylinders, which yield a reduced frequency, based on the vane half chord, of approximately 5 over the entire range of Mach numbers selected; a reduced frequency of 5 yields primary forcing frequencies at the highest Mach numbers of approximately 9 KHz and the first harmonic at 18 KHz. All unsteady pressure measurements were triggered by a transducer embedded in one of the forcing cylinders. For further details see References 1,2, and 3.

In the S&T studies, the stator vanes were instrumented with surface-mounted Kulite XCS-062 ultraminiature transducers; providing measurement locations at 7, 12, 20, 30, 40, 50, 65 and 80 percent vane-chord on both the suction and pressure sides of the vanes. Phase-locked unsteady, and time-averaged, pressure data were collected at cascade inlet Mach numbers ranging from 0.427 to 0.50, where the highest inlet Mach number resulted in a maximum Mach number over the suction side of the vanes of 0.73. Each Mach-number study yielded phase-locked, time-resolved pressure data, made up of 400 ensembles of forcing-cylinder-triggered data records (for details see References 1 and 2). The time-resolved (phase-averaged) data from each of the 16 stator locations and Mach

numbers were disassembled into their primary (forcing frequency) and harmonic components; a representative two-frequency reconstruction, for an inlet Mach number of 0.427, is shown in Fig. 2, where the peak-to-peak fluctuation is normalized by the largest response.[1,2] With the data in this form, it was possible to examine the relative phase of the pressure response along the vanes, as well as the measured amplitude trends.

Phase Information. As explained in detail in References 1 and 2, it can be shown that a potential disturbance traveling upstream across the vanes, when linearized to first order in terms of a single "free-stream" Mach number, should have a relative phase distribution of

$$\phi_{relative} = \phi - \frac{(c-x)\omega}{a_\infty(1-M_\infty)} \qquad (1)$$

where ϕ is the phase delay at the vane trailing edge, a_∞ and M_∞ are the nominal "free-stream" speed of sound and Mach number over the vane surface, c is the vane chord, x is the measurement location from the leading edge of the vane, and ω is the frequency of the disturbance in rad/sec. Figures 3 and 4 show the measured, disturbance phase distributions for the primary and harmonic frequencies on the suction and pressure surfaces, respectively. The overlaid curves in Figs. 3 and 4 are the computed, position-dependent phase delays from Eq. (1), assuming nominal "free-stream" Mach numbers for the suction and pressure surfaces of 0.59 and 0.35, respectively. These assumed "free-stream" Mach numbers are in excellent agreement with the local Mach numbers, M_L, derived from the time-averaged pressure data over the suction and pressure surfaces of the vanes using

$$M_L = \sqrt{\frac{2}{\gamma-1}\left[\left(\frac{P_o}{P_L}\right)^{\frac{\gamma-1}{\gamma}} - 1\right]} \qquad (2)$$

where P_o is the measured total pressure, P_L is the measured local static pressure, and γ is the ratio of specific heats. A plot of local Mach number versus chord is given in Fig. 5. Clearly, the results of Figs. 3 and 4 are in excellent agreement with the Mach numbers of Fig. 5. Similar Mach-number and phase agreement was found for all inlet-Mach-number cases studied; this verified that our data was good, and that the forcing method produced acoustically-propagating potential disturbances that subsequently interacted with the cascade vane to yield relatively-large unsteady pressure responses.

Amplitude Information. Along with being able to examine the disassembled data for phase information, amplitude information can also be examined. The normalized, RMS, unsteady pressure-amplitude distributions for the four Mach-number cases studied are given in Fig. 6. Normalized, unsteady pressure-amplitude distributions at the primary forcing frequency, for the same four Mach-number cases, are shown in Fig. 7.[1] The data of Figs. 6 and 7 may be compared, from which it is clear that a more-descriptive picture emerges from Fig. 7. Specifically, there are two important characteristics of the amplitude data that are of interest to us: first, although we only have data out to the 0.8 vane-chord location, extrapolation of the Fig. 7 data to the trailing edge suggests an unsteady-pressure singularity; second, an amplification of the unsteady pressure near the x/c = 0.3 location on the suction surface appears to be increasing with Mach number.

The suggestion of a trailing-edge singularity is, as far as we know, the first to have been seen with detailed data, and raises the question as to whether or not such a singularity can exist. Until we produced these data, it had been generally accepted that a trailing-edge singularity had been theoretically forbidden, as it most certainly is for waves entering from upstream; however, extensive discussions with Glegg[4] and review of the literature (for example Reference 5), now suggest that such a singularity is probably not forbidden. Clearly, if such a singularity is present in the case of acoustically-propagating upstream-traveling waves, this is of first-order importance to the rotor/stator and stage-to-stage interaction problems. It should be noted that an interesting theoretical point raised in Reference 5 concerns the presence or absence of a trailing-edge shear layer, because these authors draw a distinction between the unsteady pressure response in the presence or absence of a shear layer. In terms of cascade configurations, an unloaded vane row should produce no shear layer, while a loaded vane row might produce a shear layer.

The amplification of the unsteady pressure near the x/c = 0.3 location is also of first-order importance. Atassi, Fang and Ferrand[6] had previously predicted the occurrence of this amplification in their theory of "acoustic blockage." According to their theory, acoustic waves traveling upstream from the trailing-edge region of a vane row are impeded in their upstream progress by the oncoming flow. As this subsonic flow builds in Mach number, depending on the frequencies and wavelengths, the waves can coalesce and amplify the disturbance; amplifications of up to 20 times are theoretically possible as the subsonic Mach number approaches 0.99. The amplification noted in Fig. 7 is at the maximum Mach number location; our maximum Mach number was 0.73. We believe that our data provides the first evidence that this mechanism exists and is important at relatively low Mach numbers, becoming noticeable for maximum Mach numbers as low as 0.6. It should be noted that prior to Atassi *et. al*'s work, unsteady pressure rises near the maximum Mach number region had always been assumed to be associated with transonic flows and oscillating shocks; acoustic blockage provides a fully-subsonic mechanism for providing similar-order amplification for upstream-propagating disturbances. The present work will further address acoustic-blockage theory.

Objectives. The previous S&T studies, discussed above, identified three phenomena that we view as critical to a proper understanding of the rotor/stator, stage-to-stage interaction and HCF problems in compressible flows. These phenomena are: the possibility of a trailing-edge singularity; acoustic blockage; and the interaction between acoustically-propagated potential disturbances and convected disturbances. However, there were certain shortcomings to the previous studies. For one, the previous studies made no attempt to document either the cascade in-flow and out-flow conditions, or the unsteady forcing disturbances. Rather, only theoretical work was done to infer the nature of forcing disturbances from both the upstream and downstream sources, particularly the upstream-propagating potential disturbances. Additionally, although the data showed that the flow in the instrumented region of the cascade had excellent two-dimensional character, the use of the F109 vanes meant that the vane chord had a slight dependence on span. Among other things, this span dependence limited the vane instrumentation region to approximately the outer 25% span of the cascade vanes. Because of the need to surface mount the pressure transducers, and the small thickness of the F109 vanes, the locations where the vane could be instrumented were limited in the trailing-edge region to 0.8 vane-chords. With the suggestion of an unsteady pressure singularity at the vane trailing edge, finer resolution in pressure measurements near the trailing-edge region is important.

Finally, the small vane thickness limited the maximum inlet Mach numbers to 0.50, since the method of von Karman vortex shedding, used as the forcing technique, stabilized (stopped) once transonic flow developed on the forcing cylinders. This stabilization is most probably due to the formation of small shocklets on the cylinder surface. Clearly, because of the indication of "acoustic blockage," the phenomenon should be studied up through transonic conditions. We believe that these experimental limitations can be overcome by replacing the turning vanes with thicker specifically-designed vanes. Thicker vanes will afford the use of the central portion of the cascade, allow for higher-resolution pressure measurements, particularly near the trailing edges of the vanes, and allow for unsteady measurements through transonic vane-row Mach numbers.

The present effort includes both experimental and theoretical/computational components and will involve unsteady cascade studies both at Notre Dame and at AFIT. The Notre Dame effort will use a modified cascade section with a highly-resolved spatial distribution of pressure instrumentation in the trailing-edge region of the cascade vane row, as well as high spatial resolution near the highest Mach number regions of the vanes. Notre Dame's experimental effort will primarily deal with an unloaded cascade, while and AFIT's experimental effort will primarily deal with a loaded cascade; as noted above, both are relevant to trailing-edge, unsteady-pressure singularity issues. As discussed below, we will be exploring different airfoil cross sections, with the intent of using the same sections in both cascades, differing only in camber. As was the case for the S&T studies, the experimental studies planned for both the AFIT and Notre Dame facilities will be performed at real-engine reduced frequencies and at real-engine mass flux, Reynolds and/or Mach numbers. However, the separate studies will operate in different pressures regimes, thus affording an ability to look into different scaling issues.

Progress. Although the effort is in the initial stages, we have already made reasonable progress. The Notre Dame unloaded cascade shown schematically in Fig. 1 has been constructed, and preliminary pressure-response data have been collected and analyzed. As noted in Fig. 1, the cascade is presently set up with a single unloaded vane, primarily to test candidate airfoil cross-sections and alternatives in pressure transducers; however, early results indicate that the previously-measured trailing-edge phenomena is also distinctly present in these tests. As mentioned above, the nature of the potential disturbances for the S&T studies was inferred; thus, the first measurements made at

AFIT will take a detailed look at these forcing disturbances, using the phase-locked data acquisition methods developed for the F109 turbofan inlet studies.[7] At this writing, these tests are in the planning stage with first-data expected by mid September 1999.

Personnel. In addition to the Principal Investigator (Dr. P. King, AFIT/ENY, 937-255-3636, EXT 4628), the AFIT portion of the work will involve one graduate research assistant, GRA. The Notre Dame effort includes the Principle Investigator (Dr. E. Jumper, Dept. of Aerospace and Mechanical Engineering, 219-631-7680) and two GRA's in the first year; in addition, to speed the planned initial work, a third GRA over the first summer.

References

1. Fabian, M.K., and Jumper, E.J., "Upstream-Propagating Acoustic Waves Interacting with a Compressible Cascade," AIAA Paper Number 97-0380, 1997.

2. Fabian, M.K., and Jumper, E.J., "Rearward Forcing of an Unsteady Compressible Cascade," *Journal of Propulsion and Power*, Vol. 14, No. 6, November-December, 1998, pp. 23-30.

3. Fabian, M.K., and Jumper, E.J., "Convected and Potential Unsteady Disturbances Interacting with an Unsteady Cascade," AIAA Paper Number 96-2627, 1996.

4. Glegg, S.A.L., Personal Communication, University of Notre Dame, 8 Nov. 1995.

5. Crighton, D.G., and Leppington, F.G., "Radiation Properties of the Semi-Infinite Vortex Sheet: the Initial-Value Problem," *Journal of Fluid Mechanics*, Vol. 64, part 2, 1974, pp. 393-414.

6. Atassi, H.M., Fang J., and Ferrand, P., "A Study of the Unsteady Pressure of a Cascade Near Transonic Flow Condition," ASME Paper Number 94-GT-476, International Gas Turbine and Aerospace Congress and Exposition, The Hague, Netherlands, 1994.

7. Falk, E.A., Jumper, E.J., and Fabian, M.K., "Upstream Propagating Potential Waves in the F109 Turbofan Engine Inlet Flow, " AIAA Paper Number 98-3294, 1998.
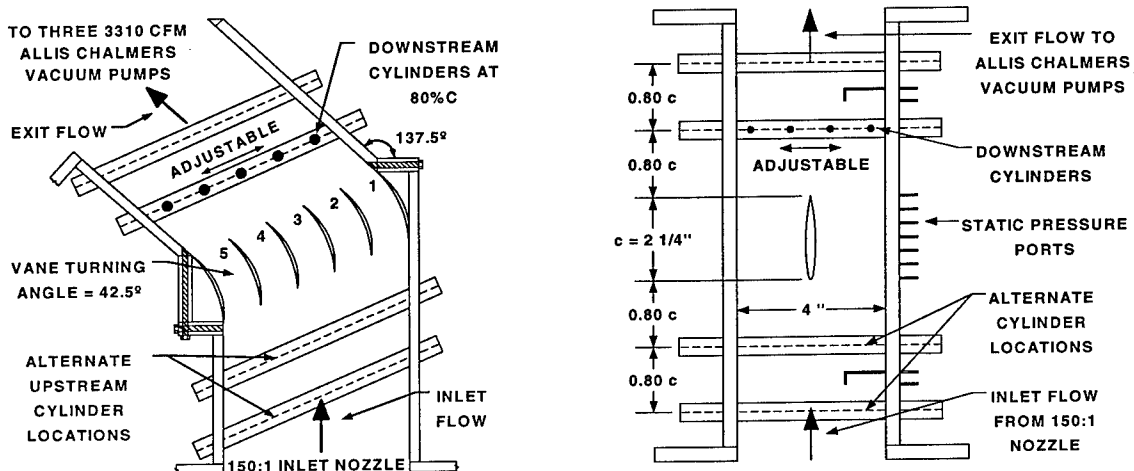
Figure 1. Top views of S&T Notre Dame cascade (left) and new, modified unloaded cascade (right).
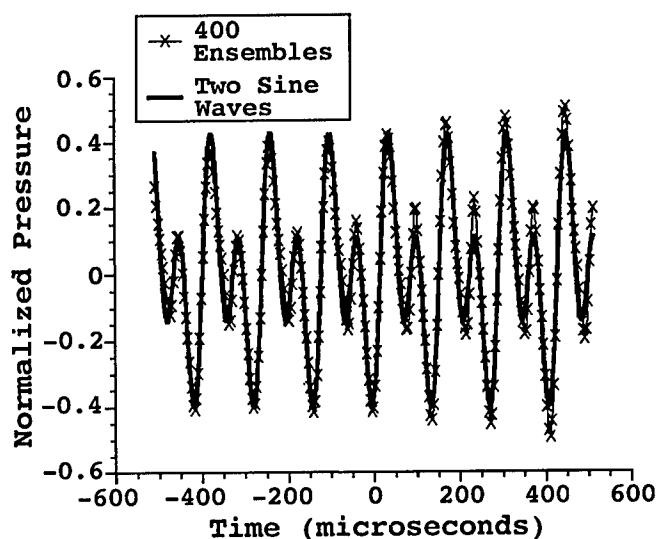
Figure 2. Two sine wave representation of S&T data.
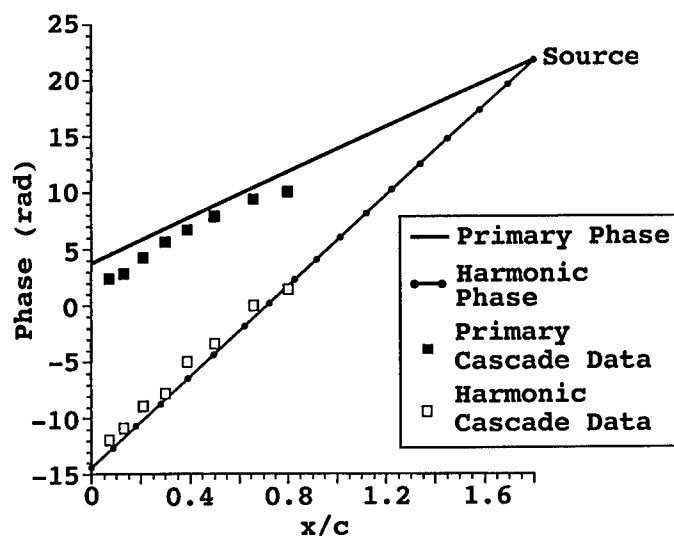
Figure 3. Suction surface upstream-traveling wave vs. primary and harmonic phase.
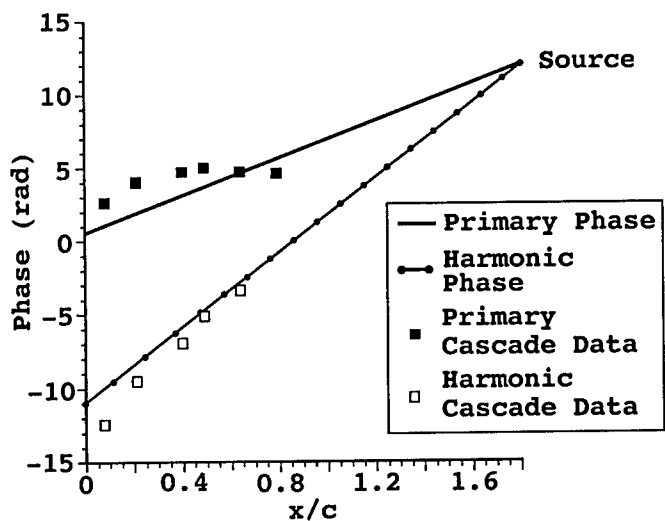
Figure 4. Pressure surface upstream-traveling wave vs. primary and harmonic phase.
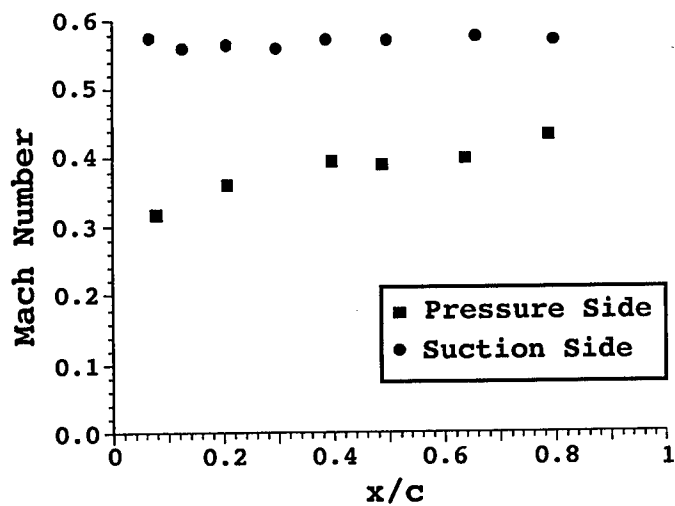
Figure 5. Local Mach number vs. chord position.
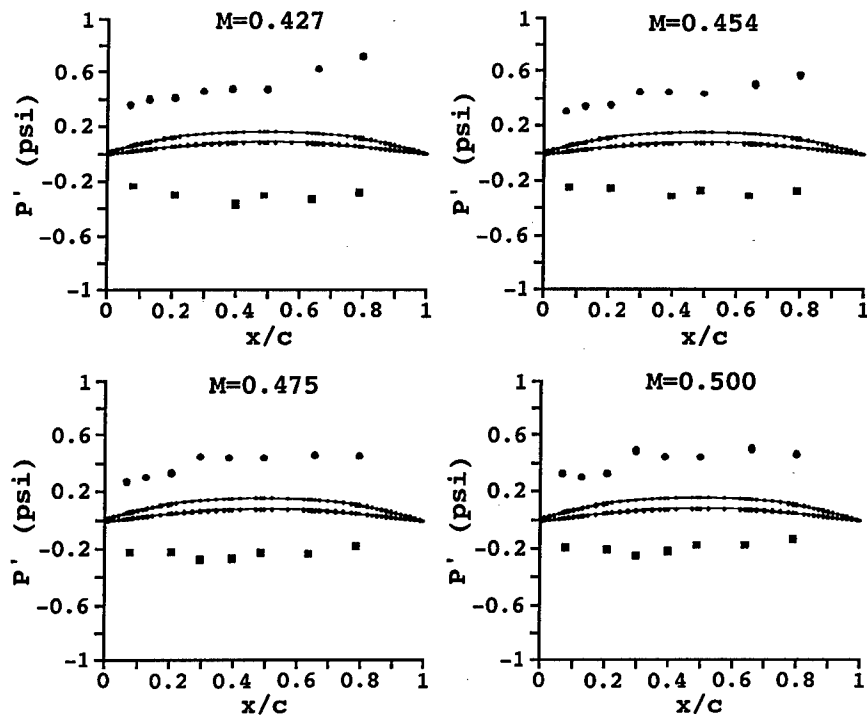
Figure 6. Engine-axis 2, RMS unsteady pressures for rearward forcing.
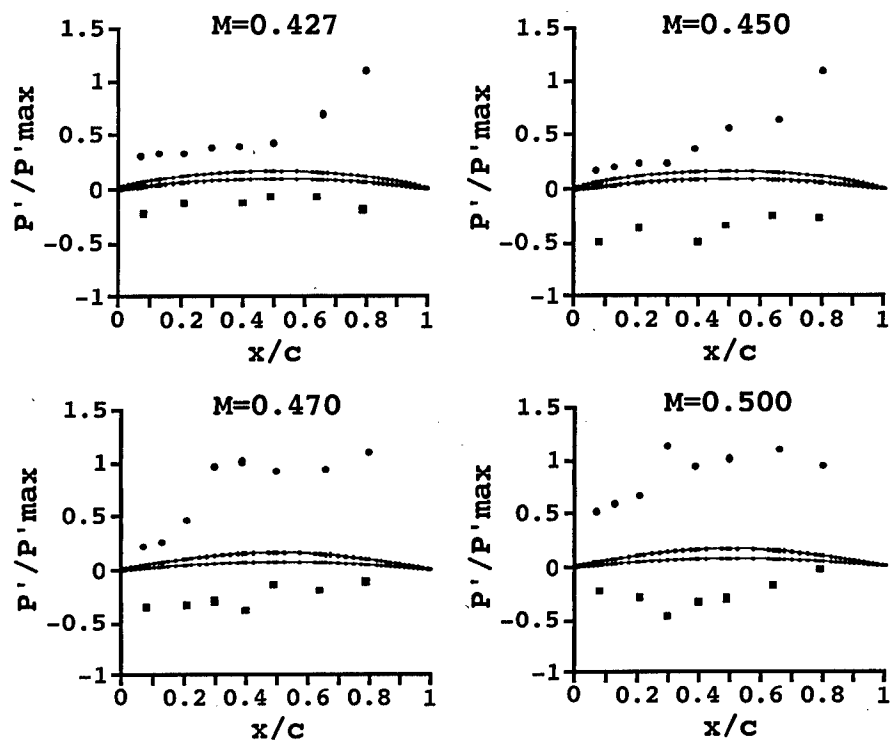
Figure 7. Normalized unsteady pressure amplitude for the fundamental
frequency with increasing Mach number.

TURBULENCE AND COMPLEX FLOW PHENOMENA
IN AXIAL TURBOMACHINES

Joseph Katz & Charles Meneveau
Department of Mechanical Engineering
The Johns Hopkins University
Baltimore, MD 21218

Abstract

The objective of this project is to measure the unsteady flow structure in axial turbomachines and use the data to address turbulence and complex flow modeling issues in complicated geometries. This report has two sections. The first briefly describes the two-stage axial test facility whose construction has been recently completed. The second section presents results from analysis of data on rotor-stator interactions in an existing centrifugal pump with a vaned diffuser. The data is used to examine flow modeling at levels of LES, RANS, and passage averaging. This report focuses on modeling of passage-averaged deterministic stresses that arise due to cyclic flow separations. We also mention conclusions on subgrid modeling for LES based on an increased data base that permits better statistical convergence.

Axial Flow Facility

The axial turbomachine test facility has been designed and constructed to allow detailed measurements of the velocity distribution within an entire stage including the rotor, stator, gap between them, inflow into the rotor and the wake structure downstream of the stator. Sketches of the system were included in the report last year but construction and assembly have been completed only recently. The facility provides unobstructed view for 2-D PIV and 3-D holographic PIV measurements within the entire stage. This unlimited access is facilitated by using acrylic rotor and stator (both precision machined), a fluid with index of refraction that matches that of the acrylic (water with NaI), and windows for illumination and observation at any desired plane. In addition to the AFOSR grant mentioned above, support for constructing this facility has also been provided by ONR. The two rotors of this two - stage axial turbomachine have a common shaft supported by precision bearings. The blades have an outside diameter of 30 cm and a hub diameter of 21.6 cm. The design flow rate is 0.195 m³/s and the total pressure rise is 100 kPa. The system is driven at 900 rpm by a 25 HP rim-driven motor that is connected directly to the rotor of the first stage. The second stage is driven by the common shaft. The test loop has a temperature control system and provides considerable flexibility in installing other devices including pressure transducers,

honeycombs and grids as well as modifying the blade rows. As noted before, construction, assembly and initial testing of this facility has been completed recently. The PIV measurements will resume next month.

Addressing Turbulence Modeling Problems in Turbomachines

Background: Numerical simulations of flows within an entire multistage turbomachine cannot be performed using unsteady RANS on a routine basis due to practical constraints. While performing RANS of each blade row separately one is faced with difficulties in matching boundary conditions. In the "passage-averaged" approach (Adamczyk, 1985) unsteady effects caused by neighboring rows are averaged out and accounted for through "deterministic" stresses. While the present axial flow facility is being constructed we have used PIV data generated in a centrifugal pump facility with a vaned diffuser (a project funded by ONR) to examine the Reynolds and Deterministic stresses associated with rotor-stator interactions. The Reynolds stresses are determined from the difference between the instantaneous and the phase averaged velocity distributions. The deterministic stresses are obtained from the difference between the phase-averaged and passage averaged (over all phases) velocity. Previous studies have shown that deterministic stresses can be of similar or higher magnitude than the Reynolds stresses (e.g. Rhie et al., 1995).

Experimental results in centrifugal pump: The experiments were performed in a transparent pump flow visualization facility that enables PIV measurements within the impeller, the gap between the rotor and the stator, between the diffuser vanes and in the volute. Detailed information on this centrifugal facility and the available data are presented in Sinha and Katz (1999) and Sinha et al. (1999). The impeller has five backward swept blades and inlet and tip diameters of 8.51 cm and 20.32 cm, respectively. The diffuser has 9 blades with chordlength of 13.44 cm, inside diameter of 24.45 cm and discharge diameter of 30.5 cm. The pump is operating at design conditions at 890 rpm. The PIV system utilizes a Nd-Yag laser as a light source and a 2K x 2K pixels^2 digital camera with hardware based image-shifter. Neutrally buoyant, ~30 μm diameter, fluorescent particles are used as tracers. We measures the phase averaged velocity distributions every 10^0 of impeller blade orientations by averaging 100 instantaneous distributions at each phase. The Reynolds stresses are determined from the difference between the instantaneous and phase averaged data.

The passage averaged velocity and deterministic stresses in the diffuser frame of reference are calculated by averaging velocity fields of the same domain that are obtained at different impeller orientations. Figures 1a,b show the resulting passage averaged velocity and deterministic kinetic energy. The dominant deterministic stresses occur along the suction side of the diffuser vane. The primary mechanism causing these stresses is variations in the incidence angle at the entrance to the vane passage that result in phase-dependent leading edge separation. Further downstream along the suction side, the stresses are caused by phase-

dependent mid-vane separation. This latter phenomenon is associated with unsteady pressure at the entrance to the passage. In both cases, the dominant phenomenon is the response of the boundary layer on the diffuser vane to the non-uniform outflux from the impeller. This non-uniformity is associated mainly with the "jet-wake" phenomenon, i.e. higher radial velocity on the pressure side of the impeller blade and low in the suction side, and conversely, high circumferential velocity in the suction side and low in the pressure side (Dean & Senoo, 1960). These non-uniformities occur in addition to the viscous wake of the impeller. In the present flow, they are dominant.
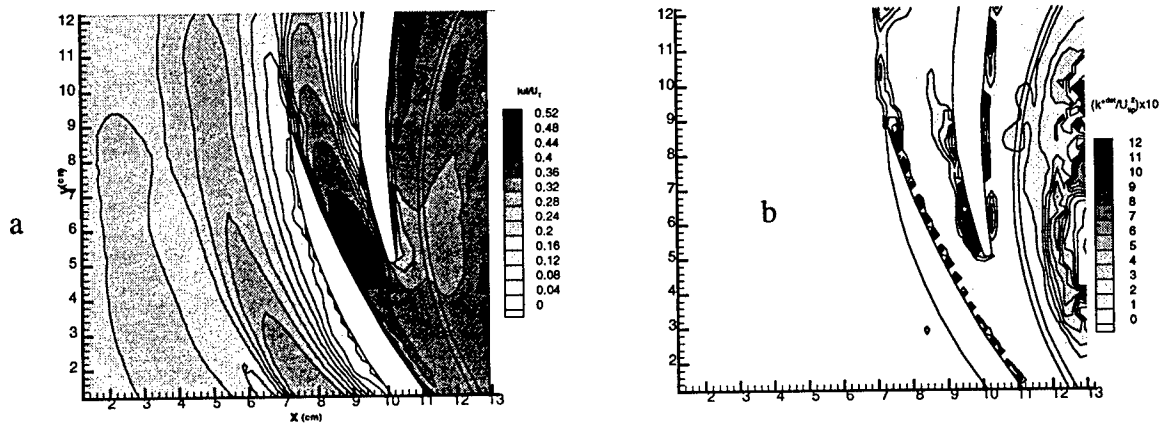
Figure 1: a. passage-averaged velocity distribution; b. deterministic kinetic energy in the stator frame of reference for flow within a centrifugal pump with a vaned diffuser.

Determination of the passage-averaged velocity and stresses in the rotor frame of reference is a more complicated process since we need to rotate the measured velocity field of different phases and match the location of the impeller blade. In order to obtain passage-averaged data over a domain that covers at least one vane passage, the rotated velocity field must be substantially larger. To obtain this data we patch two flow fields of the same domain that are recorded at different impeller phases as illustrated in Figure 2a. A series of five such pairs along with interpolated fields are then rotated and aligned such that the impeller blade is located in the same place. The rotor passage-averaged velocity distribution (Fig. 2b) clearly shows the wake of the impeller blade. Also, the high stresses (Fig. 2c) occur in the domain occupied by the diffuser vanes that have been passage-averaged out. However, high deterministic stresses occur also in the wake of the impeller. This effect is caused by meandering of the wake due to the circumferential nonuniformities of the pressure distribution upstream of the diffuser vanes.

Modeling of deterministic stresses: As a preliminary step, we focus attention on modeling the deterministic stress distributions in the stator frame due to cyclic leading edge separation. As a measure of variations in incidence angle, we evaluate α, the angle between the velocity slightly upstream (~2mm) of the stator leading edge and the circumferential direction. Shown

in Fig. 3a (squares) is α as a function of rotor orientation. At 206^0, when the stator leading edge is inside the "jet region" of the rotor outflow, α is large. Conversely, when the stator leading edge is in the rotor's wake region, α is low. It can be observed from the various phase-averaged velocity distributions (not shown here, see Sinha & Katz 1999) that at 206^0 orientation leading edge separation occurs. To model the deterministic stresses in the stator vane passage, we must rely on information that is available during simulation of passage-averaged equations, such as the passage-averaged velocity field in the rotor reference frame. As discussed before, this velocity field is dominated by the "jet-wake" phenomenon that causes the incidence angle variations observed in Fig. 3a. In order to demonstrate this trend we evaluate the circumferential variations in "incidence angle" at the same radial location upstream of the stator-blade leading edge, using the rotor passage-averaged velocity distribution (Fig. 2b),. The circumferential variations are plotted in terms of the equivalent rotor blade orientation in Fig. 3a (circles).
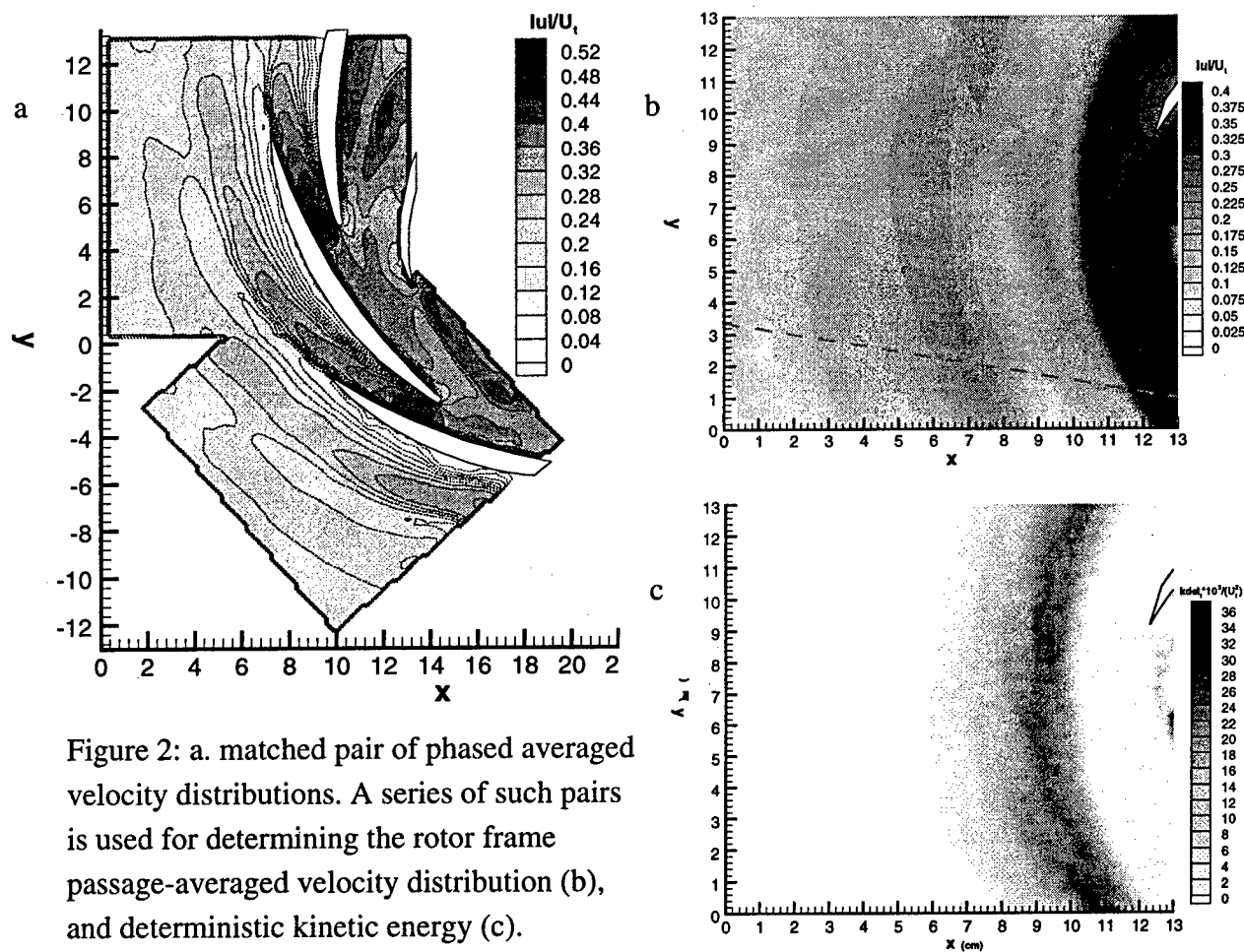
Figure 2: a. matched pair of phased averaged velocity distributions. A series of such pairs is used for determining the rotor frame passage-averaged velocity distribution (b), and deterministic kinetic energy (c).

126

The trend of decrease of incidence angle in going from the jet to the wake region is clearly reproduced. Also, the last point in the phase-averaged results shows a slight increase, as does the rotor passage-averaged distribution, although with a slight shift. The large difference (about 15^0) in angle can be reduced by repeating the comparison at a point further upstream of the stator blade, i.e. approaching conditions that are more representative of the "free-stream" inlet condition to the stator - at this stage we present these preliminary results to highlight qualitative trends only.
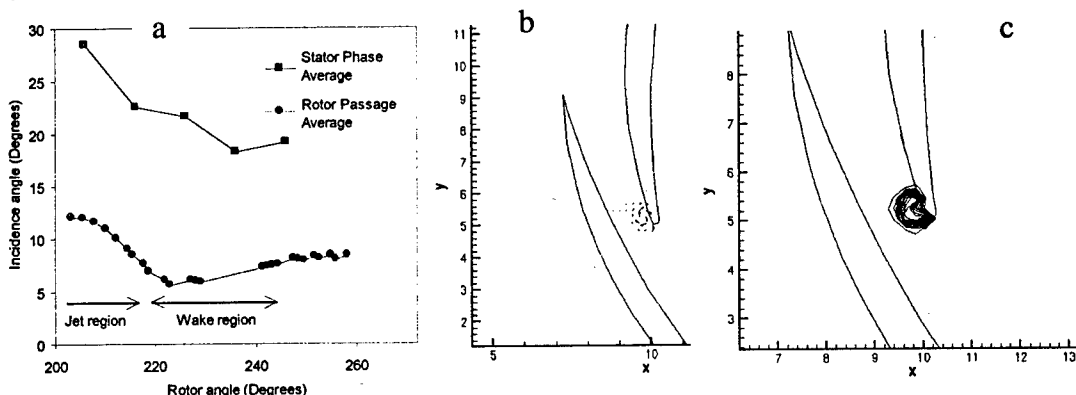
Figure 3. (a) Variation of "incidence angle" α with rotor orientation. Squares: α in phase-averaged velocity distributions. Circles: α at same location in the rotor passage-averaged velocity. (b) Simple model for leading-edge separation induced by high incidence angle. (c) Deterministic kinetic energy as determined from the difference velocity shown in (b).

The state-of-the-art modeling for deterministic stresses, the "swept wake" approximation (Adamczyk 1985), has shortcomings. Unlike the strongly peaked distribution of real deterministic stresses shown in Fig. 1b, the model predicts a circumferentially uniform stress field, since in this model the rotor flow-field is rotated (swept) neglecting the interactions with the stator. Below we present some preliminary ideas of an improved modeling approach. The idea is based on postulating a (simple) velocity field to model the difference between passage-averaged and phase-averaged velocity fields at different rotor orientations. The resulting deterministic stresses are equal to the dyadic product between the different components of the modeled velocity difference, weighted by the fraction (f) of the cycle in which the phase-averaged flow is separated. The postulated model velocity field can be obtained at varying levels of sophistication, depending on the level of accuracy desired and on available computational resources. At the one end, one could perform several (e.g. 2-D) steady calculations with varying incidence angles and build a "look-up table" from which the deterministic stresses are evaluated. The cost of this option, while still significantly lower than that of unsteady RANS, would be considerable. On the other end, one can postulate highly simplified flow fields with a few parameters, to be fitted from available data. As a very preliminary example, we add a Taylor vortex (plus its image to mimic the wall) to the

stator passage-averaged velocity. Parameters of the vortex (strength, thickness, and location along the blade) must be expressed in terms of relevant parameters. In addition, one must know the fraction f of the cycle during which the flow is separated. Figure 3b shows such a "difference" field for a specific choice of parameters, and 3c shows the implied distribution of deterministic kinetic energy. Comparing with Fig. 1b, it appears that the main peak can be described by this sort of simplified model. However, the comparison also shows that many problems remain, including mid-vane separation and the wakes. Moreover, for quantitative comparisons we must specify the "vortex model" parameters in terms of information available to the simulator. This is still an open challenge, which will be the subject of continued work for next year.

LES modeling: We have completed the analysis of subgrid-scale kinetic energy dissipation using a box-filter. Interestingly, the SGS dissipation shows negative peaks in the shear layer developing due to mid-span separation on the suction side of the stator vane. This negative peak indicates "backscatter" of kinetic energy. We conjecture that it is associated with vortex pairing in the shear layer. Such a process cannot be reproduced by the eddy-viscosity model. Last year we reported that even after phase averaging of the SGS dissipation, backscatter events persisted. At the time, only 35 data sets were available (at the same phase). This year we have completed the analysis by enlarging the sample to 100 data sets. The improved convergence (not shown) still gives backscatter in the separating shear-layer, confirming that this trend is a statistically robust phenomenon.

Acknowledgement/Disclaimer

References

Adamczyk, J.J., 1985, "Model Equation For Simulating Flows In Multistage Turbomachinery." *ASME paper No.* 85-GT-226.

Dean, R.C., & Senoo, Y. 1960 "Rotating wake in vaneless diffusers", *ASME J. of basic Engineering*, 82, p. 563

Rhie, C.M., Gleixner, A.J., Spear, D.A., Fischberg, C.J., Zacharias, R.M., 1995, "Development And Application Of A Multistage Navier-Stokes Solver. Part A: Multistage Modeling Using Body Forces And Deterministic Stresses," *ASME Paper No.* 95-GT-342.

Sinha, M. & Katz, J., 1999, "Quantitative visualization of the flow in a centrifugal pump with diffuser vanes. Part A: On flow structures and turbulence", J. Fluids Eng. (submitted).

Sinha, M., Katz, J., Meneveau, C., 1999, "Quantitative visualization of the flow in a centrifugal pump with diffuser vanes. Part B: addressing passage-averaged and LES modeling issues in turbomachinery flows", J. Fluids Eng. (submitted).

DEVELOPMENT OF DOPPLER GLOBAL VELOCIMETER (DGV)
AFOSR/DEPSCoR Grant F49620-98-1-0068

John Kuhlman, PI
West Virginia University
Mechanical and Aerospace Engineering Department
Morgantown, WV 26506-6106

Abstract
A two-component Doppler Global Velocimeter (DGV) system has been developed, along with a two-component Point Doppler Velocimeter (PDV) system. Velocity measurements have been obtained for both systems to quantify accuracy, for velocity distributions over the surface of a rotating wheel, and for simple flows such as fully-developed turbulent pipe flow, circular jet flow, and the flow over an NACA 0012 airfoil model.

Based upon rotating wheel data, PDV data linearity is $\pm$ 0.5 % (ie, $\pm$ 0.3 m/sec, out of 57 m/sec). PDV turbulent pipe flow data show consistent turbulence intensities, and mean axial velocity profiles agree with pitot-static probe data. Recent PDV data for the flow over an NACA 0012 airfoil show mean velocities that agree with hot wire data to within $\pm$ 2-3 m/sec, while the RMS data agree to within $\pm$ 0.5-0.7 m/sec. Also, recent PDV data in a turbulent circular jet show similar agreement with hot wire data. However, offset errors are observed in the mean velocity data which are on the order of 2-5 m/sec.

Accuracy of the DGV system has also been investigated. For rotating wheel results, RMS noise levels are $\pm$1 m/sec out of 58 m/sec, while total velocity range errors are $\pm$1-2 m/sec. Fully turbulent pipe and jet flow mean velocity measurements agree with pitot-static probe traverse data. The zero velocity offset error has been corrected to within about 2-5 m/sec using a reference tab to record zero velocity signals. DGV RMS data do not agree with hot wire measurements, as expected.

Introduction
Several different non-intrusive whole field velocimetry techniques are currently under development which provide velocity data in a plane, which can thus reduce the time required to map out a complex flow field. This project is exploring the accuracy of DGV, a nonintrusive, planar imaging, Doppler-based velocimetry technique, as well as the accuracy of related PDV. Both of these techniques use an iodine vapor cell to determine the Doppler shift, and hence the velocity, of small seed particles in a flow field, as these particles pass through a two-dimensional sheet of laser light. The same portion of the light sheet is viewed through a beam splitter, either by a pair of video cameras (for DGV), or a pair of photodetectors (for PDV), with the iodine cell placed in the optical path of one of the cameras or photodetectors. Laser wavelength and cell absorption band are matched such that flow velocities of interest yield Doppler shifted frequencies in the linear portion of the absorption band of the cell. As a result, the ratio of the light intensities seen by the two detectors at a point in the flow yields a signal that is proportional to the particle velocity.

A two-channel non-scanned point PDV system has been developed (Kuhlman, et al., 1997), along with a two-channel planar imaging DGV system (Naylor and Kuhlman, 1998, 1999). The accuracy limits of both systems are being systematically explored, through a series of measurements in relatively simple, unheated flows such as fully-developed turbulent pipe

flow, a circular jet, and the flow over an airfoil. A rotating wheel is also being used as a velocity standard. While current DGV systems lack the accuracy or resolution of conventional LV or PIV (accuracy of mean velocity typically on the order of 5% of full scale, versus 1% for LV), DGV has proven in a short time to be a very flexible whole-field velocimetry technique.

Apparatus and Procedure

The present point PDV system closely follows the basic DGV system that was originally developed by Meyers et al. (1991), except that photodiodes have been used, along with front lenses and pinholes, to collect scattered light from a single point in a seeded flow. Kuhlman, et al. (1997) and James (1997) have described the PDV system in detail. A reference iodine cell has been used to compensate for laser frequency drift. Calibration of the iodine cells has been accomplished using a continuous scan of the mode structure of the cw Argon ion laser, by mechanically altering the tilt of the etalon through about 10-20 mode hops (James, 1997).

DGV system hardware has been described in Naylor and Kuhlman (1998, 1999), and in more detail in Naylor (1998). Most of this hardware is similar to that used for the PDV system. Eight-bit Hitachi KP-M1 CCD cameras and a Matrox Genesis frame grabber have been used to capture images for the DGV system. All four cameras are read simultaneously using horizontal and vertical sync pulses from the Genesis board. Nikon 35-135mm, f3.5-4.5 zoom lenses have been used with the CCD cameras, because of their versatility in imaging different sized areas over a wide range of distances. Polarizing filters have been placed in front of the beam splitters to minimize effects due to polarization sensitivity of the beam splitters. Image processing software has been developed, as described by Naylor (1998), which closely follows the image processing methods developed at NASA Langley by Meyers (1992, 1996). Flow seeding for DGV and PDV measurements is provided by a commercial fog machine, which feeds a large plenum to damp out pulsations in smoke output.

Most recent results include 2-component PDV data for the flow over a nominally 11.8 inch chord NACA 0012 airfoil model at zero degrees angle of attack, as described in Kuhlman and Webb (1999). The airfoil has been mounted at the exit of a 2.25x3.25 inch flow channel, fed by a blower capable of exit velocities of 40-45 m/sec. The present results have been obtained at an exit velocity of 21 m/sec, due to limitations on removing the smoke-seeded flow from the laboratory. Several series of 2-component PDV data and single component hot wire data have been obtained at eleven chordwise stations along the airfoil, from x/c=0.13 to x/c=0.98. All data have been obtained at a fixed z location of 0.5" above the airfoil shoulder (z/c=0.04). At each location data have been obtained at a sampling rate of 10 kHz, in 1k, 4k, or 16k blocks. The present results are for 1k data records, corresponding to 0.1 sec time records. This has been done to minimize the time required to obtain a PDV data set, in order to minimize time for iodine cell stem temperatures to drift. Such drift of the temperatures of the iodine cell stems has been identified as the key source of the apparently randomly varying offset errors in mean velocity results. From these 1k time series, mean and RMS velocities, as well as time autocorrelation coefficients and power spectra, have been computed for both the PDV and hot wire data, to assess the accuracy of the PDV system for turbulence measurements. Also, recently PDV data has been obtained for flow from a 1" diameter circular jet nozzle having a 16:1 area ratio contraction and capable of velocities up to 100 m/sec.

Results

Early PDV data repeatability, as documented in the thesis by Ramanath (1997), was poor. However, improved cell calibration procedures (James, 1997) have significantly increased PDV and DGV system accuracy. Both single and 2-component PDV data measured on a rotating wheel have been presented by James (1997), and by Kuhlman, et al. (1997). Total wheel velocity range for these measurements was 57 m/sec, so the observed the velocity error magnitudes of approximately ± 0.6-1.2 m/sec, correspond to 1-2 % errors, which is quite good. Also, the standard deviations of the actual PDV wheel velocity data points from the least squares linear curve fits have been found to be 0.5-0.7 %.

Two-component PDV data obtained from a traverse across the exit of the fully-developed pipe flow at a nominal Reynolds number of 76,000, have been previously presented by Kuhlman (1998). The axial mean velocities agree well with results from a pitot-static probe survey, but circumferential mean velocities display an offset error on the order of 2-5 m/sec. Turbulent velocity levels agree with hot wire data of Laufer (1954). Significant difficulties occur near the pipe walls, both due to reduced signal-to-noise levels due to less smoke, and to secondary scattering and reflections of the scattered light off of the pipe walls. However, the greatest difficulty was in obtaining accurate, reliable zero velocity values.

Comparisons of the recent PDV data and hot wire data are shown in Figs. 1-2, taken from Kuhlman and Webb (1999). Fig. 1 compares the mean velocity results for 4 PDV data sets with 5 hot wire data sets, each taken over the NACA 0012 airfoil model at zero degrees angle of attack. PDV streamwise mean velocities show a total variation at fixed x/c of about 5-6 m/sec for the 4 runs; this variability is consistent with earlier PDV data (Kuhlman, 1998) and DGV data (Naylor and Kuhlman, 1999). These mean velocities agree with hot wire data to within ± 2-3 m/sec. PDV RMS velocities (Fig. 2) agree with corresponding hot wire data to within about 0.5 m/sec, and display a similar level of repeatability from run to run. The PDV correlation coefficients agree well with hot wire correlation coefficients; both autocorrelations decay in less than 10 msec (Kuhlman and Webb, 1999). However, PDV power spectra show a larger amount of noise than hot wire data at frequencies above 500-1000 Hz (Kuhlman and Webb, 1999).

Recent 2-component PDV data in a circular jet are shown in Figs. 3-6. Mean and RMS data at the jet exit (x/D=0.25, where D=exit diameter) are shown in Figs. 3-4, while similar results are shown in Figs. 5-6 for x/D=6. Mean streamwise velocities at the exit (Fig. 3) again show about 5 m/sec of offset from preliminary pitot-static probe results on the centerline at the exit. Measured PDV mean circumferential velocity varies by about 2 m/sec from the correct value of zero. RMS velocities are between 1 and 2 m/sec on the centerline (Fig. 4). At x/D=6, the PDV mean streamwise velocity profile (Fig. 5) appears Gaussian in shape, as expected. Both the mean streamwise and circumferential velocities display offset errors of 4-5 m/sec from the correct values at x/D=6. RMS velocities have risen to 4-10 m/sec (Fig. 6). It is planned that detailed comparisons will be made between PDV and hot wire data for this turbulent circular jet flow field. Also, the same jet flow facility has been modified to allow PDV and hot wire data to be obtained for a swirling jet as well as for an annular jet, so that more complex flows may be studied.

Recent analysis of the offset error has indicated that it is largely due to the random, uncorrelated variations in iodine cell stem temperatures. This stem temperature variation has been observed to vary with a short term RMS of 0.1 degrees C (Naylor, 1998). This has been found to correspond to an error in Doppler shift frequency of 7 MHz, resulting in a mean velocity error of from 2 to 10 m/sec, depending on the geometry and viewing direction of the PDV system. This level of velocity error is consistent with the observed mean velocity offset.

Conclusions and Future Plans

Linearity of the two-component Point Doppler Velocimeter (PDV) system, based on rotating wheel velocity results, is ± 0.3 m/sec over a velocity range of 57 m/sec (ie, ± 0.5 % of full scale). Two-component PDV velocity data have been obtained for a fully-developed turbulent pipe flow at a Reynolds number of approximately 76,000. Turbulence intensity values agree with hot wire data, and mean axial velocity data agree with pitot-static probe results. However, mean velocity results show a random offset error which is as large as 2-5 m/sec. This mean velocity error has been found to be largely due to variations in the iodine cell stem temperatures of the measurement cell and reference cell. Similar agreement between the PDV data and hot wire data has recently been obtained for the flow over an NACA 0012 airfoil, and for turbulent circular jet flow.

Additional work is under way to upgrade the iodine cells and beam splitters used in the present system. Vapor-limited iodine cells have recently been delivered and are presently being installed, along with polarization-insensitive beam splitters. Then, both PDV and DGV data will be taken in the one-inch diameter circular jet facility, for comparison with pitot-static probe and hot wire data that is presently being obtained. It is expected that the new, vapor-limited cells will largely eliminate the mean velocity offset error that has been observed in all point and DGV data taken to date. Also, a DGV system using line scan cameras is under development, and a higher power, pulsed Nd:YAG laser will be added to the existing system. These efforts are aimed at both improving measurement accuracy and allowing turbulence measurements to be made with the improved DGV systems.

Personnel

Two MS students and one PhD student have completed their degrees while being supported on this project, as listed below.

Senthilkumar Ramanath	MSME, 1997.
Kelly James	MSME, 1997.
Steve Naylor	PhD, 1998.

In addition, one MS student (Pat Collins) and one PhD student (Dawn Wu) are being supported on the new project funding.

Transitions

The new iodine cell calibration procedure developed as part of this work has been evaluated by the NASA Langley research team for use with their Argon ion laser DGV system.

References

James, K., "Determination of the Accuracy of a Two-Component Point Doppler Velocimetry System," MS Thesis, West Virginia University, MAE Department, 1997.

Kuhlman, J. M., Naylor, S., James, K., and Ramanath, S., "Accuracy Study of a 2 –

Component Point Doppler Velocimeter (PDV)," paper AIAA-97-1916, presented at AIAA 28th Fluid Dynamics Conference, June 29-July 2, 1997, Snowmass, CO.

Kuhlman, J., "Development of Doppler Global Velocimeter," Final Report for AFOSR/DEPSCoR Grant F49620-94-1-0434, May, 1998.

Kuhlman, J. M. and Webb, D. L., "2-Component Point Doppler Velocimetry (PDV) Measurements of Turbulent Flow over an Airfoil," paper AAIAA-99-3517, presented at AIAA 30th Fluid Dynamics Conference, June 28-July 1, 1999, Norfolk, VA.

Laufer, J., "The Structure of Turbulence in Fully Developed Pipe Flow," NACA TR 1174, 1954.

Meyers, J. F., Lee, J. W., and Cavone, A. A., "Signal Processing Schemes for Doppler Global Velocimetry," 14th International Congress on Instrumentation in Aerospace Simulation Facilities, Oct. 27-31, 1991, Rockville, MD.

Meyers, J. F., "Doppler Global Velocimetry, The Next Generation?," paper AIAA-92-3897, presented at AIAA 17th Ground Testing Conference, July 6-8, 1992, Nashville TN.

Meyers, J. F., "Evolution of Doppler Global Velocimetry Data Processing," 8th Int'l. Symp. On Applications of Laser Techniques to Fluid Mechanics, July 8-11, 1996, Lisbon, Portugal.

Naylor, S. and Kuhlman, J., "Accuracy Studies of a Two-Component Doppler Global Velocimeter (DGV)," paper AIAA-98-0508, AIAA 36th Aerospace Sciences Meeting, Jan. 12-15, 1998, Reno, NV.

Naylor, S. and Kuhlman, J., "Results for a Two-Component Doppler Global Velocimeter (DGV)," paper AIAA-99-0268, AIAA 37th Aerospace Sciences Meeting, Jan. 11-14, 1999, Reno, NV.

Naylor, S., "Development and Accuracy Determination of a Two-Component Doppler Global Velocimeter (DGV)," PhD Dissertation, West Virginia University, MAE Department, 1998.

Ramanath, S., "Development of a Point Doppler Global Velocimeter (DGV)," MS Thesis, West Virginia University, MAE Department, 1997.
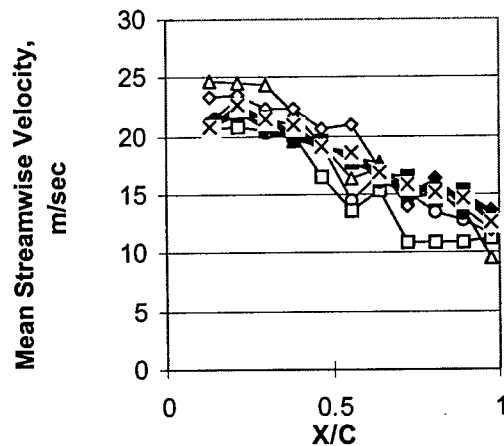
Fig. 1 Comparison of PDV and hot wire streamwise mean velocity over airfoil (open symbols-PDV, filled symbols-HW)
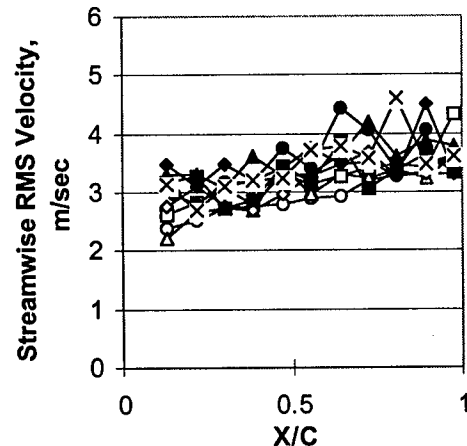
Fig. 2 Comparison of PDV and hot wire streamwise RMS velocity over airfoil (open symbols-PDV, filled symbols-HW)
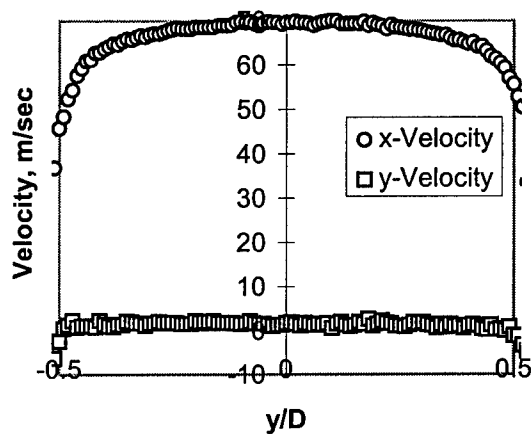
Fig. 3   2-Component PDV mean
velocity data in circular jet - X/D = 0.25
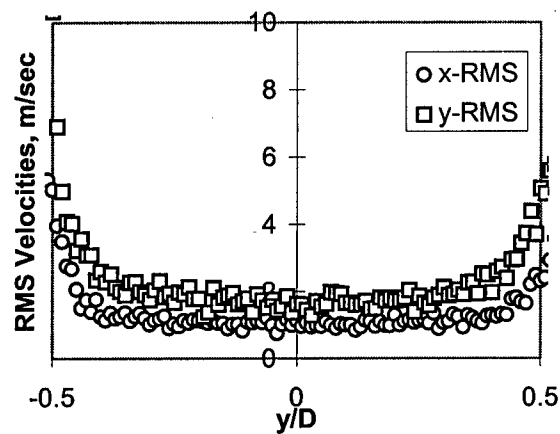
Fig. 4   2-Component PDV RMS
velocity data in circular jet - X/D = 0.25
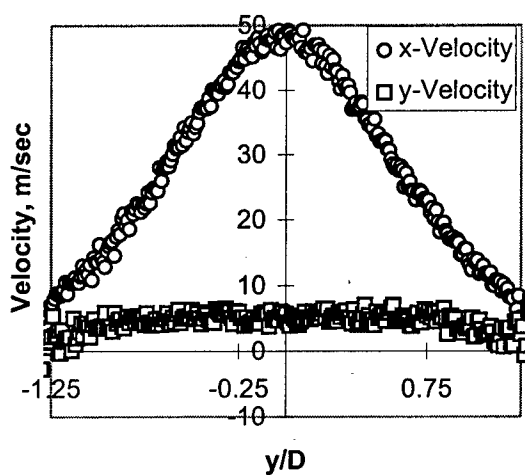
Fig. 5   2-Component PDV mean
velocity data in circular jet - X/D = 6
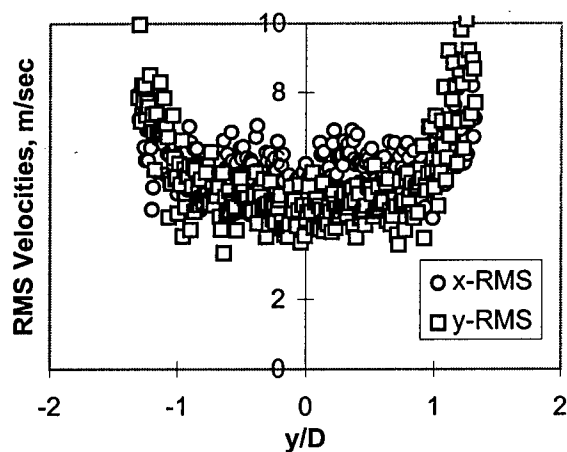
Fig. 6   2-Component PDV RMS
velocity data in circular jet - X/D = 6

LARGE EDDY SIMULATION FOR HEAT TRANSFER PREDICTION UNDER FREE-STREAM TURBULENCE

Sanjiva K. Lele

Dept. of Mechanical Engineering and Dept. of Aeronautics and Astronautics
Stanford University, Stanford, CA 94305-4035.

Summary

The primary objective of this research is to develop large eddy simulations (LES) as a tool for heat transfer prediction over a turbine blade immersed in a hot stream containing free-stream turbulence (FST). The research consists of developing and validating the LES methodology on a series of test problems, before it can be applied to the turbine blade problem. These test problems are chosen to allow a detailed validation of the elements critical to heat transfer prediction on a turbine blade. These are (in order of increasing complexity/realism) :

(1) Simulation of realistic free-stream turbulence with intensity and length scale appropriate for turbine blade heat-transfer and its interaction with blade leading edge region

(2) Simulation of the disturbed turbulent boundary layers over an idealized blade surface in presence of free-stream turbulence

(3) Simulation of boundary layer heat-transfer under free-stream turbulence in presence of film-cooling jets on an idealized blade surface

(4) Simulation of realistic turbine blade heat-transfer under free-stream turbulence.

Research under the present grant is focussed on items (1) and (2) while items (3) and (4) are subjects for future work.

Progress

A new LES code for turbine blade heat-transfer under free-stream turbulence was developed. The work completed in FY 99 has focussed on numerical algorithms, boundary conditions and the validation of the LES tool. One graduate student (Andy Xiong) is carrying out his dissertation research under this project. A summary of the key research results will be given first and is followed by a discussion of our future plans.

LES code development

A computer code recently developed for a different project (Collis and Lele, 1997) which combines high-order finite-difference schemes on curvilinear coordinates with implicit time advancement was adapted to perform the LES calculations of heat transfer under free-stream turbulence. This extension of the original code required progress in three major areas: grid-generation, boundary conditions, and implementation of solution algorithm for three-dimensional flows including the subgrid-scale models for LES.

The grid/mesh requirements for conducting LES studies of turbine-blade heat-transfer are very different from those for needed with RANS approach. The need to directly respresent the large scale energy-containing eddies of free-stream turbulence limits the grid stretching which can be used away from the body. In previous year's progress report this and other grid generation issues and appropriate boundary conditions which model the experimental wind-tunnel situation while permitting the imposition of desired inflow were detailed. Some further refinements to the boundary conditions were made. These allow smooth solutions to be obtained near the confining walls of the 'wind tunnel' without the need for artificial dissipation. This improvement also helps in accurately maintaining the free-stream turbulence. Laminar flows over idealized blade surfaces matching those used in the experiments by Van Fossen et. al. (1995) were computed at different Reynolds numbers, and temperature ratios. Figure 1 shows a schematic of geometry, the grid used (not all points shown), and the non-dimensional parameters. The converged laminar solutions obtained from the Navier-Stokes solver were compared in detail with the high-Reynolds number laminar boundary layer theory. The boundary layer analytical solutions accounted for the density variations and compressibility via the use of Stewartson tranformation (Reshotko and Beckwith, 1958). Figure-2 shows an example of the laminar flow obtained at a Reynolds number $Re \equiv \rho_\infty U_\infty R/\mu_\infty = 10^5$ and $T_w/T_{0,\infty} = 0.5$ and $M_\infty = 0.18$. Note the reference length scale is taken to be the leading-edge radius of curvature, R. Very good agreement with the theoretical boundary layer profiles is obtained. Most heat-transfer experiments on the effects of free-stream turbulence have been carried out at low-Mach number, and the range of Reynolds number Re is 10^5 to 10^6. Turbine blade flows, however, are in low-transonic range and their Reynolds number (based on chord) varies from 10^5 to 10^7 (depending on the turbine stage and altitude). The current code is expected to provide accurate solutions over the low-transonic range, but before such flows are computed it is necessary to validate the LES capability in the low-Mach number range for which detailed experimental data is available. This assessment is carried out in two steps as discussed below.

Disturbed Boundary Layers with organized disturbances

An efficient solution algorithm for LES with free-stream turbulence was developed and implemented. One important consideration in the choice of algorithms is the significant region of low-speed subsonic flow near the leading-edge region of a turbine blade. This region is also the most critical for heat-transfer predictions. The boundary layers are expected to be quite thin in this region, and to adequately resolve them requires a sufficiently fine mesh close to the body. These considerations imply that an explicit solution algorithm is inappropriate and algorithms with a single implicit direction would also be insufficient. We developed a three-dimensional extension of the implicit algorithm of Collis & Lele (1997) to overcome these difficulties.

We use Fourier spectral method in the spanwise direction. Our algorithm is based on decomposing the flow variables into a spanwise average and the deviation from this average. All transport terms involving the spanwise-average are treated implicitly and the rest are treated explicitly as source terms. These nonlinear source terms are evaluated in physical space and are dealiased using the 3/2-rule, while the time advancement is carried out in wave space. This allows the 3-D code to have the efficiency of psuedo-spectral

method. The implicit treatment allows the time step to be based on the physical unsteady behavior and not limited by the acoustic-wave based CFL restriction.

This new LES code has been tested to assess the impact of inflow disturbances on the stagnation point flow over the test-geometry. For this purpose simulations with organized inlet disturbances were carried out. Spanwise variations of 1-5% to the free-stream velocity were prescribed at the inflow boundary. The spanwise scale of these variations L was chosen to be 2 times the blade-nose-radius and the Reynolds number $Re = 10^4$, which approximates gives $\delta/R = 10^{-2}$ and thus $L/\delta \approx 200$. The large-scale free-stream disturbances are of specific interest in heat-transfer studies. Figures 3-5 shows an example of results obtained with organized inlet disturbance. Note that these are disturbed laminar flows and no subgrid model is used. Figure 3 shows a composite visualization of the flow. Contours of streamwise velocity are combined with a plot of the contours of streamwise vorticity in this figure. Also shown is are contours of spanwise velocity. Strong regions of counterrotating streamwise vortices form in the stagnation region. They are attributed to the vortex-stretching mechanism studied by Sutera (1965). In regions of common updraft the heat-transfer to the surface is reduced below it laminar value. More critical are the regions located under the common downdraft which thins out the boundary layer and causes intense heat-transfer. Figure 4 shows the variation of the two components of the velocity disturbance along the 'stagnation streamline'. The irrotational distortion of the inlet disturbance and the boundary-layer modification near the body are readily observed. Figure 5 shows the detail of the boundary-layer structure of the disturbances. The behavior observed is consistent with 'rapid-distortion' theory by Hunt (1973).

Specification of Free-stream Turbulence

In heat-transfer experiments controlled free-stream turbulence is often introduced by using a turbulence-generating grid. With proper design the generated turbulence is nearly-isotropic and homogeneous. Further downstream this turbulence interacts with the test-surface. This controlled experiment provides a good benchmark to validate the simulations. However, it is necessary to establish that the turbulence being fed into the computational domain is physically realistic and the inflow-algorithm does not deteriorate this property. Inflow turbulence was provided using a precomputed LES of isotropic turbulence and small amplitude jitter was added to ensure that inflow data was not time-periodic. Significant testing of the LES method was also carried out on the isotropic decaying turbulence. In our LES the subgrid terms are evaluated using the standard dynamic procedure (e.g. Moin et. al. 1991), however since the numerical scheme used is different detailed validation was necessary. Test-filters for the dynamic procedure were based on box-filter using Simpson's rule. As a first step the LES results were compared to low-Reynolds number DNS data and excellent agreement was found. Further comparisons were then made with higher Reynolds number experiments of Comte-Bellot and Corrsin at Taylor microscale Reynolds number $Re_\lambda = 65$. Figure-6 shows a comparison of the computed turbulent kinetic energy with the experimental data. Also shown is a computation without using the subgrid model. The present calculations were carried out using a mean-flow Mach number of 0.1 but the actual Mach number in the experiments is much smaller. Figure-7 shows a comparison of density fluctuations obtained in LES with the DNS data of Spyropoulos and Blaisdell (1996). Once again a good comparison is obtained. Calculations have also been done at higher Reynolds

numbers and higher Mach number which increases the importance of modeling the subgrid kinetic energy in calculating the pressure. Previous work has identified some numerical difficulties which were also encountered with the current LES implementation. We plan to use an alternate LES formulation (not density-weighted) which has recently been used by Bendiks and Lele (1999) for LES of compressible jets to overcome this difficulty.

LES of Disturbed Boundary Layers under Free-stream Turbulence

The LES code is currently being used to simulate boundary layer heat-transfer under free-stream turbulence on idealized blade geometry (Von Fossen et. al. 1995). Preliminary results from these will be reported at the AFOSR Contractors Meeting. Detailed comparisons with experiments and a study of the physical mechanisms responsible for the heat-transfer enhancement will be undertaken in the immediate future. The code will also be ported to run on DOD's parallel machines. A significant part of the data management to carry out this parallel implementation already exists in the current code.

Acknowledgement/Disclaimer

REFERENCES

Van Fossen, G. J., Simoneau, R. J. and Ching, C. Y. (1995) Influence of turbulence parameters, Reynolds number and body shape on stagnation region heat-transfer, *J. Heat Transfer*, v. 117, pp. 597-603.

Sutera, S. P. (1965) Vorticity Amplification in Stagnation-point Flow and its Effect on Heat Transfer, *J. Fluid Mech.*, v. 21, pp. 513-534.

Collis, S. S. and Lele, S. K. (1997) A Computational investigation of Receptivity in High-Speed Flow Near a Swept Leading-Edge, Report No. TF-71, Flow Physics and Computation Division, Department of Mech. Eng., Stanford Univ.

Moin, P., K. Squires, W. Cabot, and S. Lee (1991) A dynamics subgrid-scale model for compressible turbulence and scaler transport, *Phys. Fluids A*, v. 11, pp. 2746-57.

Boersma, B. J. and Lele, S. K. (1999) Large Eddy Simulation of a Mach 0.9 Jet, *AIAA/CEAS Paper* AIAA-99-1874, AIAA/CEAS Aeroacoustics Conference, Seattle.

Reshotko, E. and Beckwith, I. E. (1958) Compressible laminar boundary layer over a yawed infinite cylinder with heat transfer and arbitrary Prandtl number, NACA Tech. Rep. 1379.

Sypropoulos, E. T. and Blaisdell, G. A. (1996) *AIAA J.* Vol. 34, 990-998.

Hunt, J. C. R. (1973) A Theory of turbulent flow round two-dimensional bluff bodies. *J. Fluid Mech.* Vol. 61, 625-706.
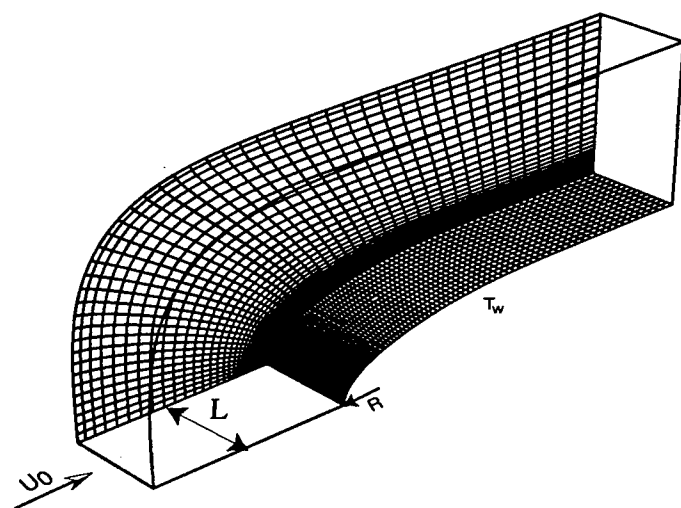
Fig.1. Computaional grid and the non-dimensional paramenters,
every other grid line is shown here for clarity.
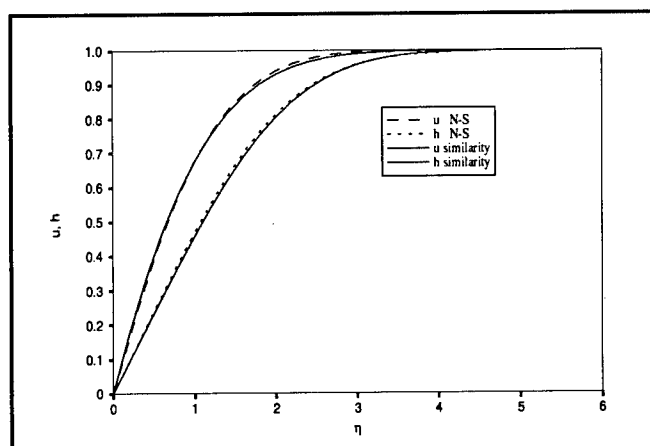
Fig.2. Velocity and enthalpy profiles at leading edge compared with
analytical self-similiar solution (Reshotko and Beckwith, 1958)
Flow conditions are Re = 100,000, Ma=0.18, Tw/T0 = 0.5, Pr =0.7.
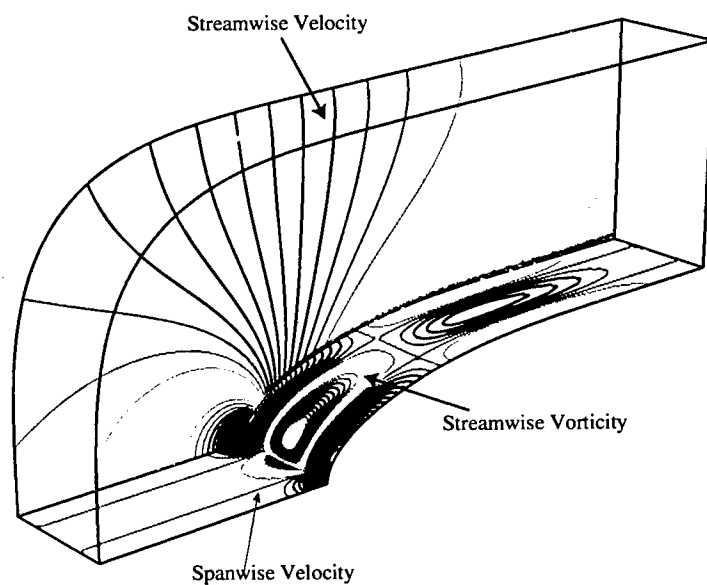
Fig.3 Composite view of flow field due to organized disturbances. Re=10,000
Ma=0.18. The amplitude of inflow distrubance is 1% of the free stream velocity.
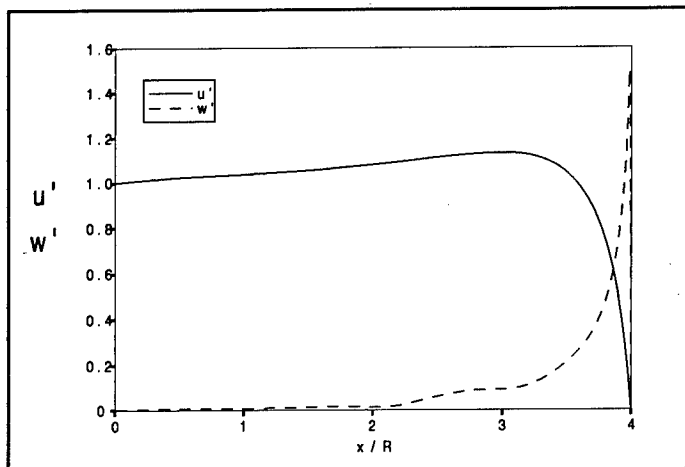
Fig.4 The evolution of velocity disturbance along the stagnation streamline showing the irrotational distortion. The amplitude has been normalized by the inlet disturbance value.
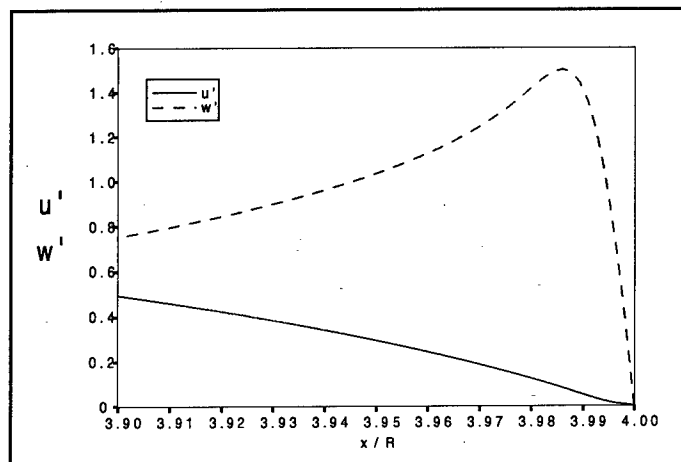
Fig.5 Detailed disturbance evolution close to the leading edge and inside the boundary layer.
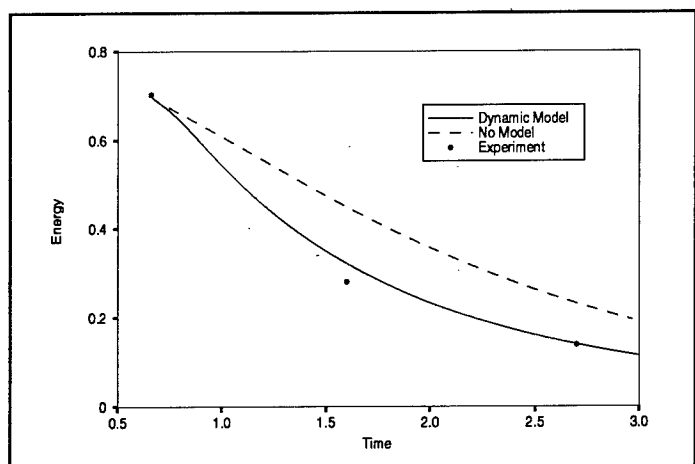
Fig.6 Turbulent kinetic energy of decaying homogeneous isotropic turbulence. Dynamic model is used for LES and the gird size is 32^3. The time scale has been normalized using Comte-Bellot and Corrsin's experimental data.
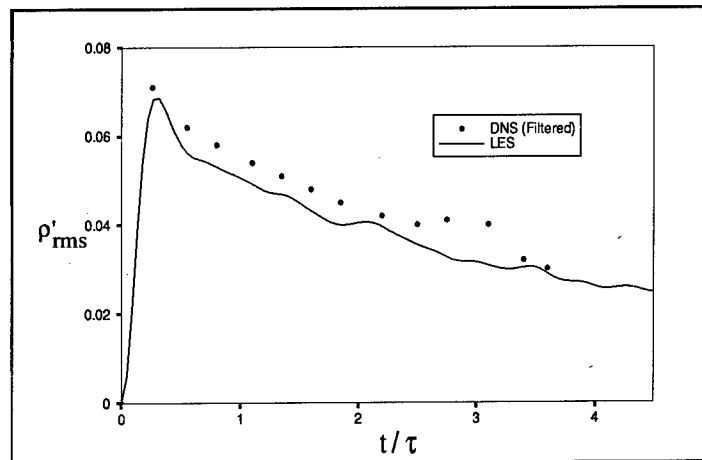
Fig.7 Time evolution of rms density fluctuation. Time has been non-dimensionalized by eddy turn over time. Mt=0.4, $Re_\lambda = 55$. The filtered DNS data is taken from Sypropoulos and Blaisdell. 1996.

NUMERICAL SIMULATION OF TURBULENT HIGH SPEED JETS

F49620-98-1-0035
Progress report on work conducted under AASERT grant
during 7/1/98 through 6/30/99

Sanjiva K. Lele
Department of Mechanical Engineering
and
Department of Aeronautics and Astronautics
Stanford University, Stanford, California 94305-4035

Abstract

High speed turbulent jets occur in many technological applications, including propulsion systems for civilian and military airplanes. The unsteady effects in these flows can influence such diverse features as thrust efficiency, infrared signature, and community noise. The aim of the present research is to develop quantitative predictions of high speed jet noise and methods for its suppression. Supersonic jet screech, a type of jet noise, has been chosen as the focus of this research because of its high emission levels and narrow frequency band. Jet screech is also a primary source of acoustic fatigue in aft structures of fighter aircraft. To gain a better understanding of screech, two model problems are being examined through direct numerical simulation and theoretical analysis: 1) the interaction of shear layer vortices with an oblique shock (screech noise source); and 2) the acoustic receptivity of shear layer instability waves to incident acoustic disturbances at a trailing edge (screech feedback mechanism).

Progress

Supersonic jet screech has been known to be governed fundamentally by a feedback cycle since the pioneering work of Powell [1]. The elements of this feedback cycle include: 1) the amplification of instability waves in the jet, 2) the interaction of vortical disturbances with the shock-cell structure in the jet, 3) the back propagation of the acoustic disturbance to the nozzle lip, and 4) the conversion of acoustic disturbances into instability waves at the nozzle lip, *viz.* receptivity which ultimately closes the feedback loop. In the screech cycle, noise is generated in the second element. To understand how the amplitude of the shear layer disturbance and shock-strength influence the amplitude of the sound field, a detailed study of this screech-tone generation is being undertaken through the use of a simplified model. This model, as depicted in Figure 1, involves the two-dimensional interaction of shear-layer vortices with an isolated region of the jet shock-cell structure.

The simplified model is studied with three progressively idealized approaches. The first is direct numerical simulation (DNS) by solution of the Navier Stokes equations. The second approach is solution of the Euler equations linearized about an unsteady base flow. The third is geometric acoustics with an unsteady base flow.

141
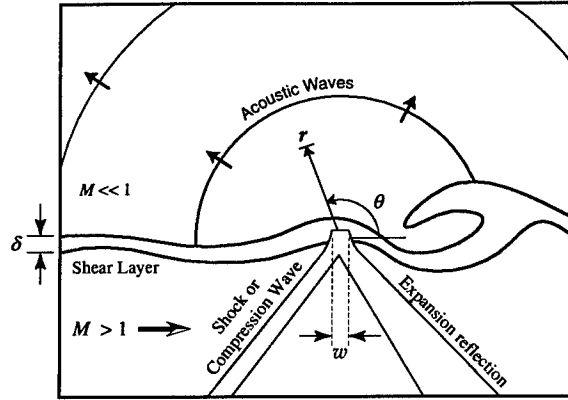
Figure 1: Schematic of the shock-vortex interaction computation.

The results of the DNS cases have been reported in previous publications [2], [3]. They indicate that when the shear layer instability waves are large, the sound generation results from large fluctuations in the position of the incident shock, with the compression front of the acoustic wave emerging between the instability wave vortices. Similar behavior was reproduced for low amplitude, oblique incident waves. This suggests that the sound generation process can be regarded as the scattering of an incident oblique stationary wave disturbance by the unsteady motion of the mixing layer. The sound field was found to scale with the strength of the incident shock.

The linearized Euler equation approach to studying the model problem was devised to take advantage of the scattering property of the sound source. In this approach, the problem is decomposed into a base flow and a perturbation field. The unsteady shear layer makes up the base flow and is therefore prescribed, usually with a previously obtained DNS solution. The "shock" is imposed as an incident disturbance; it and the resultant scattered sound make up the perturbed, or solution, field. The numerical solution method for these equations are essentially identical to the techniques used for the direct numerical simulations, including boundary conditions. The elimination of viscous terms and the reduction of boundary zones result in a significant computational savings over the the direct numerical simulations. With the shear layer prescribed and already at periodic steady-state, solutions are obtained in fewer flow-through periods, and the acoustic field is obtained directly, without the postprocessing required in the DNS.

The linearized Euler simulations yield the same acoustic source mechanism as observed in the DNS. The visualizations in Figures 2a and 2b show the interaction for the DNS case and the linearized Euler case, respectively. The base flow of the linearized Euler case is obtained by DNS under the same forcing conditions. The acoustic amplitudes are found to match. Further idealizations of the interaction process consist of replacing the incident compression wave, which closely resembles a portion of the jet shock cell structure, with an "N-wave". This N-wave imparts no net deflection on the shear layer because it consists of both positive and negative pressure disturbances. With the same unsteady base flow, the same source mechanism
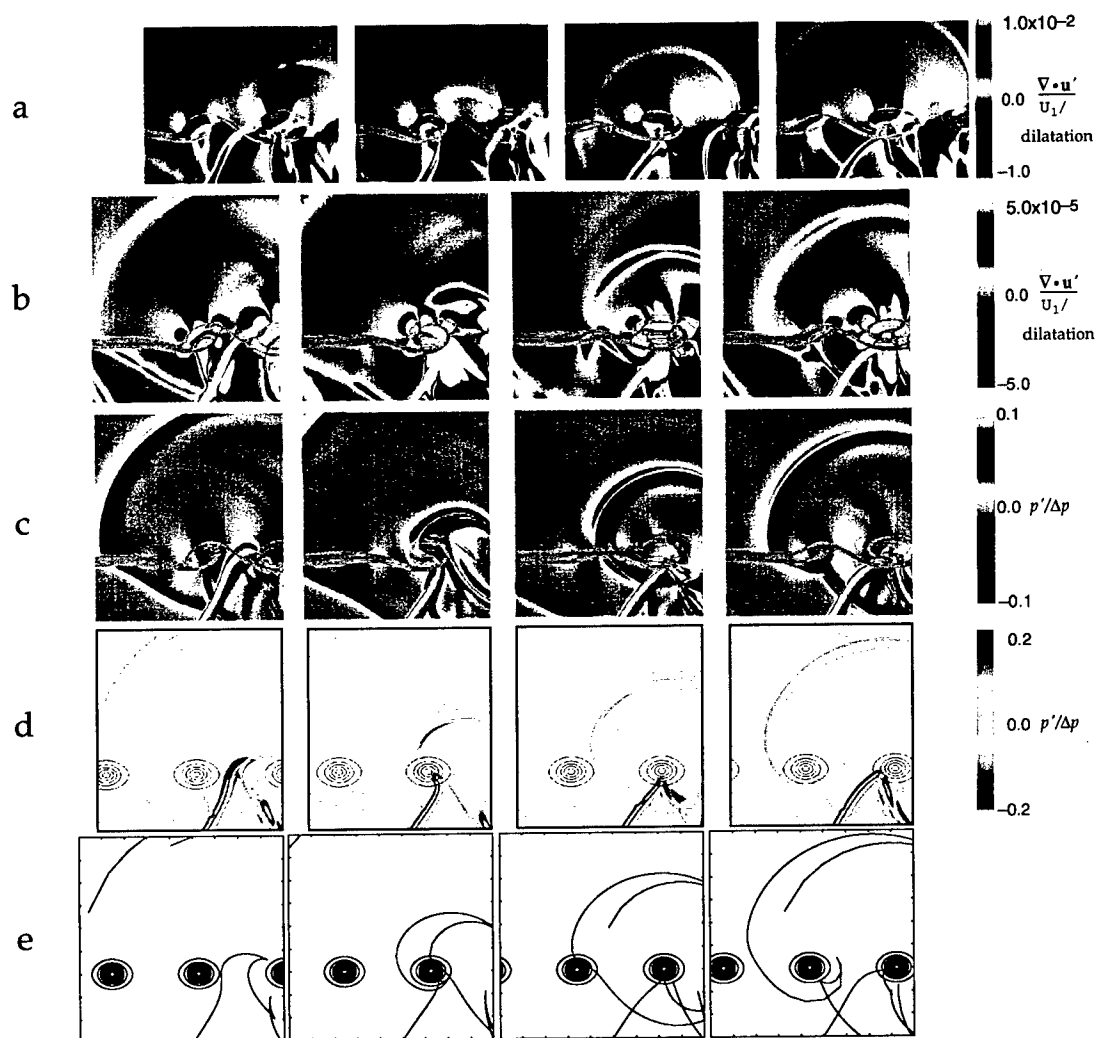
Figure 2: Visualizations of screech sound generation through interaction of oblique shock and unsteady shear layer. a) DNS with incident compression wave b) linearized Euler with DNS base flow and incident compression wave; c) linearized Euler with 'N-wave'; d) linearized Euler with Stuart vortex field for base flow; e) wave fronts as computed with geometrical acoustics and Stuart vortex field.

is captured, indicating that the basic mechanism is insensitive to the form of the incident wave (Figure 2c). The N-wave profile is radiated to the far field.

The next idealization is to replace the base flow with an analytic description of a mixing layer. We use the velocity field of the Stuart vortex mixing layer, a solution to the incompressible, inviscid equations. By including only velocity and ignoring thermodynamic variations, we show that the sound generation mechanism can be explained fundamentally in terms of the velocity field (Figure 2d). The strength of the acoustic field when interacting with an incident oblique disturbance with a Gaussian pressure distribution is shown to increase linearly with vortex amplitude A at low A, increase exponentially with A for moderate A, and saturate for high A (Figures 3 and 4). Similar trends are noted for the DNS base flow, although less convincingly.

The visualizations of the interaction and sound generation suggest that the mechanism involves refraction of the shock through an unsteady shear layer. In geometrical acoustics, the incident shock is modeled as a thin plane wave, oriented at the Mach angle in the supersonic stream so that it remains stationary in the steady case. Wave fronts based on acoustic "rays", obtained by integrating the characteristics from the Eikonal equation, are shown for a Stuart vortex base flow in Figure 2e. These and additional results indicate that the unsteadiness associated with the convection of the vortices is critical for obtaining the conditions by which the incident waves will refract across the shear layer.

Conclusions and Future Work

The investigation of the interaction of a shear layer instability wave and an oblique shock has yielded a better understanding of the mechanism governing screech generation using a variety of methods. The source mechanism for high amplitude instability waves is best characterized as the unsteady refraction of the incident shock such that it escapes the jet. The refraction process manifests itself in terms of a shock which undergoes large fluctuations in position and strength as instability waves pass over, with the release of the acoustic pulse occurring between the vortices. This basic behavior was reproduced in Navier-Stokes simulations, Euler simulations linearized about a DNS shear layer, Euler simulations linearized about an idealized shear layer, and in geometrical acoustics. Finally we show that the variation of acoustic amplitude with instability wave amplitude (in the idealized shear layer case) is made up of three distinct regions (in order of increasing instability wave amplitude): linear, exponential, and saturated. These results can be incorporated into new empirical models of screech sources.

We have now started numerical simulations of the receptivity element of the screech cycle. The appropriate model problem is that of acoustic disturbances incident on a two-dimensional shear layer shed from a thin rigid surface, or "nozzle lip." There are two competing theoretical treatments of the shear layer receptivity problem: the continuous excitation theory [4] and the trailing edge theory, see e.g. [5]. The trailing edge theory is based on a vortex sheet model of the shear layer. The singularity at the lip edge is eliminated by imposing a Kutta condition. In this way vorticity is shed from the nozzle lip and all the coupling between the incident
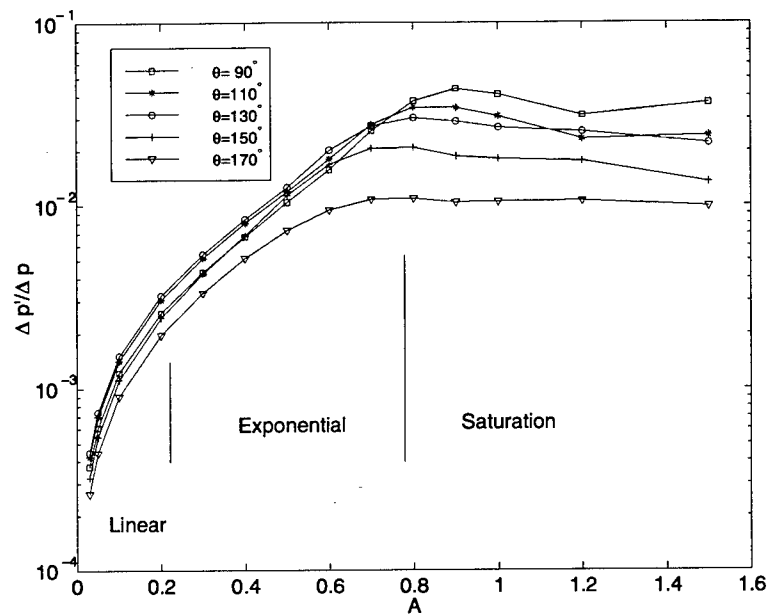
Figure 3: Pressure amplitude of acoustic field as normalized to amplitude of incident standing wave with Gaussian pressure distribution, as function of Stuart vortex field amplitude A. Exponential region is observed at moderated A, and saturation at higher A.
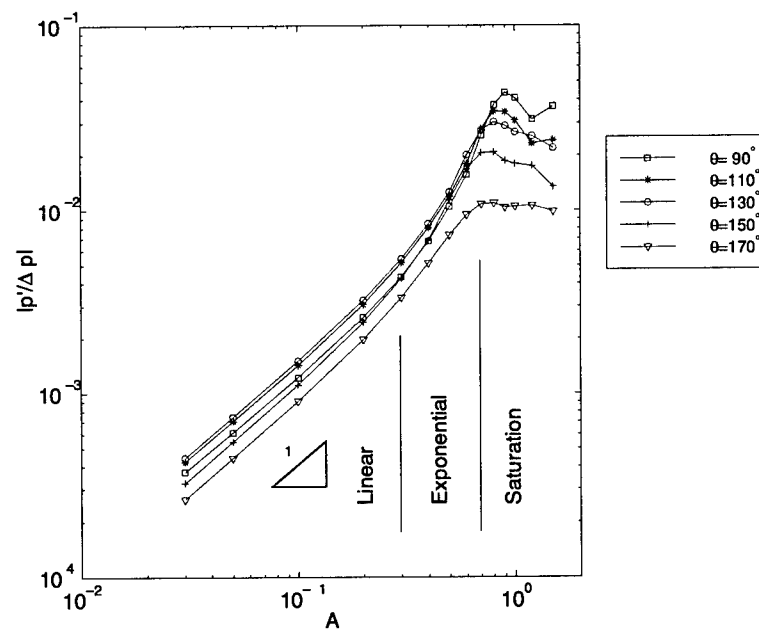
Figure 4: Pressure amplitude of acoustic field as normalized to amplitude of incident standing wave with Gaussian pressure distribution, as function of Stuart vortex field amplitude A. Linear region is observed at low A.

acoustic waves and the excited instability waves occurs right at the lip trailing edge. By contrast, the continous excitation theory predicts coupling to occur continuously over several instability wavelengths downstream of the lip trailing edge. Our initial investigations into the receptivity problem will involve direct numerical simulations using methods of the type used for studying the screech generation problem. Data from these simulations will reveal the flow region where receptivity occurs and will identify the basic mechanisms responsible for the type of receptivity found in screech. The influence of a jet co-flow on receptivity will also be examined.

Acknowledgment/Disclaimer

References

[1] A. Powell. On the Mechanism of Choked Jet Noise. *Proc. Phys. Soc. (London)*, 66(pt. 12, no. 408B):1039–1056, December 1 1953.

[2] T. A. Manning and S. K. Lele. Numerical Simulations of Shock Vortex Interactions in Supersonic Jet Screech. AIAA Paper 98-0282. Reno, Jan. 1998. 36th AIAA Aerospace Sciences Meeting and Exhibit.

[3] T. A. Manning and S. K. Lele. Numerical Simulations of Shock Vortex Interactions in Supersonic Jet Screech: an Update. In *Proceedings of FEDSM '98*, number FEDSM-5238, Washington, DC, June 1998. ASME Fluids Engineering Division Summer Meeting.

[4] C. K. W. Tam. Excitation of instability waves in a two-dimensional shear layer by sound. *Journal of Fluid Mechanics*, 89:357–371, 1978.

[5] E. J. Kerschen. Receptivity of shear layers to acoustic disturbances. AIAA Paper 96-2135. New Orleans, LA, June 17-20 1996. 1st AIAA Theoretical Fluid Mechanics Meeting.

INTERACTION BETWEEN NEAR-WALL TURBULENT FLOWS AND COMPLIANT SURFACES

AFOSR GRANT NUMBER F49620-99-1-0012

J. L. Lumley, D. Rempfer & P. N. Blossey
Sibley School of Aerospace and Mechanical Engineering
Cornell University, Ithaca, NY

Abstract

The general aim of this project is to get an improved understanding of the interaction between wall-generated turbulence and compliant surface coatings using analysis and direct numerical simulation in an integrated approach, with a view towards the reduction of turbulent sound production and turbulent drag.

As a reference for more refined models that we are working on now, we have developed a first simplified representation of the wall as a three-degree-of-freedom mass-spring system. Results from a study of the properties of that model are encouraging, and are presented below. A refined version of this model, that removes most of the limitations of the previous one, is currently under investigation. In parallel, we are also working on a computer code for the direct numerical simulation of the turbulence/compliant-wall interaction. That code will probably be functional this fall.

Due to space constraints, here we can only very briefly sketch the structure of our models, and highlight our most important results.

We have performed an analysis of the boundary conditions (for the case of small deformations of the wall as in the study of Choi *et al.* [2]) that suggests that for the purposes of our low-dimensional model, neglect of the nonlinear boundary terms is usually quite justifiable—the only relatively large nonlinear term appears in a term for the streamwise velocity component, which makes no contribution within the approximations of our model. Under these assumptions, the boundary conditions become:

$$\begin{aligned}
u_1 \quad + \quad U_{1,2}\xi_2 &= \dot{\xi}_1 \\
u_2 \quad\quad &= \dot{\xi}_2 \\
u_3 \quad\quad &= \dot{\xi}_3
\end{aligned} \tag{1}$$

Note that if the velocity field is expressed as a linear combination of eigenfunctions $u_i = \sum_{n,k} a_k^{(n)} \phi_{i_k}^{(n)} \exp(ikz)$, the boundary conditions above can be interpreted as a restriction on the combinations of $a_k^{(n)}$, ξ and $\dot{\xi}$ which are realizable.

In order to implement these boundary conditions in our model, we introduce a Fourier transform,

$$u_i(\boldsymbol{x}, t) = \sum_{k_1, k_3} \hat{u}_i(k_1, y, k_3, t) e^{(ik_1 x + ik_3 z)}, \tag{2}$$

where we can also write $\hat{u}$ using our POD modes ϕ_i,

$$\hat{u}_i = \sum_n a_n \phi_i^{(n)}. \tag{3}$$

Neglecting the nonlinear terms in the wall-normal boundary condition, we obtain

$$\sum_n a_n \phi_{2w}^{(n)} = \dot{\xi}_2 \quad \Rightarrow \quad a_1 \phi_{2w}^{(1)} \approx \dot{\xi}_2, \tag{4}$$

where it is assumed that the first eigenfunction is sufficient to represent the fluctuating velocity field[1].

The dynamical equations for the POD amplitudes (derived from the Navier-Stokes equation via Galerkin projection onto the set of POD modes) become

$$\dot{a}_m + \cdots = \frac{1}{\rho} \hat{p}_w \frac{\dot{\xi}_2}{a_1} + \cdots, \tag{5}$$

with the dots indicating the terms that are present in a model for a fixed wall, as in [1] (see eq. (14)). The pressure at the wall that is needed above can be obtained by using the instantaneous Navier Stokes equation,

$$\frac{\hat{p}_w}{\rho} = \frac{\nu a_1 \phi_{3,22w}^{(1)}}{ik_3}, \quad \Rightarrow \quad \dot{a}_m + \cdots = \frac{\nu \phi_{3,22w}^{(1)}}{ik_3} \dot{\xi}_2. \tag{6}$$

It may be a bit surprising at first to find that the lateral response of the surface apparently does not contribute. The reason for this is that—through our choice of considering only one POD mode—the boundary conditions at the wall are satisfied only in an approximate fashion. This is also the reason that it is only the wall normal motion that affects the equations: Once one has (implicitly) decided to approximate the effect of the wall motion on the boundary condition, and only include an effect through the pressure term, the influence of tangential motions is gone (since in the pressure integral for a domain with a horizontal boundary only, it is only the wall normal velocity at the boundaries that gives a contribution). Note that this approximation is quite consistent with the overall accuracy of this type of model. These limitations will be removed in the refined model described below.

Simplified Low-dimensional Model of Flow Over a Compliant Wall

We have investigated a model for a turbulent boundary layer interacting with a deformable wall, using the approximations described above. The flow is modeled via a pair of complex-valued ODEs with O(2) symmetry, and the dynamics of the wall is described using a simple damped mass-spring system. The complete set of dynamical equations consists of the equations for the flow,

$$\frac{da_1}{dt} = \mu_1 a_1 + c_{21} \bar{a}_1 a_2 + a_1(e_{11}|a_1|^2 + e_{12}|a_2|^2) + \frac{\nu \phi_{3,22w}^{(1)}}{ik_3} d_1, \tag{7}$$

$$\frac{da_2}{dt} = \mu_2 a_2 + c_{11} a_1^2 + a_2(e_{21}|a_1|^2 + e_{22}|a_2|^2), \tag{8}$$

---

[1]Note that the "$\approx$"-sign in that equation has to be taken seriously: At this level of truncation, it would in fact be inconsistent to require the boundary condition to be met exactly using just one POD mode.

and a second-order equation for the wall motion,

$$m\ddot{\hat{\xi}}_2 + c\dot{\hat{\xi}}_2 + k\hat{\xi}_2 = a_1 \frac{\nu \phi_{3,22w}^{(1)}}{ik_3}.$$

(9)

where $a_1 \frac{\nu \phi_{3,22w}^{(1)}}{ik_3} = 0.2996 a_1 \nu$ defines the pressure at the wall in Fourier space.

Figure 1 shows a comparison of the behavior of this model for the cases of a compliant and a fixed wall, respectively (in the case of the compliant wall, the last term in (7) is omitted, together with (9). One can see that for the small value of c (wall damping) that

(a) Fixed wall.

(b) Compliant wall. Behavior for small wall damping, $\alpha = 1.4$, $\nu = 1.5$, $\nu^* = 3$, $c = 1.0 \cdot 10^{-5}$, $k = 1$.
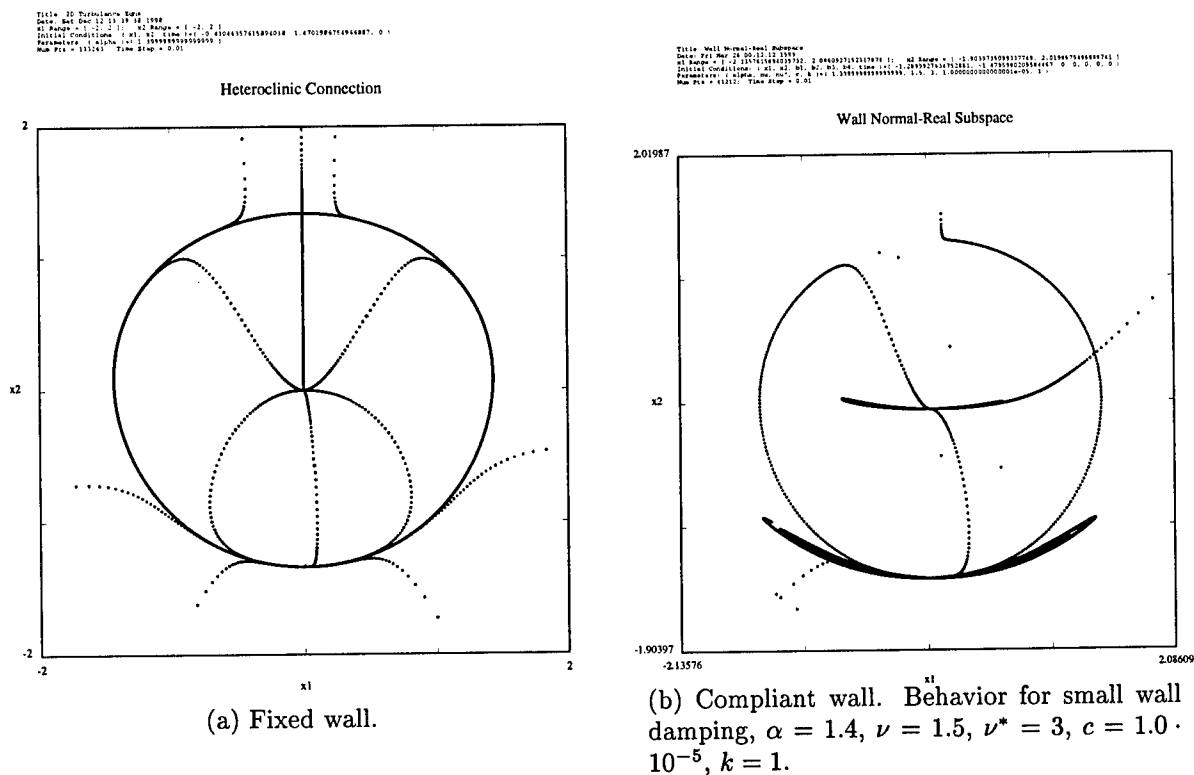
Figure 1: Phase portraits of low-dimensional models.

was chosen in the figure, the lower fixed point is no longer attracting in all directions (it is a saddle point). Solutions which are initially attracted to this point oscillate around it for an extended amount of time before diverging to infinity. This has the effect of reducing the bursting frequency and thus corresponds to a reduction of turbulent drag.

Five mode model with wall-normal compliance

To remove the limitations of the model described above, we have derived a refined model, that can take into account wall motions in all three coordinates, and that fully satisfies

the interface conditions between the moving wall and the flow. To do this, we model the compliant surface as a simple mass-spring-damper system driven by the fluid stress at the wall. In the streamwise and spanwise directions, the deformations of the wall are driven by the shear stress which is easily accessible in the models as a linear term in the model coefficients when the deformations are decomposed into Fourier space:

$$M_w \ddot{\hat{\xi}}_{1_k} + D_w \dot{\hat{\xi}}_{1_k} + K_w \hat{\xi}_{1_k} = \hat{\tau}_{1_k}|_{wall} = \sum_n a_k^{(n)} \phi_{1,2_k}^{(n)} \tag{10}$$

$$M_w \ddot{\hat{\xi}}_{3_k} + D_w \dot{\hat{\xi}}_{3_k} + K_w \hat{\xi}_{3_k} = \hat{\tau}_{3_k}|_{wall} = \sum_n a_k^{(n)} \phi_{3,2_k}^{(n)} \tag{11}$$

(We employ capital letters to describe the properties of the compliant surface for clarity.) The wall-normal deformations of the compliant surface are driven by the pressure fluctuations at the boundary.

$$M_w \ddot{\hat{\xi}}_{2_k} + D_w \dot{\hat{\xi}}_{2_k} + K_w \hat{\xi}_{2_k} = \hat{p}_k|_{wall} \tag{12}$$

The pressure at the wall in the models may be determined as in (6).

$$\left\langle -\hat{p}_{k,i}, \phi_{i_k}^{(n)} \right\rangle = \left(\hat{p}_k \phi_{2_k}^{(n)*} \right)|_{wall}^{\infty} + \int_0^\infty \hat{p}_k \phi_{i,i_k}^{(n)} \, dy = \left(\hat{p}_k \phi_{2_k}^{(n)*} \right)|_{wall} \tag{13}$$

The eigenfunctions are defined to be divergence free and are non-zero only close to the wall, leaving us with a pressure term only at the wall. As a result, the model equations now have an additional term:

$$\dot{a}_k^{(n)} = \sum_p \left(b_{kp}^{(n)meanvel} + (1 + 6.28\alpha) b_{kp}^{(n)visc} \right) a_k^{(p)} + \sum_{k',p,q} c_{(k',k-k')pq}^{(n)} a_{k'}^{(p)} a_{k-k'}^{(q)}$$
$$+ \sum_{r,k',p,q} d_{rk'pq}^{(n)} a_k^{(r)} Re\left(a_{k'}^{(p)} a_{k'}^{(q)*} \right) + \frac{1}{\rho} \left(\phi_{2_k}^{(n)*} \hat{p}_k \right)|_{wall} \tag{14}$$

Our previous models have focused exclusively on the rigid-wall case with $\phi_{2_k}^{(n)} = 0$, so that the pressure term disappears. (If the eigenfunctions are defined only in a region close to the wall, an additional term appears which was incorporated into our previous models as a forcing term. The magnitude of this term is small relative to the others and will be neglected here.) However, to incorporate the compliance of the wall and satisfy the boundary conditions in (1), we must include eigenfunctions in our model which are non-zero at the wall.

We choose to base our low-dimensional model for the turbulent boundary layer over a compliant surface on the eigenfunctions of the rigid-walled boundary layer. We will introduce additional eigenfunctions to account for the motion of the compliant surface and allow the boundary conditions to be satisfied. In the absence of surface compliance, our models will revert to the rigid-walled case. Since we do not have an experimental or computational database on the turbulent flow over a compliant surface available, we must derive our additional eigenfunctions in an *ad hoc* fashion. We choose our additional eigenfunctions as

solutions of the Stokes equation with periodic motion of the wall:

$$\left(\frac{\partial}{\partial t} - \nu\Delta\right) u = 0, \quad \hat{u}_k(y = 0, t) = \cos(\beta t) \tag{15}$$

where β corresponds to the natural frequency of the compliant surface. The Stokes equation for the streamfunction ψ is employed to determine the additional eigenfunction for the wall-normal motion of the compliant surface. In this manner, we generate three additional eigenfunctions — one for each direction of surface motion — and then orthogonalize them with respect to each other and the rigid-walled eigenfunctions and normalize them.

We now have a set of evolution equations for the coefficients of the eigenfunctions as well as evolution equations for the motion of the wall and the simplified boundary conditions. We choose to determine the coefficients for the additional eigenfunctions from the boundary conditions at the wall. If only one or at most two eigenfunctions has a particular component which is non-zero at the wall, these coefficients may be found easily. The pressure may then be determined from the evolution equation for the additional eigenfunction representing the wall-normal motion of the wall $\phi_k^{(2)}$:

$$\hat{p}_k \mid_{y=0} \approx \frac{\rho}{\phi_{2_k}^{(2)*} \mid_{y=0}} \left[\dot{a}_k^{(2)} - \sum_p b_{kp}^{(2)} a_k^{(p)} - \sum_{k',p,q} c_{(k',k-k')pq}^{(2)} a_{k'}^{(p)} a_{k-k'}^{(q)} \right] \tag{16}$$

The cubic terms disappear because this additional eigenfunction is defined to have no streamwise component, and there is no streamwise variation in our model. When this expression is substituted into the equation for the wall-normal motion of the wall (12), the time derivative term merges into the $\ddot{\xi}_{2_k}$ term resulting in a new effective mass of the wall $\tilde{M}_w$. (In fact, $\dot{\xi}_{2_k} = a_k^{(2)} \phi_{2_k}^{(2)}$ since $\phi^{(2)}$ is the only eigenfunction with a non-zero vertical velocity at the wall.) Normalizing with this new mass results in:

$$\ddot{\hat{\xi}}_{2_k} + \tilde{D}_w \dot{\hat{\xi}}_{2_k} + \tilde{K}_w \hat{\xi}_{2_k} \approx \tilde{\rho} \left[\sum_p b_{kp}^{(2)} a_k^{(p)} + \sum_{k',p,q} c_{(k',k-k')pq}^{(2)} a_{k'}^{(p)} a_{k-k'}^{(q)} \right] \tag{17}$$

Having determined the coefficient and pressure in this way, we have a complete low-dimensional model for the flow over a compliant surface.

$$\dot{a}_k^{(1)} = \sum_p b_{kp}^{(1)} a_k^{(p)} + \sum_{k',p,q} c_{(k',k-k')pq}^{(1)} a_{k'}^{(p)} a_{k-k'}^{(q)} + \sum_{r,k',p,q} d_{rk'pq}^{(1)} a_k^{(r)} Re\left(a_{k'}^{(p)} a_{k'}^{(q)*} \right) \tag{18}$$

$$M_w \ddot{\hat{\xi}}_{1_k} + D_w \dot{\hat{\xi}}_{1_k} + K_w \hat{\xi}_{1_k} = \hat{\tau}_{1_k}|_{wall} = \sum_n a_k^{(n)} \phi_{1,2_k}^{(n)} \tag{19}$$

$$\ddot{\hat{\xi}}_{2_k} + \tilde{D}_w \dot{\hat{\xi}}_{2_k} + \tilde{K}_w \hat{\xi}_{2_k} \approx \tilde{\rho} \left[\sum_p b_{kp}^{(2)} a_k^{(p)} + \sum_{k',p,q} c_{(k',k-k')pq}^{(2)} a_{k'}^{(p)} a_{k-k'}^{(q)} \right] \tag{20}$$

$$M_w \ddot{\hat{\xi}}_{3_k} + D_w \dot{\hat{\xi}}_{3_k} + K_w \hat{\xi}_{3_k} = \hat{\tau}_{3_k}|_{wall} = \sum_n a_k^{(n)} \phi_{3,2_k}^{(n)} \tag{21}$$

$$a_k^{(2)} = \frac{\dot{\hat{\xi}}_{2_k}}{\phi_{2_k}^{(2)}|_{y=0}} \tag{22}$$

$$a_k^{(3)} = \frac{\dot{\hat{\xi}}_{1_k} - \hat{\xi}_{2_k} \frac{\partial U}{\partial y}|_{y=0}}{\phi_{1_k}^{(3)}|_{y=0}} \tag{23}$$

$$a_k^{(4)} = \frac{\dot{\hat{\xi}}_{3_k} - a_k^{(2)} \phi_{3_k}^{(2)}|_{y=0}}{\phi_{3_k}^{(4)}|_{y=0}} \tag{24}$$

We are in the process of using this low-dimensional model to evaluate the potential of compliant surfaces for modification of the dynamics of near-wall turbulence and its resulting effect on the drag at the wall. In addition to our work with the models, we have begun the development of a direct simulation code for simulating turbulent channel flow with a compliant boundary. Because of the complication introduced by the linearized boundary conditions, we have chosen to implement the compliant boundary using the immersed boundary technique which was developed by a previous member of our group [4].

Acknowledgment/Disclaimer

References

[1] AUBRY, N.; HOLMES, P.; LUMLEY, J. L.; STONE, E. (1988) The Dynamics of Coherent Structures in the Wall Region of a Turbulent Boundary Layer. *J. Fluid Mech.* **192**, pp. 115–173.

[2] CHOI, K.-S.; YANG, X.; CLAYTON, B. R.; GLOVER, E. J.; ATLAR, M.; SEMENOV, B. N. & KULIK, V. M. (1997) Turbulent Drag Reduction Using Compliant Surfaces. *Proc. R. Soc. Lond. A* **453**, pp. 2229–2240.

[3] HOLMES, P. J., LUMLEY, J. L. AND BERKOOZ, G. (1996) *Turbulence, Coherent Structures, Symmetry and Dynamical Systems.* Cambridge, UK: University Press.

[4] MOHD-YUSOF, J. (1996) Interaction of Massive Particles with Turbulence. *PhD Thesis,* Cornell University.

DEVELOPMENT OF MICRO-RESOLUTION PIV AND ANALYSIS OF MICROTHRUSTERS FOR SMALL-SCALE AIRCRAFT AND SPACECRAFT

Carl D. Meinhart
Department of Mechanical and Environmental Engineering
University of California

Summary
A Particle Image Velocimetry system has been proposed to measure velocity fields of high-speed air flows in 300 μm thick 2-D silicon-micromachined nozzles. While the technique has been demonstrated successfully by measuring liquid flows, the measurement of high-speed air flows through micronozzles remains difficult, because (1) spatial resolutions on the order on a few microns are required to resolve the flow field, (2) large characteristic velocities combined with high spatial resolution requirements dictate temporal resolutions on the order of tens of nanoseconds, and (3) supersonic flows in the micronozzles may undergo characteristic accelerations on the order of 100 million times that of gravity. The micro PIV system developed during the past year under this grant has the potential to overcome these difficulties. The technique utilizes reflective Differential Interference Contrast (DIC) microscopic imaging to record images of 50 – 100 nm dia. silicate particles. Micro PIV measurements of low-speed water flow in the micronozzles are shown with a spatial resolution of 10.9 × 3.4 μm in the streamwise and cross-flow directions, respectively. The results show flow separation in a straight angle diffuser at Reynolds number, Re = 10, based on bulk velocity and throat width.

Particle Image Velocimetry System
Flow-Tracing Particles
The desire to measure high-speed velocity fields accurately inside micronozzles with order one-micron spatial resolution places significant constraints on the choice of flow-tracing particles. The particles must be significantly smaller than the length scale of the microdevice, and must be small enough to faithfully follow the flow under extremely large accelerations.

If a supersonic flow through a micronozzle accelerates from Mach 1 at the throat to Mach 2 one hundred microns downstream, and assuming uniform acceleration, the flow will accelerate at an average rate of approximately 9.0 E +08 m s^{-2}, or approximately 100 million times the acceleration of gravity. Assuming Stokes' drag, the difference between the particle velocity and the fluid velocity can be estimated by

$$\mathbf{v} - \mathbf{u} = \frac{\rho_p d_p^2 |\dot{\mathbf{v}}|}{36 \rho \nu},$$

(1)

where $\mathbf{v}$ is the particle velocity, $\mathbf{u}$ is the velocity of the fluid, $\dot{\mathbf{v}}$ represents the total time derivative of the particle velocity, and the subscript p represents the properties of the particle (Adrian, 1991). Using silica (SiO_2), which has a density of 2 g cm^{-3}, a 100 nm dia. particle will slip ~ 27 m s^{-1}, while a 50 nm dia. particle will slip ~ 7 m s^{-1}. This represents about 4 – 8% FS error for the 100 nm and 1 – 2% FS error for 50 nm dia. particles. Under these conditions, a 100 nm dia. particle represents an upper bound on the size of particle that should be used for PIV measurements of high-speed flow in micronozzles.

Flow-tracing particles must also be large enough to scatter sufficient light so that their images can be recorded. In the Rayleigh scattering regime, where the particle diameter is much smaller than the wavelength of light, $d_p << \lambda$, the amount of light scattered by a particle varies as d_p^{-6} (Born & Wolf, 1997).

Spatial and Temporal Resolution

For the purposes of this discussion, we will define temporal resolution as the duration of averaging time required to obtain a measurement. In the case of double pulse PIV, the temporal resolution is simply the time delay between pulses, Δt. The ability to make accurate measurements while averaging over a short interval in time is important in variety of experiments. It is particularly important for measuring high-speed flows in micronozzle experiments. In this situation, the desire to make PIV measurements on the micron scale coupled with the large velocity associated with supersonic flows requires nanosecond temporal resolution.

Consider a flow near Mach 1 at standard temperature, with a characteristic velocity, $u_c = 340$ m s^{-1}. If the desired particle displacement is, say, $\Delta x \approx 10 \mu$m, then the time delay between pulses should be, $\Delta t \approx 30$ ns. A standard $Nd{:}YAG$ laser can be used to generate a short pulse of green light ($\lambda = 532$ nm), which is approximately Gaussian in time with a time duration, $\delta t \approx 5$ ns. During a 5 ns period, a particle with a characteristic velocity of $u_c = 340$ m s^{-1} travels approximately 1.7 μm. If a particle moves a significant fraction of its effective image size during exposure, the particle image will be blurred. In nearly all PIV experiments reported to date, the relatively short light pulse ($\delta t \approx 5$ ns) from an $Nd{:}YAG$ laser is more than sufficient to freeze particle motion. It is only in the special case of high-speed microscale flow that the pulse duration of an $Nd{:}YAG$ laser becomes limiting.

Differential Interference Contrast (DIC) Imaging

Particles with diameters of 50 – 100 nm are required for accurate PIV measurements of high-speed flow in micronozzles. Particles of this size can potentially be imaged using differential interference contract (DIC). The reflective DIC system shown in Figure 1 consists of a linear polarizer, a mirror, an adjustable Wollaston prism, and a DIC analyzer. The illumination light enters the system through the linear polarizer and is reflected by the mirror towards the Wollaston prism. The Wollaston prism consists of a birefringent material oriented at 45° to the incoming polarized light. The birefringence causes the incoming light to be sheared. The degree of beam shear is adjusted by sliding one element of the prism relative to the second element. It is common to adjust the shear

so that it is less than the diffraction limit of the microscope so that a double image is not observed. The sheared beam illuminates the back of the objective lens, where it is refracted into the microfluidic device. Light is spectrally reflected from the surfaces of the microfluidic device, and scattered from the flow-tracing particles. The reflected light from the particles and the test section is collected by the objective lens and relayed through the Wollaston prism where the beam shear is reversed. Because optical systems are acausal, light waves that were relatively undisturbed in the test section will recover their original polarization, after reversing back through the Wollaston prism. Light waves that have been phase shifted or changed in amplitude by objects that are of the same order in size as the beam shear will recover a different polarization, after reversing back through the Wollaston prism. The light is then relayed through the mirror onto a DIC analyzer. In the current configuration, the DIC analyzer is simply a linear polarizer oriented 90° to the incoming light. This filters out light that is relatively undisturbed in the test section over length scales on the order of the beam shear. In practice, the beam shear is adjusted to obtain maximum contrast for a particular type of object (Inoué & Spring, 1997).
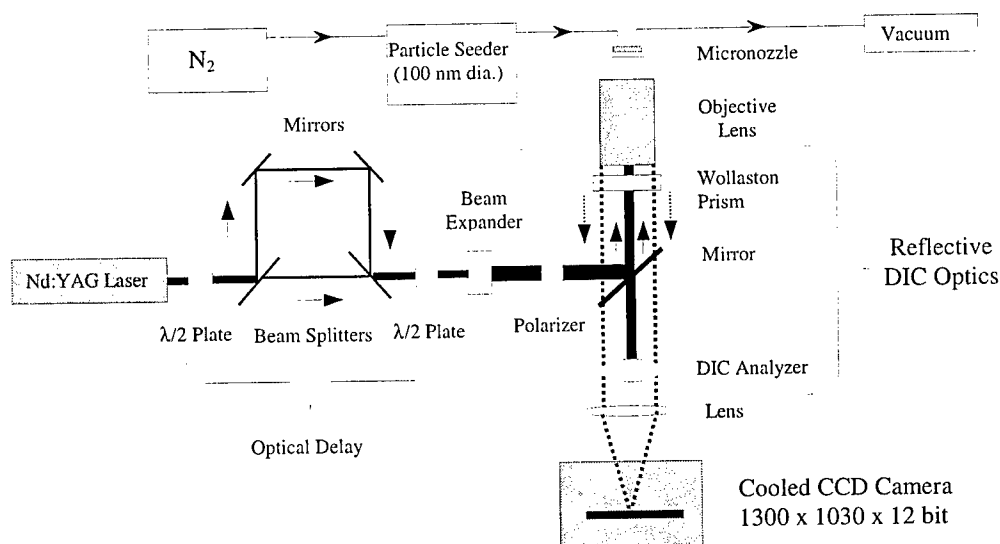
Figure 1. Schematic of a micron-resolution PIV system. The system incorporates a reflective DIC technique to record images of 50 – 100 nm dia. particles. An optical delay path can be added to the system to produce two pulses of laser light separated by tens of nanoseconds.

The ability of the DIC system to image 50 nm dia. silicate particles using elastic scattering is demonstrated in Figure 2. A 3-D shadowing feature of the particle images is characteristic of DIC, and can be observed in Figure 2. Figure 2a shows images of 50 nm silicate particles using a NA = 1.4 oil immersion 100x objective lens, while Figure 2b shows images of 50 nm silicate particles using a NA = 0.6 air immersion 40x objective lens. The particles were not observable without the aid of DIC.
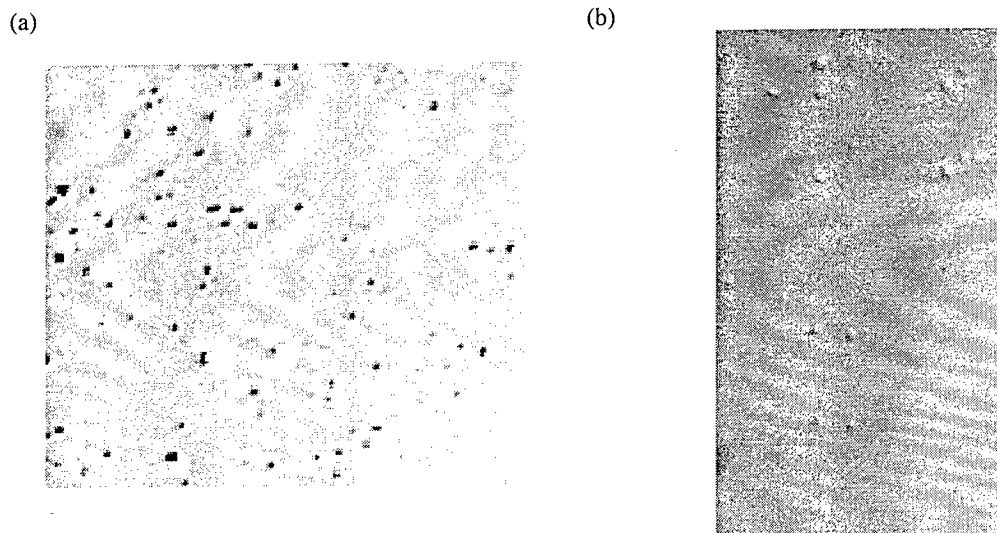
Figure 2. Differential Interference Contrast (DIC) images of 50 nm dia. silicate particles: (a) recorded using a NA = 1.4 oil immersion 100x objective lens, (b) recorded using a NA = 0.6 air immersion 40x objective lens

Velocity Measurements in a Micronozzle

Measurements of flow through a micronozzle were conducted using water as the fluid medium to determine the conditions in which PIV measurements could be obtained in the relatively deep micronozzles. The liquid flow was seeded with relatively large 700 nm dia. fluorescently-labeled polystyrene particles. The particles were imaged using a NA = 0.6, 40x objective lens, and an epi-fluorescent imaging system similar to that described by Meinhart et al. (1999). A flow rate of 4 ml hr^{-1} was delivered to the nozzle by the syringe pump.

Figure 3 is an example of an instantaneous velocity field measured in the throat and expansion section of a straight diffuser with a 24° half angle. The velocity fields were calculated using a standard cross correlation algorithm. Both interrogation windows were 64 × 20 pixels in the x and y directions, respectively. When projecting into the fluid, the correlation windows were 10.9 × 3.4 μm in the x and y directions, respectively. The correlation windows were offset to the local particle-image displacement at each measurement point. The interrogation spots were overlapped by 50%, yielding a velocity-vector spacing of 5.44 μm in the streamwise direction and 1.7 μm in the spanwise direction.
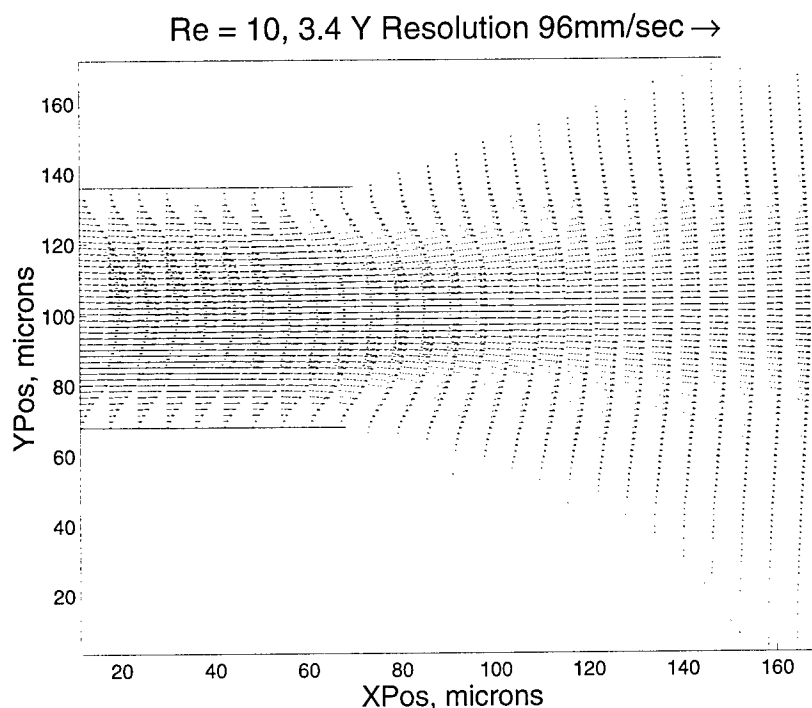
Figure 3. PIV vector field of water flow through a silicon micromachined nozzle. The nozzle throat is 70 μm wide throat and leads into a constant-angle expansion section. The spatial resolution of the PIV measurements are 10.9 × 3.4 μm in the streamwise and cross-flow directions, respectively.

Conclusions

Particle Image Velocimetry has been used to make velocity measurements of liquid flow in silicon micromachine nozzles with throat diameters of 70 μm. The velocity measurements have a spatial resolution of 10.9 × 3.4 μm in the streamwise and cross-flow directions, respectively. These results indicate that flow separation occurs in a 24° (half-angle) diffuser, with a Reynolds number based on bulk velocity and throat diameter of Re = 10.

Although we have demonstrated that micron-resolution velocity measurements can been obtained for liquid flows in micronozzles, significant challenges must be overcome for successful measurements of high-speed gas flows at the microscale. These challenges are discussed in detail, and solutions are proposed. One solution is to record 50 – 100 nm dia. silicate particles using Differential Interference Contrast (DIC) imaging. The DIC technique is demonstrated by imaging 50 nm dia. silicate particles with a NA = 1.4 oil immersion 100x lens and NA = 0.6 air immersion 40x lens.

References

Adrian R.J. 1991. Particle-imaging techniques for experimental fluid mechanics. *Annu Rev Fluid Mech,* **Vol. 23**, pp. 261-304.

Born, M & Wolf E 1997. Principles of Optics. *Pergamon Press.*

Inoué, S & Spring, KR 1997. Video Microscopy, Second Edition, *Plenum Press.*

Meinhart, C. D., Wereley, S. T. & Santiago, J. G. 1999 PIV Measurements of a Microchannel Flow. In press *Exp. in Fluids.*

PULSED INJECTION FOR NOZZLE THROAT AREA CONTROL

Daniel N. Miller, Erich E. Bender, Brian R. Smith, and Patrick J. Yagle
Propulsion Systems and Computational Fluid Dynamics
Lockheed Martin Tactical Aircraft Systems, Fort Worth, TX

Ahmad D. Vakili
Department of Mechanical and Aerospace Engineering
University of Tennessee Space Institute

Figure 1: Simulation of Pulsed Injection in a Cross flow Using CFD

3-D CFD Simulation Features

◆ 600K Grid Cells

◆ Finite Volume

◆ 3rd-Order Upwind

◆ LES Turbulence Model
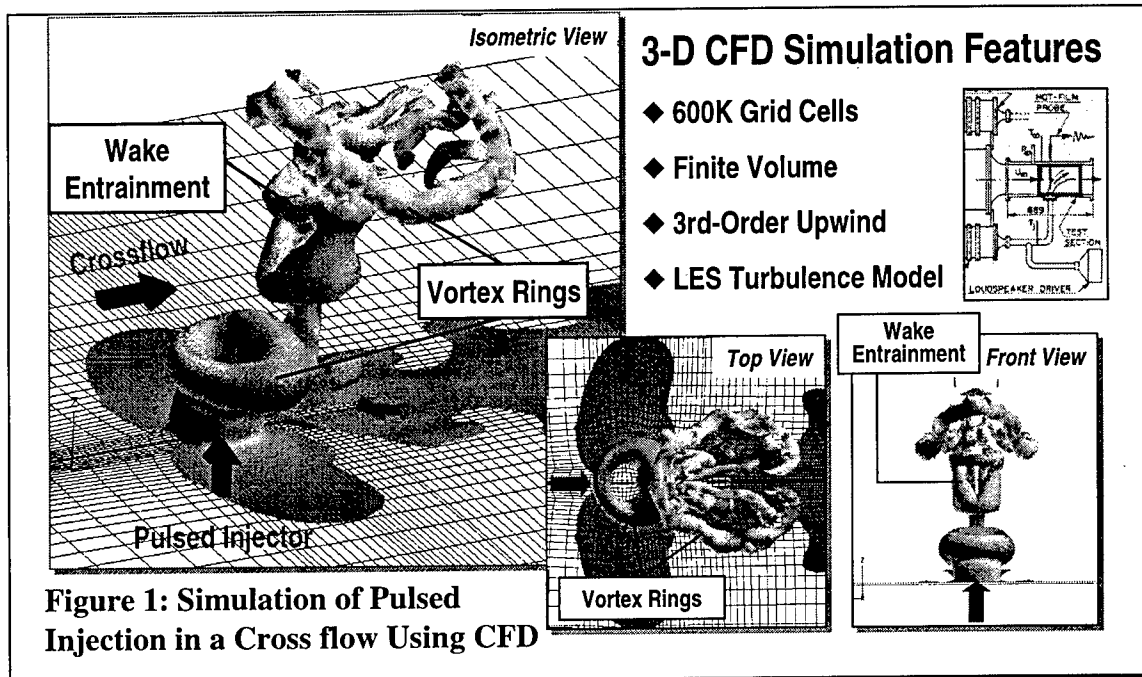
Overview

Fluidic injection is of interest to provide internal flowpath shape variation for jet control in structurally-fixed nozzles, and holds the promise of reducing the weight and complexity of future exhaust systems by eliminating mechanical flowpath actuation[1,2,3]. On-going work with *steady injection* has shown that, by introducing a transverse-mounted wall injector into the exhaust stream near the throat or the exit, the injector plume can produce a stable fluidic obstruction[2,3]. By metering injector flow rate, the size of this obstruction, and hence, the internal flowpath shape can be actively modified to control both jet throat area and thrust vector angle. This research effort is investigating unsteady methods for increasing the fluidic blockage produced by an injector blowing into an internal, high-speed cross flow (Fig. 1). If greater blockage can be generated by pulsed injection, the mass flow required to achieve nozzle jet flow control could be reduced. Reducing injector flow rate is desired to achieve the peak system-level performance. Previous experimental efforts have established that periodic modulation of

a transverse injected stream into a low-speed cross flow increases stream penetration and effective diameter by at least 100% relative to steady-state injection[4,5,6]. These results suggest that greater flow blockage may be obtained using pulsed injection. The fundamental mechanism governing this enhanced penetration is the appropriate formation, spacing, and strength of trains of vortex rings generated at the injector exit. In this project, CFD-based methodologies are being developed for modeling and simulation of the fundamental unsteady flow field to investigate the effects of compressibility and transonic injection on vortex-ring penetration and blockage. Experimental methods are being employed for evaluation of several viable, high-speed pulsed-injection actuators.

Objectives

The principal objective of this research effort is to investigate methods for increasing the effective blockage produced by an injector blowing into an internal, high-speed cross flow, without increasing injector flow rate. Specific objectives of this investigation are to:

1) Develop a CFD Simulation Methodology for Pulsed Injection

Little experimental data is available for the flow field of interest. Therefore, a simulation capability is required to provide detailed understanding of this 3-D, unsteady flow field.

2) Investigate Use of Pulsed Injection for Active, Internal Flowpath Shaping

This project will investigate the relationship between injector-jet structure, penetration, and effective blockage when introduced into an internal, high-speed cross flow.

3) Establish Fundamental Requirements for High-Speed Pulsed-Injection System

This project will investigate both the basic requirements for a pulsed-injection system and the characteristics of several available actuators for use in high-speed cross flows.

4) Develop a Rapid Analysis Method

An efficient CFD modeling methodology for pulsed injection will be developed for rapid analysis in a preliminary design environment.

Approach/Progress/Future Plans

The approach, progress and future plans for this research effort are outlined in the following task descriptions described below: (1) Pulsed-Injection Simulation, (2) Pulsed-Injection Testing, (3) Simplified Pulsed-Injection Model.

Figure 2: Low-Speed Simulations Produced Similar Qualitative Features to Test (Re$_i$ ~ 5k)
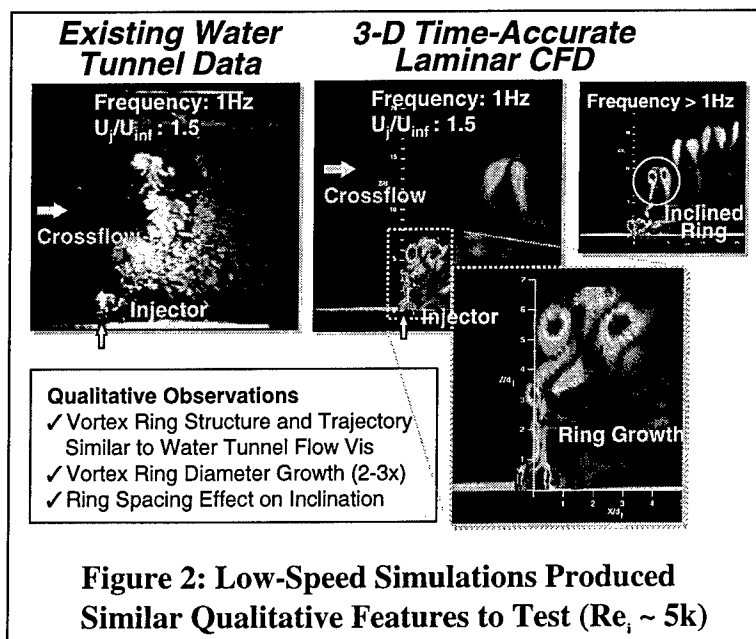
1) Pulsed-Injection Simulation

A CFD simulation methodology has been developed for pulsed injection in a cross flow. The intended application of this simulation tool is to provide adequate qualitative structure and quantitative data of the injector-jet flow field sufficient to investigate and exploit its potential for enhancing active flowpath shaping. The

Figure 3: Lessons Learned From Development of 3D, Unsteady, CFD Simulation Methodology

methodology consists of appropriate selection of turbulence model, numerical resolution, and numerical scheme. To guide the appropriate selection of these CFD parameters, simulations of an existing pulsed-injection test apparatus were conducted and compared with corresponding experimental measurements. The FALCON structured flow solver was selected for this task based on previous research that showed its ability to accurately simulate both steady and unsteady flow fields in relevant applications.

Figure 4: Unsteady Flows are More Sensitive to Grid Resolution Than Steady Flows (Re$_i$~20k)
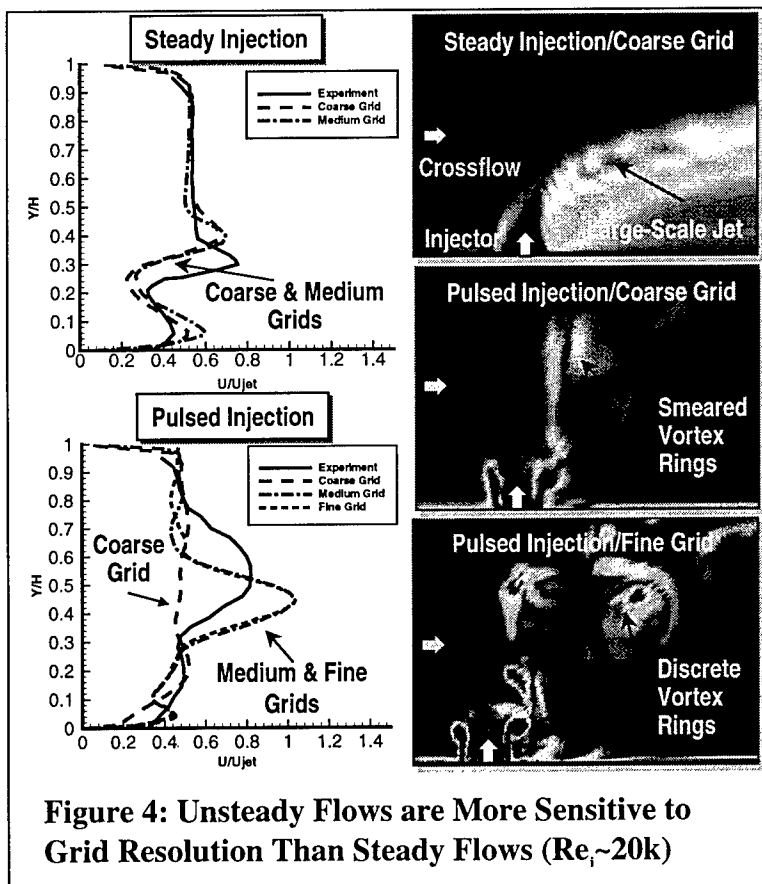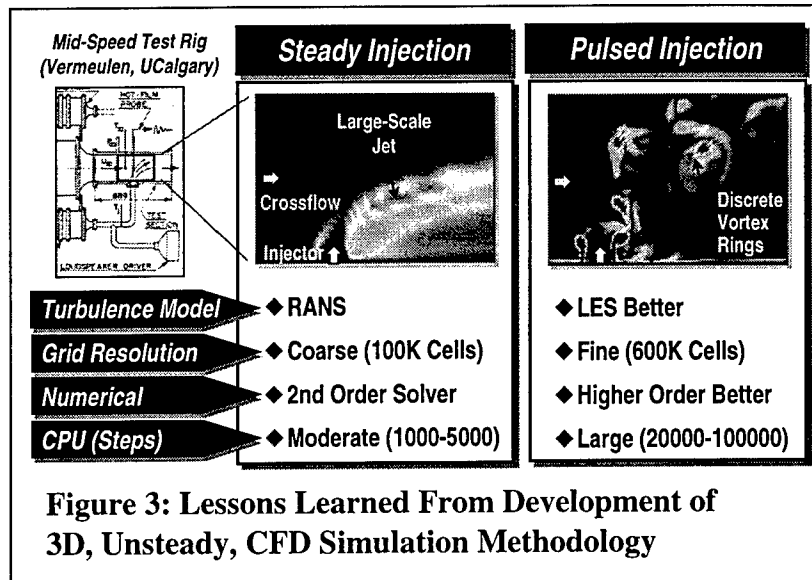
Initial simulations of previous water tunnel testing were run to ensure that the baseline CFD methodology produced the correct qualitative flow features (Fig. 2).[4] For quantitative assessment, CFD simulations of the pulsed-injection configuration tested by Chin and Vermeulen were done.[6] The configuration consisted of a 19mm diameter jet injected at 19 M/s into a cross flow of 10 M/s. Both steady and 208 Hz pulsing cases were simulated.

Fig. 3 summarizes lessons learned in the development of the simulation methodology by highlighting the differences

161

between steady and unsteady CFD requirements.[1] The steady jet solution requires much less resolution due to spatial averaging of the Reynolds averaged Navier-Stokes (RANS) turbulence model (in this case the two equation k-kl model). However, such a turbulence model filters out much of the relevant flow details in the unsteady solutions. Therefore, a Large Eddy Simulation (LES) model was used in the final simulations. Since spatial and temporal flow gradients are much higher, greater grid resolution and more accurate discretizations are used to obtain accurate solutions. Fig. 4 shows time-averaged velocity profiles of the flow at a distance of 1.43 injector diameters downstream of the injector. These results show the effect of grid resolution on CFD results for both the steady and pulsed jet. Coarse, medium, and fine grids (100K, 400K and 600K points) were used to determine spatial resolution requirements. For steady injection, coarse and medium grids agree well, although they overshoot the data somewhat (this overshoot is a RANS turbulence modeling problem which occurs in flows with high curvature). In the pulsing case, the coarse-grid completely diffuses the velocity profile, but medium and fine-grid results agree well.
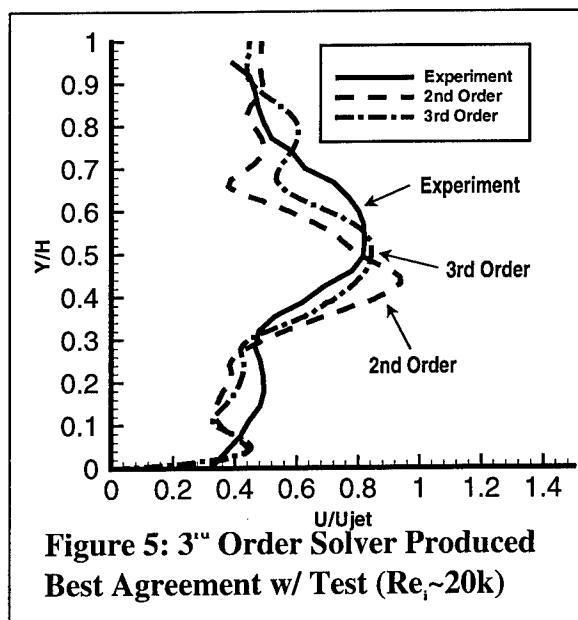
Figure 5: 3rd Order Solver Produced Best Agreement w/ Test (Re$_i$~20k)

The effect of increasing the numerical accuracy has also been investigated. FALCON uses a 2nd order upwind discretization of the inviscid fluxes. In addition, the minmod flux limiter is used to remove oscillations at discontinuities in the flow, which reduces the scheme to first order at extrema. Third-order discretization and improved limiters that maintain accuracy at extrema have been incorporated into the code. Fig. 5 shows the effect of these improvements in the pulsed-injector-jet case. The third order result compares better with the peak in the test-measured velocity profile.
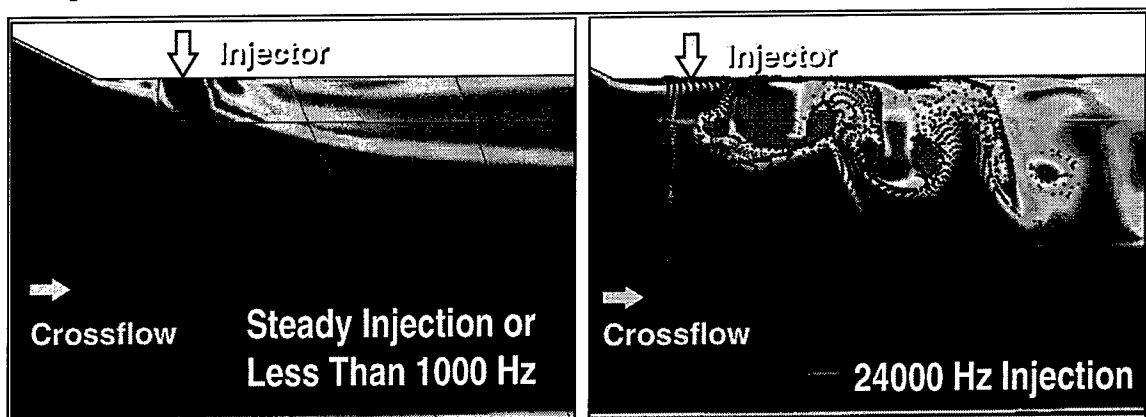
Figure 6: 3-D High-Speed Simulations Showing a Frequency Requirement of Between 12-24 kHz at Model-Scale (Re$_i$~1.5x10^6) and 1.2-2.4 kHz Full Scale

162
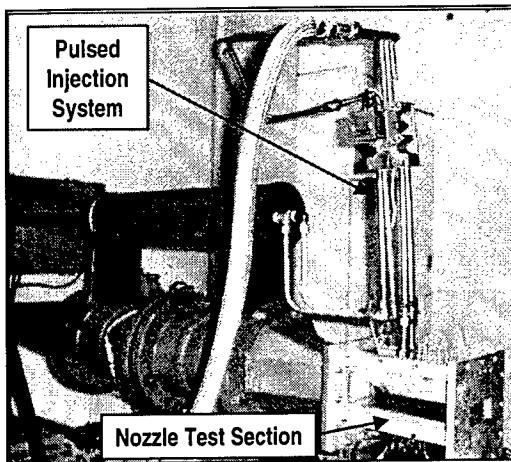
Figure 7: Experimental Setup for Pulsed Injection in a Nozzle

Work is currently ongoing in applying CFD to the current nozzle geometry to determine requirements of pulsed-injector operation for use in high-speed cross flows. In Fig. 6, solutions of steady and pulsed-injector jet flows for sonic cross flow conditions are shown. Pulsing frequency is one of the parameters being investigated – here a 24kHz case is shown. The pulsed-injector simulation shows a clear train of vortex-ring structures that penetrate much deeper than the steady-injector case. The particle traces shown in this figure illustrate the entrainment of the cross flow by the injector jet, which may affect the ability of the injector jet to increase nozzle blockage.

2) High-Speed Pulsed-Injection Testing

A complementary (to the simulation work) experimental investigation of pulsed injection is being conducted at the University of Tennessee Space Institute (UTSI).[4] The focus of this task is to investigate pulsing systems for enhancing injector-jet penetration and blockage in a compressible, high-speed, confined cross flow. To date, the experimental setup has been designed and manufactured, and the pulsing systems have been bench-tested and are ready for integration into the nozzle flow.

Experimental Investigation. The airflow of a transverse-mounted pulsed injector issuing into a 2-D nozzle is visualized through a side-view window on the test article (Fig. 7). . The effects of pulsing frequency and actuator type on jet velocity, penetration, blockage, and vortex-ring characteristics will be evaluated using Particle Imaging Velocimetry (PIV). The nozzle model is supplied by airflow from a plenum chamber. Both a fluidic and an acoustic actuator are being evaluated for pulsing the injected stream. A LabView digital data acquisition system is being used to monitor static and high-response pressure, temperatures, Mach numbers, and mass flow measurements.

Pulsing Systems. The first pulsing system is a fluidic device, developed by AlliedSignal, called a Diverter Valve (ASDV) (Fig. 7). The ASDV fluidically switches the injector stream between two exit ports, which creates a series of pulses in each exit stream corresponding to the switching frequency of the device. Characteristics of the ASDV include: variable frequency control (maximum ~200 Hz as tested), high mass flow rate capability, and relatively sharp pulse waveforms,
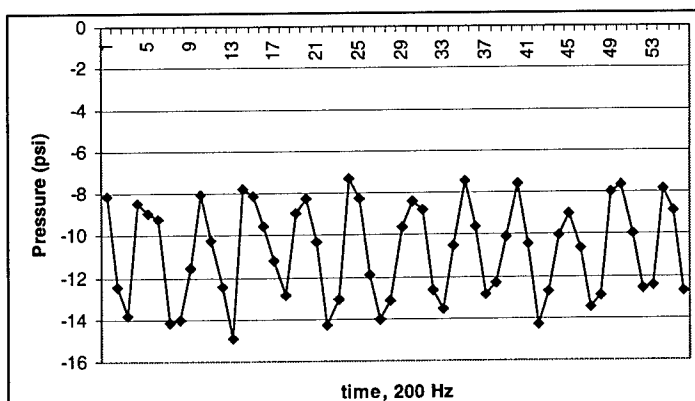
Figure 8: Measured ASDV Waveform @ 200Hz Using High-Response Measurements

163

as shown in high-response measurements (Fig. 8). While the ASDV frequency of operation is currently too low for use in a transonic cross flow, modifications can be made to increase the maximum frequency to the kHz range. PIV measurements will be made at moderate cross flow speeds to determine if a fluidic actuator can generate sufficient pulses to produce a coherent train of vortex rings. The second device is an Acoustically Pulsed Valve (APV), developed by UTSI, which can be operated in passive or active mode near very high frequencies (demonstrated in a passive mode at up to 8 kHz) required for transonic cross flows, as predicted by CFD simulations. Other characteristics of the APV include: variable frequency control, high mass flow rate capability, and relatively sharp pulse waveforms. Similar to the ASDV, detailed measurements will be made to determine if the APV can generate pulses of sufficient amplitude to produce the desired flow field.

Work is currently ongoing to calibrate the PIV measurement system for use in the high-speed nozzle cross flow. When completed, both pulsing systems will be evaluated according the plan discussed above.

3) Simplified Pulsed-Injection Model

When evaluating pulsed injection in a design environment, many solutions will be required to investigate the effects of parameters to obtain an optimum concept. Simulation of pulsed injection is computationally intensive and for applications with multiple pulsed injectors, very large computational meshes will be required for adequate resolution. For such cases, simulation is too time and cost intensive. In this task, we will develop a simplified CFD model of the pulsed injected stream that will capture its essential effect on the cross flow, without the need of a highly resolved simulation.

Acknowledgment/Disclaimer

References

1. Bender, E.E, Miller, D.N., Smith, B.R., and Vermeulen, P.J., 2000, "Simulation of Pulsed Injection in a Cross Flow Using 3-D Unsteady CFD," AIAA Fluids 2000, Paper No. TBD.
2. Gridley, M.C. and Walker, S.H., 1996, "Inlet and Nozzle Technology for 21st Century Aircraft," ASME, Paper No. 96-GT-244.
3. Miller, D.N., Yagle, P.J., and Hamstra, J.W., 1999, "Fluidic Throat Skewing for Thrust Vectoring in Fixed-Geometry Nozzles," AIAA, Paper No. 99-0365.
4. Vakili, A.D., Sauerwein, S.C. and Miller, D.N., 1999, "Pulsed Injection Applied to Nozzle Internal Flow Control," AIAA, Paper No. 99-1002.
5. Vakili, A.D., Chang, Y.K. and Wu, J.M., 1991, "Vortex Rings in Uniform Cross flow," AIAA, Paper No. 91-0522.
6. Vermeulen, P.J. et al., 1996, "NOx Measurements for Combustor with Acoustically Controlled Primary Zone," ASME, Paper No. 96-GT-129.

BOUNDARY CONDITIONS
FOR THE LARGE EDDY SIMULATION
OF WALL-BOUNDED TURBULENT FLOWS

AFOSR Grant F49620-97-1-0210

Principle Investigator:
Parviz Moin, Stanford University

Co-investigators:
Javier Jiménez, William Cabot, Jeffrey Baggett, Franck Nicoud

Period: 8/1/98 – 7/16/99

1 Objectives & Approach

The application of large eddy simulation (LES) to attached turbulent boundary layers is limited to low Reynolds numbers because the characteristic dimension of the energy containing structures scales with the distance from the wall. The goal of this research is to develop approximate "wall-boundary conditions" so that the near-wall flow need not be resolved. This will allow the computational grid to be chosen in terms of outer scales (e.g. boundary layer thickness) instead of Reynolds number dependent inner scales, thus permitting the application of LES at much higher Reynolds numbers for engineering applications. Our general methodology is to use empirical analyses of near-wall behavior in existing experimental and numerical simulation databases and theoretical analysis of highly anisotropic near-wall flow to develop and improve wall models which will be tested in select large-eddy simulations of attached and separated flows.

2 Progress & Results

The most commonly used approximate boundary condition for LES is to supply wall stresses in the first grid volume adjacent to the wall that represent the effects of the near-wall region on the outer flow. In this approach, the wall-normal velocity is assumed to be zero and the model wall stresses are determined from outer flow conditions. For low to moderate Reynolds numbers, say below 1000 based on the shear velocity, wall stress models that are based on simple instantaneous stress balances or time-dependent RANS models have shown

some success in channel flow and massively separated flow behind a step [4, 5, 6]. These RANS based models use mixing length eddy viscosities that are designed to reproduce the log law in high speed regions. The most complex of these models is based on the thin turbulent boundary layer equations that incorporate pressure gradient information from the outer flow and are found to give much better mean wall stress predictions in separated regions than simple mean stress balance models.

These wall stress models continue to be tested in turbulent boundary layer applications featuring separation. These flows include: a turbulent separated boundary layer on a flat plate induced by an imposed adverse pressure gradient [10], which allows us to study the performance of wall stress models in a situation with mild separation and no geometrical complications; and, under a different grant, a trailing edge flow featuring mild separation [13].

Preliminary results from the simulations of the separated turbulent boundary layer show qualitative agreement with direct numerical simulation results [10]. We have found, however, that the large eddy simulations are very sensitive to inflow conditions and tend to undergo large transients in the inlet section, which has correspondingly large effects downstream [7]. Compatible inflow conditions are currently being generated off-line with a recycling technique [9] using the same grid, numerics, and models as the main simulation. This will allow us to make quantitative assessments of wall stress models in the future. Simple stress balance models in a higher Reynolds number trailing edge flow have shown encouraging results, giving fairly good predictions for the mean velocity and correctly predicting the separation point at 10% of the cost of a well resolved large eddy simulation [13]. Some details of the separation region are not accurate, which may be improved by using stress models with more pressure gradient and material convection information from the outer flow.

For high Reynolds numbers we have found that the current generation of wall stress models do not correctly predict the mean velocity profile even in turbulent channel flow. The wall stresses not only have to predict mean characteristics such as the average drag, they also have to provide boundary conditions for the fluctuating velocities that can compensate for the numerical and subgrid scale modeling errors associated with the coarse near-wall grid. At low to moderate Reynolds numbers the flow is evidently able to compensate for these errors, but at high Reynolds numbers wall stress models based on first order quantities such as the mean stress balance are inadequate. To find the proper and apparently non-intuitive wall stresses that work we have turned to optimal control theory.

2.1 A new approach

The problem of finding wall stress boundary conditions to approximate the effects of the near-wall region can be regarded as a control problem in which the objective is for the coarse-grid, outer LES to yield good low-order statistics, and the unknown controls are the wall stress boundary conditions. The mathematical framework for optimal control in fluid mechanics is well established [1], but this application to LES is new. Tests in LES of turbulent channel flow have shown that this approach is very promising.
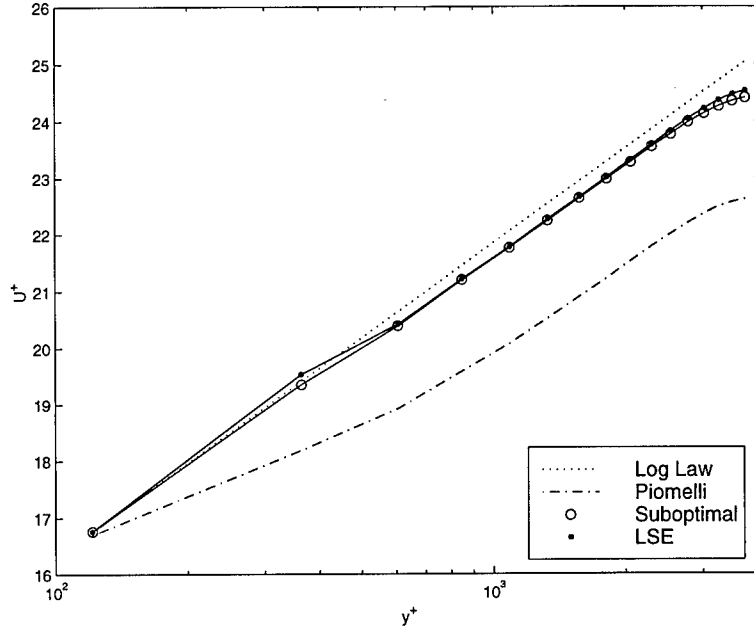
Figure 1: Mean velocity profile in turbulent channel flow at $Re_\tau = 4000$ on 32^3 uniform grid. Results with 3 wall models are shown — Piomelli shifted model, suboptimal control, and LSE.

Using a second order finite difference code with the plane averaged dynamic Smagorinsky model and a 32^3 uniform grid we have conducted several LES's at $Re_\tau = 4000$ ($\approx 110{,}000$ based on centerline velocity). For this configuration, the grid spacing, in wall units, is greater than 200^+ in the wall-normal and spanwise directions, and nearly 800^+ in the streamwise direction. Such a grid cannot capture any of the near-wall physics. As a benchmark, a simulation was conducted with the popular shifted model of Piomelli, et al. [12] in which the streamwise (spanwise) wall stress is assumed to be in phase with the streamwise (spanwise) velocity at a point slightly downstream in the first off-wall plane, and the mean wall stress is determined by the logarithmic law of the wall. As shown in Figure 1 the mean velocity gradient is severely underpredicted for several grid points resulting in an underprediction of the log. region intercept (this model does perform well at low to moderate Reynolds numbers).

Next, the sub-optimal control procedure was implemented in which the wall stresses were found that minimized the distance of the plane-averaged mean flow to the law of the wall at each time step. Nearly perfect agreement with the log. law is obtained for the first two planes and the log. region intercept is predicted to within $0.5u_\tau$ over the domain as can be seen in Figure 1. The mass flux is predicted to within 6% and this improves as the grid is refined. As shown in Figure 2, the suboptimal wall stresses produce higher values of u_{rms} than the shifted model. The suboptimal wall stresses are not necessarily the physically correct ones, instead they compensate for the numerical and subgrid scale modeling errors intrinsic to coarse-grid LES.

While the suboptimal control approach could be used as a wall model, provided a target mean velocity profile is known at least for the near-wall region of interest, the cost of the simulation
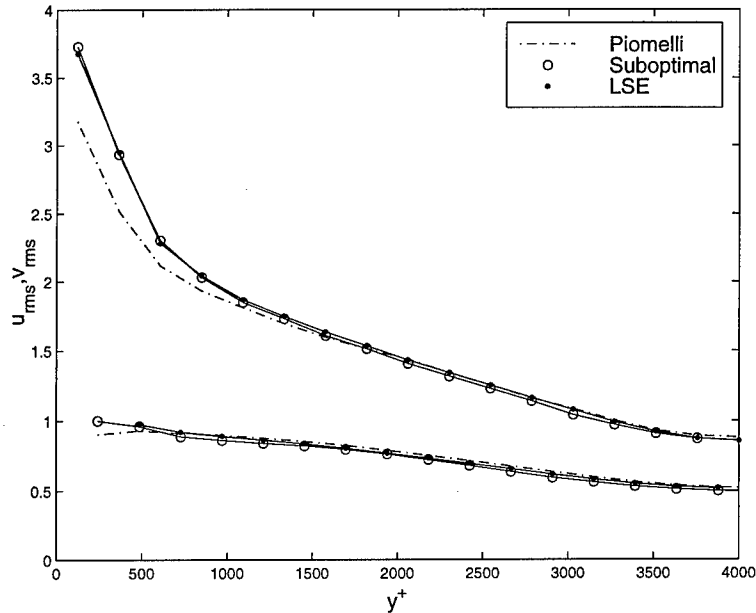
Figure 2: u_{rms} and v_{rms} at $\text{Re}_\tau = 4000$ on 32^3 uniform grid. Results with 3 wall models are shown — Piomelli shifted model, suboptimal control, and LSE.

with the suboptimal control is about 20 times greater than that with the shifted model mentioned above. Fortunately, the suboptimal control approach provides a set of reference data that can be used to derive new wall models. We would like to find the conditional average of the wall stress, that is, the best possible prediction of the wall stress, given the LES velocity field in some neighborhood of the prediction point. The conditional average embodies so much statistical information that it is unlikely that it could be found exactly, but Linear Stochastic Estimation (LSE) is a well established method for approximating it [2]. We have found that the LSE reproduces the suboptimal wall stresses extremely well given only local velocity field information. A wall model based on a single set of LSE coefficients gives good mean flow predictions over a large range of Reynolds numbers (from 180 to 20000 based on the shear velocity) and even on different grids. Figure 1 shows the result of using the LSE wall model at $\text{Re}_\tau = 4000$. Further results will be included in our presentation.

3   Future Plans

We will continue to explore the derivation of improved wall models using the optimal control / linear stochastic estimation framework. In particular, the suboptimal control mentioned above, in which the control was optimized so that the best mean flow was obtained at each time step should be extended to find the best wall stresses over a longer time horizon. We expect this to yield further improvements in mean flow prediction. The reference data generated by new simulations will be used to derive new LSE wall models and these will be investigated for grid Reynolds number dependence. The relationship to the subgrid scale model for the outer flow will also be investigated. Furthermore the optimal control framework will be used to investigate other possible approximate boundary conditions such as supplying Dirichlet

168

boundary conditions to the velocity field at some distance from the wall — an approach that has thus far met with limited success [3, 8, 11].

These new wall stress models, as well as some of the existing ones, will be tested in simulations of mildly separated flow with low to moderate Reynolds numbers using consistent inflow conditions to allow more quantitative comparisons of results. We will determine if simple stress balance models and the new LSE wall models are sufficient for accurately predicting the separated flow, or if more pressure gradient and flow convection information from the outer flow is needed, as provided by the more costly unsteady thin boundary layer equations. A less costly alternative to the thin boundary layer equations will be explored, in which the stress balance model is modified with estimates of the pressure gradient and material derivative of the outer flow near the wall; a priori tests have shown that this significantly improves the prediction of the wall stress around separation. While this approach has focused on manipulating the wall stress, improvements in the subgrid-scale model on the very coarse near-wall grid is also required. The standard subgrid-scale models currently in use cannot treat the large variations and anisotropy that occur within the near-wall cells; we will therefore explore new ways to model unresolved stresses more accurately in this region.

Finally, since it seems likely that different approximate boundary conditions will be needed in different flow regimes, we will also begin examining the problem of determining how and where to switch between different wall models.

4 Acknowledgement/Disclaimer

References

[1] F. Abergal and R. Temam. On some control problems in fluid mechanics. *Theoret./ Comput./ Fluid Dynamics*, 1:303–325, 1990.

[2] R.J. Adrian, B.G. Jones, M.K. Chung, Y. Hassan, C.K. Nithianandan, and A. Tung. Appoximation of turbulent conditional averages by stochastic estimation. *Phys. Fluids*, 1:992–998, 1989.

[3] J.S. Baggett. Some modeling requirements for wall models in large eddy simulation. In *Annual Research Briefs*, pages 123–134. Center for Turbulence Research, 1997.

[4] E. Balaras, C. Benocci, and U. Piomelli. Two-layer approximate boundary conditions for large-eddy simulations. *AIAA J.*, 34:1111–1119, 1996.

[5] W. Cabot. Large-eddy simulations with wall models. In *Annual Research Briefs*, pages 41–50. Center for Turbulence Research, 1995.

[6] W. Cabot. Near-wall models in large eddy simulations of flow behind a backward-facing step. In *Annual Research Briefs*, pages 199–210. Center for Turbulence Research, 1996.

[7] W. Cabot. Large-eddy simulation of a separated boundary layer. In *Annual Research Briefs*, pages 279–288. Center for Turbulence Research, 1998.

[8] J. Jiménez and C. Vasco. Approximate lateral boundary conditions for turbulent simulations. In *Proceedings of the Summer Program*. Center for Turbulence Research, 1998.

[9] T.S. Lund, X. Wu, and K.D. Squires. Generation of turbulent inflow data for spatially-developing boundary layer. *J. Comp. Phys.*, 140:233–258, 1998.

[10] Y. Na and P. Moin. Direct numerical simulation of a separated turbulent boundary layer. *J. Fluid Mech.*, 370:175–201, 1998.

[11] F. Nicoud, G. Winckelmans, D. Carati, J. Baggett, and W. Cabot. Boundary condition for les away from the wall. In *Proceedings of the Summer Program*. Center for Turbulence Research, 1998.

[12] U. Piomelli, J. Ferziger, P. Moin, and J. Kim. New approximate boundary conditions for large eddy simulations of wall-bounded flows. *Phys. Fluids*, 1:1061–1068, 1989.

[13] M. Wang. Progress in large-eddy simulation of trailing-edge turbulence and aeroacoustics. In *Annual Research Briefs*, pages 37–49. Center for Turbulence Research, 1997.

5   Personnel Supported

The following personnel have been supported from this grant in this period: Parviz Moin; Javier Jiménez as a senior research fellow of the Center for Turbulence Research at Stanford University; and William Cabot as a senior research associate of the Center for Turbulence Research at Stanford University.

6   Interactions/Transitions

1. Jeffrey Baggett and William Cabot presented preliminary results based on this research at the 51st Meeting of the Fluid Dynamics Division of the American Physical Society in Philadelphia in November 1998.

2. Parviz Moin presented an invited lecture on this research on June 30, 1999 at the Newton Institute of Mathematical Sciences at Cambridge.

DELTA WING VORTEX BREAKDOWN CONTROL

Julie A. Morrow, Yair Guy, Thomas E. McLaughlin
US Air Force Academy, CO

Israel Wygnanski
University of Arizona

Pressure Distribution

A parametric study of the effect of periodic flow excitation on the normal force of a delta wing was conducted in the low-speed wind tunnel at the USAF Academy. Periodic blowing and suction with zero net mass flux was applied at the leading edge of a half-span wing. The pressure distribution over the rear 2/3 of the upper surface was measured at angles of attack from $20°$ to $40°$ and the pressure was integrated to yield the normal force. The experiments were conducted at a freestream velocity of 4.3 m/s, corresponding to a chord Reynolds number of 2.1×10^5. The flow excitation frequency was varied from 0 to 20 Hz., corresponding to nondimensional frequencies of 0 to 3.5, and the momentum coefficient was varied form 0 to 0.0044. It was found that periodic flow excitation delays wing stall by $10°$ approximately and greatly increases the normal force at high angles of attack. The effect of the flow excitation is maximized at a nondimensional frequency of 1.4 and at a momentum coefficient of 0.004 approximately. A maximum increase of 40% in the normal force was obtained at an angle of attack of $40°$ at these conditions, relative to the unforced case[3, 4]. These results are consistent with results obtained in previous investigations[1, 2].

Sample plots of the results are presented in Figure 1 and 2. The variation of the normal force coefficient with the nondimensional frequency, for a constant value of the momentum coefficient is presented in Fig. 1. The variation of the normal force coefficient with the momentum coefficient, for a constant value of the nondimensional frequency, is presented in Fig. 2.

Velocity Measurement and Flowfield Visualization

The velocity distribution over the wing and across the vortex core is measured in the water tunnel at the USAF Academy. The flowfield and the vortex structure are visualized. Periodic blowing and suction with zero net mass flux is applied at the leading edge of the wing and a 2-component Laser Doppler Velocimetry system is used to survey the velocity field. The spatial and temporal location of the vortex core is visualized by dye injection. The structure of the vortex with and without flow excitation is visualized with a laser light sheet. This is an ongoing research and is aimed at in-depth understanding of the parameters that govern the efficacy of periodic flow excitation. Preliminary results indicate that periodic flow excitation delays vortex breakdown by 0.2

chordlength approximately and increases the local velocities over the wing, after the onset of vortex breakdown[5].
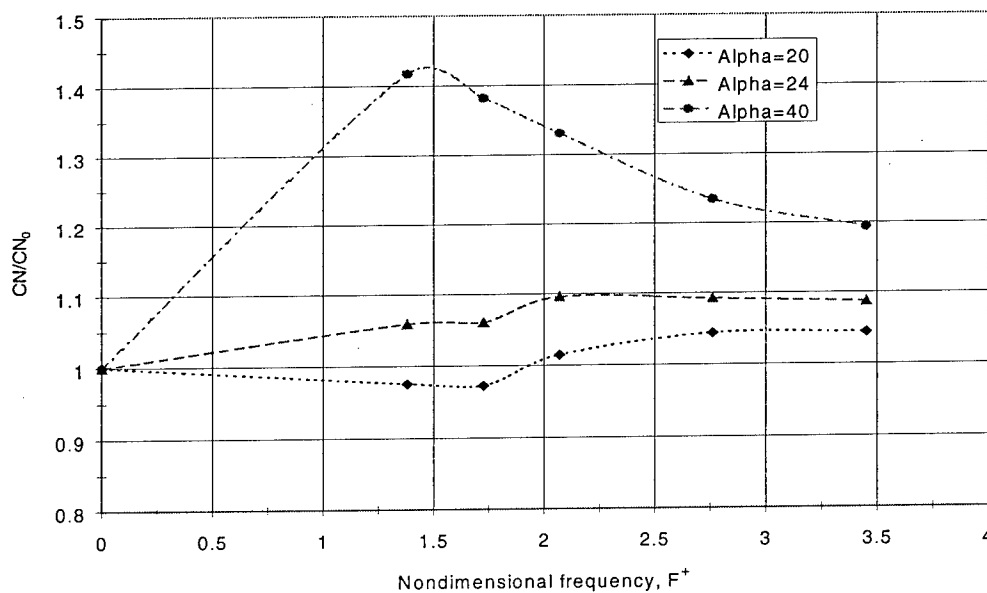
Figure 1: The variation of the normal force coefficient with the nondimensional frequency, $C_\mu=0.004$
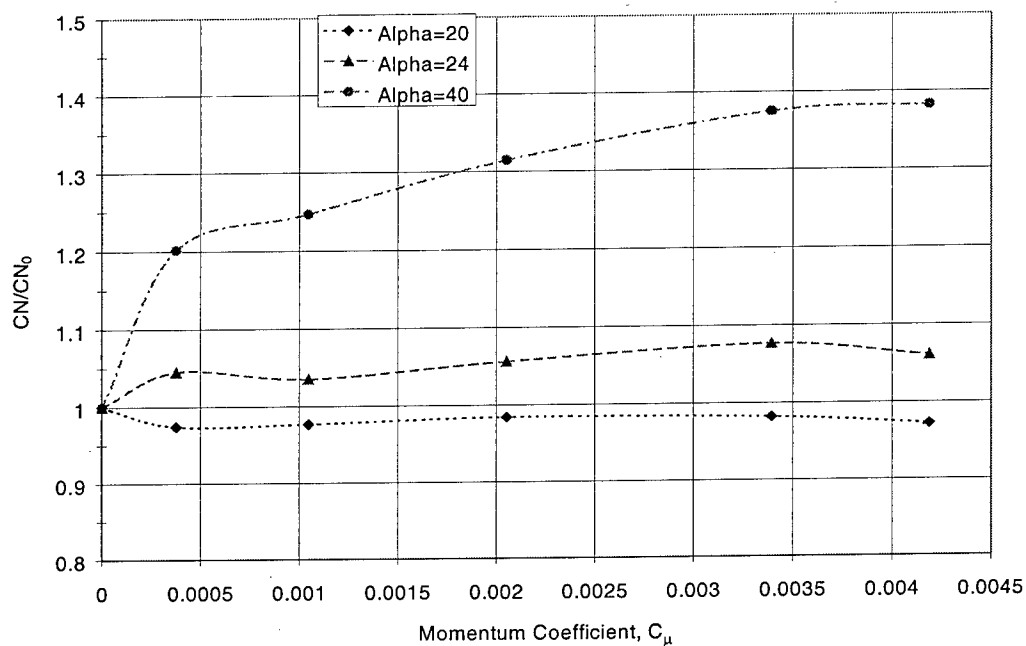
Figure 2: The variation of the normal force coefficient with the momentum coefficient, $F^+=1.7$

Sample results are presented in Figures 3 and 4. The axial location of the vortex breakdown, for several values of the nondimensional excitation frequency is presented in

Fig. 3. The effect of the periodic blowing and suction on the velocity across the vortex core is presented in Fig. 4.

Figure 3: Axial location of the vortex breakdown

Figure 4: The effect of the periodic blowing and suction on the velocity across the vortex core. Axial location X/C=0.5, α=30°, flow excitation at F^+=1.5.

References:
1. Morrow, J. A., McLaughlin, T. A and Guy, Y.: "Delta Wing Vortex Breakdown Control", AFOSR Turbulence and Internal Flows/Unsteady Aerodynamics Contractor Meeting, Aug. 19998, Annapolis, MD.
2. Guy, Y., Morrow, J. A. and McLaughlin, T. A.: "Control of Vortex Breakdown on a Delta Wing by Periodic Blowing and Suction", AIAA Paper 99-0132, 1999.
3. Guy, Y., Morrow, J. A., McLaughlin, T. A. and Wygnanski, I.: "Pressure Measurement and Flow Field Visualization on a Delta Wing with Periodic Blowing and Suction", AIAA Paper 99-4178, 1999.
4. Guy, Y., Morrow, J. A., McLaughlin, T. A. and Wygnanski, I.: "Parametric Investigation of the Effects of Active Control on the Normal Force on a Delta Wing", submitted to the 38th AIAA Aerospace Sciences Meeting, Reno, NV, 2000.
5. Guy, Y., Morrow, J. A., McLaughlin, T. A. and Wygnanski, I.: "Velocity Measurements on a Delta Wing with Periodic Blowing and Suction", submitted to the 38th AIAA Aerospace Sciences Meeting, Reno, NV, 2000.

WEAKLY COMPRESSIBLE DESCRIPTIONS OF TURBULENCE IN COMPRESSIBLE FLOWS

Robert D. Moser
Department of Theoretical and Applied Mechanics
University of Illinois, Urbana-Champaign

Motivation and Objectives

A large fraction of the effort in turbulence research, including numerical simulations, experiments, theory and modeling, has been directed toward incompressible turbulence. This is largely due to the simplifications that the incompressible assumption allows, and to the belief that turbulence is in essence an incompressible phenomenon. However, many of the flows of technological interest are compressible (e.g. external aerodynamics, propulsion systems) leading to the requirement that our understanding of incompressible turbulence be translated to these compressible flows. An example of this is that most commonly used turbulence models for compressible flows are modifications of models developed for incompressible flows (e.g. the k-ϵ model).

Fortunately, in many flows the small-scale turbulence is nearly incompressible, albeit with non-constant density, even though the flow itself is highly compressible. For example, in much of the literature on compressible boundary layers (see the review by Spina et al., 1994), differences relative to an incompressible boundary layer (up to $M = 5$, say) are understood as being caused by variations in the mean density across the layer. This has long been appreciated and is the basis of the Van Driest (Van Driest 1951, 1956) transformation and the Morkovin hypothesis (Morkovin 1961).

These observations suggest that a formulation based on low Mach number asymptotics, in which the turbulence is treated as weakly compressible while the mean is considered to be fully compressible, would provide a good description of the boundary layer to quite large Mach numbers, and a rational basis for the development of compressible turbulence models. Furthermore, such a formalism would allow the effects of compressibility on the turbulence to be precisely defined and quantified, and provide a framework for the understanding of the large qualitative differences in compressibility effects between wall-bounded and free shear flows. The research under this grant is aimed at developing such an asymptotic formulation for the description of compressibility effects in compressible turbulent shear layers.

Approach

The starting point for the analysis required for the development of our weakly compressible turbulence description is the asymptotic analysis of Zank & Matthaeus (1991). However, examination of DNS fields, indicates that in fact the Zank & Matthaeus formulation is inadequate for analysis of the boundary layer, and presumably compressible shear layers in

general. To generalize, we consider a representation of the compressible fields as follows:

$$\mathbf{u} = \mathbf{u}_I + \varepsilon(\mathbf{u}_t + \mathbf{u}_a), \tag{1}$$

$$p = 1 + \varepsilon^2(p_I + p_a), \tag{2}$$

$$T = \frac{\gamma}{\gamma - 1} + \varepsilon T_t + \varepsilon^2 T_a, \tag{3}$$

$$\rho = 1 + \varepsilon \rho_t + \varepsilon^2 \rho_a; \tag{4}$$

where subscript 'I' denotes the nontrivial incompressible part, subscript 't' denotes the variable temperature (thermal) part and subscript 'a' denotes the acoustic part. This along with the assertions that the incompressible velocity is divergence free, and that the compressible components vary on a time scale a factor of ϵ shorter than the non-acoustic variables, allow the compressible Navier-Stokes equations to be decomposed into equations for acoustic and non-acoustic variables. For example, the equation for the acoustic acoustic velocity is:

$$\frac{\partial u_{ai}}{\partial t_a} + \varepsilon\left(\frac{\partial u_{ai}}{\partial t_I} + u_{Ij}\frac{\partial u_{ai}}{\partial x_j}\right) = -\frac{\partial p_a}{\partial x_i} + \varepsilon\left(\rho_t\frac{\partial p_a}{\partial x_i} + \frac{2}{Re}\frac{\partial s_{aij}}{\partial x_j}\right) + O(\varepsilon^2), \tag{5}$$

and for the non-acoustic velocity is:

$$\frac{\partial u_{Ii}}{\partial t_I} + u_{Ij}\frac{\partial u_{Ii}}{\partial x_j} + \varepsilon\left(\frac{\partial u_{ti}}{\partial t_I} + u_{tj}\frac{\partial u_{Ii}}{\partial x_j} + u_{Ij}\frac{\partial u_{ti}}{\partial x_j}\right) = -\frac{\partial p_I}{\partial x_i} + \frac{2}{Re}\frac{\partial s_{Iij}}{\partial x_j} \tag{6}$$

$$+ \varepsilon\left(\rho_t\frac{\partial p_I}{\partial x_i} + \frac{2}{Re}\left(-\rho_t\frac{\partial s_{Iij}}{\partial x_j} + \frac{\partial \mu_t s_{Iij}}{\partial x_j} + \frac{\partial s_{tij}}{\partial x_j}\right)\right) + O(\varepsilon^2)$$

Note that to leading order, the equations for the acoustic velocities are those of linear acoustics in a uniform medium, and to the next order, they are the equations for linear acoustics through a turbulent medium defined by the incompressible and thermal fields. To leading order, the non-acoustic equations are the incompressible equations, and to next order they are the incompressible variable density equations. This is in essence a formal asymptotic version of the postulated decomposition of Chu & Kovaszney (1957).

To make use of this result in analyzing compressible turbulence, one must be able to actually determine the acoustic and non-acoustic portions of a compressible turbulent field. Thus, we extend the analysis to the fluctuations in a Reynolds (or Favre) decomposed turbulence, so that the mean is treated as fully compressible, while the turbulence is weakly compressible. satisfying equations similar to (5) and (6). A numerical decomposition procedure is then used to determine the acoustic and non-acoustic components of a compressible turbulent field obtained from Direct Numerical Simulation (DNS). DNS is an ideal source of data for this purpose, since virtually any quantity of interest can be determined from the simulation fields. The resulting decomposition can then be used as a basis for analysis and modeling of compressibility effects in turbulence.

To address the observed differences in the effects of compressibility on wall-bounded and free shear flows, the analysis and evaluation of DNS data will be done for two compressible turbulent shear layers, the flat-plate boundary layer and the mixing layer. Since not all the required simulations are currently available, particularly for the mixing layer, some
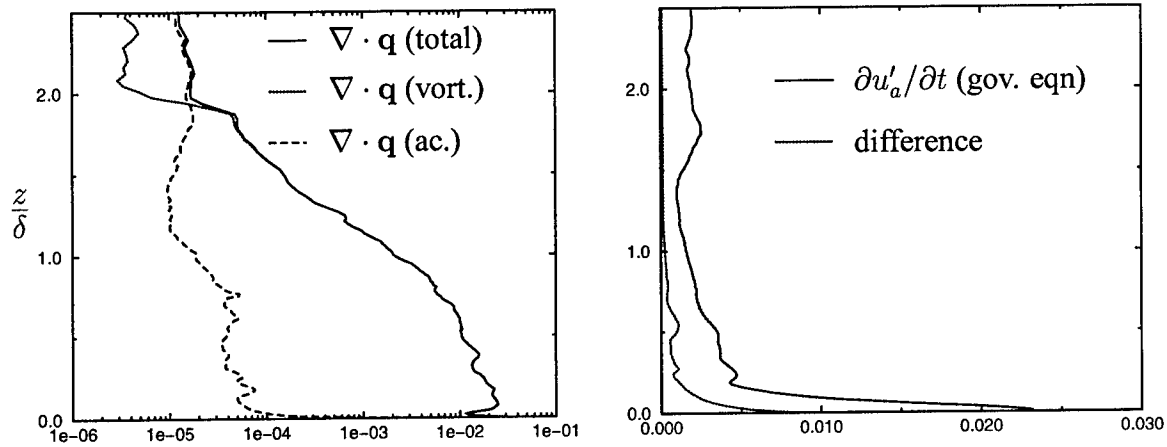
Figure 1: RMS profiles of the heat flux divergence (left) based on the total field, the non-acoustic field and the acoustic field, and the time derivative of acoustic u (right) as computed from linear acoustics, and the difference between this and the actual time derivative.

simulations must be performed as part of this effort. The code used to perform the required simulations is based on a Fourier/B-Spline representation, which provides a high-order, high resolution non-dissipative numerical approximation to the Navier-Stokes equations.

Three major activities in this research have been pursued, the development and evaluation of the decomposition into acoustic and non-acoustic fields for the boundary layer using existing DNS data (Guo & Adams, 1994); simulation and analysis of a compressible boundary layer to overcome the shortcomings of the Guo & Adams data; and preparations for the simulation of compressible mixing layers. Results from these activities are outlined below.

Decomposition of Turbulent Fields

The decomposition algorithm begins with the lowest order non-acoustic pressure equation:

$$\gamma \overline{p} \frac{\partial u'_{nk}}{\partial x_k} = \frac{\gamma - 1}{Pr\,Re} \frac{\partial q'_{nk}}{\partial x_k}, \tag{7}$$

where here the subscript "n" indicates the non-acoustic component (i.e. both the incompressible and thermal components), and q is the heat flux. If we assume that the heat flux due to acoustic fluctuations is negligible so that the non-acoustic heat flux on the right hand side can be replaced with the total heat-flux, then this is an equation for the divergence of the non-acoustic velocity. This approximation is asymptotically valid, and as shown in figure 1, the acoustic heat flux is indeed very small throughout the boundary layer.

Given the non-acoustic velocity divergence, the acoustic velocity divergence is known by difference and this is enough to determine the acoustic components of all the other variables. In the simplest case of negligible mean flow gradients, this is accomplished by noting that the acoustic field is irrotational and isentropic. A decomposition based on this assumption was applied to boundary layer turbulence. The negligible mean gradient assumption is not expected to be valid very near the wall where the mean gradients are very large. To asses how good the decomposition is, we can check if the acoustic component and the

thermal component actually satisfy the equations we assumed they did. For example, the difference between actual time derivative of the acoustic component of u and that computed from linear acoustics is also shown in figure 1. Note that the difference is relatively small, except for near the wall, where we expect this simple version of the decomposition to break down

Having performed the decomposition, we can determine the magnitude of the coupling between the acoustic and turbulent fields and the most significant terms are indeed small. Thus even at the relatively high Mach number of 4.5, the turbulence appears to be substantially decoupled from the acoustics. This is not to say that the acoustic fluctuations are necessarily small, they just have minimal effect.

To refine the decomposition, one needs to lift the restriction of negligible mean flow gradients. The problem then is to determine the acoustic flow components given only the divergence of the acoustic velocity and its time derivative, which is also known. This can be accomplished using a technique similar to that of Coleman, Kim & Moser (1995). First the eigen modes of the Euler equations (or the Navier-Stokes equations) linearized about the mean are determined, and the acoustic modes are identified. Then, the acoustic divergence and its time derivative are expanded in terms of the divergence of the eigen modes as follows:

$$\nabla \cdot \mathbf{u}_a = \sum_j b_j \nabla \cdot \mathbf{u}_a^j \tag{8}$$

$$\frac{\partial \nabla \cdot \mathbf{u}_a}{\partial t} = \sum_j i\lambda_j b_j \nabla \cdot \mathbf{u}_a^j \tag{9}$$

where $\mathbf{u}_a^j$ is the jth acoustic eigen mode. This is sufficient to determine the expansion coefficients b_j. The acoustic velocities, pressures and temperatures can then be determined from the eigenfunction expansion. This procedure is currently being developed and implemented.

Once the refined decomposition procedure is implemented, it will allow us to directly determine the impact of compressibility on the turbulence. This analysis will be applied to DNS data, including that of Guo & Adams (1994) up to $M = 6$, and the more reliable data of Guarini et al. (1999) at $M = 2.5$. Further, a similar analysis of free shear flows is planned in which we hope to learn more about the observed differences from wall bounded flows in compressibility effects. Finally, and most important, the results of this analysis will be applied to the problem of turbulence modeling to address the modeling of compressibility effects.

New Boundary Layer Simulations

A simulation of a boundary layer at $M = 2.5$ in a much larger domain than that of Guo & Adams was performed and is reported in Guarini et al. (1999). The simulation uses an advanced numerical method based on B-spline expansion functions (the method is being further refined, see below), and is arguably the most reliable compressible turbulent boundary layer DNS currently available. In addition to providing data for the analysis described above, these simulations were analyzed to evaluate several conventional descriptions of
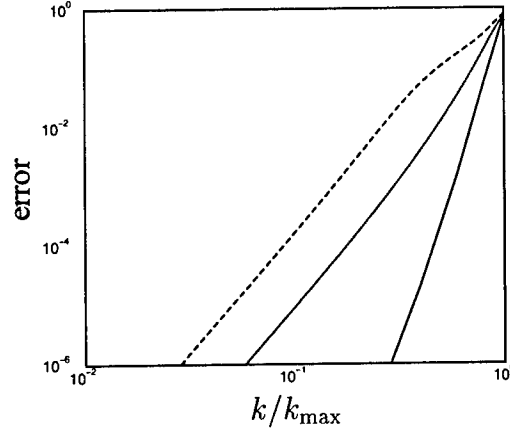
Figure 2: L_2 error in the representation of the complex exponential with wavenumber k for —— B-spline collocation, ······· B-spline Galerkin and - - - - finite element Galerkin for approximations yielding matrices of bandwidth of 7 (7th order splines for collocation, 3rd order splines or finite elements for Galerkin). k_{max} is $2\pi/\Delta$, where Δ is the knot spacing.

compressibility effects in compressible boundary layers. The most remarkable result of this analysis is that the Strong Reynolds Analogy (SRA), as commonly used in the analysis and modeling of compressible boundary layers, is incorrect. It turns out that the fundamental idea behind the SRA, an analogy between the turbulent momentum and energy transfers, is valid, but its usual expression as the SRA proposed by Morkovin (1961) is flawed (see Guarini et al., 1999).

Compressible Free Shear Simulations

The third activity currently being pursued is in preparation for performing further simulations of compressible shear layers, particularly free shear layers. It has been apparent for some time that the B-spline/Fourier numerical simulation code used for the compressible boundary layer simulations of Guarini et al. (1999) could be significantly faster. The reason for the inhibited speed is the much greater complexity of the the compressible Navier-Stokes equations relative to the incompressible equations. With these more complicated equations, the Galerkin projection used in the code, which has been used to good effect in previous DNS codes, comes at a high price. Furthermore, analysis of the B-spline collocation technique indicates that it in fact has better resolution properties at a given cost of computing derivative, and will allow much faster computation of the nonlinear terms.

An evaluation was conducted of the relative resolution properties of various numerical schemes, including finite difference, finite element, B-spline Galerkin and B-spline collocation schemes. It is on the basis of this analysis that B-spline collocation was determined to be superior to these other formulations for turbulence simulations. An example result from this evaluation is shown in figure 2, where the error of representing the complex exponential is plotted as a function of wavenumber for schemes with a matrix bandwidth of 7 (7th order splines for collocation, 3rd order splines or finite elements for Galerkin). Note that B-spline collocation significantly out-performs the other methods.

179

For this reason, our compressible shear layer code has been reimplemented using the B-spline collection method. It is beginning to be used for compressible flow simulations. A time-developing compressible plane mixing layer will be simulated to provide data for the analysis discussed above.

Other Information

Acknowledgment/Disclaimer

References

S. Borodai and R. D. Moser 1999 The decomposition of compressible boundary layer turbulence into acoustic and variable density parts. In preparation *J. Fluid Mech.*.

G. N. Coleman, J. Kim, & R. D. Moser 1995 A numerical study of turbulent supersonic isothermal-wall channel flow. *J. Fluid Mech.* **305**, 159-183.

B.-T. Chu & L. S. G. Kovasznay 1957 Non-linear interactions in a viscous heat-conducting compressible gas. *J. Fluid Mech.* **3**, 494–514.

S. E. Guarini, R. D. Moser, K. Shariff & A. Wray 1999 Direct numerical simulation of a supersonic turbulent boundary layer at $M = 2.5$. Submitted to *J. Fluid Mech.*

Y. Guo and N. A. Adams 1994 Numerical investigation of supersonic turbulent boundary layers with high wall temperature. *Proceedings of the 1994 Summer Program of the Center for Turbulence Research,* Stanford University, 245.

W. Y. Kwok, R. D. Moser and J. Jimenez 1999 A critical evaluation of the resolution properties of B-spline and compact finite difference methods. In preparation for *J. Comput. Physics.*

M. V. Morkovin 1961 Effects of compressibility on turbulent flows. In *Mecanique de la Turbulence,* ed. A. Favre, 367-380.

E. Spina, A. Smits, and S. K. Robinson 1994 The Physics of Supersonic Turbulent Boundary Layers. Ann. Rev. Fluid Mechanics, **26**, 287.

E. R. Van Driest 1951 Turbulent Boundary Layer in Compressible Fluids. J. Aeronaut. Sci., **18**, 145.

E. R. Van Driest 1956 On Turbulent Flow Near a Wall. J. Aeronaut. Sci., **23**, 1007.

G. P. Zank and W. H. Matthaeus 1991 The equations of nearly incompressible fluids. 1. Hydrodynamics, turbulence and waves. Phys. Fluids A, **3**, 69-82.

TOWARDS OPTIMUM FORMULATIONS OF LARGE EDDY SIMULATION OF TURBULENCE

R. D. Moser, S. Balachandar and R. J. Adrian
Department of Theoretical and Applied Mechanics
University of Illinois, Urbana-Champaign

Motivation and Objectives

One of the most promising techniques for the prediction of turbulent flows is that of Large Eddy Simulation (LES), in which an underresolved representation of the turbulence is simulated numerically by modeling the effects of the unresolved small-scales on the simulation. Such simulations have been applied in several flows with reasonable success. However, there are several outstanding problems that need to be addressed before LES can fulfill its promise as a tool for turbulence prediction in engineering flows. The most serious problems limiting the usefulness of LES is the representation of turbulence near walls and other strong inhomogeneities. Other difficulties include the dependence of models on the filter and/or numerical discretization, the treatment of inhomogeneous filters and the lack of understanding of the modeling errors and their impact.

Our objective in this research is to address these issues and develop a rigorous framework in which to develop and analyze LES models and simulations. The basis for this analysis is an optimum LES formulation discussed below.

Approach

The starting point for the development of LES is the definition of a spatial filter $\tilde{\cdot}$, which can be applied to the Navier-stokes equations to obtain an equation for the filtered velocity $\tilde{u}_i$:

$$\frac{\partial \tilde{u}_i}{\partial t} = -\frac{\partial \tilde{u}_i \tilde{u}_j}{\partial x_j} - \frac{\partial \tilde{p}}{\partial x_i} + \frac{1}{\text{Re}} \frac{\partial^2 \tilde{u}_i}{\partial x_j \partial x_j} + M_i, \tag{1}$$

Where M_i is the sub-grid model (force) term, which includes the divergence of the sub-grid stress as well, as terms that arise when the filter does not commute with differentiation. The problem in LES of course is to model M_i. A very important result of our research (Langford & Moser, 1999) is that an LES w will match the one-time statistics of filtered turbulence $\tilde{u}$ if and only if the model $m_i(w)$ of M_i is given by

$$m_i(w) = \langle M_i(u) | \tilde{u} = w \rangle \tag{2}$$

This model also minimizes the difference between M_i and m_i (in the mean-square sense), and so this model has all the properties that one could ask of a sub-grid model. We therefore call it the ideal sub-grid model.

Unfortunately, the conditional average in (2) cannot practically be determined, since the conditions are that the entire filtered velocity field match the entire LES field. However, it can be estimated using stochastic estimation (Adrian et al, 1989) which is a well-established
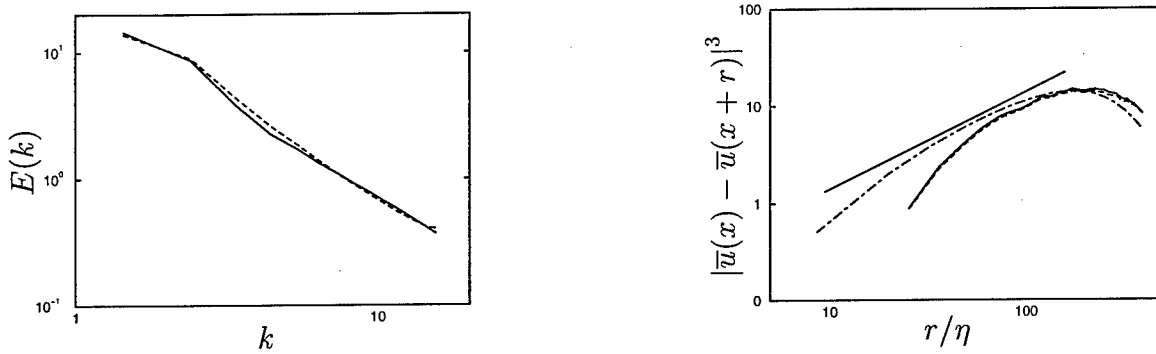
Figure 1: The (a) 3-D energy spectrum and (b) third-order structure function for filtered DNS (———), optimal linear LES (- - - -) and in (b) the unfiltered DNS (- · - · -). In (b) the straight line indicates a slope of 1, which is the inertial range result.

technique for estimating conditional averages. To perform stochastic estimation one requires large quantities of two-point correlation data. For example, in linear estimation one needs $\langle \tilde{u}_j(\mathbf{x}')\tilde{u}_k(\mathbf{x}'')\rangle$ and $\langle M_i(\mathbf{x})\tilde{u}_k(\mathbf{x}'')\rangle$.

It would clearly not be useful if for every flow in which one was to perform an LES, large quantities of correlation data had to be gathered. Thus the approach taken in this research is to develop estimation-based models for a few representative model problems, and to use this experience to devise new model formulations that will be more broadly applicable. The model flows being used are isotropic turbulence, turbulent channel flow and a bluff-body wake.

DNS is an obvious source for the required correlation data, but DNS is limited to low Reynolds number. On the other hand, it is difficult to get three-dimensional data from physical experiments. To avoid these weaknesses we use both DNS data and two-dimensional experimental data from PIV (particle image velocimetry) to extrapolate the three-dimensional data to higher Reynolds numbers.

Isotropic Turbulence
Using direct numerical simulations of forced isotropic turbulence at $Re_\lambda = 164$, the correlation data required for one-point linear and quadratic estimation was gathered for three Fourier-cutoff filters. In addition, for the coarsest filter, a variety of estimation terms were considered, these include cubic terms suggested by RNG analysis of Zhou & Vahala (1993), and terms constructed to subsume Smagorinsky and scale-similarity models (see Langford & Moser, 1999 for details). An estimate was constructed using all of these terms, which included 46 different terms in all.

The mean square errors of these estimates were measured as a function of wavenumber and normalized by the magnitude of the sub-grid term. These errors are quite large (of order 1), suggesting that the estimates are rather poor approximations of the sub-grid terms. There is reason to suspect that this is because the irreducible error associated with (2) is large, rather than it being due to errors in approximating the conditional average. It may thus be that in isotropic turbulence with Fourier cut-off filters, the LES sub-grid term is largely unpredictable, except for the energy transfer (dissipation) represented by the linear term. This would explain why simple eddy viscosity models such as Smagorinsky work rather
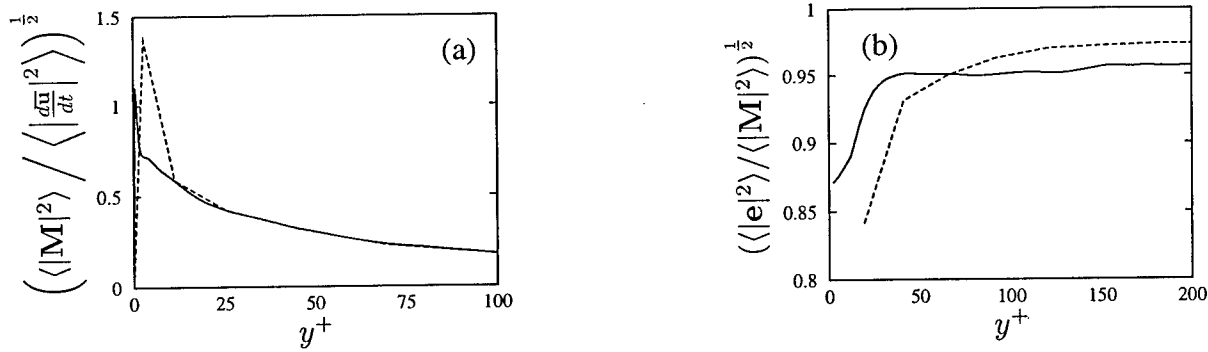
Figure 2: Results of analysis of the turbulent channel near the wall (y coordinate is in wall-units, where the center of the channel is at $y^+ = 590$). (a) The magnitude of the sub-grid term normalized by the magnitude of the filtered time-derivative and (b) the magnitude of the relative error in estimating the sub-grid term, with no wall-normal filter (———) and Chebychev filter (– – – –).

well in many flows, though their correlation with the actual sub-grid stress in *a priori* tests is poor. To further test the validity of the estimation models, LES were performed using both the linear and quadratic estimates. Results for spectra and third-order structure function are shown in figure 1. The results for the LES are remarkably good. Though it is interesting to note that the third-order structure function of the filtered turbulence does not match that of the unfiltered turbulence, even for large separation.

The isotropic turbulence analysis is being extended to include different filters and local estimates. In particular, a formulation using a finite-volume type filter is being pursued to obtain "LES finite volume flux models."

Turbulent Channel Flow
An analysis similar to that described above is being pursued for turbulent channel flow at friction Reynolds number $Re_\tau = 590$, using DNS data from Moser, Kim & Mansour (1999). The filters used for these studies include Fourier cut-off filters in the streamwise and spanwise directions. In the wall-normal direction several filters have been used, including no filtering, and Chebychev cut-off filter. Also, a cut-off filter defined in terms of POD eigenfunctions is currently being pursued.

Preliminary results of this analysis are shown in figure 2. Unlike the case of isotropic turbulence, near the wall, the magnitude of the sub-grid force term can be as much as 70% of that of the filtered time derivative (note that we are not counting the sharp peak near the wall which appears to be associated with imposition of boundary conditions). It is also interesting that, except for the peak near the wall, the curves for the two y filters shown (no-filter and Chebychev filter) are essentially identical. This suggests that the effects of commutation error are not particularly significant. Also shown in figure 2 is the relative error in estimating the sub-grid force term. Away from the wall, the relative error is of order 95% consistent with the isotropic turbulence results. Near the wall, the relative error is smaller (as small as 80%), but this does not make up for the relatively large error near the wall. Thus the relative error in estimating the time derivative will be significantly larger near the wall than away. The consequences of this are not clear at this time.

Bluff Body Wakes

Large eddy simulation of wake flows pose unique challenges. The wake as a whole has a wide range of length and time scales, but the dynamics is controlled by the thin shear layers that separate from either side of the bluff body. This poses interesting challenges to accurate implementation of large eddy simulation since the dynamically significant thin shear layers must be filtered out, while their effect on the wake dynamics must be modeled. Two different model problems are being pursued to develop optimum LES formulations for such wake flow simulations: 1) optimal two-dimensional projections of a flat-plate wake, and 2) Optimal LES formulations for a cylinder in a cross-flow.

One can define an LES filter to be the average in one spatial direction (spanwise in this case), and this is appropriate in the case of a bluff body wake since wakes are commonly dominated by two-dimensional structures. Here the optimal estimation approach is applied to such a two-dimensional projection in the flow over a flat plate held normal to a cross-flow at $Re = 250$ (based on plate height and free-stream velocity). The two-point correlations required to perform the estimations were obtained from the direct numerical simulation of (Najjar & Balachandar, 1998; Balachandar, Mittal & Najjar, 1997). The formulation used here differs from (1), in that the vorticity equation is used, and the sub-grid torque, rather than sub-rid force is modeled.

Some important outcomes of this investigation include: 1) The contribution of the sub-grid torque to the two-dimensional dynamics is significant. 2) A gradient diffusion model is inadequate for predicting the dynamics of the two-dimensional projection. 3) For inhomogeneous flows, limited statistical sample introduces difficulties, which have been addressed using a novel eigen projection technique. 4) The best closure results in large errors (about 60%), consistent with the isotropic turbulence and channel results. 5) The improvement of the quadratic closure over the linear closure is not significant.

In the case of cylinder in a cross flow, a spectrally accurate code is being used to perform DNS to obtain the necessary correlations for optimal estimation. Simulations have been performed for a reasonably high Reynolds number of 1500. Particular care is being taken to assure that all features of the attached boundary layer, the separated shear layers and the wake are adequately resolved. We plan to collect data spanning 10 or more shedding cycles based on which the requisite two-point correlations will be computed. Subsequently we plan to employ the optimal closure procedure to develop optimal filters and sub-grid models suitable for the wake flow simulation.

High Reynolds Number Correlations

The correlations obtained from DNS of wall-bounded flows are limited to low Reynolds number, but they are needed at high Reynolds number. To address this problem, we look for general scaling properties in the space-time correlations of wall turbulence, so that results of low Reynolds number DNS can be extended to higher Reynolds number. We have taken a two-pronged approach to this problem, one based on developing deeper physical insight into the structure of turbulent eddies using DNS of special eddy systems, and the other based on experiments that allow us to obtain data on the space time correlations beyond the Reynolds numbers attainable via DNS.

In scaling the two-point correlations of wall-bounded flows, the unexplained long tail in
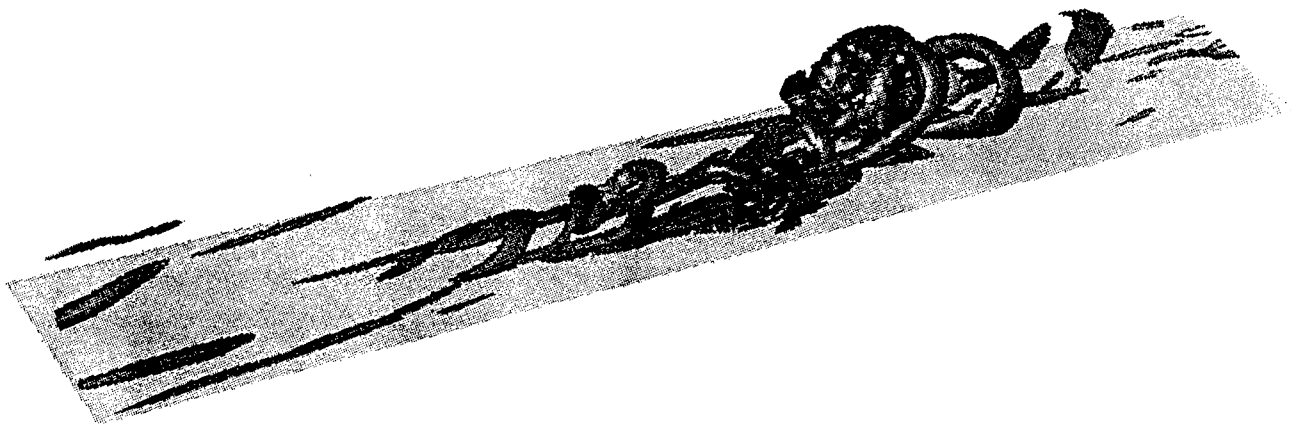
Figure 3: Hairpin packet that evolves out of a lightly noisy initial hairpin.

the streamwise correlation function of the streamwise velocity, first observed by Townsend (1958) and Grant (1958). Recent experimental results by Meinhart & Adrian (1995) suggest that the long correlation is associated with the streamwise alignment of hairpin-like eddies. The scaling of the small eddies and the scaling of the length of the packet (i.e. the length of the long correlation tail) differ. This sort of mixed scaling is difficult to untangle without a physical model for guidance. Hence the thrust towards understanding the eddy structure that underlies the structure of the correlation functions.

In previous work, Zhou, et al (1999) showed how one hairpin eddy of sufficient strength in a clean, non-turbulent background flow field could generate a long packet. It was the cause of some concern that these packets had not been observed in DNS, so an effort was initiated to search for them in a $Re_\tau = 300$ channel DNS, using the tools of Zhou et al. Indeed, many hairpin packets were found, but they contained many short, convoluted segments of vortices, unlike the ideal vortices simulated by Zhou et al. However, by adding low-amplitude noise to the initial eddy in a simulation like that of Zhou et al, the field shown in figure 3 results. It contains a hairpin packet with many convoluted eddy segments, much like those in the fully turbulent channel flow. This is all further evidence that hairpin packets are an important feature of near-wall turbulence.

To allow direct comparison with results of channel flow DNS, a channel flow facility has been constructed using air flow. It is 2in high, 24in wide, and 216in long, with glass windows to allow access for PIV and LDV measurements. The tunnel is capable of matching precisely the Reynolds numbers of the available DNS ($Re_\tau = 150$, to 590), and its highest Reynolds number, $Re_\tau = 1800$, gives us a 12:1 range over which we can test scaling. To obtain the best possible spatial resolution, we use super-resolution software that gives 10 times more vectors and about 3 times better linear resolution than standard interrogation techniques. This yields a resolution of $30\mu m = 2$ viscous length scales or one Kolmogorov scale.

The channel flow apparatus is instrumented with a 2 camera TSI PIV system capable of taking sequential velocity fields with time delay less than $50\mu s$. This system is being used to measure the space-time correlation for small time delays and long time delays.

Other Information
Supported under this grant in whole or in part over the last year have been Stefan Volker,

185

Jacob Langford, John Wu, Ken Christensen and Arup Das graduate students in the MIE (Volker) and TAM departments at the University of Illinois. The work supported here was presented at the 1997 and 1998 meetings of the Division of Fluid Dynamics of the American Physical Society, the 1998 Canadian Congress on Applied Mechanics (Hamilton Ontario), and the Second AFOSR International Conference on DNS and LES (Rutgers University) and several papers have been produced (Moser & Adrian, 1998; Jimenez & Moser, 1998; Langord & Moser, 1999; Moser, Langford & Volker, 1999; Najjar & Balachandar, 1999).

Acknowledgment/Disclaimer

References

Adrian, R. J., Jones, B. G., Chung, M. K., Hassan, Y., Nithianandan, C. K. & Tung, A. 1989 Approximation of turbulence conditional averages by stochastic estimation. *Phys. of Fluids* **1**, 992-998.

Balachandar, S., Mittal, R. & Najjar, F. M. 1997 Properties of the mean recirculation region in the wakes of two-dimensional bluff bodies, *J. Fluid Mech.* **351**, 167-199.

Balachandar, S. and Najjar, F. M. 1999 Optimal two-dimensional projections of wake flows, In preparation for *J. Fluid Mech.*

Berkooz, G. 1994 An observation on probability density equations, or, when do simulations reproduce statistics? *Nonlinearity* **1994** 313-328.

Grant, L. 1958 The large eddies of turbulent motion, *J. Fluid Mech.* **4**, 149.

Jimenez, J. & Moser, R. D. 1998 LES: Where Are We and What can We Expect, AIAA 98-2891, 29th AIAA Fluid Dynamics Conference, June 15-18, Alburquerque, NM (invited), also to appear in *AIAA J.*

Langford, J. A. & Moser, R. D. 1999 Optimal LES formulations for isotropic turbulence. To appear in *J. Fluid Mech.*

Meinhart, C. D. & Adrian, R. J. 1995 On the existence of uniform momentum zones in a turbulent boundary layer, *Phys. of Fluids* **7**, 694-696.

Moser, R. D. & Adrian, R. 1998 Turbulence Data for LES Development and Validation, ASME paper FEDSM98-5092, ASME Fluids Engineering Division Summer Meeting, June 20-25, Washington, DC, (invited).

Moser, R. D., Kim, J. & Mansour, N. N. 1999 Direct numerical simulation of turbulent channel flow up to $Re_\tau = 590$, *Phys. of Fluids* **11**, 943-945.

Moser, R. D., Langford, J. A. & Volker, S. 1999 Optimal LES: How Good Can and LES Be? *Proceedings of the Second AFOSR International Conference on DNS and LES*, June 7-9, Rutgers Univeristy (invited).

Najjar, F. M. & Balachandar, S. 1998 Low-frequency unsteadiness in the wake of a normal flat plate, *J. Fluid Mech.* **370**, 101-147.

Townsend, A. 1958 The turbulent boundary layer, in *Boundary Layer Research*, ed. H. Gortler, Springer-Verlag, Berlin, 1.

Zhou, J., Adrian, R. J. Balachandar, S. & Kendall, T. M. 1999 Mechanisms for generating coherent packets of hairpin vortices in channel flow, *J. Fluid Mech.* **387**, 353-396.

Zhou, Y. & Vahala, G. 1993 Reformulation of Recursive-Renormalization-Group-Based Subgrid Modeling of Turbulence, *Phys. Rev. E* **47**, 2503-2519.

MEMS ACTUATORS AT SUPERSONIC SPEEDS FOR JET EXCITATION

AFORSR CONTRACT NUMBER F49620-96-1-0459

Hassan M. Nagib, Chris S. Christophorou, Emad Alnajjar, and Drazen Fabris
Department of Mechanical, Materials, and Aerospace Engineering
Illinois Institute of Technology, Chicago, Illinois 60616

Ahmed Naguib
Department of Mechanical Engineering
Michigan State University, East Lansing, Michigan, 44

Khalil Najafi and Chun-Chieh Huang
Center for Integrated Sensors and Circuits
University of Michigan, Ann Arbor, Michigan 48109

Abstract
This study tested the capability of MEMS (micro-electro-mechanical-systems) based mechanical actuators to introduce jet instabilities at supersonic speeds. The eventual application is the control of jet screech. A MEMS device can provide a very localized perturbation into a flow. As such, an array of MEMS devices has the possibility of providing complicated forcing for fluid control applications. In the jet application the actuator forces the initial shear layer at the edge of the jet promoting a linear rollup instability. In the full configuration, up to sixteen actuators are used to force either an axisymmetric or helical mode of jet instability.

Another important question is whether the actuators are rugged enough to survive the flow conditions. An actuator redesign was attempted. The previous work focused on the design of the actuators and demonstrating the effectiveness of a single actuator. These results will also be summarized here. The actuators were capable of introducing disturbances of sizeable amplitude. The actuator positioning was found to be most important in optimizing the fluid response. Control experiments using the actuator array were less successful. The natural resonant frequency of the individual actuators varied slightly, due to their manufacturing tolerance and it was only possible to hold all the actuators in phase for a limited number of cycles (0(10)). The forcing over this limited time was not sufficient to provide a reasonable fluid response. Therefore, even with laser trimming of actuators, the current MEMS manufacturing technique does not produce sufficiently identical devices.

An extensive amount of work was also focused on associated MEMS sensors. That work is documented in the listed publications.

MEMS Devices
The actuators, shown in Figure 1, are driven by capacitive combs which produce a linear oscillatory motion. The element that moves in the flow is the "T" shapes structure at the end of the device. In the jet implementation, the actuator moves normal to the flow path

and is placed near the edge of the jet nozzle. The modified design provided a thicker and stiffer overall mechanism where the "T" structure is reinforced with cross supports. The modified design was found to be more prone to cessation under high speed conditions.

The majority of experiments were run at Ma = 0.2, 0.4, and 0.6. The actuators were found to be sufficiently resilient to operate up to supersonic speeds, but considering the complexity of the actuator array as a whole, extensive experiments were not carried out in the range of jet screech.
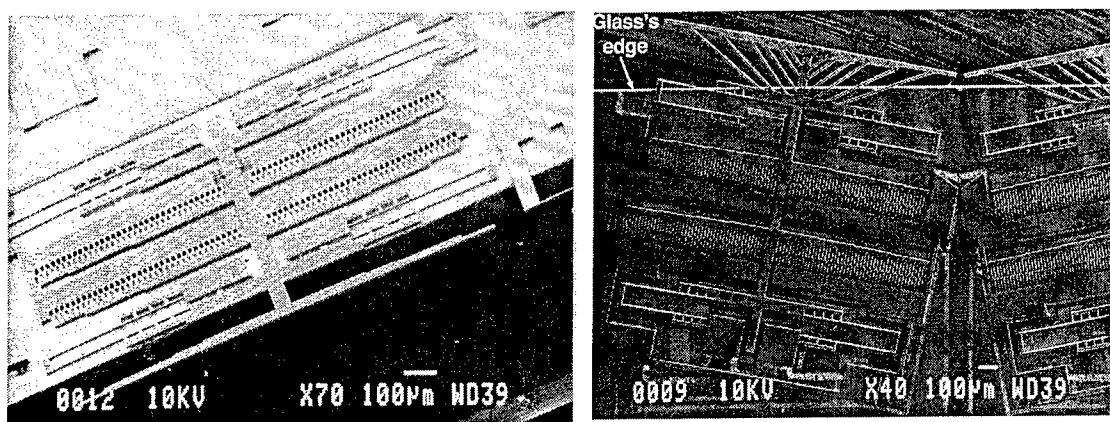

Figure 1: Magnified images of the two actuators. The earlier design on the left with the actuator on the bottom and the later design on the right with the supported actuator in the top.

Results

The actuators were shown to be effective in introducing a disturbance into the shear layer. Figure 2 shows the power spectral density at several locations downstream. A hotwire measures the velocity. At each downstream location the jet's shear layer was traversed radially and the point of maximum disturbance amplitude was recorded. In this case the forcing frequency is matched to the most unstable mode of the shear layer. The flow responds at the forcing frequency and its first harmonic.

The higher speed jet flows also showed response of sizeable amplitude, Figure 3. In all cases (Ma = 0.2, 0.4, 0.6 & 0.5 < x/λ < 1.2, λ is the wavelength of the perturbation) the dominant frequencies were the forcing frequency and its associated harmonics. In the cases where the forcing was away from the most amplified mode, the total disturbance energy is less but development is still evident. In more recent measurements, a region of exponential growth was found nearer to the actuator. When the disturbance reaches one wavelength the amplitude has saturated.

The fluid response is very sensitive to the actuator positioning in both frequency (in some instances the higher harmonics are not evident) and amplitude as shown in Figure 4. The optimum forcing was with the actuator within the shear layer one momentum thickness from the wall with a total peak to peak oscillation of half of the momentum thickness about that point. It was not possible to vary the amplitude. The actuator could be

positioned within half a momentum thickness and still have a reasonable effect on the flow.

Figure 2: Power spectral density of the velocity as a function of downstream position, Ma = 0.2, single 14 kHertz actuator ($f^* = 0.014$).
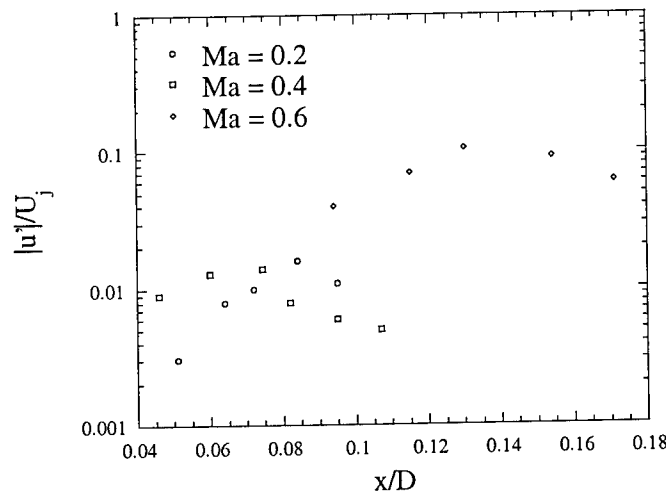
Figure 3: Disturbance level induced by one 14 kHertz actuator.

The main goal was to force with multiple actuators in either an axisymmetric or a number of helical modes. Each actuator had a different resonant frequency. Each was then started with a different phase offset in order for the array to be in the desired phase when the data is collected. The correct phase could only be held for a few cycles, about 20 with a maximum phase error of 60^0, and then the array would lose its coherence. During

the time the array was in phase the data was collected. A plot of the total amplitude of the induced disturbance is plotted in Figure 5. In addition, the generated disturbance downstream of a solo operating actuator is also shown. The array was found to be less effective in generating the disturbance. Two explanations are possible. First, the difficulty in positioning the array and running each actuator could induce enough incoherence to reduce the overall effectiveness. Second, the limited number of cycles may not be enough to provide an effective forcing.
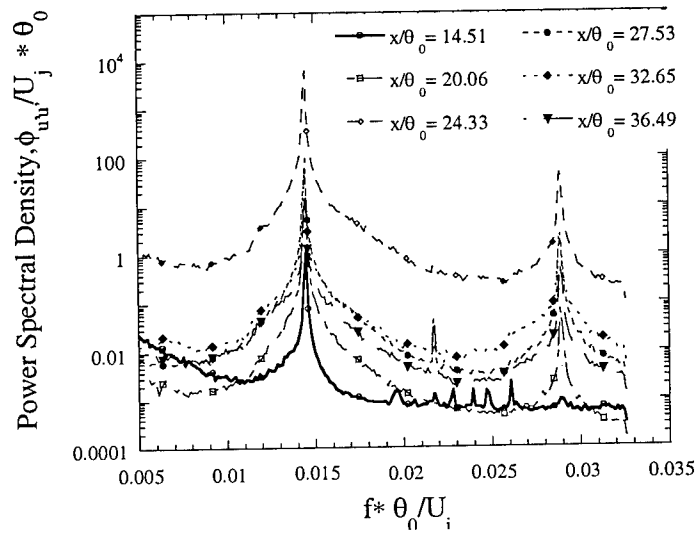
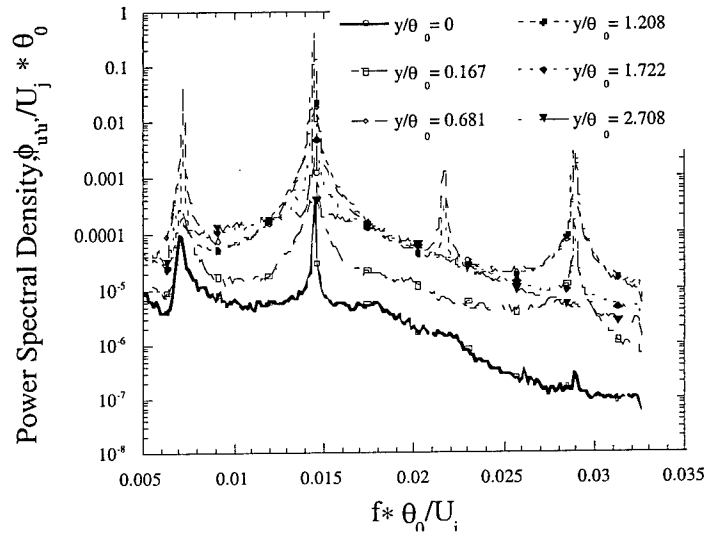Figure 4: Power spectral density of the velocity as a function of actuator positioning, Ma = 0.2, single 14 kHertz actuator ($f^* = 0.014$), y = 0 indicates the actuator is in the shear layer throughout its motion.
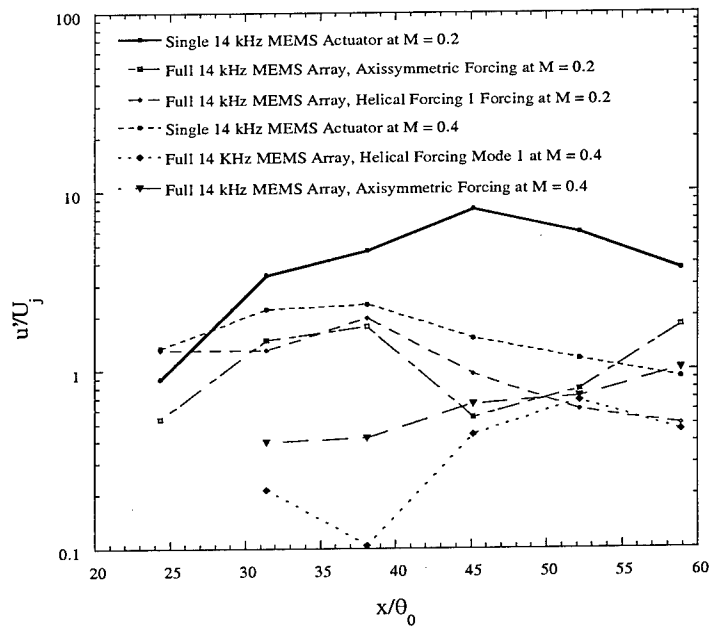
Figure 5: Measure of disturbance level under different forcing conditions.

Conclusions

The MEMS systems have a good potential as actuators due to their small size and mechanical effect, but difficulties still exist. The actuators are capable of introducing very large perturbations into the flow. They are also robust enough to survive in the supersonic range. Unfortunately, there exists variability in the resonant frequency from device to device due to the limitations of the current MEMS manufacturing technique. When combined in an array the net effect was less than anticipated.

Personnel

Hassan Nagib, Ahmed Naguib, Khalil Najafi, Drazen Fabris, faculty
Chris Christophorou, Emad Alnajjar, Elias Soupos, Chun-Chieh Huang, students

Acknowledgment/Disclaimer

Publications

A. Naguib, D. Benson, H. Nagib, C. Huang, K. Najafi, "Assessment of new MEMS-based hot wires," Proceedings of the 3rd ASME/JSME Joint Fluids Engineering Conference, July 18-22, 1999, San Francisco, CA.

A. Naguib, E. Soupos, H. Nagib, C.-C. Huang, K. Najafi, "A piezoresistive MEMS sensor for acoustic noise measurements," paper no. 99-1992, 5th AIAA/CEAS Aeroacoustics Conference, May 10-12, 1999, Bellevue, WA.

A. Naguib, E. Soupos, H. Nagib, C.-C. Huang, K. Najafi, "Characterization of a MEMS Acoustic Pressure Sensor," paper no. 99-0520, 37th AIAA Aerospace Sciences Meeting Jan. 11-14, 1999, Reno, NV.

Reference

Christophorou, Chris S., *Implementation of MEMS Based Mechanical Actuators for the Excitation of a High Speed Jet*, Masters thesis, Illinois Institute of Technology, 1998.

NEW INTERPRETATIONS FOR THE OVERLAP REGION OF TURBULENT BOUNDARY LAYERS BASED ON HIGH REYNOLDS NUMBER DATA

Hassan M. Nagib, Drazen Fabris, William Ornt, and Michael H. Hites
Department of Mechanical, Materials, and Aerospace Engineering
Illinois Institute of Technology, Chicago, Illinois 60616

Jens M. Österlund and Arne V. Johansson
Royal Institute of Technology, 100 44 Stockholm

Abstract
The present work investigates in detail an external zero pressure gradient turbulent boundary layer at relatively large Reynolds numbers. There has recently been some debate as to the behavior of the mean velocity including questions regarding the appropriate scaling and existence of an asymptotic state at high Reynolds numbers[1,2,3,4]. The essential question is whether it is sufficient to describe the boundary layer classically with an inner scale (law of the wall) and an outer scale (deficit profile) which overlap in some intermediate region. The scale and form of the overlap is important if the current understanding is to be extrapolated to Reynolds numbers of practical application. Furthermore, a detailed understanding of this flow can lead to better descriptions of more complex turbulent boundary layers.

Introduction
In the classical description, the size of the boundary layer provides an outer length scale for the flow while the turbulence is determined by a length scale dependent on the Reynolds number and related directly to the skin friction. This description characterizes the inner behavior by the law of the wall in wall units,

$$\frac{\overline{U}}{u_\tau} = f\left(\frac{y u_\tau}{\nu}\right). \tag{1}$$

The outer behavior is provided by a deficit law and a scale based on a measure of the boundary layer thickness,

$$\frac{U_\infty - \overline{U}}{u_\tau} = F\left(\frac{y}{\delta}\right). \tag{2}$$

Matching leads to a hypothesized log dependence, log law, in the overlap region,

$$\frac{\overline{U}}{u_\tau} = \frac{1}{\kappa}\ln\left(\frac{y u_\tau}{\nu}\right) + B. \tag{3}$$

This current work directly tests this analysis in two different experiments.

Boundary layer profiles were measured on a cylinder model at the Illinois Institute of Technology (IIT) by Hites[5] These data are supplemented by recent direct measurements of the skin friction used to determine the inner scale. In addition, an identical

193

set of data was collected on a flat plate at the Royal Institute of Technology at Stockholm (KTH) by Österlund[6]. These data are used to provide a detailed evaluation of the log law. In both cases, the experimental range is $4{,}100 < Re_\theta < 24{,}000$.

Results

A direct measurement of the skin friction in necessary to objectively scale the mean data. To make this measurement two methods are applied and compared. The first method uses the transient development of a small oil droplet on the wall surface to measure the stress applied to it by the boundary layer[7]. This method has been calibrated in the shear channel facility at IIT and found to be accurate to 3%. The second method fits the experimental mean velocity measurement near the wall to the law of the wall. This has typically been done for measurements below y^+ of 5 where u^+ is linear with y^+. But in the current application it is physically not possible to make an accurate measurement that close to the wall, so the experimental data in the range $6 < y^+ < 20$ is fitted to the law of the wall as determined by lower Re DNS simulations. A turbulent Couette simulation is found to be the best fit since it best approximates a uniform shear stress in this range of the profile[8,9].
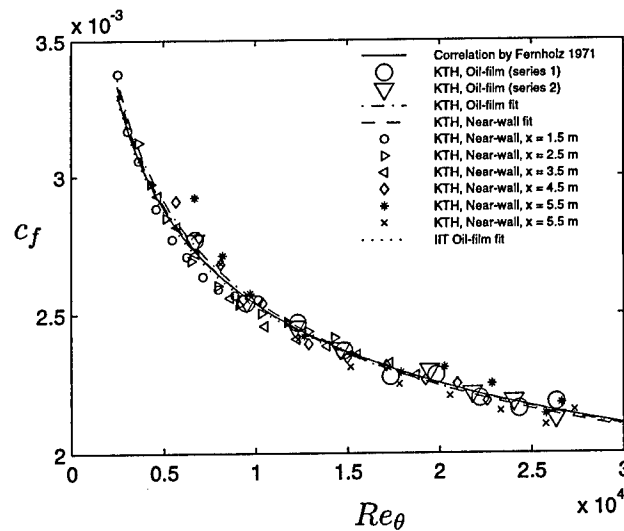
Figure 1: Skin friction coefficient.

The resulting data for the skin friction coefficient is shown in Figure 1. There is excellent agreement between the fitting method shown in small symbols and the oil method shown in larger symbols. In addition, there is also excellent agreement between the two experiments, IIT and KTH which use a axisymmetric model and a flat plate respectively. For the purpose of scaling the $\bar{u}$ data, only the skin friction coefficient derived from the oil film is used.

The mean data using the inner and outer scaling is shown in Figure 2. In both experiments and in both cases the measured shear stress is very good at scaling the

data. The resulting friction velocity is found to be very close to the friction velocity determined by the Clauser method in the previous work[10].
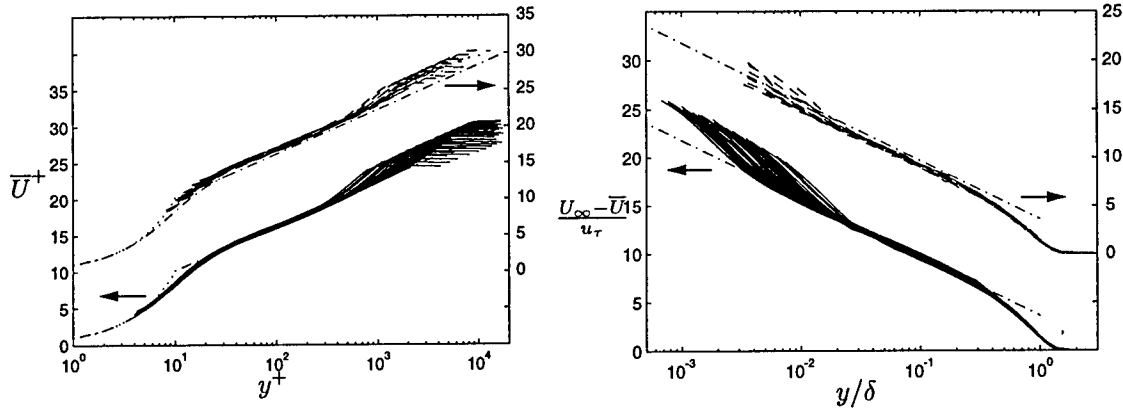
Figure 2: Mean velocity profiles at both facilities: KTH, solid lines; IIT, dashed lines. The inner scaling uses u_τ determined from the oil film measurements and the outer scale uses $\overline{U} = 0.99U_\infty$.

A more detailed analysis is attempted on the KTH data to determine the applicability of a log profile in the overlap region. A diagnostic function is defined,

$$\Xi = \left(y^+ \frac{d\overline{U}^+}{dy^+} \right)^{-1}, \tag{4}$$

which should be constant in a region of log dependence, Figure 3.
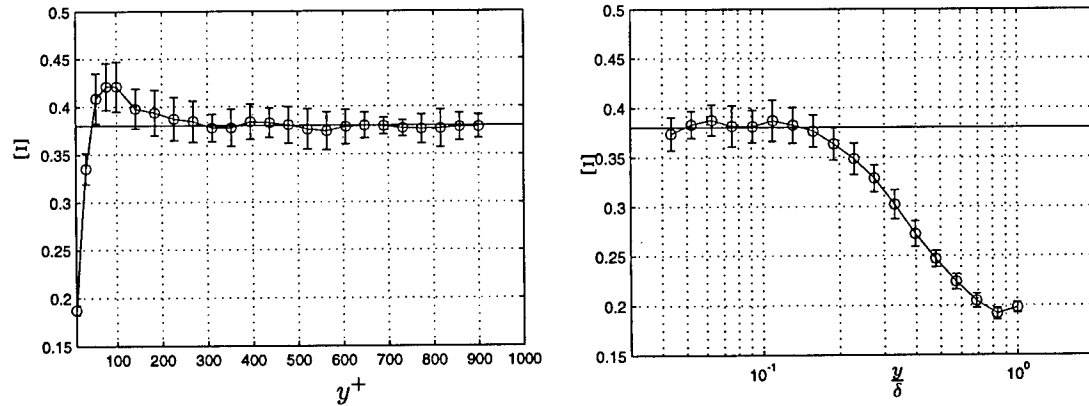
Figure 3: Diagnostic function. The function is presented on both an inner and outer scale and includes all the experimental cases. The inner scaled data truncates the outer region and the outer data truncates the inner region.

In terms of the inner scaling, the data asymptotes to the log behavior at $y^+ \sim 200$ and in the outer scaling the data fits below $y/\delta < 0.15$. Using this range the values of the von Karman coefficient, κ, and B are found to be 0.38 and 4.1. These differ

slightly from commonly accepted values which are based on the range $y^+ > 50$ to $y/\delta < 0.1$. The evaluation of κ over the range of experiments at both facilities shows no significant Reynolds number dependence if the new range is used and a significant dependence if the traditional range is used, Figure 4. This result is significant for two reasons. First, it shows agreement with traditional values if only low Reynolds number data are considered. Second, it shows the sensitivity that can be derived from the choice of the range and the difficulty in extrapolating the data to high Reynolds numbers. Considering the new range, a true overlap region does not develop until the Reynolds number exceeds 6000. In a similar analysis, a power law has been applied and shown less appropriate[8].
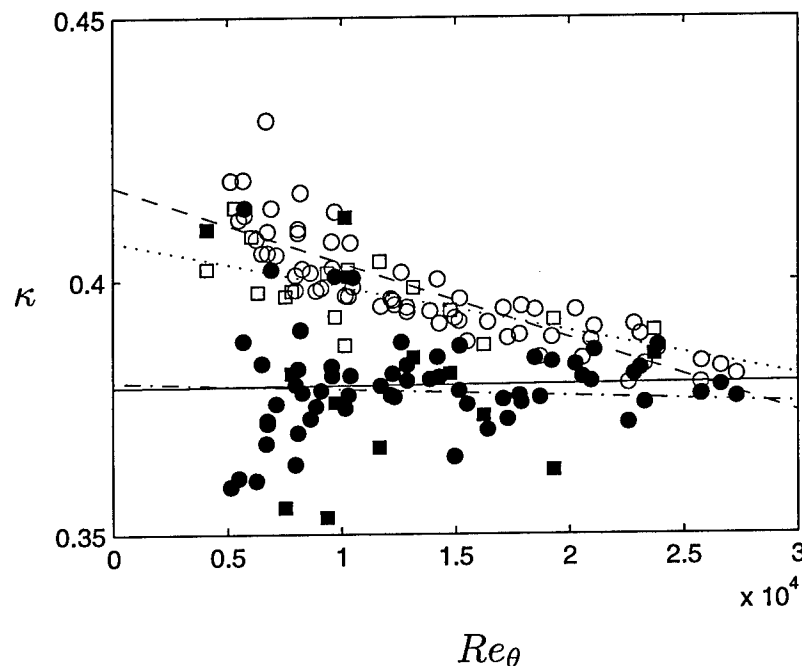
Figure 4: Value of the von Karman coefficient determined from a least squares fit using data from y^+ in the traditional range, open symbols, and the new range, closed symbols, IIT data squares, KTH data circles, lines represent fits to each set of data.

A similar argument can be made considering the spectral data at different positions in the boundary layer, Figure 5. Above y^+ of 200 the spectra is dominated by low frequencies connected to fluctuations that scale with the outer layer. For $20 \leq y^+ \leq 200$ a bimodal distribution exists in both experiments here and in previous work[11]. And at $y^+ < 20$ the high frequencies are more evident. It has been shown that this type of distribution can be constructed from representative eddies which represent wall effects and wake effects[4]. It is interesting to note that the low frequency contribution at near wall locations only develops for large Reynolds numbers, beyond the suggested 6000. It could therefore be argued that the nature of the boundary layer requires sufficient influence of wake effects into the near wall region before a reasonable log overlap can be achieved.
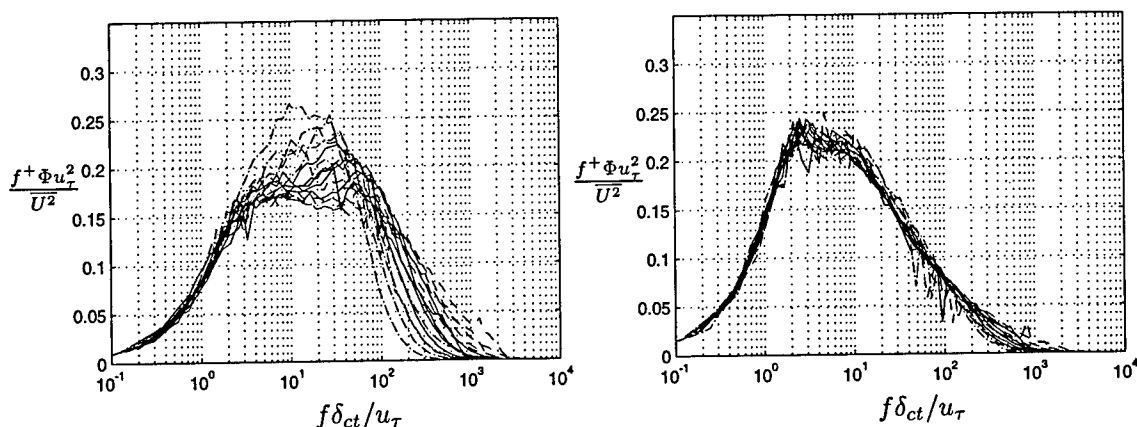
Figure 5: Outer scaled power spectral density, left at $y/\delta = 0.0093$, inner range and right with $y/\delta = 0.12$, outer range. Low Reynolds number, dash-dot line, intermediate Reynolds number, solid, and high Reynolds number, dashed.

Conclusions

High Reynolds number turbulent boundary layers experiments have shown a log relationship in the overlap region. This region has been determined to be in the range $200 \leq y^+ \leq 0.15\delta^+$ which only exists for $Re_\theta > 6000$. New values of the coefficients, $\kappa = 0.38$ and $B = 4.1$, have been determined and found to be constant of the range of Reynolds number examined. Consistency between two boundary layer experiments, a flat plate boundary layer and an axisymmetric boundary layer with a large radius of curvature, has been shown.

Personnel Information

Hassan M. Nagib, Arne V. Johansson, Drazen Fabris, Michael H. Hites, faculty; Jens M. Österlund, Bill Ornt, students

Publications

J. M. Österlund, A. V. Johansson, H. M. Nagib, and M. H. Hites, "Wall shear stress measurements in high Reynolds number boundary layers from two facilities," AIAA 99-3814, 30th AIAA Fluid Dynamics Conference, Norfolk, VI, June, 1999.

Acknowledgment/Disclaimer

References

1. M. V. Zagarola and A. Smits. Mean-flow scaling of turbulent pipe flows. *J. Fluid Mech.*, 373:33–79, 98.

2. W. K. George and L. Castillo. A theory for turbulent pipe and channel flows. In *Disquisitiones Mechanicae*. University of Illinois, Department of Theoretical and Applied Mechanics, Urbana, Ill., Oct. 24-26 1996. Expanded and revised version of the paper by George et al. from the conference.

3. G. I. Barenblatt and A. J. Chorin. Self-similar intermediate structures in turbulent boundary layers at large Reynolds numbers. Technical Report PAM 755, Center for Pure and Applied Mathematics, University of California at Berkeley, 1999.

4. A. E. Perry, I. Marusic, and J. D. Li. Wall turbulence closure based on classical similarity laws and the attached eddy hypothesis. *Physics of Fluids*, 6(2):1024–1035, 1994.

5. M. H. Hites. *Scaling of high-Reynolds number turbulent boundary layers in the National Diagnostic Facility*. PhD thesis, Illinois Institute of Technology, 1997.

6. J. M. Österlund. *(in Preparation)*. PhD thesis, Royal Institute of Technology, Sweden, 1999.

7. L. H. Tanner and L. G. Blows. A study of the motion of oil films on surfaces in air flow, with application to the measurement of skin friction. *J. Phys. E. Sci. Instr.*, 9:194, 1976.

8. J. M. Österlund, A. V. Johansson, H. M. Nagib, and M. H. Hites. Wall shear stress measurmeents in high Reynolds number boundary layers from two facilities. In *30th AIAA Fluid Dynamics Conference, June 28 to July 1, Norfolk, Virginia*, number AIAA 99-3814, 1999.

9. J. Komminaho, A. Lundbladh, and A. V. Johansson. Very large structures in plane turbulent Couette flow. *J. Fluid Mech.*, 320:259–285), year=1996,.

10. M. H. Hites. Turbulent boundary layers at high Reynolds numbers. In *AFOSR Contractors' Meeting in Tubulence and Unsteady Flows*, 1998.

11. A. E. Perry and C. J. Abell. Asymptotic similarity of turbulence structures in smooth- and rough-walled pipes. *J. Fluid Mech.*, 79(4):785–799, 1977.

TURBINE ENGINE CONTROL USING MEMS FOR REDUCTION OF HIGH-CYCLE-FATIGUE

F49620-97-1-0521

Wing F. Ng
Chris Kraft Professor of Engineering
Virginia Tech, Blacksburg VA
(540) 231-7274
wng@vt.edu

and

Ricardo A. Burdisso
Associate Professor of Mechanical Engineering
Virginia Tech, Blacksburg VA
(540) 231-7355
rburdiss@vt.edu

Abstract
A research program is pursued to use the emerging technology of micro-electro-mechanical-systems (MEMS) in gas turbine engines. In particular, MEMS-based microvalves are employed in a scheme by which they can control precisely the amount of blowing air used to energize the low velocity wake coming off stationary blades. This low velocity fluid, which causes unsteady loading of the downstream rotating blade row, has been shown in the past to be a major contributor of high-cycle-fatigue (HCF) of compressor blades. The use of trailing edge blowing (TEB) will reduce the vibration of the downstream blade row. The use of MEMBS-based microvalves and active control to individually adjust the flow rate of each trailing edge blowing hole has the potential to significantly reduce the unsteady blade loading, thus reducing the high-cycle-fatigue of engine components.

The main objective of this research effort is to experimentally demonstrate on realistic environments the potential of the active flow control system to re-energize the wakes to improve the HCF life and reduce the radiated noise from turbofan engines. Additional goals are to develop and integrate the necessary technologies, such as MEMS-based actuators, sensors, control concepts, algorithms and so forth, for the transition of the trailing edge blowing approach to practical system.

Background
The High-cycle-fatigue (HCF) of compressor components is due to blade vibration and the accumulated damage of the fatigue stress cycle. One major source of such fatigue stress cycles

is the forced response of the blade from unsteady aerodynamic excitation. In particular, the unsteady effect on the rotor blade loading due to the movement of the rotor through disturbances from the stationary wake of an upstream stator or inlet guide vane (IGV) had been shown to have a major effect on the HCF of compressor blades. In addition to HCF damage for core compressors, in military engines, the disturbance generated by the IGV has also been proven to be especially damaging in terms of HCF for the first stage fan rotor.

This research program uses trailing edge blowing for wake-filling to minimize disturbances seen by the downstream rotor blades. Because the flow is 3D and non-uniform along the blade span, the amount of T.E. blowing air must be carefully tailored, from the hub to the tip on the stator blade, to achieve the desired effect of minimizing the stator wake velocity defect along the entire blade span. To accomplish this, MEMS-based micro-valves are used to control the blowing of each individual hole at the trailing edge. Flow and acoustic measurements are used as error information to the control system.

Progress
The undertaken experimental efforts are being performed on three unique experimental facilities. The first facility consists of a small high-speed turbofan simulator, which is used to test active flow control concepts. The second setup is a turbofan engine experiment, which is used to study trailing edge blowing (TEB) in a realistic environment. The third facility is a high speed single stage compressor at the Wright Laboratory, which will be used to investigate the effect of the TEB on the blade HCF life. The work carried out in these facilities is described below.

Simulator Setup: Active Control of Wake Filling Using Microphone Error Sensors
The active flow control experiments were performed in the high-speed turbofan simulator shown in Figure 1a. A bellmouth was used at the inlet entrance to eliminate lip separation. Figure 1a shows the four upstream stator blades implemented with trailing edge blowing. Figure 1b shows a single strut with six orifices along its span. The blowing from each hole is adjusted by a MEMS-based microvalve. The controller adjusts the voltage to the microvalves based on error sensors to optimize the filling of the wakes as the flow condition changes in an engine.

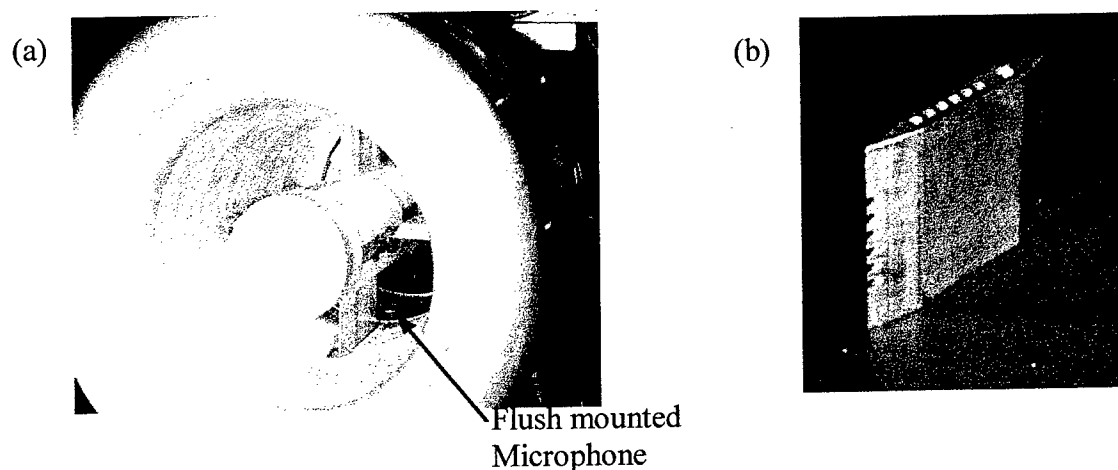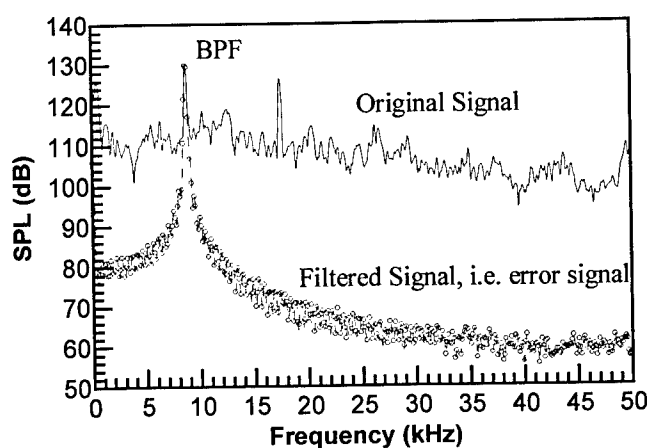(a)   (b)   Flush mounted Microphone

Figure 1: (a) High-speed turbofan simulator with four struts used in active flow control experiments and (b) strut with TEB.

The first set of experiments consisted of using as error signal the differences between a Pitot-Static probe measuring the free stream flow and Pitot-Static probes measuring the wake velocities. The results from these experiments were presented at the August 1998 review in Annapolis, Maryland. In these experiments, the advantages of using active flow control to optimize the wake filling was demonstrated. Monitoring of the far-field radiation showed noise reduction of up to 9.8 dB at the blade-passage-frequency (BPF) tone. However, the sound power level is probably a better metric to determine the effect the TEB has on the unsteady interaction. The reduction in sound power level was 4.4 dB.

The above experimental tests in the simulator demonstrated the potential of using active control for optimum re-energizing of the wakes. The use of Pitot probes positioned in the flow has the advantage of providing to the controller information directly related to the flow velocity deficit. The drawback of this sensing is that it is an intrusive sensor that generates wakes in itself. Thus, one of the key tasks undertaken was to develop non-intrusive sensing strategies. The approach pursued here was to use acoustics measurements to infer the filling of the wakes. The velocity deficit produced by the strut results in noise due to the strut-rotor interaction effect. Thus, the re-energizing of the wake will lead to noise reduction due to the elimination of the strut-rotor interaction. The acoustic sensing approach consisted of placing microphones flush mounted on the casing of the simulator in between each strut and the rotor, i.e. four microphones. One of the flush-mounted microphones can be seen in Figure 1. The microphones will sense the acoustic signature as the blades pass and cut the wake from the strut generating strong tonal components at the BPF and its harmonics. Minimizing the signals from the microphones will result in the optimum re-energizing of the wakes. It is important to remark that the noise will not be driven to zero because the strut-rotor interaction is not the only noise source at the BPF tone and harmonics. The other noise sources are the rotor-rotor and the rotor-EGV (exit guide vane) interaction, which are probably unaffected by the strut wakes. The noise from the strut-rotor interaction is the most dominant source.

The implementation of the acoustic sensing strategy required some unique sensing signal processing. The radiated noise spectrum from the inlet consists of a set of dominant tones and a broadband component. The tonal components at the BPF and harmonics are due to the strut-rotor interaction, i.e. noise due to the wakes. Thus, the BPF tone was selected as the error component to be used in the active flow control system. To this end, a novel notch filter device was developed and tested to adaptively capture the BPF tone component from the total acoustic signature (See patent disclosure below). Figure 2 shows the spectrum of the original microphone signal and the signal after being filtered by the adaptive notch filter.

Figure 2: Acoustic spectrum from an inlet mounted error sensor microphone before and after novel adaptive notch filter.

The results from the active flow control of the wakes using acoustic sensing are presented in Figures 3 and 4. Figure 3 shows the root-mean-square time history of the BPF tone during the adaptation process as well as the control signal driving the microvalves. The error time history clearly show the significant variability of the power of the tone, which is typically observed in turbofan engines. It is clear that the control system was effective in reducing the error signals by about 6 dB. The reduction of the BPF tone radiated by the inlet noise is shown in Figure 4. This figure shows the radiation directivity with and without control of the wakes. The far-field noise was reduced over the 10° to 80° sector with reduction of up to 8 dB. The sound power level was reduced by 4.9 dB, which is similar to the power reduction of 4.4 dB using Pitot probe as error sensors. These results demonstrate the effectiveness and potential of this non-intrusive acoustic sensing strategy for active TEB.
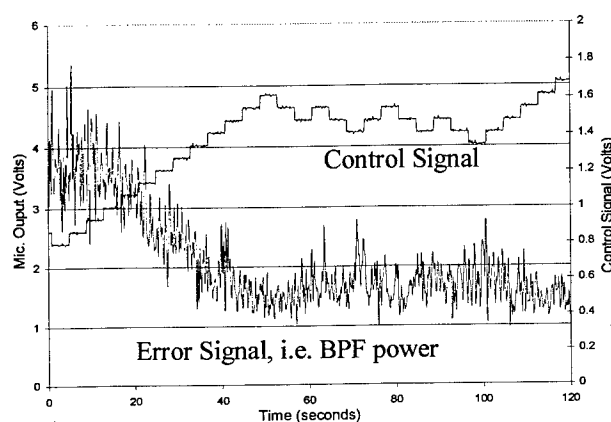
Figure 3: Error (BPF tone power) and control signal time histories.
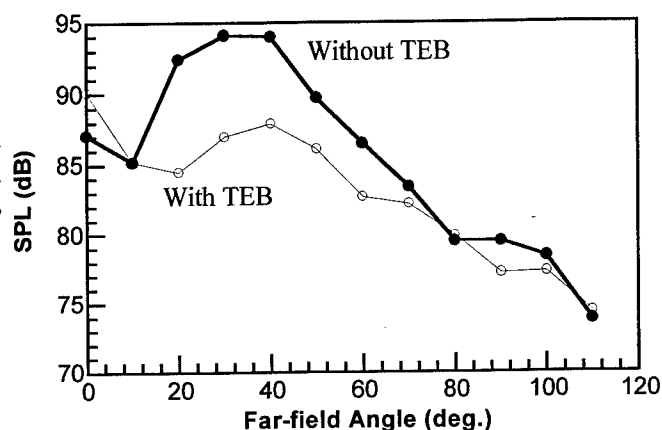
Figure 4: Radiation directivity with and without active TEB (BPF = 9 kHz).

Wake Filling Experiments on a Turbofan Engine

The simulator is an excellent test bed to efficiently evaluate, in terms of cost and time, concepts for wake management. However, this setup is not realistic in terms of the characteristics of the wakes, e.g. scaling of the simulator to the dimensions of a real engine yields wakes that are substantially larger than the ones produced by typical IGVs. Thus, wake management experiments on an AlliedSignal F109 turbofan engine have been performed to address the potential of the TEB technique on a more realistic environment. Figure 5 shows the engine inlet with a single non-turning IGV. The wake was mapped using time average Pitot-static probe measurements (see figure 5). The wake with and without blowing at 50% of the strut span is shown in Figure 6. In this figure, it is clear that the wake was successfully re-energized. It is important to remark that the wake produced by IGV is typical, both in depth and width, of real engines. A critical issue for the implementation of this TEB technique is the air mass needed for wake management. Measurement of the mass flow demonstrated that only 0.03% of the total engine mass flow is used to re-energize the wake of the IGV tested. This demonstrated the potential for bleeding air from the engine compressor to supply the TEB system without degrading the performance of the engine.

Figure 5: AlliedSignal F109 turbofan engine and single IGV with TEB.

Figure 6: Normalized axial flow velocity variation with and without TEB (Blade thickness t = 11.4mm).

Wake Filling-Rotor Strain Measurement Experiments

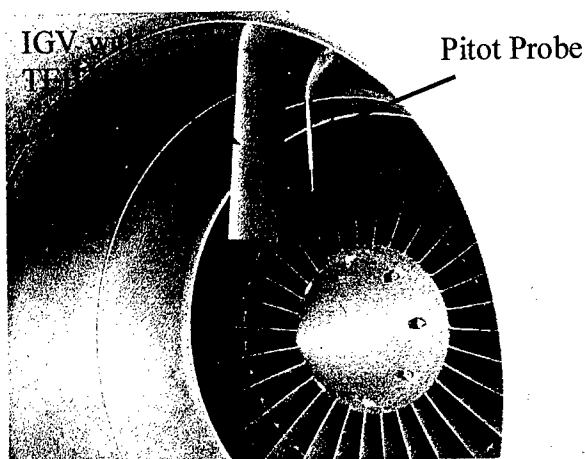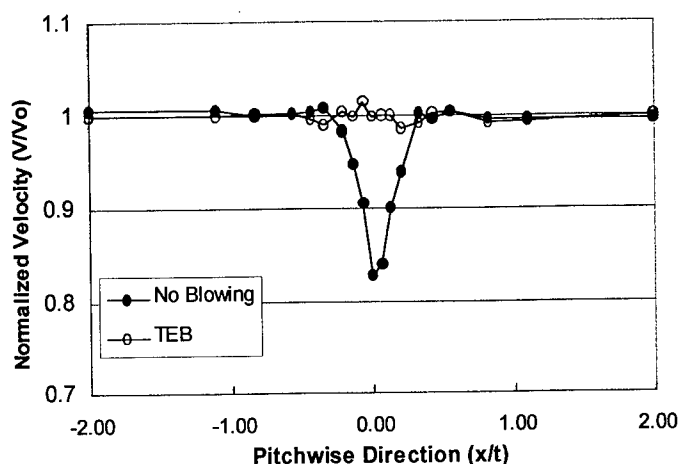The previous research tasks addressed critical issues for the practical implementation of the active TEB technique. Both flow and acoustic sensors have been used to provide the control system information on the filling of the wake. However, the main goal of the technique is to reduce the HCF damage due to the wake induced unsteady forcing function on the blades. Thus, experiments are planned for this Fall to monitor the strain on the blades of a compressor with and without TEB. The facility for these experiments is the high-speed compressor at the Wright Laboratory in the Compressor Aero Research Lab (CARL). These measurements will provide fundamental information about the impact on the strain, and thus on the HCF, of the wake filling. Experiments will be performed to investigate: the effect of various percentages of wake fillings (i.e. from partially to fully re-energized wakes), the effect of filling only part of the wake along the IGV span (i.e. filling of the wake near the outer casing as compared to the full span), and the effect on the noise generated to allow improvements of the acoustic sensing approach.

Technology Transitions

Extensive interaction between the Virginia Tech team and personnel at the Wright Laboratory in the Compressor Aero Research Lab (CARL) was held to coordinate the rotor strain measurement effort. Numerous technical discussions were held with Dr. Copenhaver of the CARL to define the experiments to be performed. These experiments are scheduled to take place during this Fall.

Future Plans

The research effort will continue in all three tasks described above. In the simulator experiments, the effort will focus on improving the acoustic sensing and development of the control algorithm tailored to this application. The main goal is to further improve the time response of the control system. Experiments on the turbofan engine will continue to complete the unsteady measurements. Studies for various strut-to-rotor spacing will be carried out. In the last research

task, the experiments on the high-speed compressor at CARL will be undertaken this Fall. Simultaneous measurements of strain, flow, and acoustic signals will be performed. The work will then proceed to reduce, analyze, and relate wake filling to HCF damage.

Personnel

Principal Investigators:	Ng, Rappaport, Burdisso
Ph.D. Students (4):	J. Feng, J. Kozak, T. Bailie, C. Kontogeorgokis
MS Student:	N. Rao

Awards and Citations
1. W. F. Ng, Dean's Award for Excellence in Teaching, Virginia Tech, 1999.
2. W. F. Ng, Plaque of appreciation from ASME International Gas Turbine Institute for serving as the technical program Chair for the 1999 Turbo Exposition Conference.
3. W. F. Ng, Plaque of appreciation from ASME Council on Education for advancing engineering education as Mentor-at-Large on the Board on Professional Development.

Publications
1. J. Feng, N. Rao, Burdisso R.A., and W. Ng., "Active Flow Control Using MEMS Actuators to Reduce Fan Noise," 137th Meeting of the Acoustical Society of America and the 2nd Convention of the European Acoustics Association ASA/EAA, Berlin, Germany, March 14-19 1999 (Invited presentation).

2. N. Rao, J. Feng, J. Kozak, T. Bailie, R. A. Burdisso, and W. Ng., "Active Flow Control To Reduce Fan Blade Vibration and Noise," 13th Annual Review of The Center for Turbomachinery and Propulsion Research, Virginia Tech, Blacksburg, VA, April 1999.

3. N.M. Rao, J. Feng, R.A. Burdisso and W.F. Ng, "Active Flow Control to Reduce Fan Blade Vibration and Noise," 5th AIAA/CEAS Aeroacoustics Conference, AIAA 99-1806, Seattle, Washington, 10-12 May, 1999 (also submitted for publication to the AIAA Journal).

Patent Disclosure
Burdisso, R. A., Feng, J., and Ng, W. F., "An Analog Adaptive Notch/Bandpass Filter," VPI Patent Disclosure 99.023, June 1999.

EFFECTS OF SHOCK AND TURBULENCE ON THE FILM COOLING HEAT TRANSFER IN TRANSONIC TURBINE BLADES

F4620-96-1-0465

Wing F. Ng
Professor of Mechanical Engineering
Virginia Tech, Blacksburg
(540) 231-7274
wng@vt.edu

Tom Diller
Professor of Mechanical Engineering
Virginia Tech, Blacksburg
(540) 231-7198
tdiller@vt.edu

Abstract

A research program is continued to study the effects of steady and unsteady shock impingement on the film cooling heat transfer in transonic turbine blades. Fundamental physical understanding is gained of how these unsteady phenomena affect the heat transfer with and without film cooling. Thermal and aerodynamic conditions are set to simulate engine conditions. The experimental program is being conducted in the Virginia Tech heated, transonic turbine cascade wind tunnel. A shock wave is generated in a shock tube and passes into the cascade upstream of the blade row to simulate the interaction of a shock emerging from the trailing edge of an upstream nozzle guide vane on the downstream rotating blade row. The rotor blade geometry and film cooling hole pattern were designed by GE Aircraft Engines.

Progress

A fully instrumented blade was completed, accommodating six *Vatell* HFM-7/L Heat Flux Microsensors, six high speed *Kulite* Pressure Transducers and six surface thermocouples. A schematic view of this blade is shown in Figure 1.

The steady-state values of Heat Transfer Coefficient and Film Cooling Effectiveness were determined for all six measurement locations in an experiment using heat exchangers to heat the mainstream air and cool the film cooling flow. A sample time history of heat flux and all relevant temperatures is shown in Figure 2.

Detail View of Showerhead
Film Cooling Configuration

Kulite Pressure
Transducer

Vatell HFM-7/L
Heat Flux Sensor

Surface
Termocouple

Detail View of One
Measurement Location

Measurement
Locations
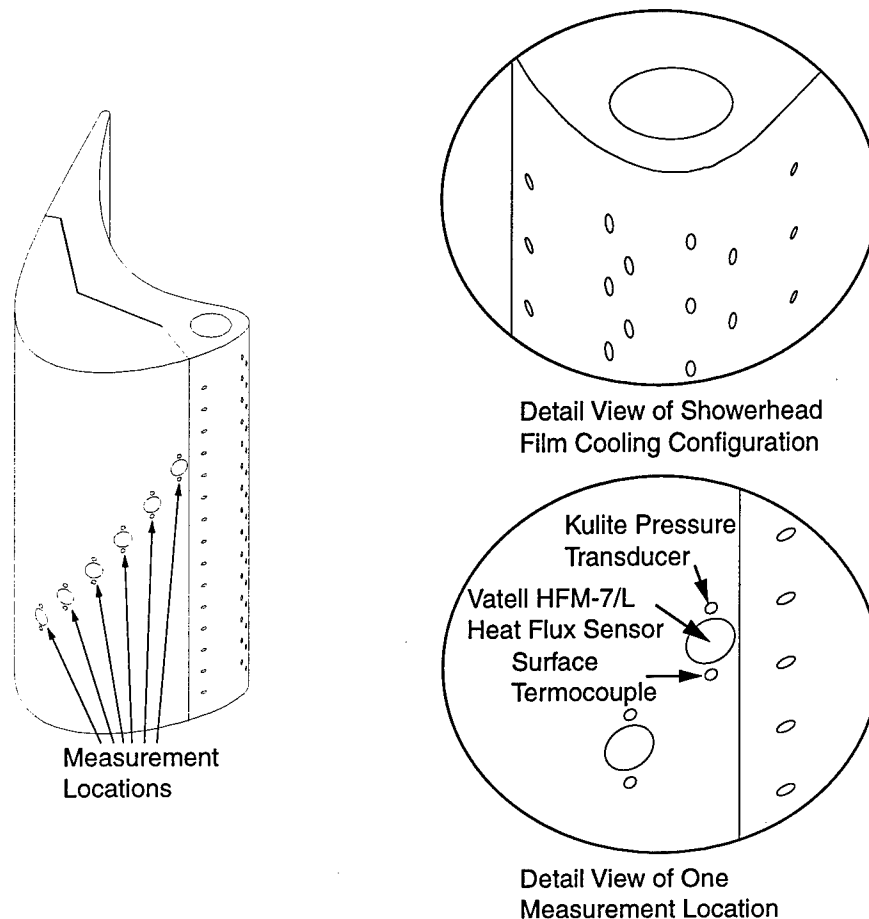
Figure 1: Fully Instrumented Blade with Details of Sensors and Showerhead Film
Cooling Configuration

The effect of the passing shock wave on the heat transfer was then investigated by means
of high speed shadowgraphs taken with a *Hadland* high speed digital camera capable of
taking four successive pictures at up to 8MHz. One sample view of the shock interacting
with the layer of cooling film is shown in Figure 3.

High-speed time histories of pressure and heat flux were recorded with all available
gauges during the shock passage. A sample heat flux time history from one shock passing
event is shown in Figure 4.

A wide variety of parameters were varied (shock strength, coolant pressure, initial level
of heat flux) in order to determine the effect of the passing shock on the heat transfer
coefficient and the film effectiveness. By comparison of different traces it was found that
the heat transfer coefficient is not influenced strongly by the passing shock. The majority
of the effect of the shock is a transient change in the fluid temperature.
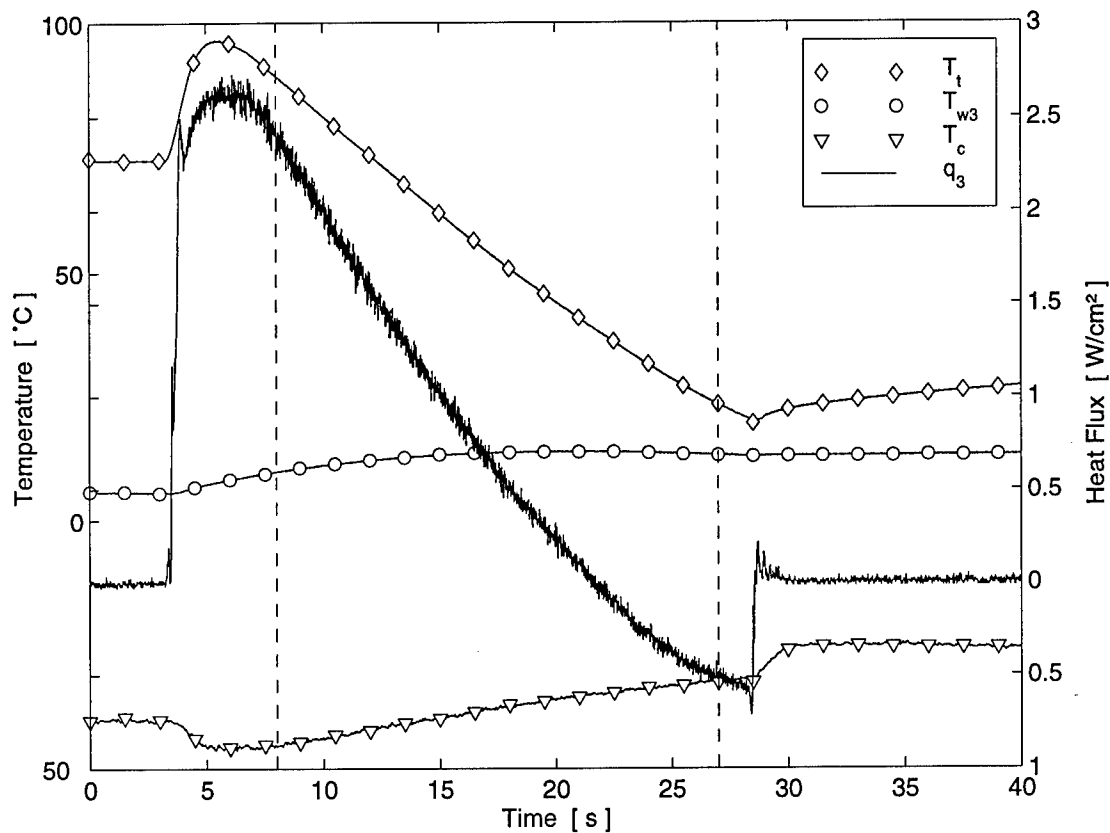
Figure 2: Sample Time History from Gauge #3, Cooled Experiment. Dashed Lines Indicate the Range of Useful Data.
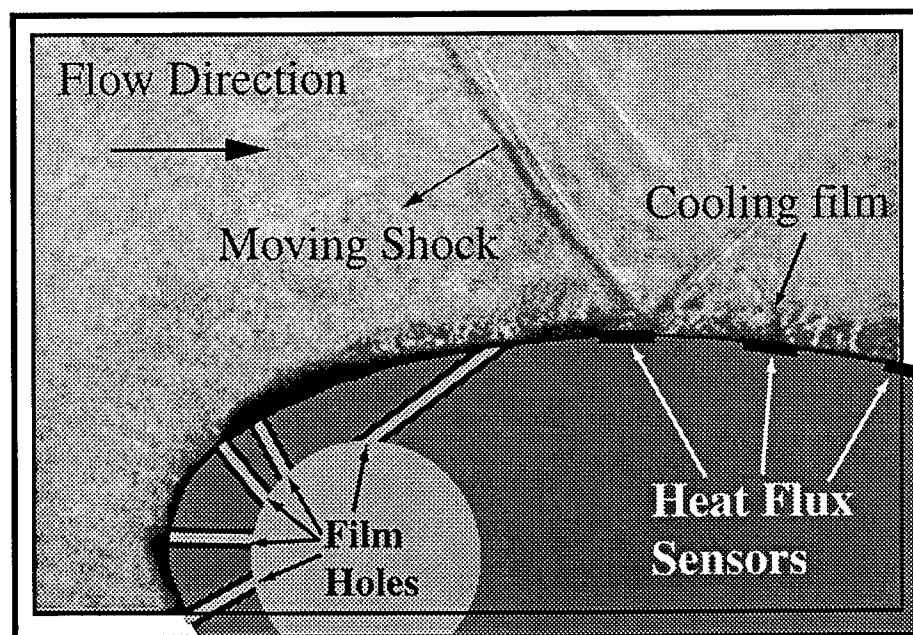
Figure 3: Sample Shadowgraph Illustrating the Interaction of the Passing Shock and the Coolant Layer
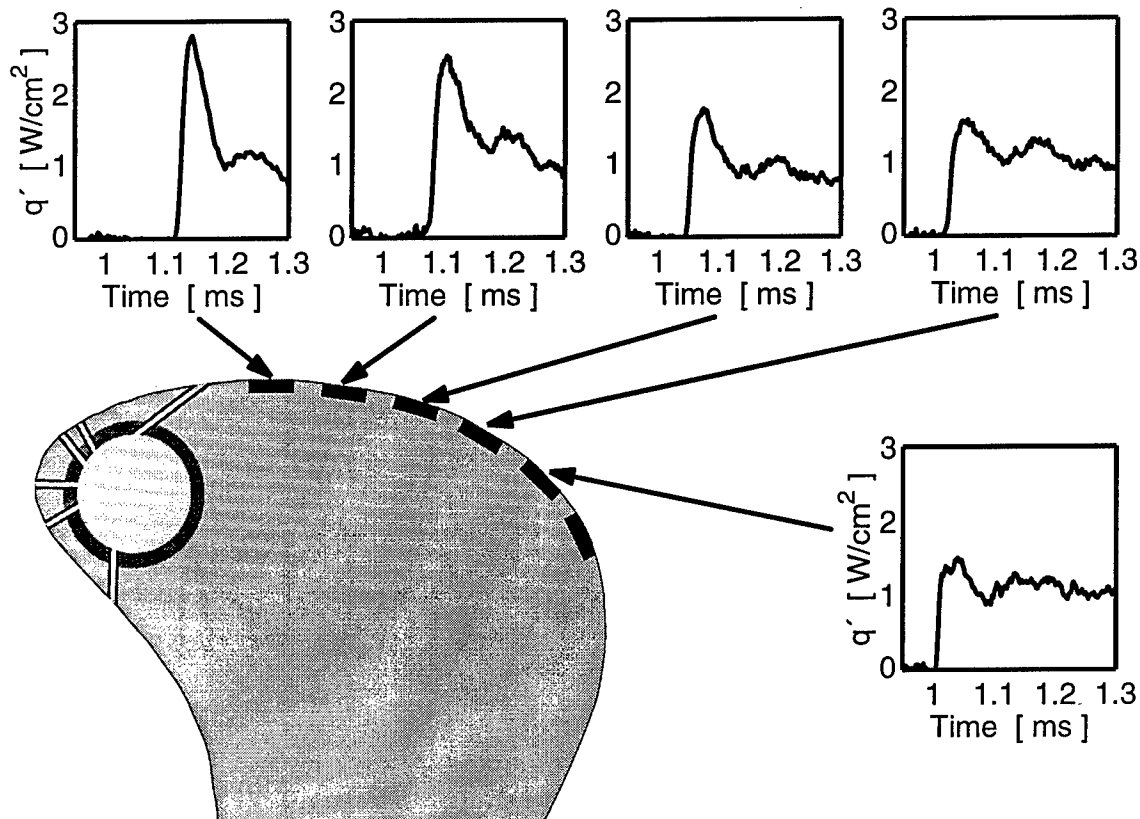
Figure 4: Sample Time History of Shock Induced Heat Flux from *Vatell* HFM-7/L Heat Flux Sensors #1 through #5.

The data was compared to different predictive models published in the literature. Of all the models evaluated, the best agreement could be found for a model assuming a constant heat transfer coefficient.

Further tests are needed with higher turbulence flow through the cascade. The present turbulence level (about 1%) is significantly lower than the turbulence level in an actual engine (exceeding 15%). The boundary layer behavior was shown in the literature to be dependent on the turbulence intensities, turbulent length scales and turbulent time scales. The reaction of a boundary layer to the passing shock is most likely different for different scales and intensities of turbulence.

Transitions

Vatell Corp.

As part of the Virginia Tech research project from AFOSR, Vatell Corporation has press-fit Heat Flux Microsensors directly into the aluminum gas turbine blade models. The sensors measure both heat flux and temperature at the blade surface using sputtered thin films. Heat Flux is measured using the output of 300 thermocouple pairs arranged as a differential thermopile across a thin thermal resistance layer. Surface temperature is measured with an adjacent thin-film resistance element.

Testing, modeling and designing new sensors is being done cooperatively with Vatell Corp. A joint evaluation of new calibration methods has been recently completed. Vatell Corporation markets Heat Flux Microsensors produced in its Thermateq facility in Blacksburg, VA. They continue to modify their production line to increase capacity and quality.

General Electric Aircraft Engines (GEAE)

Interaction with GEAE has continued with research discussions and a presentation held at GEAE during the past twelve months. The film cooling hole pattern was designed by GEAE based on their experience on state-of-the-art film cooling hole pattern on aircraft engine blades.

Wright Laboratory

Discussions have continued with Wright Laboratory personnel including a visit and a presentation. Topics included measurement technology, film cooling experimentation and unsteady shock simulation.

Personnel

Principal Investigators: Wing Ng and Tom Diller

Graduate Students:

Name	Degree	Source of Funding
Oliver Popp	PhD	AFOSR
Dwight Smith	MS	ASSERT
Jim Bubb	MS	AFOSR
Hank Grabowski	MS	AFOSR
Candy Nelson	BS	AFOSR

Publications

Chapters of Books, Editor of Books or Proceedings

Diller, T. E., "Heat Flux," Ch. 34, in The Measurement, Instrumentation and Sensors Handbook, Ed. J. G. Webster, CRC Press, Boca Raton, Florida, 1999, pp. 34.1-15.

Conference Papers

Diller, T. E., Ng, W. F., and Schetz, J. A., "Time Resolved Measurements of Turbine Blade Flow Phenomena," in Advanced Non-Intrusive Instrumentation for Propulsion Engines, AGARD-CP-598, 1998, Paper No. 40.

Peabody, H. L., and Diller, T. E., "Evaluation of an Insert Heat Flux Gage in a Transonic Turbine Cascade," in Proceedings of the ASME Heat Transfer Division - 1998, HTD-Vol. 361-5, Ed. R. A. Nelson, Jr., et al., pp. 625-630.

Holmberg, D. G., Diller, T. E., and Ng, W. F., "A Frequency Domain Analysis: Turbine Pressure Side Heat Transfer," ASME Paper No. 98-GT-152, 1998.

Reid, T. V., Schetz, J. A., Diller, T. E., and Ng, W. F., "A Computational Approach for Investigating Unsteady Turbine Blade Heat Transfer Due to Shock Wave Impact," ASME Paper No. AJTE99-6286, 1999.

Popp. O., Smith, D. E., Bubb, J. V., Grabowski, H. C., Diller, T. E., Schetz, J. A., Ng. W. F., "Steady and Unsteady Heat Transfer in a Transonic Film Cooled Turbine Cascade," ASME Paper No. 99-GT-259, 1999.

Publications Accepted but Not Yet Published

Smith, D. E., Bubb, J. V., Popp, O., Diller, T. E., and Hevey, S. J., "A Comparison of Radiation Versus Convection Calibration of Thin-Film Heat Flux Gauges," accepted for the 1999 IMECE, Nashville, Nov. 14-19, 1999.

Publications Submitted

Holmberg, D. G. and Diller, T. E., "Simultaneous Heat Flux and Velocity Measurements in a Transonic Turbine Cascade," submitted to the ASME Journal of Turbomachinery.

Awards

Tom Diller	Who's Who in the South and Southwest, 27th Ed., 1999
	Dictionary of International Biography, 27th Ed., 1999
	International Directory of Distinguished Leadership, 8th Ed., 1998

Wing Ng	Dean's Award for Excellence in Teaching, VaTech, 1999
	Plaque of Appreciation from ASME International Gas Turbine Institute for serving as the technical program chair for the 1999 Turbo Expo Conference.
	Certificate of Appreciation from ASME Council on education for advancing engineering education as Member-at-large on the Board on Professional Development.

Acknowledgement/Disclaimer

ACTIVE CONTROL OF AEROELASTICITY AND INTERNAL FLOWS IN TURBOMACHINERY

AFOSR GRANT #F49620-96-1-0407

J. D. Paduano, C. E. S. Cesnik, A. H. Epstein, Z-W Lee
W. Farahat, H-Y Hong, G. Maahs, D. Sahoo, K. Willcox
Department of Aeronautics and Astronautics
Massachusetts Institute of Technology

Abstract
This year marks the first year that the program has concentrated exclusively on modeling, system identification, and control of the aerodynamics associated with flutter and high cycle fatigue. The review is divided into two sections. The first describes modeling and analysis of high cycle fatigue, using unique state-space and control-theoretic techniques. A first-principles model has been used both to analyze flutter control and to predict worst-case behavior for probabilistic methods. Also, model order reduction techniques have been used to create CFD-based state-space models of blade-scale aerodynamics, which have been incorporated into a mistuning analysis of flutter, as well as other stability and control analyses. The second part of the review reports on progress of the active rotor development. A 20,000 RPM spin test facility has been completed, and testing of blades for the active rotor is proceeding.

1.0 Modeling, Identification, and Control of Flutter and Forced Response in Turbomachinery

Two techniques have been developed for system analysis of flutter and forced response in turbomachinery. Both modeling approaches are unique in the aeromechanics community because they capitalize on a systems and control perspective to yield new insight and new approaches to the aeromechanics problem. The first model [1,10] is based on first principles models like those introduced by MIT for rotating stall. This model is incompressible and very low order (12-16 states per interblade phase angle), which allows systems studies to be performed at low cost. The second model [9] is compressible, based on CFD, but employs state-of-the-art model order reduction techniques to reduce the models to tractable order: 100-200 states for the aerodynamics of an entire rotor, as compared to 10,000-100,000 states for the original CFD model.

Having completed the initial development of these models, the past year has concentrated on applying them to answer questions about identification and control of flutter and forced response. The following sections describe some of the results.

1.1 Control and Sensitivity Studies Using a First Principle Flutter Model

Two primary questions have been studied using our first-principles models of an aeromechanically coupled rotor. The first question is related to active control: what sensor and actuator types are best suited to active control of flutter? To study this question, a model of the GE "Fan C" rotor was developed, using performance data from a NASA-funded aeroelasticity study by GE. The GE report provides performance data, structural properties, and aeroelastic response characteristics of a 22" scale model of a transonic fan, similar to the GE 90 fan. By using 2D equivalent structural and performance properties, and by adjusting the mechanical damping in the low-order model, aeromechanical properties very similar to those measured by GE were achieved.
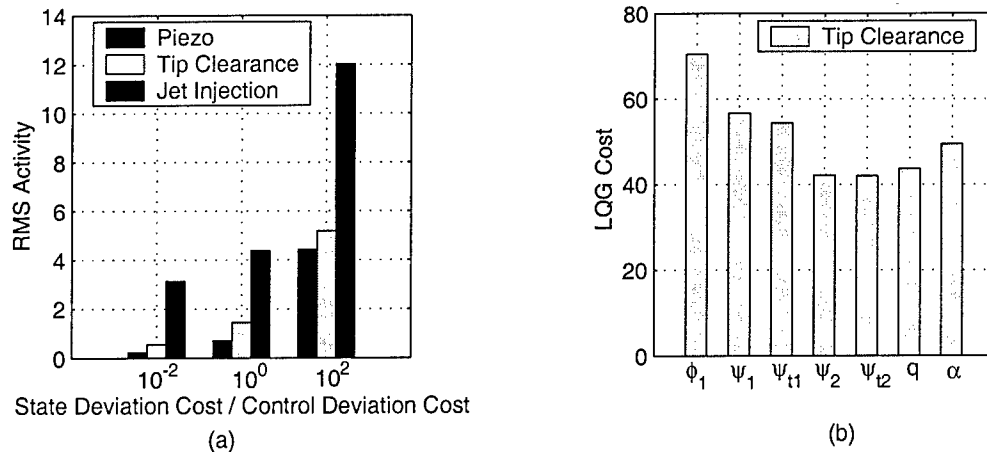
Figure 1: Actuator-sensor studies for active control of flutter. (a) Actuator activity required to stabilize torsion flutter for three types of actuation. Relative weighting of state deviations and actuator activity determine the required RMS actuator activity. (b) LQG cost for tip clearance actuation, for various sensors (notation: ψ, static pressure; ψ_t, total pressure; ϕ, velocity; α, q, direct pitch and plunge measurement; 1, upstream, 2, downstream).

Using this validated model, various actuators and sensors were introduced, and feedback control was applied to the most critical instabilities in the system. Optimal control methods were used to determine the theoretical limit of performance of the postulated actuation and sensing systems. Static pressure, dynamic pressure, and velocity sensors were considered; injectors, tip clearance modulation, and on-blade piezos were considered for actuation.

Figure 1 gives the results. Figure 1a shows the results of comparing various actuator types, using LQG control methods to predict the minimum actuator activity required to stabilize the compressor with various actuators. On-blade piezo actuation is chosen as the baseline actuator, because on-blade actuation like this can directly affect the damping of the blades, yielding high performance but impractical implementation. Figure 1a shows that off-blade actuation affecting the tip clearance flow can achieve stabilization with comparable levels of effort, but much more practically. Figure 1b compares various sensor choices for tip clearance actuation, with LQG cost (RMS errors) as the metric for performance. Downstream actuation consistently performs better than upstream, and static pressure sensors (which are best suited to high speed applications) have performance comparable to other types of sensing. Our study shows that both off-blade sensing and off-blade actuation can be used to stabilize lightly damped (forced response) or unstable (flutter) modes in compressors.

The second study, currently in progress, applies control-theoretic methods to determine the robustness of a given rotor design to manufacturing tolerances. This study directly addresses the 'probabilistic design' and 'three-sigma engine' thrusts that are currently important to engine manufacturers. The idea is to start with industry-standard forced-response analysis, and add robustness analysis methods to these, to determine the effects of manufacturing tolerances and parametric uncertainties.

Figure 2 illustrates the approach. Using the modeling techniques developed at MIT, a theoretical Campbell diagram can be constructed. This Campbell diagram agrees well with the properties measured in the "Fan C" tests. But, unlike standard methods for
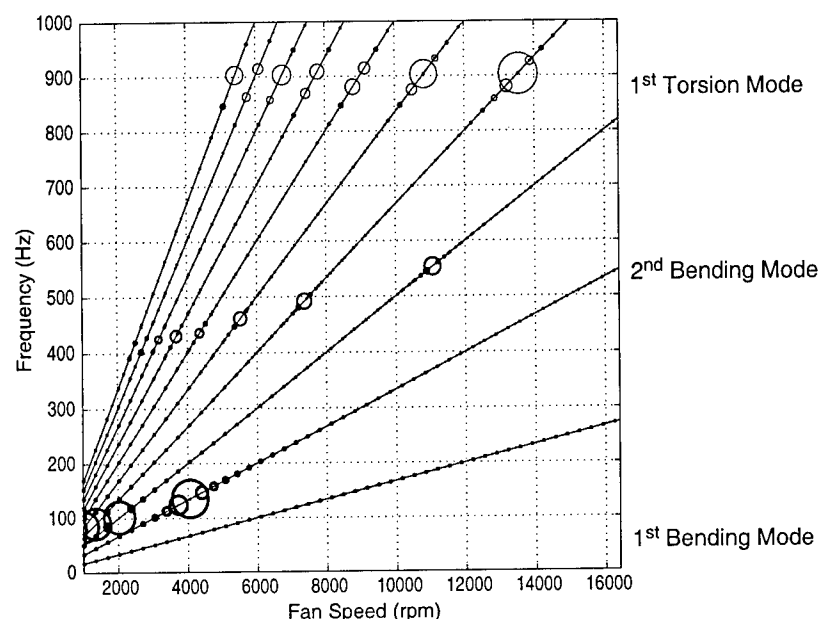
Figure 2: Analytical Campbell diagram for GE Fan C, based on first-principles low-order model. Lines represent 1st through 4th harmonics of rotor frequency excitation. Large circles represent structural frequency crossing circles size indicates forced response amplitude.

constructing Campbell diagrams, the MIT model provides information on the damping ratios of various aeromechanical modes, which in turn determine the forced response resonant stress amplitudes. This information is indicated in Figure 2 by the size of the circles at each crossing of an engine mode with a blade eigenvalue frequency.

Based on this analysis, sensitivity studies are straightforward to perform. For example, the same analysis has been done for a fictitious compressor with the same overall pressure rise, but with higher pressure losses due to deviation and lower pressure losses due to viscous effects. This is the type of information that is useful to compressor designers.

Currently we are taking this analysis one step further. Using robustness analysis tools from control theory, we can actually determine the worst-case (from the standpoint of stability and resonant response) set of parameter variations among a given uncertainty set. This information will allow designers to determine the effects of manufacturing tolerances, uncertainty/variability of the operating conditions, and poorly predicted off-design performance.

1.2 Reduced-Order Modeling of CFD-based Blade Row Aeromechanics
Although the model described in the previous section is useful for system-level studies, it lacks accurate representation of the higher-order flow field physics, especially in transonic flows where shocks have a strong impact on aeroelastic response. What is really needed is a low-order model which accurately captures the response behavior computed by a CFD code over a broad range of spatial and temporal frequencies. An approach to model order reduction which yields just such models has been completed during the past year.

213

Two significant improvements to previous work have been implemented. First, model order reduction has been applied to Euler codes that accurately capture shock effects. Second, a frequency-domain Proper Orthogonal Decomposition (POD) method for model order reduction has been developed, and shown to be a special case of 'block Arnoldi' methods for input-output model order reduction [10]. Arnoldi methods are generalizations of Pade approximations, yielding extremely low order, efficiently computed models based on frequency-domain unsteady aerodynamics. Models developed using this approach have been used for mistuning analyses [3] as part of the cooperative PRET program between MIT, Caltech, University of California, and UTRC.

Another application of the models is estimation of aerodynamic damping based on off-blade measurements. The premise of low order modeling is that based on the values of the fundamental states of the process (of which there are a very low number, even though CFD is required to identify them), the entire unsteady flow field can be constructed. A corollary is that a set of off-blade measurements, if they can be used to deduce the states (*i.e.* the system is observable from those measurements), can be used to deduce the pressure distribution on the blade surface. This argument obviously relies on the accuracy of the model, and assumes that the blade motion is known (forced response testing), or that an estimator can also be constructed for the blade motion (free vibration). Current work considers estimators based on low order modeling to do this job.

Figure 3 shows the beginnings of the study of off-blade aerodynamic damping measurements. These plots show the amplitude of the off-blade signals that would result from 1 degree blade deflections, and compares these to the signals used in previous system identification experiments [4]. These results give confidence that signal strength will be sufficient to do off-blade system identification.
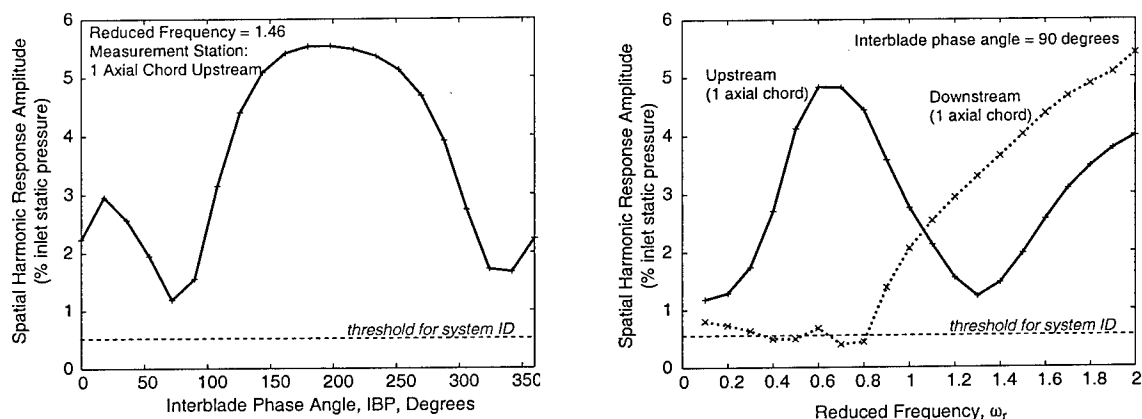
Figure 3: Off-blade pressure amplitudes induced by blade vibration, as a function of interblade phase angle (left) and frequency (right). Threshold levels are based on signal levels used for system identification in a transonic compressor at NASA Glenn [4,5].

2 Active Rotor Development

The goal of this project is to build a transonic rotor whose blades actively oscillate and thereby excite the aerodynamics associated with flutter and high cycle fatigue. Figure 4 illustrates the twin spar concept that we have adopted for the blade. This 'active rotor' is a new instrument for investigating the unsteady aerodynamic properties of turbomachinery. Because it must be constructed of composites, because it uses piezos

in a high-g environment, and because transonic rotor blades are thin and highly twisted, the active rotor is a multi-disciplinary design challenge. The development is being carried out systematically, and supporting research is being done to design experiments and understand their implications. In this section we discuss work that is essentially completed (active blade prototyping and spin pit development and construction), as well as work that is ongoing (blade testing and rotor design).

2.1 Active Blade Prototypes
Mechanical Design
Mechanical design of the active rotor blades is the core effort for the active rotor project. As in all active structures, there is a fundamental trade-off between strength and actuation capability. Mechanical design considerations that have been resolved include the following:

- Choice of materials (for the piezos, foam shell, and spars);
- Location of the spars within the blades;
- Location and bonding procedure for the piezos; and
- Layout of components for transfer of power and signals to and from the blade.

All of these items have been carefully considered to improve strength, durability, and manufacturability while maintaining actuation capability. Three separate design concepts will be tested during the summer to determine the one best suited for implementation.

Spar material (graphite-epoxy), fiber angles (±20 degrees), thickness, and taper ratio were all optimized for the severe loading environment of the transonic rotor. Spar orientation within the aerodynamic shape of the blade was also studied, to determine the stress associated with off-axis lean in the spars. Because the spars have a rectangular cross-section, the twist orientation of the spar has a large impact on the stresses. Initial studies on optimizing the off-axis lean of the spars with respect to their twist angle were conducted. Finite-element analysis of the blade's untwist properties, frequency response characteristics, and stress levels has been conducted.

The most carefully considered aspect of the mechanical design was the piezos. Because PZT is relatively heavy and brittle, and because the bond between the piezo and the structure strongly affects the strain transmission, manufacturing for high-load, and characterization under load, were considered the highest-risk elements of the blade design. Several concepts were considered. Embedding the piezos within the graphite epoxy structure was seen as a way to pre-compress the piezos and reduce their ultimate strain; however analysis showed that, because of the near-axial orientation of the graphite fibers, very little pre-compression in the radial (primary strain) direction was achieved. Surface bonding with the spar under tension was also considered, so that after the bond had cured and the spar was released, the piezo would be under compression. This pre-compression relieves the ultimate tensile stress on the piezo. Finally, pre-compression by actuating the piezos during curing was considered and ultimately chosen as the most effective and simple method of manufacture.

Two critical unknown issues relating to surface bonding exist: bond relaxation both
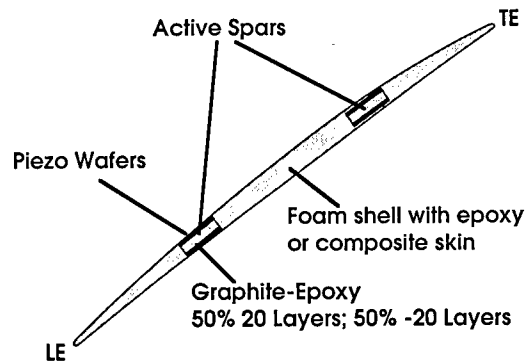

Figure 4: Active rotor blade cross-section. Spars are actuated simultaneously for bending oscillations, and out-of-phase for pitch oscillations.

215

initially and over time (creep), and strength of the bond. Shear lag analysis, as well as coupon testing, resulted in a manufacturing procedure that tested well beyond the ultimate stress of the unbonded piezo material, and which showed no loss in properties due to creep. This was due both to the careful bonding procedure and the extra strength provided by the Kapton layer supporting the electrodes.

Blade Manufacture

Figure 5 shows the primary components of the active rotor. These figures were generated from three-dimensional models of the GE "Fan C" compressor. The three-dimensional models have been used to make molds (both by numerical machining and 3D printing methods) for the spars and the aerodynamic envelope of the blade. Three manufacturing procedures are being tested. All three start with the graphite-epoxy lay-up shown on the left-hand side of the figure. This lay-up consists of 40 layers of graphite-epoxy prepreg, tapering to 4 layers at the tip of the blade to reduce stresses at the root, and a triangular root attachment, also of graphite-epoxy. Numerically machined molds and precisely patterned prepreg layers create the initial shape in this figure. This is the backbone of all three blade concepts.

Figure 5: Spar-and-shell construction of the active rotor blade.

The primary blade concept is the spar-and-shell construction. In this construction. the graphite-epoxy lay-up is cut using a water jet into two spars and a support tab (not shown in Figure 5). Rohacell foam, chosen for its light weight, high strength, and relatively low stiffness, is thermoformed in a second mold, and bonded to the spars. The thermoforming and bonding procedures have been the subject of recent research, and the strength and stiffness properties after thermoforming are currently being tested. We are also assessing the effect of an epoxy outer skin on the surface properties and stiffness of the blade.

A second concept relies on a graphite-epoxy skin, rather than foam with an epoxy skin, for structural integrity of the blade. The skin is attached to the root section and supports its own weight to prevent additional stress on the spars. Although this construction may have superior surface properties, it will have additional bending stiffness and thus will achieve primarily twist actuation.

The third blade concept uses a plate-like backbone for the active rotor blade, instead of a twin-spar arrangement. This blade promises to be much stiffer and stronger in twist, while affording extra surface area for placement of piezos. Although this blade promises to have the lowest untwist properties and the highest overall robustness, it will be more difficult to actuate its torsion mode, so it will achieve primarily plunge actuation.

All three blade concepts use a potted base near the root attachment to provide strain relief for instrumentation wires. For the blade with graphite epoxy skin, this base also supports the fibers of the skin. The base, shown on the right-hand side of Figure 5, is cast in during the final step in the construction procedure, forming a simple mechanical interface to the slotted rotor hub.
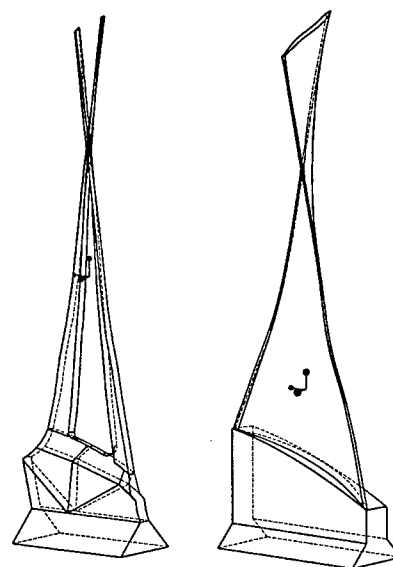
Prototype (untwisted) blades have been constructed for the first blade concept and are currently being tested. The tapered, twisted blade backbones for all three concepts are currently being laid up in numerically machined molds.

2.2 Spin Pit Design and Construction

A major effort during the past year has been design and construction of a spin pit for testing the active rotor (Figure 6). This evacuated facility has two unique properties which suit it for testing the active rotor: first, an integrated power slip ring can provide up to 25 channels of high voltage power to the rotor, to actuate the piezos on the blades. Second, the 20,000 RPM spindle of the rotor is designed to be compatible with the MIT blowdown compressor facility. Once spin testing is complete and the structural integrity of the active rotor has been demonstrated, the entire spindle assembly will be mounted in the blowdown compressor facility for short duration testing under full aerodynamic loads. Limited aeroelastic testing will also be conducted in the blowdown compressor, but the ultimate goal is to install the rotor in a continuously-operating facility such as the CRF at Wright-Patterson Air Force Base, or the W8 transonic compressor test facility at NASA Glenn.
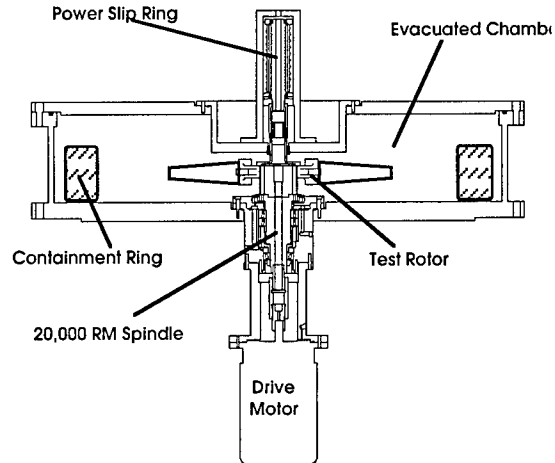

Figure 6: Spin pit facility assembly drawing. Support structure and instrumentation not shown.

As part of the current design effort, a test rotor was designed and built. This rotor supports up to three blades, in clips which can be replaced if the root attachment design changes. In addition, the rotor is designed to allow *in situ* rebalancing of the rotor, so that the imbalance created by changing the blades can be canceled. *In situ* rebalancing, a connector in the slip ring attachment (instead of the more typical, hard wired approach), and a stiff shaft structure all make the spin pit well suited for testing prototype blades and the active rotor. The instrumentation for the spin pit is being procured under support from the DURIP program.

2.3 Prototype Blade Testing

To date, testing has been performed on prototype blades for the spar-and-shell blade concept. Initial tests have verified that the graphite-epoxy lay-up can withstand the centrifugal loads, including the weight of the piezos and the blade. Frequency response tests of the spars, with and without the Rohacell shell, have been conducted. Currently, deflections of up to 1 degree peak to peak have been achieved in bench tests. These deflections will be somewhat reduced by centrifugal effects, but recent results in the literature, as well as the analysis shown in Figure 3, indicate that good results can be obtained with 0.2 to 0.4 degrees of blade deflection, due to the high sensitivity of the shock location to incidence in a transonic fan.
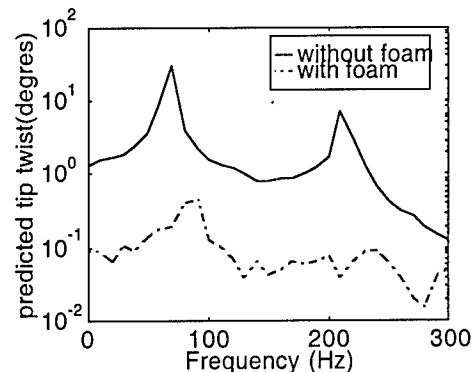

Figure 7: Measured active rotor spar deflections, plotted on an axis which predicts the tip deflection achievable.

217

Figure 7 shows preliminary blade deflection results. Clearly, the foam shell has a significant impact on the tip deflection of the blade, reducing the effectiveness by one order of magnitude. Although the resulting deflection would still be sufficient for system identification studies, additional work is underway to reduce the detrimental impact of the shell on control power.

3 Acknowledgement/Disclaimer

4 Publications

1. Hong J.Y., Wong M. T.M., Paduano J.D., "Modeling For Control of Compressors with Aerodynamic And Aerostructural Instabilities," Invited paper, *Proceedings of the US-Japan Seminar on Abnormal Flow Phenomena in Turbomachinery*, November 1998, Osaka, Japan.

2. Nelson, E.B., Paduano, J.D., and Epstein, A.H., "Active Stabilization of Surge in an Axi-Centrifugal Turboshaft Engine," presented at the ASME Turbo Expo, Indianapolis, June 1999.

3. Shapiro, B., and Willcox, K.E., "Analyzing Mistuning of Bladed Disks by Symmetry and Reduced Order Modeling," submitted to ASME Turbo Expo and the *Journal of Propulsion*, Munich, June 2000.

4. Spakovsky, Z., Weigl, H.J., Van Schalkwyk, C.M., Paduano, J.D., Bright, M.M., Strazisar, T., and Suder, K., "Rotating Stall Control in a High-Speed Stage with Inlet Distortion" (two parts), to appear, *Journal of Turbomachinery*, Vol. 121, July 1999.

5. Spakovsky, Z., Gertz, J.B., Sharma, O.P., Paduano, J.D., Epstein, A.H., and Greitzer, E.M., "Influence of Compressor Deterioration on Engine Dynamic Behavior and Transient Stall Margin," presented at the ASME Turbo Expo, Indianapolis, June 1999.

6. Vo, H.D., Paduano, J.D., and Epstein, A.H., "Experimental Development of a Jet Injection Model for Rotating Stall Control" presented at the ASME Turbo Expo, Stokholm, Sweden, June 1998.

7. Wang, Y., Paduano, J.D., and Murray, R.M., "Nonlinear Control Design for Rotating Stall with Magnetic Bearing Actuators," presented at the Conference on Control Applications, Honolulu, June 1999.

8. Willcox, K.E., Paduano, J.D., Peraire, J. and Hall, K.C., "Low Order Aerodynamic Models for Aeroelastic Control of Turbomachines," AIAA 99-1467, 40th SDM Conference, St. Louis, April 1999.

9. Willcox, K.E., Peraire, J., and White, J, "An Arnoldi Approach for Generation of Reduced Order Models for Turbomachinery," to be presented, AIAA Aerospace Sciences Meeting, Reno, NV, January 2000.

10. Wong, M., "System Modeling and Control Studies of Flutter in Turbomachinery," M.S. Thesis, August 1997.

A FUNDAMENTAL STUDY OF GAS AND VAPOR BUBBLE DYNAMICS IN MICRO-CHANNELS

A. Prosperetti, H.N. Oğuz, H. Yuan, X. Geng, and E. Ory
Department of Mechanical Engineering, The Johns Hopkins University
Baltimore, MD 21218

Abstract

The general aim of this project is to carry out a fundamental study of the basic physics underlying the possible applications of gas and vapor bubbles in heat transfer systems, pumps, actuators, and other small-scale systems. The major development during the period June 98 to July 99 has been the implementation of yet another novel pumping principle (different from the one described in the previous report) based on the action of a single vapor bubble asymmetrically generated in a channel (see Figure 1). A patent application covering this device has been filed. Furthermore (a) full Navier-Stokes simulations of the growth and collapse of a vapor bubble in a channel have been carried out, and (b) experiments on the simultaneous action of flow and acoustic forces on a gas bubble have been conducted.
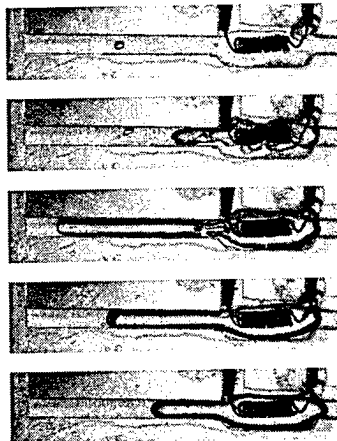
Figure 1: Photographic sequence of the evolution of a vapor bubble in the new single-bubble pump; only part of the channel is shown.

A FUNDAMENTAL STUDY OF GAS AND VAPOR BUBBLE DYNAMICS IN MICRO-CHANNELS

A. Prosperetti, H.N. Oğuz, H. Yuan, X. Geng, and E. Ory
Department of Mechanical Engineering, The Johns Hopkins University
Baltimore, MD 21218

Abstract

The general aim of this project is to carry out a fundamental study of the basic physics underlying the possible applications of gas and vapor bubbles in heat transfer systems, pumps, actuators, and other small-scale systems. A summary of progress during the period June 98 to July 99 is presented. The major development has been the implementation of yet another novel pumping principle (different from the one described in the previous report) based on the action of a single vapor bubble asymmetrically generated in a channel. Furthermore, experiments on the simultaneous action of flow and acoustic forces on a gas bubble have been conducted.

Introduction

While a great deal is known on gas and vapor bubble dynamics, very little work has been done on bubble mechanics in the situations that might arise in micro-mechanical applications. Issues are the presence of boundaries such as a bubble in a channel or chamber of comparable size, the effect of wetting phenomena and nucleation, bubble stabilization against gas diffusion, interaction with acoustic fields and temperature gradients, and others. The physical mechanisms, characteristic times and lengths, reproducibility, control, etc. all constitute promising features for practical applications but are essentially virgin territory in terms of basic physics.

The work described here summarizes our progress in this area over the period June 98 to July 99. During this period the work has followed two main lines, one concerning vapor bubbles and one gas bubbles. For the first topic we have carried out an experiment and conducted numerical simulations on a novel type of bubble-based pump. This device is based on a principle that was initially discovered in the course of the study of a simplified theoretical model and subsequently proven experimentally. For gas bubbles we have set up an experiment to study the possibility of positioning a bubble by acoustic means in the presence of a flow.

Novel vapor-bubble pump

Consider a channel connecting two liquid reservoirs (Fig. 1). We assume that a bubble is generated in the channel starting from a small high-pressure cavity. In practice this can be obtained by a localized heating of the fluid by means of a small heater. Shortly after the bubble starts to expand the pressure is brought to zero
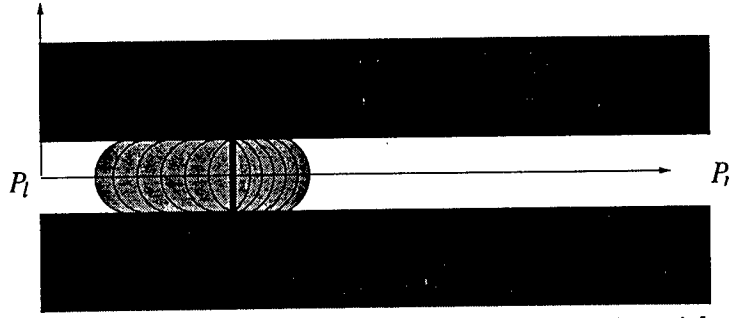
Figure 1: Sketch of a microchannel joining two liquid reservoirs with a bubble growing from a heater indicated by the vertical bar.

simulating the turning off of the heater and the cooling of the vapor. We have found that, if the initial bubble position is not in the middle of the channel, every time the bubble grows and collapses, a small amount of liquid is pushed in the direction of the reservoir farther from the bubble.

This unexpected and potentially useful effect was first discovered by studying a simple one-dimensional model of the situation [2]. For the sake of simplicity we present here an even more simplified version of the model that nevertheless contains the essential idea. Consider the column of liquid to the left of the bubble and apply an integral momentum balance to it to find

$$\rho \ell_l \frac{dU_l}{dt} = P_l - p_b, \qquad (1)$$

where the index l refers to the left liquid column, ρ is the liquid density, $\ell_l = \ell_l(t)$ the length of liquid between the bubble surface and the left tube exit, U_l the velocity of this liquid, P_l the pressure in the left reservoir, and p_b the pressure in the bubble. The complete model of Ref. [2] accounts also for viscous effects as well as surface tension. A similar equation holds for the right liquid column. When he bubble collapses the two liquid columns collide; we assume that momentum is conserved in the impact so that the liquid in the tube has a residual velocity given by $LU = \ell_l U_l + \ell_r U_r$, with L the tube length. With prescribed p_b, P_l, P_r the equations can be solved to give the liquid velocity and bubble volume vs. time. As mentioned before we assume that the bubble pressure is initially large, and falls to near 0 shortly after the bubble begins to expand. The remarkable fact is that when the two columns collide at the end of the collapse, there is a residual velocity directed towards the right, i.e. toward the reservoir farther from the bubble.

This simplified simulation has been considerably refined with the results shown in Fig. 2. Here the full incompressible Navier-Stokes equations are solved by means of a volume-of-fluid method coupled with a marker treatment of the free surface. The channel simulated has a diameter of 62 μm and a length of 2000 μm; the initial position of the bubble is at 750 μm from the left reservoir and only the part of the computational domain near the bubble is shown. The upper panel is a sequence of bubble shapes during growth and the lower panel during collapse. Note that the point where the bubble collapses is displaced to the right of the point where the bubble was initially generated. By repeating sequentially the growth and collapse process, one would generate a net motion of the liquid from right to left.
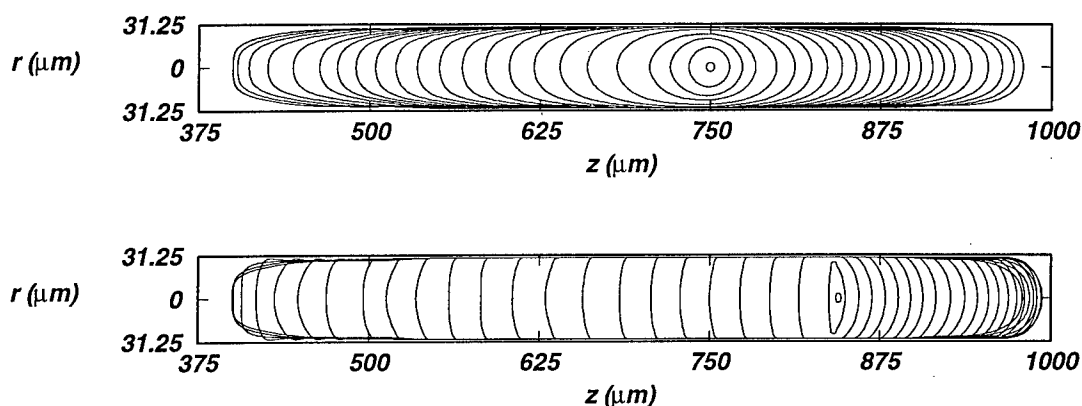
Figure 2: Growth (upper panel) and collapse (lower panel) of a vapor bubble in a 2,000 μm-long, 62.5 μm-diameter liquid-filled tube connecting two liquid reservoirs. (The images show only part of the tube). The bubble is nucleated at a distance of 750 μm from the left reservoir. Note that during the collapse it displaces toward the other reservoir with a resulting pumping action on the liquid that has been verified in the laboratory. Successive contours are separated by 1.6 μs. The internal pressure falls to 0 after 2 μs, i.e. between the second and the third frames. The simulation is based on a full Navier-Stokes incompressible calculation. (from [3]).

Figure 3: (Left) Sketch of the new single-bubble pump. The lower part of the diagram shows the powering sequence of the heater.

Figure 4: (Right) Experimental pressure head developed by the pump sketched in the diagram at left as a function of the interval T between successive powerings of the heater.

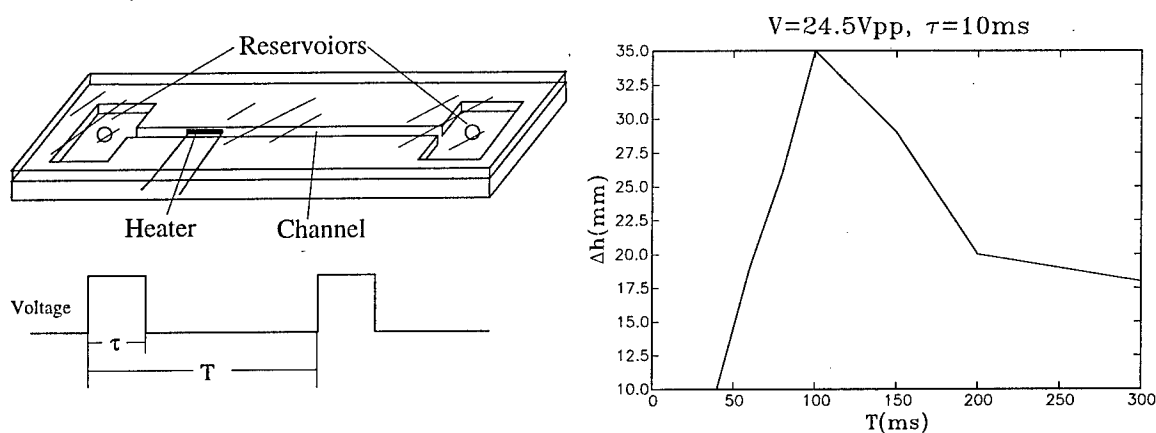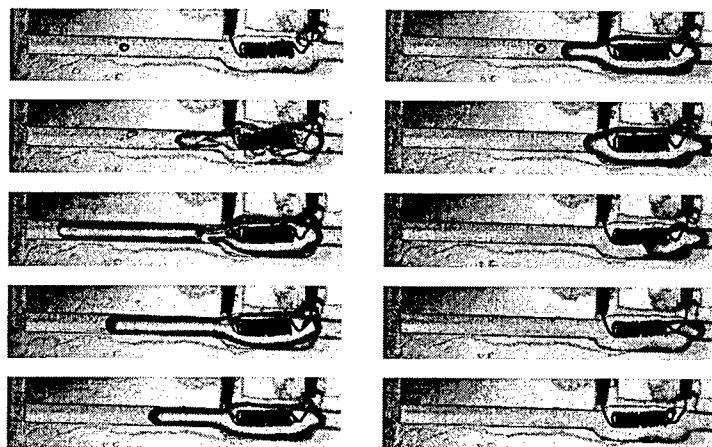Figure 5: Photographic sequence of the evolution of a vapor bubble in the device schematized in Fig. 4; only part of the channel is shown.

We have conducted an experiment to demonstrate the actual existence of this unexpected phenomenon. The experimental set-up is sketched in Fig. 3. Data on the pressure head developed by this device as a function of the time interval between successive powerings of the heater are shown in Fig. 4. A photographic sequence of the bubble growth and collapse is shown in Fig. 5. The channel is cut in a piece of Plexiglas and covered with another piece of the same material. The two parts are sealed by a plastic glue. The heater is a short piece of thin wire suspended in the channel. The two ends of the wire are clamped to the inside of two hypodermic needles that, offering a much lower resistance to the current, do not heat up and therefore do not damage the Plexiglas. The channel is approximately square in cross section with sides of 1 mm and a length of 6 cm.

Multi-bubble pump

By means of the same quasi-one-dimensional model summarized before, we have conducted simulations of the functioning of a multibubble pump. In the example that we show here there are three heaters in the channel as shown in Fig. 6. These heaters are powered in succession cyclically as indicated in the lower part of the figure. The evolution of the three bubbles in two cases is shown in Fig. 7. The dynamics of the system – and therefore its pumping effectiveness – is clearly strongly affected by the precise timing of the generation of the bubbles. This and other features of the system can be studied with our model.

Gas bubbles subjected to flow and acoustic forces

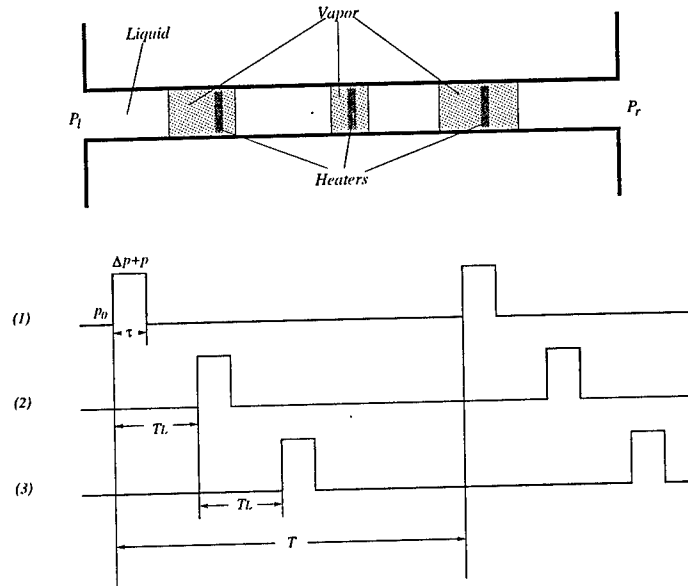Gas bubbles immersed in a sound field are acted upon by pressure-radiation (or Bjerk-

Figure 6: Sketch of a multi-bubble pump with three heaters (upper panel) and powering sequence (lower panel).
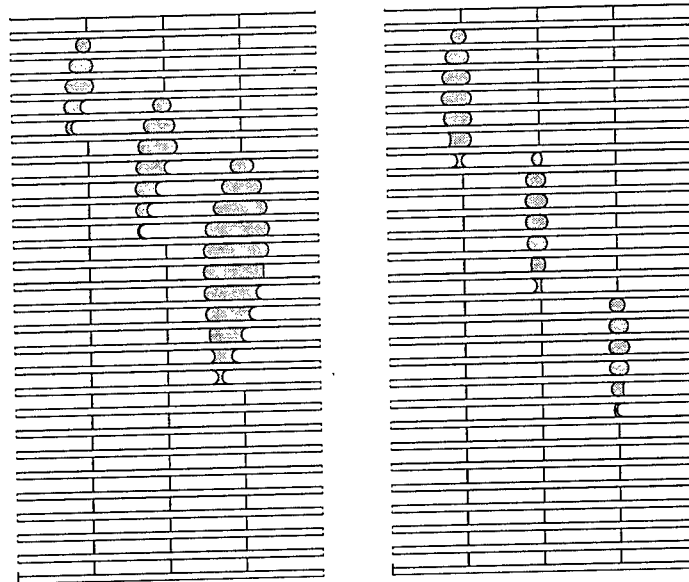

Figure 7: Examples of the growth and collapse cycle of three bubbles in the device shown in the previous figure. The two cases differ in the time lapse T_L between the powering of successive heaters.

nes) forces. These forces can be quite intense and can not only overcome buoyancy, but also the drag imposed by a liquid flow. Since ultrasound readily propagates through living tissue, this circumstance opens the possibility, for instance, of positioning bubbles in the blood stream e.g. to deliver drugs to specific places of the circulatory stream. Similar application would be possible in other – non biological – liquid-carrying circuits. The bubble could be encapsulated in a soft material and thereby attached to a structure that might in this way be positioned wherever desired.

The first step to investigate this possibility is to study the effects of flow and sound acting simultaneously on a gas bubble. For this purpose we have set up the following experiment. A standing acoustic wave is generated in a glass cell by two ring transducers mounted at the top and at the bottom of a glass tube. A soft plastic tube is inserted vertically along the axis of the cell and a recirculating flow is maintained in the system by means of a small pump that draws liquid from the side of the cell and pumps it back through the tube. A gas bubble is generated electrolytically and trapped in the standing sound wave. The water flow is increased until the drag force becomes too large and the bubble is lost.

Refereed Journal Publications

During the period January-June 1999 the following papers have been published in or submitted to refereed journals:

1. Yuan, H, Oğuz, H.N. and Prosperetti, A. Growth and collapse of a vapor bubble in a small tube, *Int. J. Heat Mass Transfer* 42, 3643-3657, 1999.

2. Yuan H. and Prosperetti, A. The pumping effect of growing and collapsing bubbles in a tube, submitted to *J. Micromech. Microeng.*

3. Ory, E., Yuan, H., Prosperetti, A., Zaleski, S. and Popinet, S. Growth and collapse of a vapor bubble in a narrow tube, submitted to *Phys. Fluids.*

4. Geng, X., Yuan, H., Oğuz, H.N., and Prosperetti, A. Single-bubble based micropump, submitted to *Sensors and Actuators.*

The following patent application has been filed:

Prosperetti, A., Oğuz, H.N., and Yuan, H. Bubble-based micropump

Personnel

In addition to the PI A. Prosperetti, the work has involved Dr. Hasan N. Oğuz, Associate Research Professor, Dr. He Yuan, Research Scientist, Dr. Emmanuel Ory, post-doctoral fellow, and the doctoral student Mr. Xu Geng.

Acknowledgment/Disclaimer

MEMS-BASED PROBES FOR VELOCITY AND PRESSURE MEASUREMENTS IN UNSTEADY AND TURBULENT FLOWFIELDS

Othon K. Rediniotis
Department of Aerospace Engineering
Texas A&M University, College Station, Texas

Thomas R. Tsao
United Micromachines
El Monte, California

ABSTRACT
This work presents our progress in the development of MEMS (Micro-Electro-Mechanical Systems)-based, high-performance, fast-response, multi-sensor pressure probes of miniature size for velocity and pressure measurement in unsteady and turbulent flowfields. The fabrication and calibration of a miniature 5-sensor hemispherical-tip probe, are discussed. The first stage of the development process has been to fabricate a sensitive MEMS pressure sensor array and to develop calibration theory, algorithms and environments for a fast-response probe. We fabricated an array of 5 bossed-diaphragm absolute pressure sensors 250×250 μm^2 in size. One of the challenges in the pressure sensor development is the design of sensors with sensitivity sufficient for accurate measurements in flow conditions most commonly of interest to the scientific and industrial community. We have also fabricated the probe tip components that will house the MEMS sensor array. New probe calibration techniques are introduced. Both theoretical and experimental approaches are employed to develop calibration techniques suitable for unsteady and turbulent flow environments with fine time and length scales.

Although multi-hole probes have been employed in the measurement of unsteady flowfields (Kerrebrock et al., 1980; Matsunaga et al., 1980; Ng and Popernack, 1988; Naughton et al., 1993) they have typically been limited in terms either of frequency response or minimum achievable probe size. For example, although Kerrebrock et al.'s (1980) probe had a decent overall frequency response (30 kHz), it had a rather large size (5mm tip diameter), and, although Matsunaga et al.'s (1980) probe had a relatively small size (2mm tip diameter), it had a limited frequency response (500 Hz). Ng and Popernack (1988) developed a four-sensor probe with a size of 5.2mm and a frequency response of 20 kHz. Naughton et al. (1993) developed a 5-hole probe for supersonic flow measurements. A small tip diameter was maintained (1.1mm) but the frequency response was limited to 50 Hz. Typically, in these efforts the frequency response limitations are caused by the need to have pressure tubing leading from the probe tip to the pressure transducers. From the above one can infer that the current state-of-the-art cannot simultaneously achieve large measurable bandwidth and good spatial resolution of the fine flow structure when applied to turbulent flow measurements. To overcome these limitations we are developing MEMS-based, multi-sensor pressure probes that largely eliminate the limitations described above. The new probes combine miniature size with high frequency response and will extend the application regime of multi-sensor probes to unsteady and turbulent flows.

Although probe calibration techniques for steady-state measurements are well established today, largely unresolved issues persist, pertaining to the calibration of such instruments for measurements in unsteady and turbulent flows. In Gossweiler et al. (1994), a 4-hole, fast-response probe was introduced. The probe tip did not have any of the conventional geometries (conical or hemispherical) but was rather formed into a wedge. The tip diameter was 2.5mm and the frequency response was 45 kHz. The unsteady aerodynamic effects on the probe calibration were not taken into account. The same group (Humm et al., 1994) tested several fast response probes with tip geometries, in order to assess the measurement error made if a static probe calibration is used to reduce probe measurements taken in time-dependent flowfields. Several error sources were identified, the most important of which are: inertial or apparent mass effects (potential flow effects, the most important contribution to the error), dynamic boundary layer effects, dynamic stall effects and vortex shedding effects. For a flow oscillation frequency of 5.9 kHz, and depending on probe geometry and size (two probe tip sizes were tested, 4mm and 8mm), errors as high as 100% were identified.

PROBE DESIGN AND FABRICATION

Fabrication of Miniature Components

Several components of the probe are built by the Miniaturization Laboratory of the Aerospace Engineering Department of Texas A&M University. Miniaturization can be defined as fabrication of parts and/or features that are too small for conventional metal-cutting machines and tools, but too large for today's micro- or nano-fab processes. Typical features include holes between 0.005 inches and 0.030 inches in diameter, or pockets requiring a cutter diameter of 0.010 inches. For comparison, most human hair is approximately 0.002 inches in diameter. The challenges of miniaturization evolve from parameters common to all metal-cutting practices and familiar to all machinists. These are speeds, feeds, and precision or tolerance. A major challenge of miniaturization is the relative precision of location and size. For example, conventional machines can easily produce reamed holes of 0.500" diameter with a tolerance of 0.001", or 0.2 % error. It is intuitively impossible to achieve this low percentage of error with features smaller than 0.020" (tolerance of 0.000004"). Further, there are no tools to measure such features with that degree of accuracy. Hence, it is imperative the designer accounts for the imprecision of fabrication when mating parts are involved. The Miniaturization Laboratory of the Aerospace Engineering Department has developed the hardware and the techniques to deal with such challenges.

Probe Design

Figure 1 is an exploded view of the probe, showing the various components as they are assembled. The tip, sealing tubes, and mounting stage are fabricated by the Miniaturization Laboratory, as well as tools to facilitate final assembly. The tip is relatively easy to fabricate, as it consists of simple drilling and counter-boring operat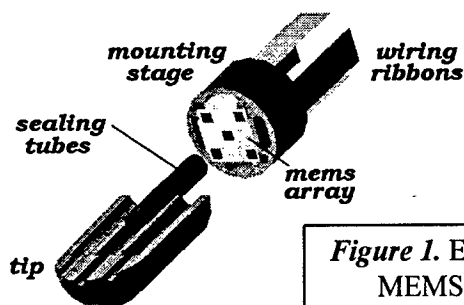ions, although great care is taken in producing the hemisphere as accurately as possible. The tubes are off-the-shelf and only require machining to length. The

Figure 1. Exploded view of the MEMS 5-sensor probe.

mounting stage is the most difficult piece to fabricate, as it has features requiring the smallest of tools and the highest precision of location. Figure 2 below shows the stage in detail. The stage is 2 mm diameter brass, approximately 1 mm thick. The pocket is 0.005 inches deep, and is machined with a 0.010" diameter cutter, as are the four slots. The pocket corners are cleared to allow the MEMS array to be accurately positioned relative to the outside diameter of the stage. The slots for the wiring ribbons go completely through the stage, to allow access to the soldering pads on the wires from the MEMS array. The stage plays a crucial role in the assembly of the probe components. The MEMS array, the sealing tubes, and the tip of the probe are placed relative to the outside diameter of the stage, which also serves as the final connection to the probe housing, after the sensor wires are connected. Each of the pressure sensors must be coupled with its corresponding hole in the tip, with no chance of leakage or cross-talk between ports. This is accomplished by sealing all of the tubes to the MEMS array in one epoxy setting, then sealing the tip to the tubes in a separate epoxy setting. A fixture is used to accurately position the t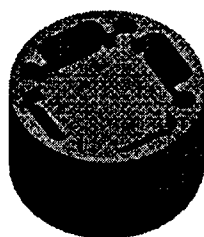ubes on the MEMS array, holding the tubes by their inside diameter, so the epoxy can be placed around the outside diameter of each tube. After the epoxy has cured, the tip is fitted over the ends of the tubes and new epoxy is placed around the outside of

Figure 2. Detail of the stage, where the MEMS pressure array is housed.

each tube before completing the joint.
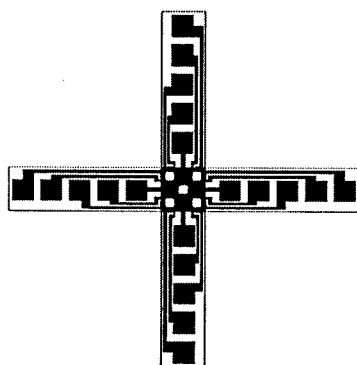
MEMS Sensor Array

Figure 3. Layout of the pressure sensor skin.

The MEMS pressure sensors used in this project are surface micromachined and contain bossed diaphragm structures for improved sensitivity. In last year's progress report, initial pressure sensor designs and testing results were presented. Currently, the knowledge gained from those tests is used to design and fabricate a pressure sensor skin in the shape of a cross. The layout (some layers hidden for the sake of clarity) for the skin is shown in Figure 3. The central square is approximately 1.2 mm on a side and contains 5 pressure sensors (shown as white squares). Each sensor sits atop a silicon island, but the arms of the cross are composed entirely of polyimide and metal lines and are completely flexible. United Micromachines is currently finishing up the 5-pressure-sensor flexible skin process. We have improved upon our original flexible skin process in the areas of robustness and packaging. The original process (Jiang et al., 1997) (simplification shown in Figure 4 (left)) uses a wet silicon etch such as TMAH or KOH to create the backside cavities. For process compatibility issues, this choice necessitates creating the cavities early in the process, thus implying that a relatively fragile wafer be carefully handled through the rest of the

process. The new process (simplification shown in Figure 4 (right)) uses deep reactive ion etching (DRIE) to create the cavities near the end of the process, after the sensors have been formed. Thus the yield increases significantly, wafer warpage issues are of no concern, and the processing is greatly simplified.
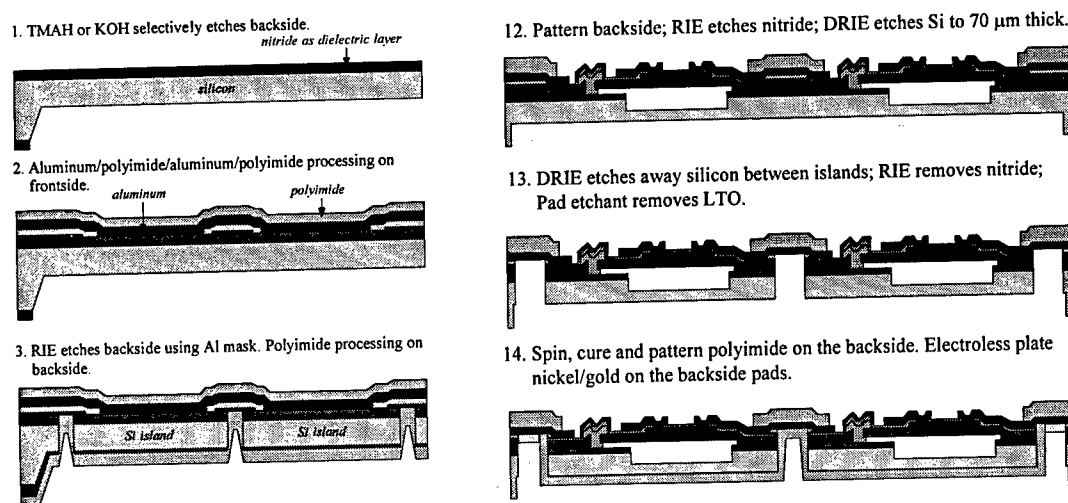

1. TMAH or KOH selectively etches backside.
   nitride as dielectric layer

2. Aluminum/polyimide/aluminum/polyimide processing on frontside.
   aluminum   polyimide

3. RIE etches backside using Al mask. Polyimide processing on backside.
   Si island   Si island

12. Pattern backside; RIE etches nitride; DRIE etches Si to 70 µm thick.

13. DRIE etches away silicon between islands; RIE removes nitride; Pad etchant removes LTO.

14. Spin, cure and pattern polyimide on the backside. Electroless plate nickel/gold on the backside pads.

Figure 4. (left) Simplified process flow for original flexible skin. (right) Improved process flow using DRIE, backside contacts, and electroless plating.

Another important innovation is the fabrication of backside contacts on the flexible skin. In short, the aluminum metalization is sandwiched between top and bottom layers of polyimide. We open up the bottom layer and use electroless gold plating to deposit a composite layer of ni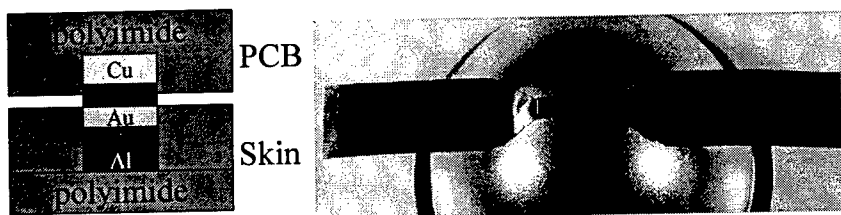ckel and gold on top of the aluminum. The top layer of gold is then easily attached to other packaging by means of solder paste, for example. This technology can simplify packaging immensely, as it minimizes hand assembly. A conceptual drawing of this bond is shown in Figure 5 (left), and an example of a packaged shear stress sensor skin using all of the above-mentioned technologies is shown in Figure 5 (right).

Figure 5. (left) Conceptual drawing of new packaging technology. (right) Picture of a shear stress sensor flexible skin packaged on a flexible PCB using all of the above mentioned technologies.

PROBE CALIBRATION

The unsteady flow around a probe may be considered to contain apparent mass/inertial, circulation induced lift, dynamic stall as well as dynamic boundary layer effects. In the present implementation, dynamic flow behaviour is assumed to be dominated by inertial or apparent mass effects; these are accounted for. The pressure measured at each port on the probe is decomposed into a steady and an inertial term, where the steady term is determined from a static calibration, and the inertial term is estimated using inviscid theory as follows from the unsteady Bernoulli equation (ignoring rotations of the body coordinate system) i.e.,

$$\frac{\Delta P}{\rho} = -\frac{1}{2}(\nabla\phi)^2 - V_\infty \cdot \nabla\phi - \frac{\partial\phi}{\partial t}$$

where the first two terms on the right hand side constitute the steady component, and the third term, the unsteady component. The solution methodology to account for the inertial effect is as follows (subscript i goes from 1 to 5 and indicates the specific port on the probe tip):

(i) pressure is decomposed into $p_i = p_i' + p_{inertial}$, where p_i' may be considered the steady pressure.

(ii) assume initially that $p_i = p_i'$, i.e. that $p_{inertial} = 0$

(iii) using the current p_i' values, calculate velocities, flow angles, etc using steady calibration methodology.

(iv) find the perturbation potential, ϕ, at each port of the probe.

(v) find ii $\Rightarrow$ iv for all of the time series.

(vi) find $d\phi/dt$ using time series.

(vii) find inertial term at each port on probe using Bernoulli's equation, i.e., $p_{inertial} = -\rho d\phi/dt$.

(viii) p_i' = steady pressure = $p_i - p_{inertial}$.

(ix) go to (iii) and iterate until $(p_i')^{n+1} - (p_i')^n <$ a prescribed small value.
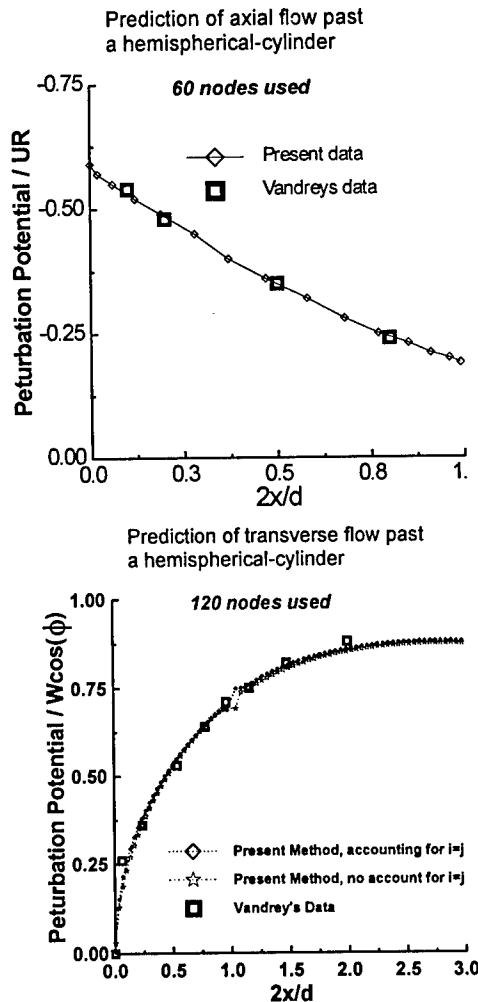

Figure 6. Perturbation potential on probe tip. (upper) axial flow, (lower) transverse flow.

Naturally, in implementation of the correction procedure, accurate determination of the potential on the probe face is essential. Matsunaga et al. used a distribution of singularities (doublets) along the axis of the probe to model the hemisphere-cylinder representation of the probe. However, for this type of body, an axial distribution of singularities does not yield an accurate representation of the flow, essentially due to a discontinuous second derivative of the surface.

In the present study, the surface singularity method was used to model the flow despite a significant increase in complexity and computational expense. As Laplace's equation is linear, the perturbation potential due to axial flow and that due to transverse flow can be decomposed and solved independently. To reduce the computational cost, different methods were used for the axial and transverse flow solutions. The potential due to axial flow was determined using the surface vortex ring method of Landweber[8]. The surface velocities were integrated to yield the potential. To ascertain the accuracy of the present scheme, results were compared with those of Vandrey, who used a somewhat more complicated surface vortex ring formulation. The presented data is for a hemispherical cylinder. 60 nodes were used in the present method. As may be seen in figure 6 (upper), the agreement between the present method and that of Vandrey is very good. A typical run time for 60 nodes was of the order of 5 sec on a Pentium class machine. The cross flow potential was determined

using the method of Lotz[9], which uses surface sources. The greater complexity of this method resulted in a typical run taking of the order of 60 secs. Figure 6 (lower) shows comparisons between the present method and that of Vandrey. 120 nodes were used in the solution, with 30 nodes placed on the hemispherical head. The figure shows that the present prediction methods closely matches the numerical results due to Vandrey. The potential has been reduced by the transverse flow velocity and ϕ, the angle from the transverse flow attachment line to the point of interest. Decomposition of the potential into the axial and transverse components allows the determination of the total potential for any freestream orientation. Consequently, the apparent mass/unsteady term in Bernoulli's equation ($\partial\phi/\partial t$) can be readily evaluated.

COLLABORATIONS, TECHNOLOGY TRANSITION AND FUTURE PLANS

We are working closely with Dr. Avi Seifert at NASA Langley on the experimental calibration of the probe. We are in the process of preparing an invention disclosure to Texas A&M which will transition to a patent funded by Aeroprobe Corp. who have indicated very strong interest in marketing the technology. In terms of future plans, once the 5-sensor probe is completed, we will proceed with the development of a MEMS-based, spherical, omni-directional pressure probe that will overcome the angularity limitations of the 5-sensor probe.

ACKNOWLEDGEMENT/DISCLAIMER

REFERENCES

1. Kerrebrock, J.L., et al., "A Miniature High Frequency Sphere Probe," *Proceedings of ASME Symposium on Measurement Methods in Rotating Components of Turbomachinery,* editors B. Lakshminarayana and P. Runstadler, ASME 1980, pp. 91-98.

2. Matsunaga, S., Ishibashi, H., and Nishi, M., "Measurement of Instantaneous Pressure and Velocity in Nonsteady Three-Dimensional Water Flow by Means of a Combined Five-Hole Probe," *Transaction of the AME J. of Fluid Engineering,* Vol. 102, 1980, pp. 196-202.

3. Ng, W.F. and Popernack, Jr., T.G., "Combination Probe for Hi-Frequency Unsteady Aerodynamic Measurements," *IEEE Transactions on Aerospace and Electronic Systems,* Vol. 24, No.1, 1988, pp. 76-84.

4. Naughton, J.W., Cattafesta III, L.N., and Settles, G.S., "Miniature Fast-Response Five-Hole Conical Probe for Supersonic Flowfield Measurements," *AIAA J.,* Vol. 31, No. 3, 1993, pp. 453-458.

5. Gossweiler, C.R., Kupferschmied, K. and Gyarmathy, G., "On Fast-Response Probes: Part 1-Technology, Calibration and Application to Turbomachinery," *presented at the International Gas Turbine and Aeroengine Cogress and Exposition,* The Hague, Netherlands, June, 1994.

6. Humm, H.J., Gossweiler, C.R. and Gyarmathy, G., "On Fast-Response Probes: Aerodynamic Probe Design Studies," *presented at the International Gas Turbine and Aeroengine Cogress and Exposition,* The Hague, Netherlands, June, 1994.

7. F. Jiang, Y. C. Tai, K. Walsh, T. Tsao, G. B. Lee, and C. M. Ho. "A Flexible MEMS Technolog and Its First Application to Shear Stress Sensor Skin". MEMS-97, Nagoya Castle, Japan, pp. 465-470, 1997.

8. Landweber, L., "The Axially Symmetric Potential Flow About Elongated Bodies of Revolution "Rep. Taylor Model Basin, Washington, No. 761, 1951.

9. Lotz, I., "Calculation of Potential Flow Past Airship Bodies in Yaw," NACA TM 675, D.C., 1932.

DEVELOPMENT AND CALIBRATION OF WALL-SHEAR-STRESS MICROSENSOR SYSTEMS

AFOSR GRANT F49620-96-1-0482

Eli Reshotko
Department of Mechanical and Aerospace Engineering
Case Western Reserve University
Cleveland, Ohio

Mehran Mehregany
Department of Electrical Engineering and Applied Physics
Case Western Reserve University
Cleveland, Ohio

Abstract
The long term objective of this program is to develop the requisite technologies for integrating different sensors and actuators in desired combinations with electronics and telemetry on the same substrate. This is a multi-year program. We are now in the middle of the third year.

Our concentration so far has been on wall-shear-stress sensors. To date we have produced and calibrated floating element wall-shear-stress sensors, both active and passive. We have developed a calibration channel and a calibration procedure based on continuum isothermal compressible channel flow. We have also developed and tested a wall-shear-stress sensors with integrated electronics initially based on the Analog Devices Inc. (ADI) airbag accelerometer circuitry, and more recently on one developed at CWRU.

This year's work continued the emphasis on the accuracy of the calibration process. We are trying to reduce the uncertainty of measurement from the past estimate of 5% to a goal of 1%. We have also continued our work toward the development of shear-stress and pressure sensors on the same chip.

Past Work
Prior to the start of this grant, we built a new calibration channel satisfying the requirements for non-leakage, non-choking, and having appropriate pressure and temperature measurements. The pressure measurements are required to evaluate the shear stress and the temperature measurements are to assure the isothermal character of the flow. It has been shown in our past work that in order to separate shear forces on the sensor element from pressure forces on the edge of the element, it is necessary to know the pressure gradient in the flow at the sensor location both during calibration and in operation.

The major new effort of the first year of the grant was the development of a chip that has both shear-stress sensors and pressure sensors together with on-chip circuitry. Based on our prior design experiences, the shear-stress sensor floating element has been optimized for sensitivity without compromising its strength. There are two pressure sensors respectively at the upstream and downstream ends of the chip. To insure a good measurement of the pressure difference, the reference sides of the two pressure sensors are connected to each other by a small micromachined channel. The fabrication of this chip is a five-mask, two-polysilicon-layer surface micromachining process.

For reasons unknown to either principal investigator, the shear stress sensor was removed from the design prior to fabrication. The remaining pressure sensor with on-chip circuitry is described below.

Current Work
1. Improving accuracy of the calibration process
In an effort to improve the accuracy and reduce the uncertainty in the calibration process, each element of the procedure was investigated in detail. The basic calibration relationship is

$$\tau = - (b/2)(dp/dx)(1- \gamma M^2)$$

where b is the height of the channel, dp/dx is the measured pressure gradient at the sensor location, γ is the ratio of specific heats of the test gas (nitrogen) and M is the Mach number at the sensor location. During the past year, we have had our rotameters recalibrated by the manufacturer so that our Mach number determination is within 1%. The pressure measuring circuits have been cleaned out and now give reliable readings. Since it is the pressure *gradient* that is required, the absolute value of pressure is of lesser importance, but we are trying to get an independent verification of the pressure transducer calibration. The largest inaccuracy is in the measurement of the channel height, b. Since this height is if the order of 200 μm, it is not measurable within 1% by any standard means. It is difficult to bring a microscope to the channel or vice-versa.

We have instead used the microwave technique called "Microstrip" (Pozar, David M.: Microwave Engineering, 2nd Ed., Wiley, 1998, pp.160 ff). A gold microstrip line is printed on the glass cover plate of the channel. The metal bottom of the channel is grounded. The transmission frequency that minimizes the reflected signal is directly related to the gap between the glass and the metal. Our measurements indicate a sensitivity of about ± 3μm which is about ±1.5% for a channel height of 200 μm. We believe our overall uncertainty now to be about ± 2%.

We are now in the process of calibrating new floating element sensors with on chip electronics. We tried to calibrate a strip of surface hot-wire sensors received earlier from Ho and Tai (UCLA/Caltech), but did not succeed because of difficulties with the supporting electronics.

2. Fabrication of monolithically integrated surface micromachined capacitive pressure sensor

Capacitive pressure sensors have been developed for industrial applications for many years with their advantages of high sensitivity, low temperature drift, robust structure and relative insensitivity to environmental effects. The out put capacitance of miniaturized sensors is normally a few pF to less than 1 pF and is very susceptible to parasitic effects. In order to detect such small capacitances, a well-matched readout circuit is required and it has to be placed as close as possible to the sensor. Therefore on-chip integration of sensors with their interface circuits is significantly important in this application.

A monolithically integrated touch mode capacitive pressure sensor has been fabricated successfully by surface micromachining technology based on a conventional 2.0-mm double-poly, double-metal n-well CMOS process. The CMOS interface circuits include the capacitance/voltage, capacitance/frequency conversion, and temperature compensation circuits on the same chip. The yield of both sensors and circuits exceeds 80%. Results indicate that the CMOS interface circuit works properly with the sensors. There is no obvious shift in threshold voltage observed after the additional sensor fabrication steps are added in the CMOS process. Measurement results are in agreement with simulation results. Since the membrane thickness and cavity depth can be very well controlled, devices can be designed with this technology for different pressure ranges, higher sensitivity, or better overpressure protection. The technology also allows inexpensive batch fabrication and integration of sensors with dedicated signal detection circuits.

Continuation Effort

The continuation work will include further work on the integration of the sensor elements with circuitry on the same chip. Following calibration of the sensors in our calibration channel, they will eventually be tested on a flat plate model in our 28" x 28" wind tunnel and the results compared with expectations from in-flow measurements..

Personnel

The work on this grant is being carried out by the following graduate students, Shuwen Guo under the supervision of Prof. Mehregany and Mehul Patel under the supervision of Prof. Reshotko.

Honors and Awards

Co-Chair, Technology Advisory Board, Micro Air Vehicle Program, DARPA, DoD, 1998 –

Designated the 1999 Distinguished Lecturer of the Department of Mechanical and Aerospace Engineering, Illinois Institute of Technology, Chicago, IL, The lecture was given on April 16, 1999

Ohio Aerospace Institute Distinguished Lecturer, Cleveland, OH. June 25, 1999

1999 Otto Laporte Award for Research in Fluid Dynamics, American Physical Society, "For lasting contributions and leadership to the understanding of transition to turbulence in high-speed flows and non-homogeneous flows."

Acknowledgement/Disclaimer

Publications and Presentations
Mehregany, M., DeAnna, R.G. and Reshotko, E.: "Microelectromechanical Systems for Aerodynamics Applications," AIAA Paper 96-0421, Jan. 1996

Reshotko, E., Pan, T. Hyman, D. and Mehregany, M.: "Characterization of Microfabricated Shear Stress Sensors," Eighth Beer-Sheva International Seminar on MHD Flows and Turbulence, Jerusalem, Israel, Feb. 1996

Reshotko, E., Saric, W.S. and Nagib, H.M.: "Turbulence and Noise Criteria and their Implementation in NWTC-Type Wind Tunnels, invited paper presented at AGARD/FDP Symposium on Aerodynamics of Wind Tunnel Circuits and Their Components, Moscow, Russia, Oct. 1996. In AGARD CP 585, pp. 28-1 to 28-14, 1997

Liang, F-P., Reshotko, E. and Demetriades, A.: "A stability study of the mixing layer formed by two supersonic streams," Physics of Fluids, vol. 8, no. 12, Dec. 1996, pp. 3253-3263

Mayer, E.W. and Reshotko, E.: "Evidence for transient disturbance growth in a 1961 pipe flow experiment," Physics of Fluids, vol. 9, no. 1, Jan. 1997, pp. 242-244

Reshotko, E., Saric, W.S. and Nagib, H.M.: "Flow Quality Issues for Large Wind Tunnels," AIAA Paper 97-0225, Jan. 1997 (Outstanding Paper Award)

Reshotko, E.: "Progress, Accomplishments and Issues in Transition Research," AIAA Paper 97-1815, June 1997

Reshotko, E., Mehregany, M. and Bang, C.: "MEMS Applications in Aerodynamic Measurement Technology,": AGARD-CP-601, May 1998, pp. 35-1 to 35-10. (Invited paper presented at RTO/AGARD FDP Symposium on Advanced Aerodynamic Measurement Technology, Seattle, Sept. 1997)

Saric, W.S. and Reshotko, E.: "Review of Flow Quality Issues in Wind Tunnel Testing," AIAA Paper 98-2613, June 1998

Saric, W.S., Reshotko, E. and Arnal, D.: "Hypersonic Laminar-Turbulent Transition," in J. Muylaert, A. Kumar and C. Dujarric, eds. *Hypersonic Experimental and Computational Capability, Improvement and Validation*, AGARD-AR-319, vol. II, 1998

Reshotko, E., Pan, T., Hyman, D. and Mehregany, M.: "Characterization of Microfabricated Shear Stress Sensors," in H. Branover and Y. Unger, eds. *Progress in Fluid Flow Research: Turbulence and Applied MHD*, Progress in Aeronautics and Astronautics, vol. 182, chapt. 22, AIAA, 1998, pp.335-351

Fang, Yung-Che and Reshotko, Eli: "Inviscid Spatial Stability of a Developing Supersonic Axisymmetric Mixing Layer," AIAA Journal, vol. 37, no. 1, Jan. 1999, pp. 23-28

Pan, T., Hyman, D., Mehregany, M., Reshotko, E. and Garverick, S.: "Microfabricated Shear Stress Sensors, Part I: Design and Fabrication," AIAA Journal, vol. 37, no.1, Jan.1999, pp.66-72

Hyman, D., Pan, T., Reshotko, E. and Mehregany, M.: Microfabricated Shear Stress Sensors, Part II: Testing and Calibration," AIAA Journal, vol. 37, no. 1, Jan. 1999, pp.73-78

July 1999

STRUCTURE-BASED TURBULENCE MODELING

AFOSR AF F49620-98-1-0138

W. C. Reynolds and S. C. Kassinos
Department of Mechanical Engineering
Stanford University

Objectives and previous accomplishments

The objective of this project is to develop a superior turbulence model for aerodynamic and propulsion system engineering. Our approach incorporates new concepts for parameterizing turbulence structure, such as the "dimensionality" of the turbulence, which allow representation of turbulence dynamics with greater physical fidelity than afforded with current turbulence models ([1], [2], [3]).

For the past several years we have developed and explored these new ideas, drawing heavily on the extensive DNS database for turbulent flows now available in the Center for Turbulence Research ([6]). We showed why current turbulence models fail in flows with strong swirl or frame rotation. We demonstrated that, by including new tensor parameters of the turbulence, more accurate prediction of homogeneous turbulence subjected to arbitrary rapid or slow mean strain, mean rotation, or frame rotation could be obtained. Using these ideas, we developed a Particle Representation Model (PRM) for arbitrarily deformed homogeneous turbulence that is now used by others in pdf-based codes for turbulent combustion ([4], [5]). The PRM is essentially a two-point model, which we believe is at the present too computationally intense for general turbulent flows because Large Eddy Simulation is preferred at this computational intensity. We also developed some rather complicated one-point multi-tensor models that do a good job for arbitrarily complex distortions of homogeneous turbulence ([5], [8], [9]).

Current focus: an algebraic structure-based model

Because our one-point models including the dynamics of all of the new tensors are quite complex, we have turned our attention to the creation of an "affordable" structure-based model that draws upon many of the ideas and the knowledge we have developed over the past several years. The idea is to use an *algebraic* structure-based procedure to relate the local turbulent stresses $R_{ij} = \overline{u'_i u'_j}$ to the local mean velocity gradient tensor, the turbulence time scale τ, and the turbulent kinetic energy $k = q^2/2$. In essence this assumes that the structure is in equilibrium with the local mean deformation and current scales, for which the body of our earlier work provides some justification. Partial differential transport equations for the kinetic energy and reciprocal time scale $\omega = 1/\tau$ are used to evolve the slowly changing scales of the flow. Thus, the *algebraic structure-based model* that is now emerging from our work is essentially a *two-equation model* with a structure-based algebraic relationship between the R_{ij}, the mean flow, and the two turbulence scales. This algebraic relationship replaces the constitutive equation based on an eddy viscosity (linear or non-linear) used in current two-equation turbulence models.

The algebraic procedure for homogeneous turbulence

For homogeneous turbulence, the structure-based model relates the normalized stresses $r_{ij} = R_{ij}/q^2$ to the *eddy axis tensor* a_{ij}, the *stropholysis vector* γ_k, and the *eddy jetal parameter* ϕ. An improved model under development adds the *eddy flattening parameter* β and the *eddy flattening tensor* f_{ij}. These quantities are determined from the mean deformation rates and time scale τ using a three-step algebraic process:

1. First, the eddy axis tensor a_{ij}^* that would result under just the mean strain rate $S_{ij} = \frac{1}{2}(U_{i,j} + U_{j,i})$ is calculated from

$$a_{ij}^* = \frac{1}{3}\delta_{ij} + \frac{(S_{ik}^* a_{kj} + S_{jk}^* a_{ki} - \frac{2}{3}S_{nm}^* a_{mn}^* \delta_{ij})\tau}{a_0 + a_1 S_{pq}^* S_{qr}^* a_{rp}\tau}$$

   where S_{ij}^* is the *anisotropic strain rate* $S_{ij}^* = S_{ij} - \frac{1}{3}S_{kk}\delta_{ij}$ and a_0 and a_1 are constants. By comparison with Rapid Distortion Theory (RDT), $a_1 = 2$. a_0 is a "slow" model constant, which we determine as 3.8 for consistency with the eddy viscosity of standard k-ε models in the r_{ij} for arbitrary weak deformation.

2. Then the eddy axis tensor a_{ij} is computed by applying a rotation operator H_{pq} to a_{ij}^*,

$$a_{ik} = H_{in}H_{jm}a_{nm}^*.$$

   The rotation operator is chosen to give the correct limiting eddy axis for shear flow in a rotating frame. No empirical constants are involved. The idea of the rotation comes from our observation that the effects of mean rotation on the eddy axis tensor and dimensionality are primarily kinematic. The rotation rate in the frame is used in determining H_{pq}, ignoring the frame rotation.

3. The parameters ϕ and γ_k are then modeled in terms of the total rotation rate, eddy axis tensor, and τ. This draws on our observation that the velocity within an eddy is affected dynamically by rotation. One empirical "slow" constant is involved.

4. The normalized stresses r_{ij} are then calculated using the structure-based algebraic relationship. Because of the multi-step process, full realizability is guaranteed.

Inhomogeneous turbulence

For inhomogeneous turbulence we make a further modification of a_{ij} and r_{ij} to account for wall blockage. An elliptic scalar equation is solved, from which the *wall blockage vector* b_k is calculated. This vector is perpendicular to the wall at the wall, decreases away from the wall at a rate determined by the length scale of the turbulence, and varies across the flow as it is influenced by other surfaces, Then, the a_{ij} and r_{ij} computed assuming homogeneity are projected onto planes perpendicular to the wall blockage vector to obtain the wall-corrected tensors. The net result is that the r_{ij} all have the correct behavior in the near-wall region ($r_{22} = O(y^2)$, $r_{12} = O(y)$, $r_{11} = O(1)$, $r_{33} = O(1)$ as $y = x_2 \to 0$), and realizability is guaranteed.

ω equation

The approach above could be used in any two-equation model. We have chosen to use $\omega = 1/\tau$ and then to model ε in terms of k, ω, and the kinematic viscosity ν. We differ from Wilcox ([7]), the pioneer of k-ω modeling, in three ways. First, we say that for high Reynolds numbers $\varepsilon = k\omega$, whereas he inserts a constant in this model. More important, we insist that the changes in scales that result from very rapid deformations must be consistent with RDT, which sets the coefficient of the ω production term. And third, because we have information on the eddy structure through a_{ij}, we have incorporated this information. Our model displays *material indifference to rotation* in the limiting case where the turbulence becomes 2D (eddy axes all aligned) with the axis of rotation aligned with the axis of independence. No other current turbulence model has this feature because no other model carries any parameterization of the dimensionality of the turbulence.

Status of the affordable structure-based model

The basic new ideas for the model are now in hand for the unflattened eddy version. We are testing the model in a variety of inhomogeneous flows, and will report results at the Contractors Meeting.

Eddy flattening is also straight forward but not yet implemented. Flattening will improve the stresses for shear flow, and will enable us to predict one of the most remarkable counter-intuitive observations from our past work; for axisymmetric expansion flow, the stresses are *more anisotropic* if the deformation is *slow* than if it is *rapid!*

Acknowledgement/Disclaimer

References

1. S. C. Kassinos and W. C. Reynolds, A Structure-Based Model for the Rapid Distortion of Homogeneous Turbulence. Report TF-61, Thermosciences Division, Department of Mechanical Engineering, Stanford University, Stanford, 1994.

2. S. C. Kassinos and W. C. Reynolds, An Extended Structure-Based Model Based on a Stochastic Eddy-Axis Evolution Equation. Annual Research Briefs 1995, Center for Turbulence Research, 133-148.

3. W. C. Reynolds and S. C. Kassinos, One-Point Modelling of Rapidly Deformed Homogeneous Turbulence. Proceedings of the Royal Society of London, 1995, **A,451**, 87-104.

4. S. C. Kassinos and W. C. Reynolds, A Particle Representation Model for the Deformation of Homogeneous Turbulence, Annual Research Briefs 1996, Center for Turbulence Research, 31-51.

5. S. C. Kassinos and W. C. Reynolds, Particle and One-Point Structure-Based Modeling of Slow Deformations of Homogeneous Turbulence. Proceedings of the Eleventh Sympo-

sium on Turbulent Shear Flows. Institut National Polytechnique, Université Joseph Fourier, 1997.

6. S. C. Kassinos, W. C. Reynolds, and M. M. Rogers, One-Point Turbulence Structure Tensors. Submitted for publication to the Journal of Fluid Mechanics, 1998.

7. David C. Wilcox, Turbulence Modeling for CFD, DCW Industries, California, 1998.

8. W. C. Reynolds and S. C. Kassinos, Linear Dependencies in Fourth-Rank Turbulence Tensor Models, Applied Mathematics Letters, 1998, Vol. 11, No. 5, pp. 79-83.

9. S. C. Kassinos and W. C. Reynolds, Developments in Structure-Based Turbulence Modeling, in Modeling Complex Turbulent Flows, 1999, Kluwer Academic Publishers.

TURBINE AEROTHERMAL RESEARCH

Task 2307B/W

Richard Rivir
Rolf Sondergaard
Shichuan Ou

Air Force Research Laboratory
Propulsion Directorate
Wright-Patterson AFB Ohio

The objective of the effort is to provide a fundamental understanding of the high turbulence and unsteady heat transfer and aerodynamics encountered in the turbine. This currently involves film cooling at high freestream turbulence levels, aerodynamic losses at low Reynolds numbers with active and passive boundary layer control in low pressure turbines, Vane-Blade interaction effects, and new instrumentation/control concepts using MEMS and MOMS.

Operation of low pressure turbines at high altitudes can result in 4 to 6% loss in LP turbine efficiency or typically a loss of 1% in SFC at cruise altitude for a turbine designed at sea level as is illustrated in Figure 1. This loss occurs as a result of separation on the suction surface, which becomes important at low Reynolds numbers. The objective of the LPT effort is to accurately predict the separation and to reduce the losses through active and passive turbine boundary layer control.
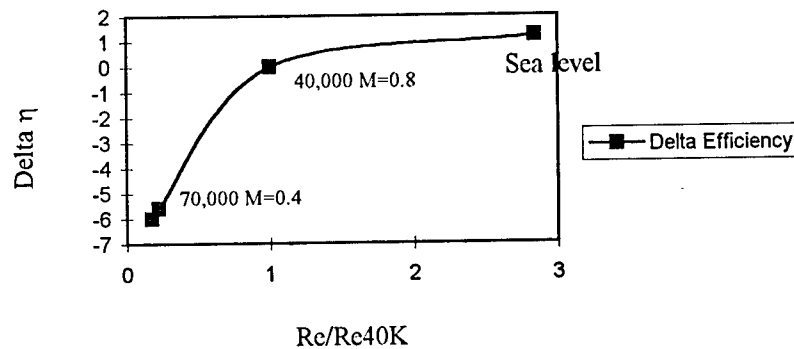

Figure 1. Efficiency Penalty for Low Reynolds Number Operation of the LPT

This problem also can arise in ground power LPT's as is illustrated by the 2 to 4 % losses in the Japanese CGT turbine illustrated below in Figure 2.
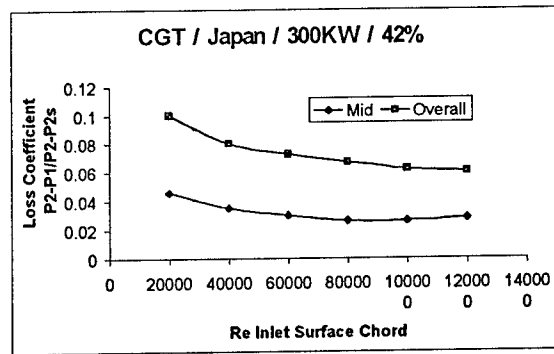
Figure 2. Loss Coefficient Due to an Increase in Turbine Inlet Temperature for a Ground Power Turbine

A 2D cascade (AR=4) of 7 highly loaded LPT blades with grid generated turbulence of 4% has been investigated at low Reynolds Numbers typical of LPT operation at altitude. Boundary layer profiles defining the location of separation on the suction surface were obtained and surface treatment applied ahead of, at and after the separation location. The loss coefficient with and with out treatment was compared. Treatment provided a 58% reduction in the loss coefficient for the passive treatment and a 30% reduction for the active case, as is illustrated in Figures 3 and 4 below. The loss coefficients showed no significant increase at higher Reynolds numbers for either passive or active treatments. Boundary layer control of Low Reynolds Number low pressure turbine flows was demonstrated to be effective with both passive and active techniques (AIAA 99-0242, AIAA 99-0367). The basic approach is to apply longitudinal vorticity generated by various techniques to reenergize the boundary layer. Boundary layer and receptivity theory can also be applied to this problem, however current results show that this level of detail is not necessary for effective separation control, although this level is also under investigation.
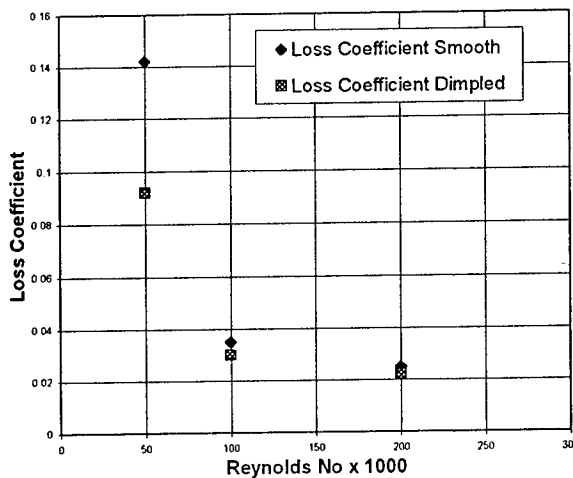

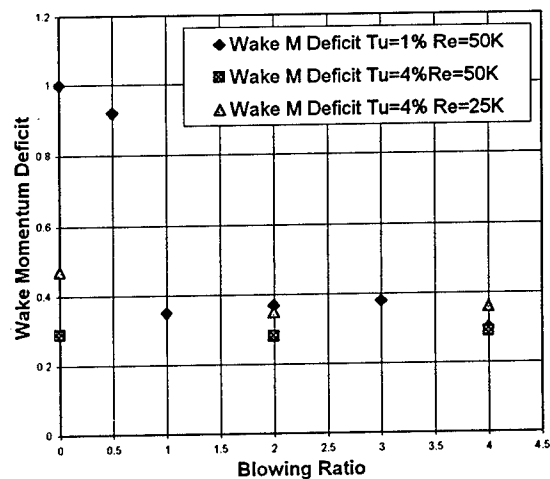Figure 3. Loss Coefficient for Dimpled Blades Figure 4. Wake Deficit for Blown Vortex Generators

Currently non-steady active techniques (non steady blowing) are being evaluated. Several variations of piezo electric arrays have also been fabricated which will be applied as both active and passive surface treatments. Other longitudinal vortex generation techniques to be investigated include thermal and acoustic mechanisms.

The optical pressure measurement efforts for the High Cycle Fatigue program have successfully demonstrated Fabry Perot devices, which can provide an enhanced measurement capability. Dasgupta, et al. has demonstrated an optical device with a frequency response of > 180KHz, @ 30psi, with a resolution of >0.05 psi, and spatial resolution of ~1mm. These devices will now go into a fan measurement demonstration. They should be capable of resolving wakes quite well. In another effort Physical Sciences has fabricated and demonstrated 4x4 arrays in which Fabry Perot Silicon sensors are activated and interrogated externally. The next step will be to fabricate larger arrays, multiplex them, apply to 3D surfaces, and provide simultaneous temperature measurements.
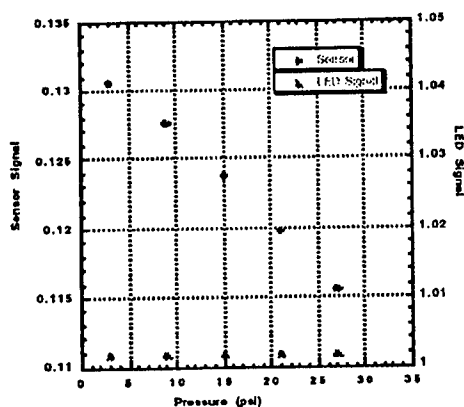

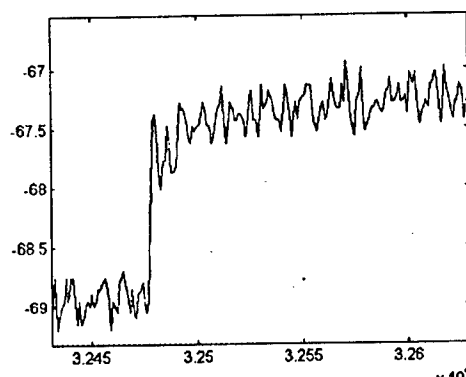Figure 5. Calibration of MOMS Against a Kulite

Figure 6. Frequency Response of MOMS in Shock Tube

Work has continued on the leading edge film cooling CRDA with Pratt with the submittal of a draft final Report in January. A similar effort with GE is anticipated to be initiated and completed this year. A new joint APD, AFIT, and Mississippi State effort for the investigation of roughness effects on performance and lifetime of ground power turbines was initiated with AGTSR in February. A F18EF/F22 carbon/carbon heat exchanger will be tested at APD late this year. Professor Pavo Sepri from the Florida Institute of Technology studied the differences between rod and vane simulations using Allison's Vane Blade Interaction program under the AFOSR Summer Faculty program at APD. Two PhD's defended their work this year, Capt. James Lake, AFIT and Marc Polanka (Palace Knight), University of Texas.

endorsements, either expressed or implied, of the Air Force Office of Scientific Research or the U.S. Government.

1999 Publications

Bons, Sondergaard, and Rivir, "Control of Low-Pressure Turbine Separation Using Vortex Generator Jets," 37th AIAA Aerospace Sciences meeting, Reno NV, AIAA–99-0367, Jan 1999.

Lake, King, and Rivir, "Reduction of Separation Losses on a turbine Blade with Low Reynolds Numbers," 37th AIAA Aerospace Sciences meeting, Reno NV, AIAA–99-0242, Jan 1999.

Dasgupta, Zhou, Boyd, Jackson, Glawe, and Rivir, "Optically Integrated Micromachined Sensor Arrays for Propulsion Applications," Instrument Society of America, Albuquerque, NM, 3-6 May 1999.

Baughn, Mayhew, Butler, Byerley, and Rivir, "Turbine Blade Flow Separation and Reattachment at Low Reynolds Number," 1999 Journal of Heat Transfer Picture Gallery.

James P. Lake "Flow Separation Prevention on Turbine Blade in a Cascade at Low Reynolds Number," Air Force Institute of Technology, PhD Dissertation, June 1999.

Pavo Sepri , "A Computational Study of Turbine Blade Interactions with Cylinder Wakes at various Reynolds Numbers," Final Report AFOSR Summer research Program, Oct 1999.

RECTANGULAR SUPERSONIC JETS MODIFIED FOR MIXING ENHANCEMENT AND NOISE REDUCTION

F49620-97-1-0493[*]

M. Samimy
Department of Mechanical Engineering
The Ohio State University

Abstract

Trailing-edge modifications in a rectangular Mach 2 nozzle with an aspect ratio 3 was used to explore passive mixing enhancement capabilities of these modifications in various flow regimes. The results revealed that 1) the trailing edge modifications, that are in the plane of the nozzle, do not affect the thrust force, 2) the spanwise surface pressure gradient set up by the trailing edge modifications is the main source of streamwise vortices, and 3) by proper design and arrangement of trailing edges, one can change the level and rate of mixing and thus perhaps the level, directivity, and frequency content of generated noise. Sample results will be presented here. Detailed results can be found in Kim and Samimy (1999).

Introduction

Large scale turbulence structures in the mixing layers of high speed jets are responsible for gross mixing between the jet fluid and the ambient air, and are also the main source of jet noise. Controlling infrared signature of the jet can be achieved by controlling the characteristics of large scale structures and thus mixing of the jet with ambient air. Controlling jet noise can also be achieved by controlling the characteristics of large scale structures. However, it has been known for over a decade that it is difficult to control spanwise or ring-type vortical structures in highly compressible supersonic mixing layers because of their three-dimensional nature and lack of organization (Samimy et al. 1992 and Clemens and Mungal 1992). In highly compressible mixing layers, these lead to reduced entrainment and mixing (Papamoschou and Roshko 1988), and also to reduced Reynolds stresses (Samimy and Elliott 1990 and Goebel and Dutton 1991). In contrast to these large scale structures, the streamwise vortices do not seem to be much affected by the compressibility (Elliott et al. 1992, Samimy et al. 1993, Zaman et al. 1994, and Reeder and Samimy 1996). Thus, generating streamwise vortices appears to be an effective way to enhance mixing and to reduce noise in supersonic jets.

In the past, several techniques have been explored to generate streamwise vortices for mixing enhancement and noise reduction purposes (reviewed in Gutmark et al., 1995). Tabs, as streamwise vortex generators, have been found to be effective devices in reducing jet noise and enhancing mixing not only in subsonic but also in supersonic axisymmetric jets (Ahuja and Brown 1989, Samimy et al. 1993, and Zaman et al. 1994). The generated streamwise

---

vortices by half-delta wings resulted in significantly enhanced mixing in Mach number 0.6 circular jets (Surks et al. 1994) and rectangular jets (Rogers and Parekh 1994). Although the use of tabs or vortex generators to enhance mixing and to reduce noise is effective in subsonic and supersonic flows, it results in thrust losses due to the blockage effects of the tabs or vortex generators.

An alternative technique for generating streamwise vortices to enhance mixing and to reduce noise is the use of trailing edge modifications. Samimy et al. (1998) have shown that mixing in a rectangular supersonic jet can be significantly enhanced. The most recent results in supersonic rectangular jets (Kim and Samimy 1999), reveal that 1) the trailing edge modifications do not affect the thrust force, 2) the spanwise surface pressure gradient set up by the trailing edge modifications is the main source of streamwise vortices, and 3) by proper design and arrangement of trailing edges, one can change the level and rate of mixing and thus perhaps the level, directivity, and frequency content of generated noise. Sample results will be presented here. Detailed results can be found in Kim and Samimy (1999).

Results

A short summary of major findings in four categories will be presented here. Schematics of the nozzle and the modified trailing edges used in the present work are shown in Fig. 1.

1. **Thrust measurements:** A one-component thrust measuring system was designed, constructed, and used to find out the effects of trailing edge modifications on the thrust force. The results shown in Fig. 2 indicate that none of the many trailing edges examined had any effect on the thrust force and all the data from various cutouts fall on top of each other. This is very important from practical stand point, and makes the trailing edge cutouts very attractive to aircraft industry.
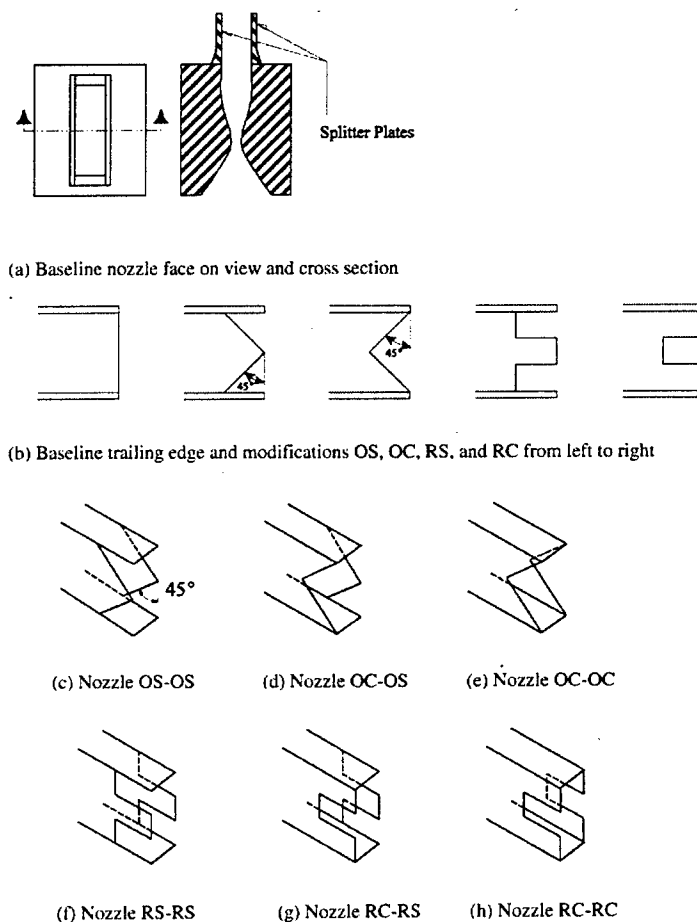

(a) Baseline nozzle face on view and cross section

(b) Baseline trailing edge and modifications OS, OC, RS, and RC from left to right

(c) Nozzle OS-OS (d) Nozzle OC-OS (e) Nozzle OC-OC

(f) Nozzle RS-RS (g) Nozzle RC-RS (h) Nozzle RC-RC

Figure 1 Schematics of the nozzle and the modified trailing edges.

2. Generation of large scale streamwise structures:

From the jet cross-sectional images, such as those in Fig. 3, it is obvious that these trailing edge cutouts generate strong streamwise vortices in the underexpanded flow regime, relatively weak streamwise vortices in the overexpanded flow regime, and no streamwise vortices in the fully expanded flow regime. It should be mentioned that in order to simplify the problem, and to make it easy to identify streamwise vorticity sources, the cutouts in these experiments were on the extension plates, that were attached to the nozzle, or were on the splitter plate itself. Therefore, in the fully expanded flow regime, the flow expanded to the ambient pressure before the cutouts. Currently we are in the process of incorporating the cutouts into the design of the nozzle,

Figure 2 Variation of thrust force with jet Mach number for various nozzle trailing edges
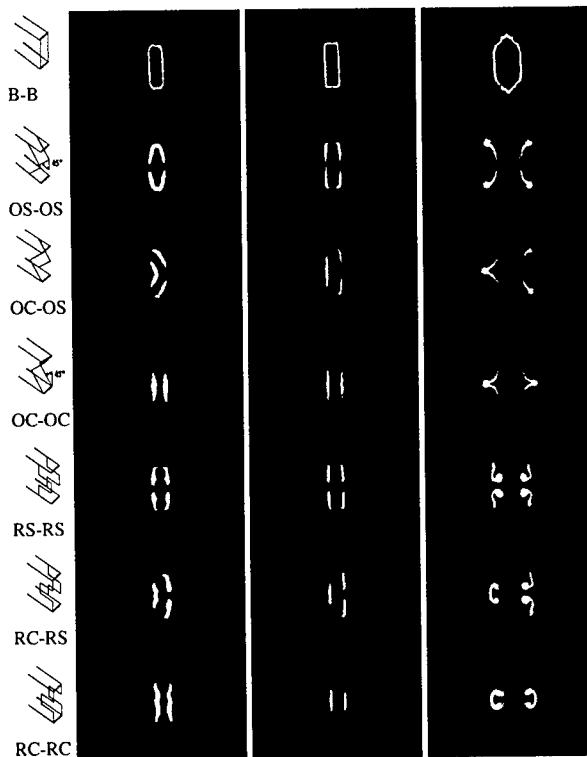
similar to the practical cases, in which the flow will interact with the cutouts while still expanding. In these situations, we expect to see the effects of cutouts even in the ideally expanded flow regime. It should also be noted that these images visualize only a portion of the mixing region that has sufficient condensed water particles, generated due to the mixing of the moist ambient air with dry and cold jet air. Therefore, in cases where the streamwise vortices are imbedded in the mixing regions (such as those in nozzles RS-RS, RC-RS, & RC-RC in the underexpanded flow regime), they can be easily identified. In cases where the streamwise vortices are at the edges of the mixing region, these vortices cannot be visualized, but their effect on the mixing layer leaves no doubt about their presence and strength (such as those in nozzles OS-OS, OC-OS, & OC-OC in the underexpanded flow regime).

Figure 3 Average cross-sectional jet images at $x/D_{eq} = 1$ for $M_j = 1.75$, 2.0, 2.5 from left to right.

3. Streamwise vorticity generation mechanisms:
Originally, the suspects were a) shedding of vorticity in the boundary layer, b) baroclinic torque due to potential misalignment of density and pressure gradients, and c) spanwise surface pressure gradients due to the cutouts. Our most recent surface flow visualizations and surface pressure measurements, Fig. 4, indicate that the last mechanism, namely the spanwise pressure gradient, is the main source of streamwise vorticity. The results show that there is negligible spanwise pressure gradient on the cutouts in the fully expanded case (as expected), small gradient in the overexpanded case due to flow separation, but very strong gradient in the underexpanded case. Note that the surface pressure gradient must be in the vicinity of the edge of a trailing edge in order to be effective.
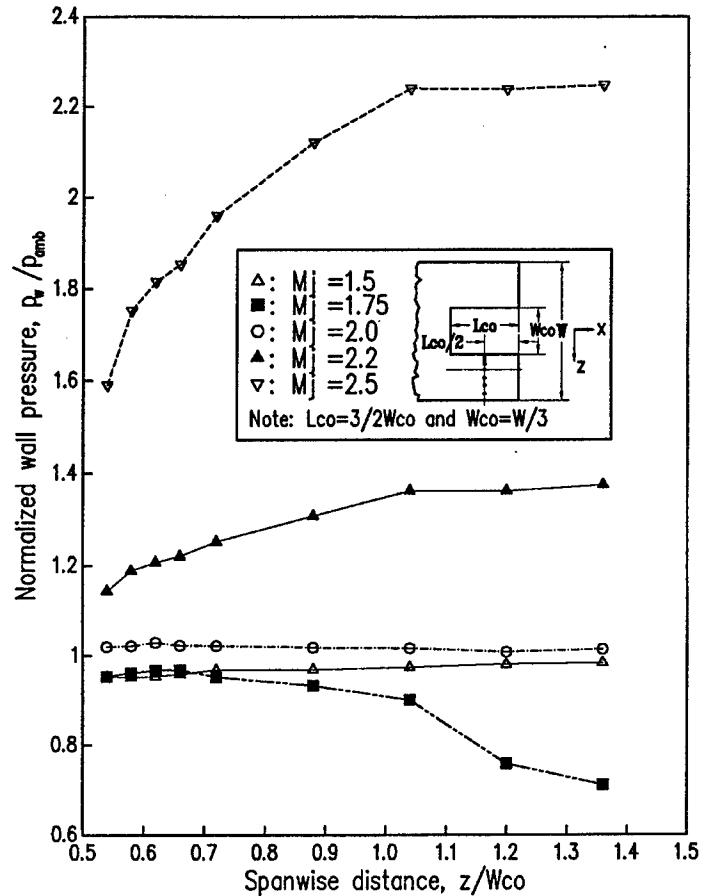

Figure 4 Spanwise pressure gradient for RC cutout at different flow regimes
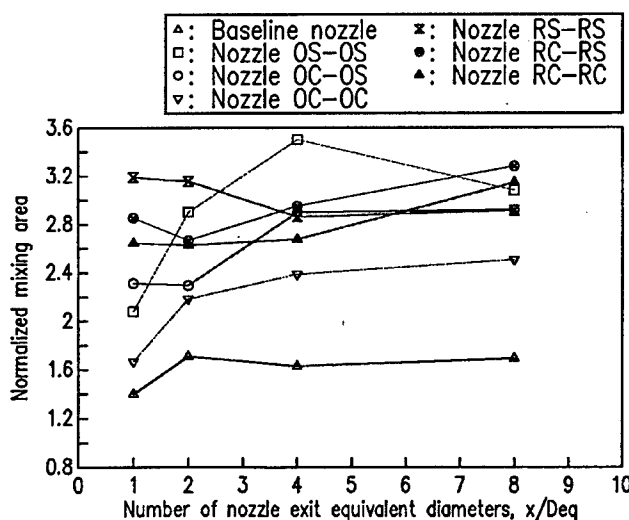

Figure 5 Variation of mixing level with streamwise direction for M_j=2.5.

Simple calculations also show that probably, mechanisms a) and b) are negligible in the current flow conditions. Note that incorporating the cutouts into the nozzle block probably will set up spanwise surface pressure gradient even in the fully expanded flow regime.

4. Control of strength of streamwise vortices and their interactions:
There is a considerable interest on whether one can control the strength of these vortices and the interaction between them and thus to control mixing level and rate, and also noise level and perhaps noise frequency content and directivity. Our results indicate that this kind of control is quite possible. As shown in Fig. 3,

250

the cutouts with edges in the streamwise direction (e.g. nozzles RS-RS, RC-RS, & RC-RC) generate stronger streamwise vortices than the cutouts with oblique edges (e.g. nozzles OS-OS, OC-OS, & OC-OC). In the first set of configurations, the vorticity induced by the surface pressure gradient is already aligned with the streamwise direction, while in the second set, the induced vorticity has to go through a tilting process to convert to streamwise vorticity – thus the streamwise vortices generated by the first configurations are stronger than those induced by the second set. On the other hand, the induced vortices by the first set are much closer to each other and thus could destructively interact with each other very close to the jet exit (e.g. nozzle RS-RS), while in the other set, the vortices are far apart and do not interact until much farther downstream. This gives one a control mechanism to force the vortices to interact earlier or later and thus to start the breakdown process of larger structures to smaller structures or the energy cascading process earlier or later in the jet development. This obviously has important ramifications in both jet mixing level and rate, and also jet noise level and frequency content. Figure 5 shows the normalized mixing areas obtained from flow visualization results similar to the one in Fig. 3. Comparing the mixing level and rate for nozzles OS-OS and RS-RS, for example, makes this point very clear.

We have not looked at the noise frequency content as we did not have an anechoic chamber. But we just designed and built a very high quality anechoic chamber with full optical access and are in the process of looking at the noise aspect in detail soon.

References

Ahuja, K. K. and Brown, W. H., 1989, "Shear Flow Control by Mechanical Tabs," AIAA-89-0994, AIAA Shear Flow Conference, March 13-16, Tempe, AZ.

Clemens, N.T. and Mungal, M.G., 1992, "Two- and Three-Dimensional Effects in the Supersonic Mixing Layer," AIAA Journal, Vol. 30, No. 4, pp. 937-981.

Elliott, J.K., Manning, T. A., Qui, Y. J., Greitzer, E.M., Tan, C. S., and Tillman, T. G., 1992b, "Computational and Experimental Studies of Flow in Multi-lobed Mixers," AIAA Paper 92-3568.

Goebel, S.G. and Dutton, C.J., 1991, "Experimental Study of Compressible Turbulent Mixing Layers," AIAA Journal, Vol. 29, pp. 538-546.

Gutmark, E. J., Schadow, K. C., and Yu, K. H., 1995, "Mixing Enhancement in Supersonic Free Shear Flows," Annual Review of Fluid Mechanics, Vol. 27, pp. 375-417.

Kim, J.-H. and Samimy, M., 1999, "Mixing Enhancement via Nozzle Trailing Edge Modifications in a High Speed Rectangular Jet," To be appear in Phys. Fluids, Vol. 11, No. 9, September 1999.

Papamoschou, D. and Roshko, A., 1988, "The Compressible Turbulent Shear Layer: an

Experimental Study," Journal of Fluid Mechanics, Vol. 197, pp. 453-477.

Reeder, M.F. and Samimy, M., 1996, "The Evolution of a Jet with Vortex-Generating Tabs: Real-Time Visualization and Quantitative Measurements," Journal of Fluid Mechanics, Vol.311, pp. 73-118.

Rogers, C.B. and Parekh, D. E., 1994, "Mixing Enhancement by and Noise Characteristics of Streamwise Vortices in an Air Jet," AIAA J., Vol. 32, p. 464.

Samimy, M. and Elliott, G.S., 1990, "Effects of Compressibility on the Characteristics of Free Shear Layers," AIAA Journal, Vol. 28, No. 3, pp. 439-445.

Samimy, M., Reeder, M.F., and Elliott, G.S., 1992, "Compressibility Effects on Large Structures in Free Shear Flows," Physics of Fluids A, Vol. 4, No. 6, pp. 1251-1258.

Samimy, M., Zaman, K. B. M. Q., and Reeder, M. F., 1993, "Effect of Tabs on the Flow and Noise Field of the Axisymmetric Jet," AIAA Journal, Vol. 31, No. 4, April, pp. 609-619.

Samimy, M., Kim, J. -H., Clancy, P. S., and Martens, S., 1998, "Passive Control of Supersonic Rectangular Jets via Nozzle Trailing Edge Modifications," AIAA Journal, Vol. 36, 1230.

Surks, P., Rogers, C. B., and Parekh, D. E., 1994, "Entrainment and Acoustic Variations in a Round Jet from Introduced Streamwise Vorticity," AIAA Journal, Vol. 32, p. 2108.

Zaman, K.B.M.Q., Reeder, M.F., and Samimy, M., 1994, "Control of an Axisymmetric Jet Using Vortex Generators," Physics of Fluids, Vol. 6, pp. 778-793.

CONTROL OF TRANSITION IN SWEPT-WING LAYERS USING MEMS DEVICES AS DISTRIBUTED ROUGHNESS

AFOSR GRANT F49620-97-1-0520

William S. Saric and Helen L. Reed

Mechanical and Aerospace Engineering
Arizona State University, Tempe AZ 85287-6106
saric@asu.edu
http://wtsun.eas.asu.edu

Abstract. Recent experiments at ASU on the stability and transition of swept-wing boundary layers have shown that under certain flow conditions, properly selected surface roughness elements can significantly delay transition[1,2]. These roughness elements are typically 6–18 μm high and 2–4 mm in diameter and are placed near the attachment line of the swept airfoil where the boundary-layer thickness is of the order of 600 μm. The present effort uses surface-mounted metal foils that cover 3 mm diameter holes. The holes are pressurized and a micron-sized bubbles duplicate the previous results and provide a versatile scheme for changing the roughness pattern and height as flow conditions change. The control of the bubble displacement will be implemented with commercially available MEMS valves and pressure regulators. This technique is a significant change from the silicon-based technique reported on a year ago. New methods for transition detection developed during ASU experiments[3]—using surface-mounted hot-film arrays and proper orthogonal decomposition (POD)—will give real-time analysis of transition location. The experiments will be supported by ASU-developed[4], nonlinear PSE computations to predict the unstable growth prior to transition.

Introduction. The control of laminar-turbulent transition is still one of the important challenges of aerodynamics. The problems extend from low-Reynolds-number inlet design of high-altitude hypersonic air breathers to the design of long-range transports to the reduction in heat transfer in gas turbines. Of particular importance is transition within three-dimensional boundary layers characteristic of swept wings and swept turbine blades. The combination of sweep and pressure gradient produces a crossflow within the boundary layer that perpendicular to the inviscid streamlines. The crossflow profile is inflectional and has an instability that manifests itself as streamwise-oriented, co-rotating vortices that may be either traveling or stationary. Whereas linear theory predicts that the traveling waves are more unstable, stationary waves dominate in low-turbulence environments[1]. In contrast to streamwise instabilities (T-S waves), crossflow waves are insensitive to sound but sensitive to freestream turbulence. They are also insensitive to 2-D roughness and sensitive to 3-D roughness. The sensitivity to 3-D roughness is such that the boundary layer responds to values of Re_k less than 1. The transition control results of Saric et al.[2] can be summarized in following table. At a chord Reynolds number of 2.4 million:

Roughness height [μm]	Spacing [mm]	Transition location x/c
0.2	random	65%
6	12 (most unstable)	45%
6	8	>80%
48	8	>70%

Basically the nonlinear response of the streamwise vortices creates harmonics in wavenumber space but not subharmonics. One introduces higher wavenumber disturbances that initially grow and inhibit the growth of lower wavenumber disturbances. The higher wavenumber disturbances then decay, leaving nothing.

Swept-Wing Model. Based on the already successful experiments at ASU[1,2], we fabricated a new model called the *Dynamic Flow Control swept wing (DFC)*. This 45° swept model has the capabilities for (1) pure Crossflow (C-F) dominated transition in accelerated flow, (2) combined weak C-F and weak T-S in a region of a flat C_p, and (3) strong T-S and weak C-F in the pressure recovery region. Figure 2 shows the airfoil profile and the C_p for $\alpha = -3°$. The profile is a modification of *NACA-67-1-015* and Fig. 2 shows that it generates significant C-F for these experiments. The designation for this airfoil is *ASU (67)–0315*.

The model is made of a solid foam core with a fiberglass skin. Solid aluminum is used in the leading edge region to control background roughness. The tolerances are carefully controlled on this insert and the surface is polished to 0.2 μm rms. In Fig. 1, one can see that there is a 0%–20% chord opening in the center of the model with a 762 mm spanwise gap used for inserting different test fixtures such as micro-bubble array and the MEMS devices. Figure 1 also shows a photograph highlighting the leading-edge region of the DFC model. The aluminum section is indicated by light gray area. A 720 mm span is available for actuators and measurements. Contoured end liners are used to simulate infinite-span swept-wing flow conditions.

A solid insert is made with the model in order to calibrate in non-roughness case. Another solid insert has been fabricated in order to accommodate the roughness actuators. This insert has a spanwise slot centered at 3% chord for the installation of the MEMS devices. The 762 mm span of the insert provides ample test area in which to perform the experiments.

Roughness Elements. Previous reports described roughness elements made of silicon using MEMS technology. Implementation of this technology proved difficult and whereas the devices could be successfully built, we would not have had time to test them in the wind tunnel. We have changed the direction of our approach and chose instead to use the displacement of thin foils as roughness elements. We worked with mylar, aluminum and stainless steel and had the most success with 110 μm thick aluminum. The foil is placed over a 3 mm hole which is pressurized. The subsequent error-function-like dis-

placement is different than the static roughness used in the previous experiments so its effect needed to be verified.

A series of experiments were conducted that demonstrated that an 8 μm displacement of the microbubbles produced the same transition location as the 6 μm fixed roughness of Saric et al[2]. We have demonstrated *proof of concept* for the new technique and now have a robust method for creating micron-sized roughness on the wing surface near the attachment line.

Fabrication and Assembly of Roughness Actuators. Distributed arrays of microbubbles will be placed near the leading edge in order to vary the roughness height and spacing under a variety of flow conditions and attempt to control transition. Initially, roughness heights will vary from 4 to 20 μm. Three rows of actuators, 720 mm in the span direction, will be utilized on the model and will consist of 2 mm and 3 mm diameter microbubbles on 4, 6, and 8 mm spacings. The amplitude of the microbubbles will be varied by changing the pressure within the subsurface cavity. This is an ideal application of MEMS technology since a large number of valves and regulators will be confined to a small volume.

Three modes of operation will be utilized.
1. A quasi-static, spanwise-uniform array whose amplitude can be varied incrementally during the experiment. See Figure 4.
2. An oscillating, spanwise uniform array whose amplitude would be a combination of DC and AC components operating to 100 Hz. See Figure 4.
3. An oscillating, phase-shifted array whose AC component would initiate a spanwise traveling wave. See Figure 5.

These devices will then need to be mounted in a wing insert for the ASU wing. The insert has a groove machined about 1.5 mm deep and 30 mm wide to contain the three rows of devices. Furthermore, the groove will have slots machined into the bottom at appropriate locations for the connectors. The devices will be placed in the groove such that the top surface of the devices is flush with the wing insert surface, and the connectors are positioned in the through slots.

Transition Measurements. Detailed hot-wire measurements (100 profiles per x/c location) will determine amplitude-growth conditions. These data are also useful for the eventual development of prediction and control schemes that are vitally needed in C-F-dominated problems. Hot-film sheets, specifically designed to simultaneously measure the surface shear stress across the transition front, are used for transition detection. The 16 parallel sensors are spaced 10 mm apart, thus spanning a range of 150 mm. The sensing elements are 0.127 mm wide and 1.5 mm long. The length is designed to capture the larger scales in the flow, such as the C-F vortices themselves. Once the hot-film sheet is placed across the transition front, the signals from all sensors are acquired simultaneously. A multi-point correlation technique known as proper orthogonal decomposition (POD) is then used to independently identify the fundamental instability modes, thereby allowing an objective detection of the entire transition region (Chapman et al.[3]). The

technique isolates the primary instability in the first POD mode and the secondary instability in the second POD mode. The peak of the first POD mode identifies the onset of transition while the peak of the second mode indicates the onset of turbulence.

Summary of Recent Computational Work. For 3-D boundary layers, nonlinear distortions of the basic flow may occur early on due to the action of the *stationary* primary instability. These flows are characterized by an extensive distance of nonlinear evolution with eventual saturation of the fundamental disturbance, leading to the strong amplification of very-high-frequency inflectional instabilities and breakdown. Here linear stability theory (LST) is not successful[5]. However, the NPSE, which have significantly less resource overhead associated with them compared with direct numerical simulations (DNS), have been shown to accurately model transition in a variety of flows when the environmental conditions are modeled correctly[5]. In recent years the parabolized stability equations (PSE) have become a popular approach to stability analysis owing to their elegant inclusion of the nonparallel and nonlinear effects which are ignored by LST. In the PSE approach the explicit streamwise diffusion term is neglected based on physical arguments. The resulting system of disturbance equations is parabolic and thus requires boundary and initial conditions. To complete the problem formulation, initial values of the disturbance quantities are specified at some streamwise location for the start of the analysis.

At ASU, Haynes and Reed[4] have already formulated, coded, verified, and validated the PSE (including curvature) for the ASU experiments[1,2]. As an example of the power of the NPSE, a sample of the excellent agreement between the NPSE and the experiments is presented here. A spanwise array of roughness elements is used near the airfoil leading edge to introduce 12 mm spanwise-periodic C-F disturbances into the boundary layer. In this particular case, the initial conditions for the NPSE calculation were obtained by solving the local LST equations at 5% chord location for the fundamental mode and adjusting its rms amplitude such that the *total* disturbance amplitude matched that of the experiment at 10% chord. Figure 3 shows the comparison of experimental N-factor curves with PSE and LST. After a region of linear growth, the disturbance modes achieve large amplitudes and interact nonlinearly, saturating at 30% chord. There is a large region of nonlinear interaction from 30%–50% chord before transition occurs.

Similar agreement is found for all experimental freestream and roughness conditions. These results validate the ASU PSE approach for cases where the disturbance inputs are known or controlled. For the research under this proposal, we shall investigate various initial conditions modeling the roughness, including various receptivity models.

Nonlinear Parabolized Stability Equations. The detailed hot-wire measurements are supplemented with NPSE calculations following Haynes and Reed[4]. Roughness-receptivity models will be developed to provide initial conditions for the computations. These will be validated in the wind-tunnel experiments. The goal is to produce a computational model that duplicates the experiment and provides a means for analyzing a wider parameter space.

Control. We have brought together the means for changing roughness height and distribution during an experiment, the means for measuring the details of transition location in real-time, the means for calculating the observed behavior, and the means for modeling the physical mechanism in order to provide initial conditions for the computations. The initial distributed microbubble array will be used to delay transition under different flow conditions. After code and initial-condition validation, a rational prediction and control scheme can be developed, first for stationary disturbances and then for traveling disturbances.

Near Term Goals. July 1999 will be spent implementing the quasi-static roughness and conducting preliminary transition measurements. An important issue to be resolved is the nature of the secondary instability leading to transition. There is strong evidence that this part of the breakdown may be an absolute instability. By the end of summer, we will implement the MEMS valves and regulators for dynamic flow control.

References

1   Reibert, M.S., Saric, W.S. 1997 Review of Swept-Wing Transition. *AIAA 97-1816*.

2   Saric, W.S., Carrillo, R.B., Reibert, M.S. 1998 Leading-Edge Roughness as a Transition Control Mechanism. *AIAA 98-0781*.

3   Chapman, K.L., Reibert, M.S., Saric, W.S., Glauser, M.N. 1998 A multi-point correlation analysis of a crossflow-dominated boundary layer. *AIAA 98-0186*.

4   Haynes, T.S., Reed, H.L. 1998 Numerical Simulation of Swept-Wing Vortices Using Nonlinear Parabolized Equations. Submitted J. Fluid Mech. (also SAE 97-1479).

5   Reed, H.L., Haynes, T.S., Saric, W.S., CFD Validation Issues in Transition Modeling. AIAA Journal, 1998, 36,5: 742-51.
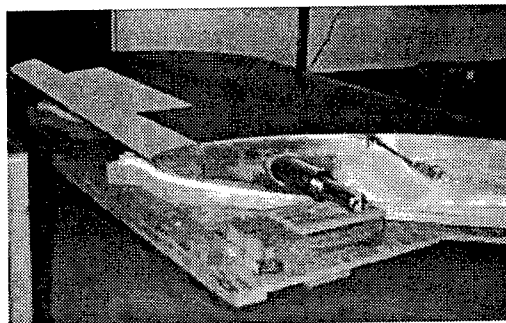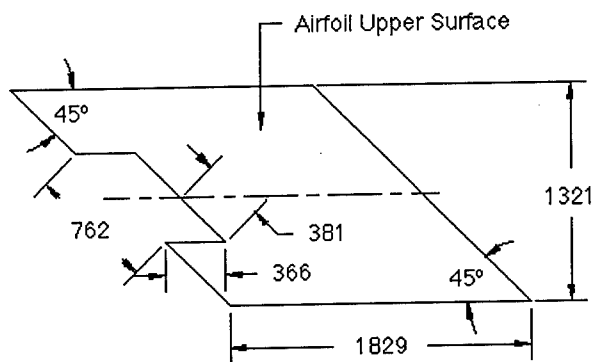
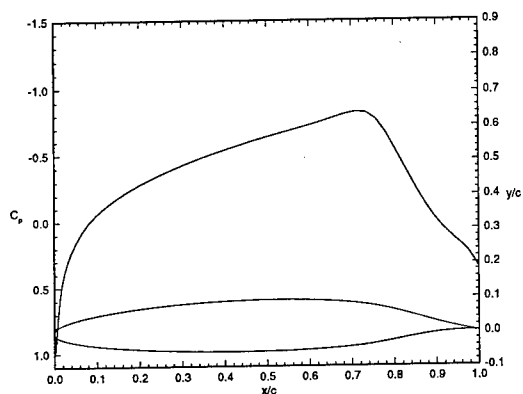Figure 1. ASU airfoil model: *ASU (67)-0315*. All dimensions in mm.

Figure 2. Profile and C_p for *ASU (67)-0315* at $\alpha = 3°$. The unswept (2-D) cross section is shown.
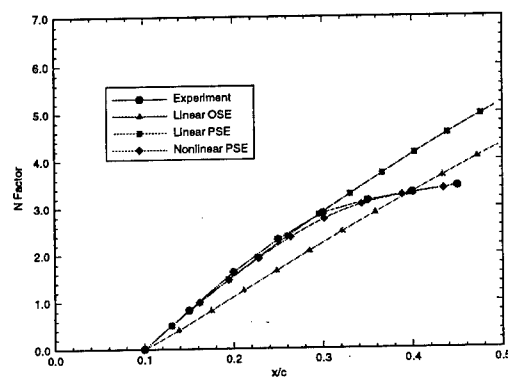

Figure 3. Growth of C-F vortex: Theory[4] and experiment[1] for 12 mm wave.
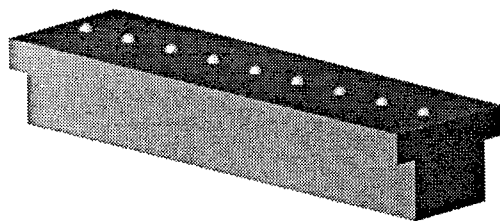

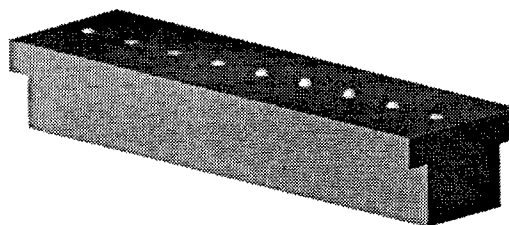Figure 4. Microbubble device with static, spanwise-uniform roughness array deployment.

Figure 5. Microbubble device with unsteady, traveling wave roughness array deployment.

MICRO HEAT EXCHANGER USING MEMS IMPINGING JETS

Yu-Chong Tai
Division of Engineering and Applied Science
California Institute of Technology
Pasadena, CA 91125

Chih-Ming Ho
Mechanical and Aerospace Engineering Department
University of California, Los Angeles
Los Angeles, CA 90095

Goal

The objective of this project is to obtain a set of design rules that can be used to develop an efficient and economical heat exchanger, that will meet present and future integrated circuit micro chip cooling requirements. The two factors which largely determine the efficiency of a heat exchanger in this situation is (1) its ability to transfer heat from the chip surface to a transport medium, usually air, and (2) this medium's capacity to convect the heated fluid away from the chip. Our proposed solution to this conundrum is to develop and characterize a micro jet impingement cooling system, as conceptually illustrated in Figure 1.
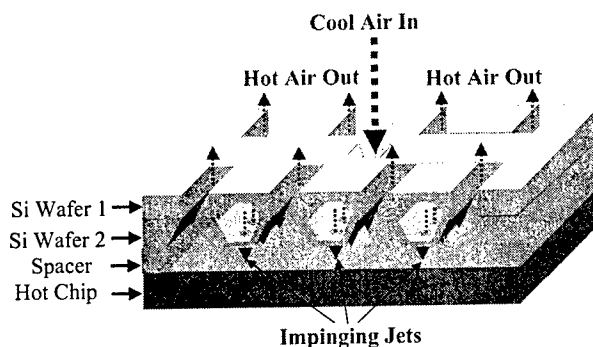

Figure 1. Conceptual illustration of MEMS impinging jet heat exchanger.

Approach

The problem had been broken up into three distinct engineering and research focus areas. During the period covered in this report, we have (1) tested single micro nozzles and nozzle arrays at various operating conditions, (2) rigorously characterized a "target sensor chip" which also simulates heat fluxes via backside heaters has and (3) determined heat convection characteristics away from the impingement region via the investigation of high-pressure fluid flow in instrumented micro channels. The data obtained from experiments with these devices can be used to formulate rules for the optimal design of

micro impinging jet heat exchangers based on air inlet conditions or maximum allowable surface temperature.

Progress and Results

During this reporting period, August 1998 to January 1999, we have accomplished the following achievements.

Testing of Target Chip with Integrated 64 Sensor Array

A second-generation, temperature-sensor-array chip was successfully used as a test target for the impinging jet system. This 2 cm x 2 cm chip has integrated heating resistors along the bottom and 64 temperature sensors on the top. Figure 2 shows a completed 2nd generation chip embedded into a vacuum chuck for impinging jet testing. The uniformity of the surface temperature distribution produced by these backside heaters was verified using an infrared thermal imaging microscope, and by direct measurement from the calibrated surface sensors.
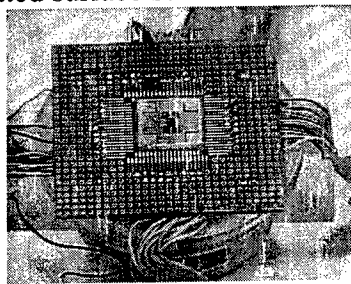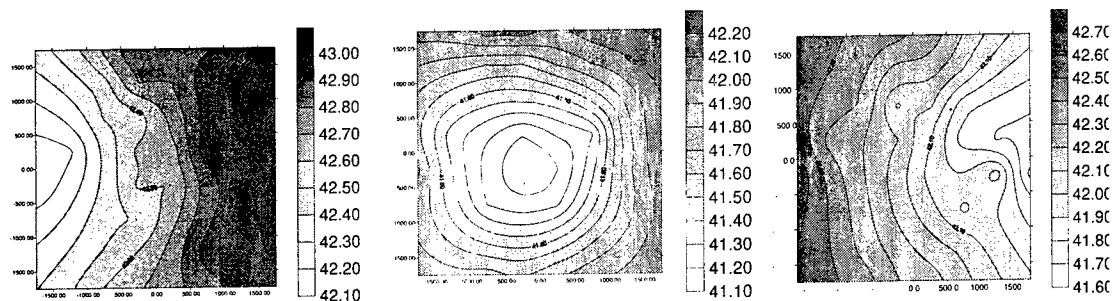

Figure 2. Target chip with integrated sensors and heaters mounted onto test chuck

Figures 3A,B, and C show some typical temperature distribution data imaged by the sensor chip. By moving the jet around the sensor chip, we should get reasonable 2-D temperature distributions. This allows us to quickly confirm that the target chip is functioning properly.

Figures 3A,B, and C. Thermal sensor image of a 500 um nozzle that is 750 um above the surface and tracking movement from left to center to right.

With the target chip sensor array precisely calibrated, experiments were conducted with micromachined nozzles and arrays. A single glass nozzle, a MEMS single nozzle, a MEMS nozzle array and a MEMS slot array were tested at a height range from 100 μm to 3000 μm and a pressure range from 0.5psi to 5psi. The MEMS nozzle results are compared to results obtained from a similar diameter glass nozzle. This is essentially a comparison of a confined versus a free micro jet configuration.

Single Impinging-Jet Cooling

Figure 4 is a composite of the sensor chip temperature profiles constructed from instantaneous sensor array data for each of the three cases. First, the temperature profile, shown as the bottom plane, was measured in the room temperature without any heating and cooling. The uniformity (±0.1 °C) of the measured temperatures in time shows good system reliability. The top plane is the temperature profile measured with 1.12 W applied via the backside heaters and no cooling on the frontside. The uniform temperature implies heat was envenly generated by the MEMS heater across the chip. The middle plane is temperature profile under the cooling by a 500 μm diameter MEMS nozzle which is 750 μm above the surface and drived by 5 psi of compressed air . A large total temperature drop (>35 °C) after the applied cooling shows the high cooling efectiveness by a impinging jet. A small temperature variation across the sensing area implies a large effective cooling area, enough to cause a measureable temperature profile even considering the large thermal conductivity of silicon.
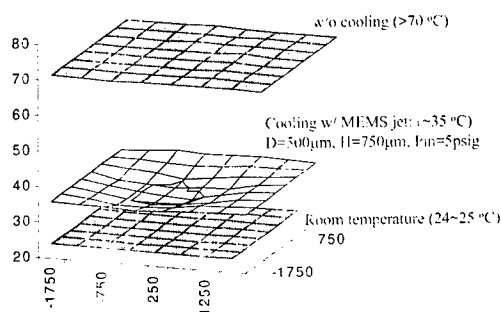

Figure 4. Composite illustration showing the effectiveness of impinging jet cooling.

In the case of the MEMS jet, it is more of a confined jet situation. Since the MEMS jet is a hole fabricated into an approximately 4 mm by 4 mm silicon chip, at heights less than 1mm, the top wall combines with the bottom sensor chip to produce a channel flow effect. This reduces the volume of cold air next to the MEMS nozzle available to be entrained and circulated past the heated bottom chip. This leads to a higher measured surface temperature for similar height and pressure conditions when compared to the free jet. However, at larger heights, this confined flow effect is greatly reduced and the MEMS jet cooling effectiveness is comparable to the free jet, as evident by the heat transfer coefficients calculated in Figure 6 for the MEMS jet. The heat transfer coefficient for the free jet is approximately constant at 0.032 W/cm^{2}K at 5 psi

and 0.025W/cm²K at 3 psi. Thus the MEMS jet (with an approximately 16 mm² chip area) has similar cooling characteristics to a free jet when the H/D ratio is greater than 3. Comparison of Reynolds numbers indicates the observed results agree with the expected flow regime. The Reynolds number for H/D less than 1 for the MEMS jet is as low as 1300, which is in the lower end of the transition region, near laminar flow, which is known to have poorer heat transfer qualities than turbulent flow.

Jet cooling efficiency, defined as heat transfer coefficient normalized by the kinetic energy of the gas, has been calculated and plotted in Figures 5 and 6 show for the single free jet and MEMS jet respectively. For both types of jet, a low gas driving pressure gives a high cooling efficiency. This gives us a practical guide for cooling system design: Low gas pressure is preferred if the gas source and power limitation is the constraint. Otherwise, high pressure and a high speed jet can be used to achieve low cooling surface temperature.
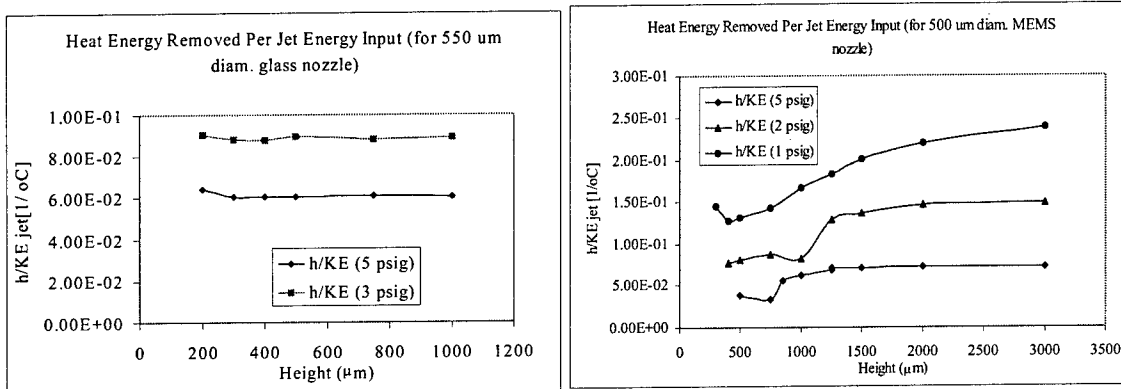
Figures 5 and 6. Cooling efficiency at various heights for a given inlet pressure of a free single jet (left) and a MEMS jet (right).

Jet Array

Preliminary data images with a nozzle array and slot array are presented in Figures 7 and 8. Although the temperature images are not as simple as the image of a single jet because of the more complicated gas flow pattern, the temperature distribution is more uniform than any single jet. The unexpected slot nozzle image in Figure 8 is due to the array inlet geometry. It seems that the inlets are acting as nozzles and the slots serve to confine the flow along the slot direction. Hence the inlet nozzle effect is being imaged by the temperature sensors.
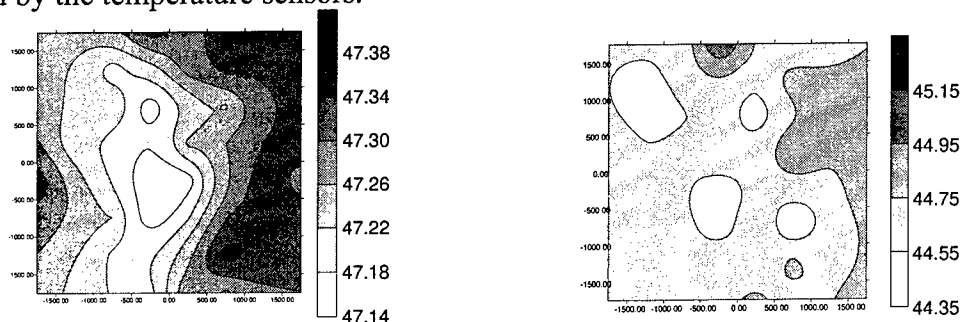
Figures 7 and 8. Temperature distribution recorded from a nozzle array at 500 μm height, Pin = 0.5 psig, and power in = 1.12 W (left). Slot array temperature distribution at height = 1000 μm, Pin = 1 psig, and an input power of 1.12 W (right).

In practice, cooling fans can only provide a limited pressure gradient for electronic cooling. Since it is assumed that standard PC-level cooling fans will be eventually interfaced with these MEMS devices, in practice, it is reasonable to evaluate cooling effectiveness by comparing surface temperature as a function of inlet pressure, irregardless of total mass flow rate. With this consideration in mind, a quick comparison method between the single nozzle and nozzle array is available, as evident in Table 1. From Table 1, it is apparent that if one design parameter is a small available pressure drop, then a MEMS nozzle array is the optimal cooling configuration

	Single MEM S Jet	Single Glass Jet	Slot Array	Nozzle Array
Gas Pressure (psig)	2.0	1.0	0.7	0.5

Table 1. Comparison of pressure required to cool the test chip to approximately 47 °C with Q = 1.12 W and height = 500 μm.

Temperature Profile Along the Channel

In the past year, we have conducted experimental studies of the temperature distribution of a gas flow through a micro channel under high inlet pressures. The freestanding micro channels that were used in the following experiments have integrated internal thermal sensors (our 2nd generation design) and were fabricated using surface micromachining techniques, which were also outlined in detail in the last progress report.

After we have rigorously characterized the flow inside the channel, we proceed to examine the temperature profile along the channel for various inlet pressures. Figure 9 shows the temperature profile at various inlet pressures, as measured by the 8 free standing temperature sensors within the 2nd generation micro channel. Even at 300 psig, there is no appreciable temperature difference (less than 0.1 °C) along the length of the channel. This would indicate that energy loss due to the conversion of flow energy into viscous frictional energy is negligible in this micro channel configuration.
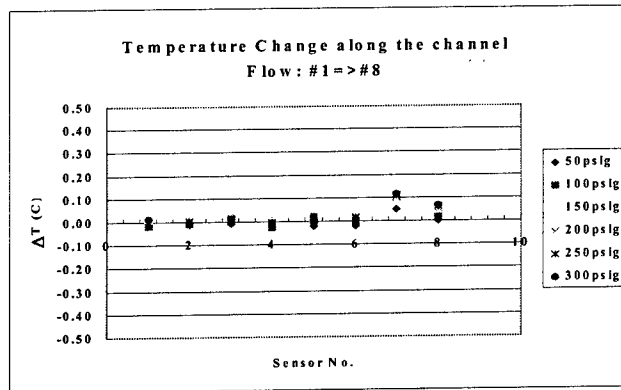
Figure 9. Temperature distribution within a micro channel at various inlet pressures.

Future Plan

As evident in the previous sections, preliminary results for the design of an effective MEMS heat exchanger are now available. We have identified optimal nozzle configurations for a given set of design constraints (available inlet pressure or maximum allowable surface temperature). In addition, we have demonstrated a large decrease in global surface temperature using micro jet impinging cooling. The following are the two things that we will do in the near future that will finish the proposed project as the project is expiring.

(1) Integrate these results into a MEMS heat exchanger design, which optimizes spatial flow frequency, as well as nozzle size, nozzle height, and the distance between nozzles.

(2) Produce a 2nd generation heat exchanger via an optimized fabrication process.

Acknowledgement/Disclaimer

References

1. Kasagi, N., "Forced Convection and Turbulence in Thermal Control," Chapter 3, Cooling Techniques for Computers, Win Aung, ed., Hemisphere Publishing Corporation, New York, 1991 pp. 97-140.

2. S. Wu, J. Mai, K. Zehetleitner, Y.C. Tai, and C.M. Ho, "Micro Heat Exchanger by Using MEMS Impinging Jets," 12th Annual IEEE International MEMS'99 Conference, Orlando Florida, January 17-21, 1999.

3. J. Seyed-Yagoobi, "Enhancement of Heat and Mass Transfer with Innovative Impinging Jets", Drying Technology, 14(5), 1173-1196, 1996

OPTICAL DIAGNOSTICS FOR TURBULENT FLOWS

C. Randall Truman
Mechanical Engineering Department
University of New Mexico

Abstract
Flow diagnostic instrumentation to measure turbulent flow in research and instructional wind tunnels is being acquired with a DURIP equipment grant. These instruments include a multi-channel hot-wire anemometer and a recently developed optical analysis system based on a two-dimensional Hartmann sensor. This instrumentation will provide the University of New Mexico with the capability to make measurements of turbulent flow similar to that established in the Air Force Phillips Laboratory FOTTOS project. Graduate and undergraduate students will be trained to make turbulent flow measurements with traditional anemometry as well as state-of-the-art optical techniques. With AASERT student support, flow control techniques will be studied for wall-bounded and free shear flows.

Approach
In collaboration with the Air Force Research Laboratory/Phillips Research Site, we previously studied the effect of large-scale (or coherent) structure on optical propagation through a low-Reynolds-number round jet (Luna et al. 1997; McMackin et al. 1997, 1998; Sapayo & Truman 1997; Truman et al. 1996, 1998). The experiments were carried out at the AFRL/Phillips Research Site in collaboration with the AeroOptics working group led by Dr. Lenore McMackin. An experimental turbulent jet facility was developed at the Phillips Lab in which flow and optical parameters can be measured simultaneously. The Fast Optical Tomography of Turbulent Organized Structures (FOTTOS) system was developed as well as a steering mirror control system for propagation of a thin beam through the jet. Some of these same techniques will be employed in studies at the University of New Mexico.

The wind tunnel to be used in the present work has been loaned by the Air Force Research Laboratory/Phillips Site. It is a subsonic open-circuit tunnel designed and built by Rocketdyne for optical studies of turbulent wall-bounded flow at the AFRL Starfire Optical Range in support of the AirBorne Laser (ABL) program. Nominal design velocity is 18 m/s through the 50 cm (high) by 10 cm (wide) test section. The maximum flow Reynolds number is of the order 10^6 per meter. Silicon rubber heating pads are attached to the aluminum walls in the upstream part of the test section; the temperature of each wall may be controlled separately. Optical-quality windows (13 and 35 cm) are installed in the downstream portion of the test section to allow optical measurement of the flow field. Both thermal anemometry and laser-based diagnostics will be used.

A unique two-dimensional Hartmann wavefront sensor will be used to characterize turbulent flow in the tunnel. Light from an established source (here a laser diode) is passed through the

turbulent flow where temperature fluctuations will aberrate the wavefront. This light is focused upon a 2-D array of micro-lenses (or lenslets) that generates a grid of focal spots on a 2-D CCD camera. The wavefront slope over each lenslet is determined from the focal spot displacements and the wavefront is reconstructed by integrating the slopes. These wavefronts will be analyzed to characterize the turbulent structure. Neal et al. (1996, 1998) discuss applications of this sensor including aero-optic measurements in supersonic flow. Dr. Dan Neal has established a company, WaveFront Sciences Inc. (Albuquerque), to produce these systems.

Figure 1 shows a schematic of the wind tunnel with the optical path for the Hartmann sensor. Figure 2 shows the optical components of the Hartmann sensor from the light source to the lenslet array and CCD camera. The relation between the average slope of an aberrated wavefront and the displacement measured in the CCD camera plane is illustrated for one lenslet in Figure 3.
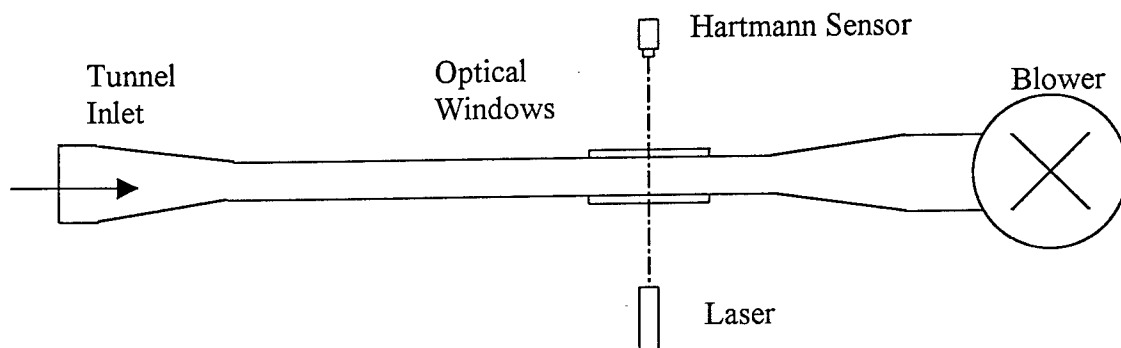

Figure 1. Schematic of wind tunnel with optical path of Hartmann sensor through optical windows in test section.
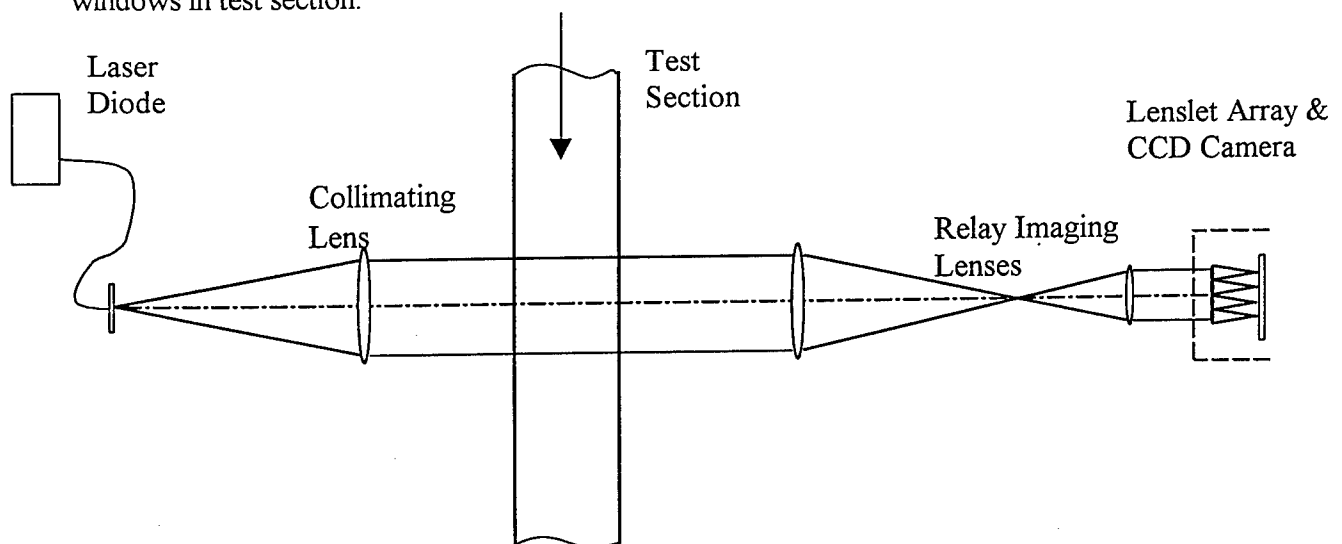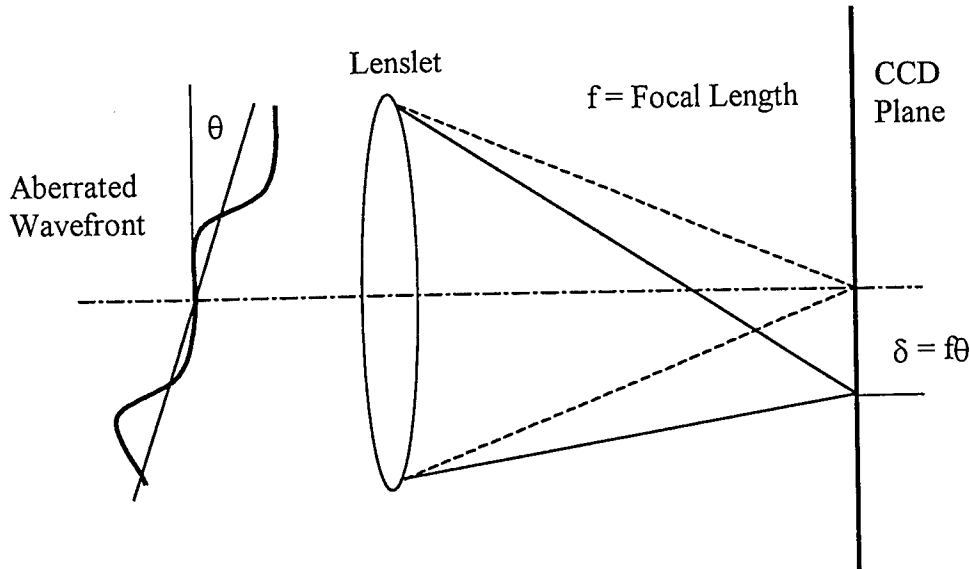

Figure 2. Hartmann sensor components.

266

Figure 3   Schematic of Hartmann sensor measurement of average tilt across a lenslet by displacement along CCD camera plane.

Progress/Results

The instrumentation will support research in two areas:
1) continued study of optical propagation through turbulent shear flows, and
2) studies of the interaction between deformable surfaces and flow fields, including laminar, transitional and turbulent flows.

The latter includes flow control technologies for aircraft control surfaces and for localized flow control to reduce separation, delay transition or reduce drag. These materials offer the promise of continuous deformable control surfaces with high dynamic response. Ionic polymer-metal composite materials are among those that will be tested in the tunnel, in collaboration with Prof. Mohsen Shahinpoor in Mechanical Engineering at the University of New Mexico.

Interactions/Transitions

A project in collaboration with Prof. A. Domaradzki and Dr. Darek Bogucki, University of Southern California, and Dr. Bob Ecke, Los Alamos National Laboratory, was initiated. This experiment uses the optical diagnostics available at the Phillips Lab to study optical propagation through a Rayleigh-Benard cell containing water that simulates turbulent oceanic conditions for velocity and temperature fluctuations. The data is being analyzed and will be reported this coming year.

Acknowledgment/Disclaimer

References

Luna, T.L., Truman, C.R. and Masson, B.S., 1997, "Linear Stochastic Estimation of Optical Beam Deflection Through a Heated Jet," AIAA Paper 97-0072

McMackin, L., Hugo, R.J., Bishop, K.P., Chen, E.Y., Pierson, R.E., and Truman, C.R., 1997, "High speed optical tomography system for imaging dynamic transparent media," Optics Express, Vol. 1, No. 11 (electronic journal: http://epubs.osa.org/opticsexpress)

McMackin, L., Hugo, R.J., Bishop, K.P., Chen, E.Y., Pierson, R.E.,and Truman, C.R., 1999, "High speed optical tomography system for quantitative measurement and visualization of dynamic features in a round jet," Experiments in Fluids, Vol. 26, pp. 249-256.

Neal, D.R., Alford, W.J., and Gruetzner, J.K., 1996, "Amplitude and Phase Beam Characterization using a Two-Dimensional Waverfront Sensor," SPIE Vol. 2870, pp. 72-82.

Neal, D.R., Hedlund, E., Lederer, M., Collier, A., Spring, C., and Yanta, W., 1998, "Shack-Hartmann Wavefront Sensor Testing of Aero-Optic Phenomena," AIAA Paper 98-2701.

Nelson, I.I. and Truman, C.R., 1998, "Identification of Large Scale Structures in a Turbulent Jet Using Optical Techniques," AIAA Paper 98-3016.

Sapayo, J. and Truman, C.R., 1997, "Study of the Development of Axisymmetric and Helical Modes in Heated Air Jets Using Fast Optical Tomography," AIAA Paper 97-1809.

Truman, C. R., Masson, B.S., and McMackin, L., 1996, "Optical Tomographic Study of the Effect of Excitation of a Heated Round Jet," AIAA Paper 96-2323.

Truman, C.R., McMackin, L., Pierson, R.E., Bishop, K.P., and Chen, E.Y., 1998, "Open-loop Control of Compensation for Optical Propagation Through a Turbulent Shear Flow," AIAA Paper 98-2832.

AN EXTREMELY SENSITIVE PZT-BASED MEMS MAGNETOMETER FOR USE AS AN ORIENTATION SENSOR

Dennis K. Wickenden
Applied Physics Laboratory
The Johns Hopkins University, Laurel, MD

William D'Amico
Weapons and Materials Research Directorate
Army Research Laboratory, Aberdeen, MD

Madan Dubey
Sensors and Electronic Devices Directorate
Army Research Laboratory, Adelphi, MD

Program Goals

The overall program goals are to develop an extremely sensitive microelectromechanical (MEMS) magnetometer, based on a resonating xylophone bar[1-3], to measure the angular orientation of projectiles with respect to the Earth's magnetic field. The accuracy of this device (due to its inherent sensitivity and the use of multiple sensors on the same structure) and its small size (resonators < 0.5 mm in length) provides a unique capability that surpasses the performance of existing MEMS-based angular rate sensors. Its successful development will revolutionize inertial measurement concepts and applications. Specific goals of the first phase of the program, covering the period August 1, 1998 to July 31, 1999, include:

- investigating the existing MUMPs18 devices for shock survival and operation after shocks;
- designing polysilicon xylophone structures of varying size and geometry to be fabricated on available MCNC MUMPs runs. These will enable limits to be set on the frequency, quality factor, sensitivity, and shock survivability as a function of size and geometry of the MEMS-based magnetometers;
- characterizing SmartMUMPs18 devices;
- preliminary processing development of sol-gel derived Pt/PZT/Pt xylophone structures; and,
- formulating a detailed program plan to develop, characterize, and field test MEMS-based resonating xylophone bar devices with the sensitivity required to meet the intended application.

PROGRESS

Shock testing existing devices

Existing MUMPs device structures, including xylophones, cantilevers, and diaphragms, were selected for shock testing, diced into 5 x 5 mm chips, released, and mounted and bonded into 40-pin dual-in-line ceramic packages. An empty such package was fitted with a sapphire window and subjected to shock testing to verify structural survivability. The package was placed in an aluminum housing and encapsulated in a clear potting material. A "window" was fabricated in the top surface by milling out a small patch and refilling by hand pouring a thin layer of epoxy. This technique allows for the optical inspection and characterization of the sensor die without having to release them from the epoxy. The packages were shock tested from 1,000 to 40,000 g's , 0.5 to 0.1ms duration and survived all shocks in this range. Therefore, the device packages were fitted with sapphire windows were shock tested in two orientations up to 30 Kg's. All of the magnetometer elements survived the shock testing. However, it was observed that a few of the magnetometer elements became stuck to the capacitor plates as a result of the shock testing. It is hoped that these devices will be released from the potting agent and examined further to determine whether they can be freed. Newly designed magnetometer die will be tested shortly.

MUMPs27 Device Design and Characterization

Various polysilicon magnetometers were designed and fabricated on a 1 cm square site processed on the first available MUMPS run (MUMPs27) in September 1998. The site was divided into 4 quadrants, with each quadrant containing different series of designs. All of the devices have small dimples placed in the center and near the ends to alleviate stiction problems encountered in the past. The support electrodes are anchored either to the poly0 or silicon nitride using a "5 of diamonds" pattern to minimize the loss of vibrational energy.[4] SEM micrographs of one of the released 300 x 30 μm xylophones are shown in Figure 1.

x 900   *x 2000*

Figure 1.   SEM micrographs of 300 x 30 μm MUMPs27 xylophone.

These micrographs demonstrate the clean release of the structure and clearly show the "5 of diamonds" support system anchored to the nitride layer, and morphological evidence of the dimple on the under side of the xylophone bar.

The preliminary evaluation of the devices has been undertaken in a vacuum test chamber. All devices tested to date have worked very well in static magnetic fields and exhibit quality factors, Q, of almost 22,000 at pressures of 15 – 20 mTorr. A beam deflection microscope has been used to transduce the Lorenz force induced motion of the xylophone magnetometers.
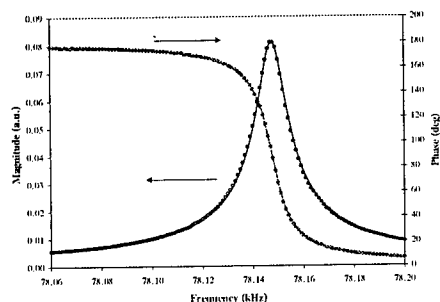

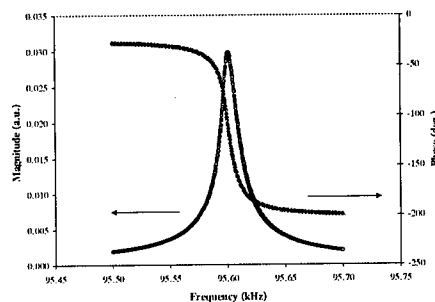*Figure 2. Response of 500x50μm xylophone with 4 μm supports.*

Figure 3. Response of 500x50μm Xylophone with 10μm supports.

Figure 2 illustrates the results obtained by scanning the frequency of the current through a 500 μm long xylophone with 4 μm wide supports operating in a static magnetic field. The rms current through the device was 22 μA, the magnetic flux density was on the order of mT (from a nearby permanent magnet) and the test chamber pressure was 35 mTorr. From this data, the resonance frequency was found to be 78.1 kHz and the Q-factor was almost 6700. The predicted frequency, using a modulus of elasticity and mass density for polysilicon of 160 GPa and 2320 kg/m³, respectively, is 67.6 kHz.

The results obtained from a neighboring xylophone with 10 μm wide supports are depicted in Figure 3. The magnetic field and chamber pressure were the same for this measurement, however the xylophone current was increased to 31 μA due to lower total resistance of the structure caused by the wider support arms (183 Ω compared to 270Ω). The resonant frequency of this device was 95.6 kHz and the Q-factor was 7500. The dramatic increase in resonance frequency is attributed to the increased torsional stiffness of the xylophone support arms. This was confirmed by a detailed analysis of the mechanical properties of the structures. In this analysis each of the support arms was modeled as a combination of vertical and torsional springs (K_V and K_T, respectively) and a concentrated mass (M) and the resonator was modeled as a beam using the Bernoulli-Euler beam theory. Use of this theory, rather than the more complex Timoshenko theory is justified because the wavelength of vibration is much larger than the thickness of the beam. The differential equation governing the motion of a Bernoulli-Euler beam undergoing harmonic motion $w(x,t)$ at a frequency ω is given by

$$EIw^{iv} + \omega^2 \rho A w = 0$$

271

where I is the moment of inertia and A is the cross sectional area of the beam. The effects of the two springs and concentrated mass enter into the expressions for the boundary conditions. Here, the boundaries include both ends of the beam as well as the support points. The zero-moment and zero-shear boundary conditions are used at both of the free ends. The motion of the beam is restrained to some degree in both displacement and rotation by the two elastic springs. The concentrated mass also adds inertia to the beam. Because the springs and mass are attached to the nodal points, neither K_V nor the mass M have any influence on the first bending mode of vibration. Only the torsional spring K_T has an influence on this mode. The results of this analysis, plotted as resonance frequency as a function of support arm width, are given in Figure 4. In this figure the solid line denotes the results of the analysis and the open circles represent the practical results.
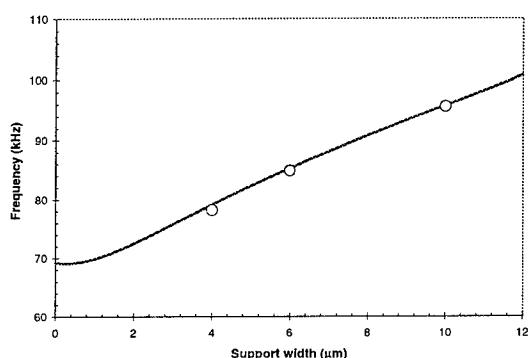

Figure 4. Resonance frequency as a function of support arm width for 500x 50 μm polysilicon xylophone 2μm thick
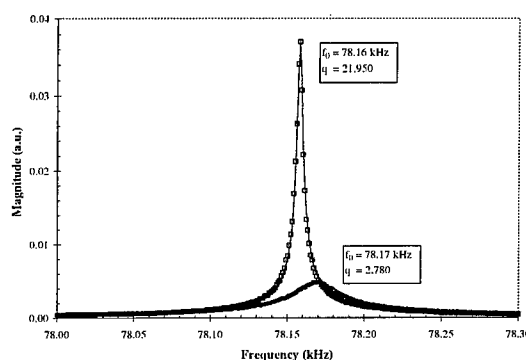
Figure 5. Response of a 500x50μm xylophone at 15 mTorr (squares) and 85 mTorr (circles)

It is well known that air pressure greatly influences the performance of MEMS resonators and an example of this effect on the xylophone with 4 μm wide arms is shown in Fig. 5. For this measurement, the magnetic flux density was on the order of 10 μT (Earth + other background fields) and the xylophone current was 22 μA. The test chamber pressure was varied between 15 mTorr and 85 mTorr and the resulting Q-factors were determined to be 21,950 and 2,780, respectively. The 9 Hz decrease in resonance frequency at the lower pressure is believed to be due to thermal effects (lower stiffness). Moderate temperature sensitivity of the resonance frequency has also been observed at constant pressure by varying the intensity of a broad illumination source or by repositioning the mW beam deflection laser. There has also been evidence that mechanical energy losses at resonance contribute enough thermal energy to measurably lower the resonance frequency of a device.

Further evaluation of the performance of the various MUMPs27 devices will be undertaken as functions of magnetic field, drive current, pressure and temperature. However, a major disadvantage of the design is the restriction on drive current that can be used placed on it by the high sheet resistance (10 Ω/square) of the poly1 material. Therefore, a redesign of the was undertaken and manufactured on the MUMPs30 production run. In this design the drive current to the magnetometer is fed from both sides, giving an immediate doubling of

the drive current capability. In addition the use of poly1/poly2 supports are examined, as is the use of gold strips along the length of the xylophone bar.

SmartMUMPs18 evaluation

Examination of the SmartMUMPs18 devices, when finally received from MCNC, showed that the xylophone bars were stuck firmly to the substrate and could not be released.
This was attributed to a fault in the APL design and, in no way, reflects on MCNC's release technology. In view of this no further work was undertaken on the devices. MCNC has recently announced that they are no longer offering SmartMUMPs as an option. Alternative approaches are being pursued.

Process and fabrication of PZT magnetometer

A cross section of the prototype magnetometer, primarily designed for process development rather than operational performance, is shown schematically in Figure 5.
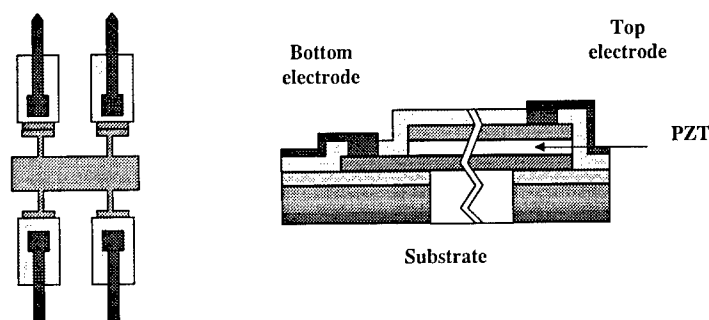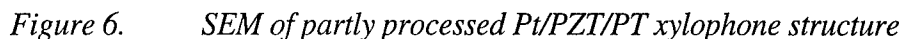

Figure 5   Schematic plan (left) and side (right) views of PZT device

The process steps include:

1. sol-gel deposit PZT on Si/SiO2/Pt substrate;
2. sputter the top Pt electrode;
3. photolithography define the xylophone structure, ion mill the top Pt, dry etching the PZT, and ion mill the bottom Pt;
4. selectively expose bottom Pt at contact;
5. deposit PECVD oxide and open up contact vias for top and bottom electrodes;
6. deposit and lift-off contact metallization; and,
7. deep RIE etch substrate and oxide from beneath the xylophone.

An SEM micrograph of a xylophone structure that has completed all the process steps with the exception of final substrate release, is shown in Figure 6.

Figure 6.   *SEM of partly processed Pt/PZT/PT xylophone structure*

Work is continuing to further develop the process to minimize the residual stress in the Pt/PZT/Pt structure and thus allow the release of an undistorted xylophone bar.

Detailed Program Plan

A proposal formulating a expanded program plan to develop, characterize, and field test MEMS-based resonating xylophone bar devices with the sensitivity required to for a projectile-based angular rate sensor was submitted to and accepted by AFOSR. This program is due to commence on June 15, 1999.

Acknowledgment/Disclaimer

References

1. R.B. Givens, T.J. Kistenmacher, J.C. Murphy, R. Osiander, and D.K. Wickenden, Applied Physics Letters, 1996, 69: 2755-2757.

2. D.K. Wickenden, R.B. Givens, R. Osiander, J.L. Champion, D.A. Oursler, and T.J. Kistenmacher, *SPIE Conference Proceedings on Micromachined Devices and Components IV*, 1998 , 3514 ; 350-358.

3. R.B. Givens, D.K. Wickenden, D.A. Oursler, R. Osiander, J.L. Champion, and T.J. Kistenmacher, Applied Physics Letters, 1999, 74: 1472-1474.

4. D. Sherman, "An Investigation of MEMS Anchor Design for Optimal Stiffness and Damping," Master's Project, Univ. of Calif., Berkeley, May 1996.

HIGH PERFORMANCE WOVEN MESH HEAT EXCHANGE

F49620-99-1-0286

Richard Wirtz
Mechanical Engineering Department
University of Nevada, Reno

Abstract

In 1955, Kays and London pointed out that a most effective way to increase the performance of a heat exchanger is to increase its heat transfer surface area-to-volume ratio, β [1]. Small-particle packed beds result in large values of β. Unfortunately, due to the tortuosity effect, the effective thermal conductivity of the solid phase of the packed bed, k_{eff} is relatively small, so that much of the gain in performance obtained by having a large β is lost by having a relatively small k_{eff}.

An *anisotropic* porous matrix having large β and a large k_{eff} *in a particular direction* will result in a very effective exchange surface. A woven or braided mesh of heat conducting wires can be configured to have these characteristics. In order for the technique to be applicable to a wide range of applications, the woven mesh must be structured such that high thermal performance is maintained while coolant pressure drop is held at reasonable levels. This objective can be achieved through careful configuration of the woven structure.

The overall objective of this work is to develop woven mesh heat exchanger technology, with particular attention to single-fluid, parallel plate heat exchangers as deployed to cool high power avionics. The technical approach includes the following elements:

1. Analytical Modeling. Develop analytical thermal/fluid performance models that can be used to assess the design of woven mesh heat exchangers. Complete parametric studies and document thermal/fluid performance characteristics as a function of mesh configuration.

2. Weave/Braid Characterization. Quantify thermophysical characteristics of woven-wire meshes/braids (porosity, effective thermal conductivity, etc.). Find or develop and verify (through experimental measurement) analytical or empirical models for these quantities.

3. Prototype Testing. Design, construct and test prototype heat exchangers that use this technology. Benchmark analytical models.

4. Fabrication Technology. Develop and document fabrication and manufacturing methodology.

First Year Work Plan. First year project activity will focus on demonstrating feasibility by designing, constructing and testing a simple (parallel-plate) woven-mesh test article. The exchanger core will be an orthogonal 3-D weave made up by stacking orthogonal 2-dimensional weaves (similar to window screening) interconnected with straight shute wires inserted through the 2-D weave stack [2]. This weave pattern will be bonded

between two parallel plates, with shute wires perpendicular to the plate surfaces, to form a plate-fin heat exchanger test article. Pre-tinned solid copper wire and screening will be used so that wire bonding can be accomplished using reflow-soldering techniques.

Specific first-year tasks include:

A. Analytical Modeling Develop an analytical exchanger core performance model, complete a parametric analysis and design a prototype orthogonal 3-D weave parallel plate heat exchanger. Initial modeling is based on a two-energy-equation model that treats the mesh as a porous thin fin [3]

B. Weave/Braid Characterization. Adapt models for the porosity and effective thermal conductivity of 2-D weaves to the three-dimensional case [4]. Develop a measurement capability of the local heat transfer coefficient within a orthogonal 3-D weave.

C. Prototype Testing. Develop a parallel-plate heat exchanger test rig. Complete performance testing on initial prototypes (heat transfer /pressure drop).

D. Fabrication Technology. Copper screening comes in a wide variety of configurations. However, 2-D copper-wire weaves with a bond at the wire intersection points are not available. Therefore, the methodology to develop such a screen must be developed. We expect to do this in conjunction with a company that has experience with vacuum braising.

Acknowledgement/Disclaimer

References

1. Kays, W. and London, A.L. (1984) *Compact Heat Exchangers*, McGraw Hill.

2. Chou, T.W. and Ko, F.K. (1989) *Textile Structural Composites*, Elsevier, New York.

3. R.A. Wirtz, "A Semi-Empirical Model for Porous Media Heat Exchanger Design", *Proc. 32nd National Heat Transfer Conf.*, ASME, HTD-Vol. 349, pp 155-162, Baltimore, August 8-12, 1997.

4. Chang, W.S. (1990) "Porosity and Effective Thermal Conductivity of Wire Screens", *J. Heat Transfer*, Vol. 112, pp. 5 - 9.

THE FORCED TURBULENT WALL JET AND WALL WAKE

Israel J. Wygnanski

AME Department

The University of Arizona, Tucson

Abstract
We have attributed the rapid rate of spread of a wall jet over a curved surface to a centrifugal instability that contributes to the transport of momentum across the flow. For this reason a wall jet flowing over a circular cylinder in the absence of an external stream becomes extremely wide before separating and for this reason perhaps, vortex generators placed at the leading edge of a curved slotted flap work so well.

The centrifugal instability associated with the curvature of the surface generates streamwise vortices that may exist even in turbulent flow. The existence of such vortices was often inferred from secondary observations rather than from direct measurements of the streamwise vorticity and therefore only the scale of theses vortices could be estimated from time-averaged properties.
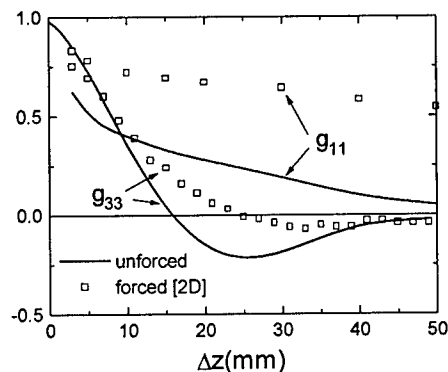
Figure 1. Cross correlation in the presence and the absence of plane excitation.

Two point, cross correlation measurements are often used to infer spanwise periodicity and serve as an indicator for the existence of streamwise vortices. When these measurements are done in the presence of an adverse pressure gradient the flow might be also unstable to other modes due to the existence of an inflection in the mean velocity profile. The competition among these modes may be exacerbated in the presence of plane excitation as we have demonstrated already last year (fig. 1).

The measurements were made using two hot wire probes that were separated by a spanwise distance, Δz. The g_{11} correlation shown in the figure refers to a normalized product of the streamwise velocity component, u'_θ while the g_{33} correlation refers to the product of the spanwise velocity component. Streamwise vortices would generate alternating directions in the spanwise velocity component that are dominant near the surface and thus observed there in the most clear manner. The u_z-component provides the strongest indication for the existence of streamwise, large-scale vortices since the normal component u_r, vanishes near the wall and the u_θ-component represents a secondary effect (i.e. a downward motion brings in high-momentum fluid to the vicinity of the surface that increases the local velocity and vice versa.). In the example shown, the natural g_{33} correlation attained a sizeable negative value when the spanwise separation between the probes was approximately one half of the mean spanwise wave-length. It implies that the averaged spanwise dimension of a counter-rotating pair of the streamwise vortices is $\approx 50mm$ in this case. It was also shown that this correlation was invariant when the spanwise location of the stationery probe was altered negating the possibility that it was generated by surface imperfections. The g_{11} correlation decayed exponentially with increasing probe separation and it only provided a measure to the scale of the naturally occurring spanwise vortices that are generated by the spanwise vorticity existing in the mean flow (in this case the plane wall jet). Two-dimensional excitation emanating from the nozzle had a tremendous impact on the three-dimensionality of the flow. The g_{11} correlation at $\Delta z = 50mm$ increased 10 fold (from approximately 0.05 to 0.5). The negative g_{33} decreased very significantly (by a factor of 4) and its spanwise wavelength increased somewhat. This suggests that plane periodic perturbations cause a diminution in the strength or in coherence of the streamwise vortices but in order to assess this interaction detailed, measurements of a different had to be made.
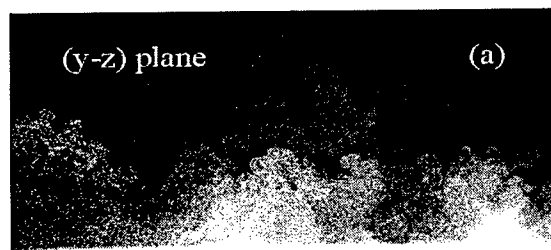

Figure 2. Flow visualization in the y-z plane.

A comprehensive investigation of the streamwise vortices occurring naturally in the flow was first undertaken. Flow visualization (fig.2) in the plane normal to the flow direction,

revealed clearly the existence of streamwise eddies whose scale was comparable to the scale educed from the g_{33} correlations. However the determination of the strength of these eddies could only be achieved with the use of a PIV and this was done with the assistance of Professor L. Lorenzo from Florida State University.
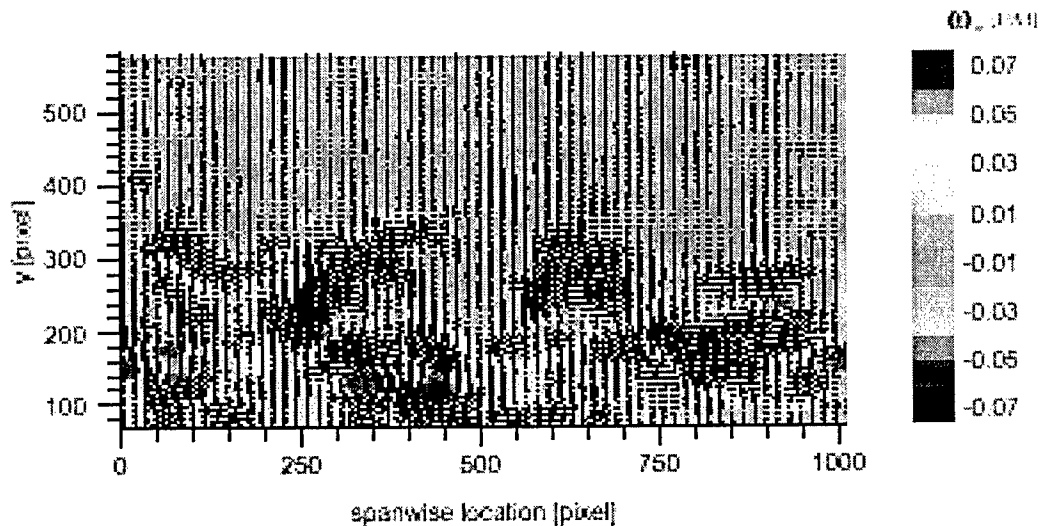

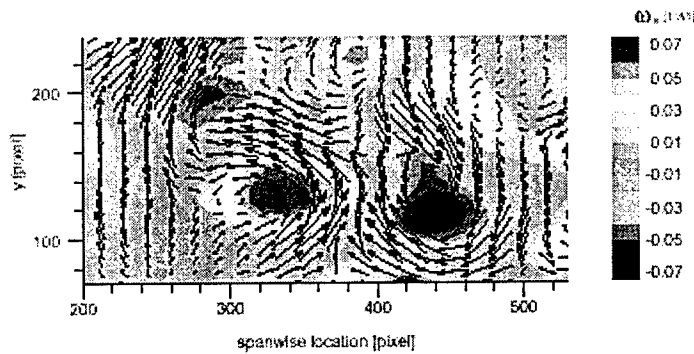Figure 3a. Contour plot of instantaneous vorticity in the y-z plane.

Figure 3b. Contour plot of a vortex pair.

Instantaneous velocities in the *y-z* plane were measured and the streamwise vorticity was calculated from these measurements (figs. 3a&b). The existence of strong longitudinal vortices was thus verified but they proved to be quite different from the regular stationary vortices predicted by Gortler. In fact, when the vorticity calculated from 500 realizations was ensemble averaged the pattern disappeared suggesting that the flow is perfectly two-dimensional in the mean. This implies that these longitudinal vortices are buffeted by the other eddies existing in this highly turbulent flow and they meander across the entire flow field wrapping themselves around one another in a random fashion as they proceed

downstream. Consequently, a pattern recognition procedure had to be used in order to evaluate the means size and strength of these vortices.
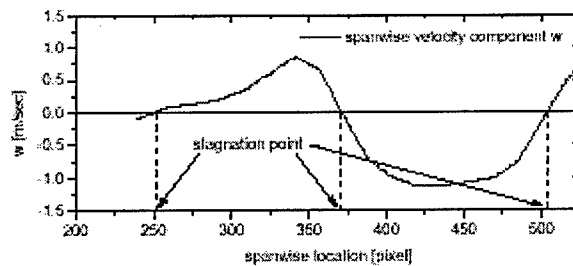

Figure 4. W-component of the velocity near the wall.

When the spanwise velocity component (near the wall) was evaluated from each realization it revealed a surprising periodicity that is also shown in (fig. 4). The spanwise distance between adjacent zero-crossings having the same direction of inclination in this figure provide the instantaneous wave length associated with the streamwise vortices next to the surface, because each such crossing represents the location of the instantaneous stagnation point in the y-z plane. One could thus generate a histogram showing the most probable number of vortex-pairs in a given cross section (fig. 5). This number turned out to be small and it decreased with increasing streamwise distance suggesting again that the longitudinal vortices braid themselves forming larger vortices with increasing x. One could also obtain the location of each zero-crossing and assess its dispersion around the mean location by looking at the histogram accumulated from the 500 individual realizations. The standard deviation from the most probable location approaches 20% of the spanwise dimension of the image, nevertheless it is of the same order of magnitude as the scale of a vortex pair containing opposing vorticity (fig. 6).
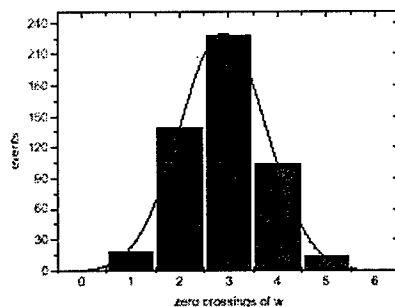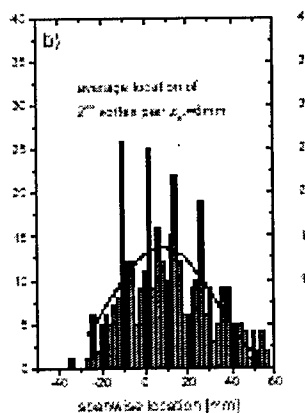

Figure 5. Histogram of vortex pairs.

Figure 6. Location probability for the vortex pairs

Since the entire data base is stored on the computer, one could shift each image in the spanwise direction aligning all the stagnation locations that were obtained near the center of each image. Such an alignment created an ensemble average pattern that already revealed the existence of the streamwise vortices and the spanwise periodicity existing in the flow. The pattern is distorted in the normal direction and does not represent the location of the vortex-cores that were observed in the individual realizations. To overcome this shortcoming each pattern was again correlated with the ensemble average and the location of the maximum correlation in the y-z-plane was recorded. A second ensemble average was generated by moving each realization in y and in z and aligning it with the location of the maximum correlation. The pattern that emerged from this procedure resembles a pair of streamwise vortices that are comparable to those derived using a stability approach. A second iteration of the procedure did not sharpen the image in any significant manner suggesting that the procedure converges rather quickly.
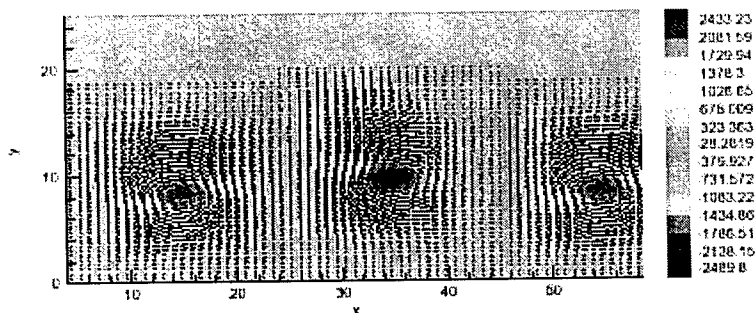

Figure 7. Enhanced ensemble averaged vorticity contours.

The application of this procedure to a periodically excited flow enables one to evaluate the possible interactions that may take place between entirely different mechanisms of instability. They may point the way to optimization of the excitation necessary to exert maximum control over flow that is otherwise about to separate.

Acknowledgment/Disclaimer

PHYSICAL ANALYSIS OF ACTIVE VORTEX GENERATORS

Chungsheng Yao
NASA Langley Research Center
Hampton, VA 23681

Jason T. Lachowicz and Osama A. Kandil
Old Dominion University
Norfolk, VA 23529

Objective

Our previous studies, under the current effort, have shown that a single actuator can generate free-jets, wall-jets, and near-wall vortex flow fields. That is, the actuator can be operated in different modes by varying the driving frequency, amplitude, and geometry of the actuator. Current research primarily focuses on the vortex flow field; the actuator serves as an active vortex generator. Our application is to replace fixed micro-size vortex generators with active devices that introduce quasi-steady vortices in the boundary layer in order to delay flow separation in high-lift systems. The objectives of this research are to develop active vortex generators in order to study the physics of the actuator-induced flow, to validate computational simulations of the actuator generated flows, and to conduct experimental studies of flow control using these active vortex generators. This work should provide an impetus for designing similar active flow control systems suitable for aircraft applications.

Approach

The actuator system consists of a cavity with a lightweight plate. The actuator plate acts like a piston pumping air out of the cavity on the down-stroke and sucking air into the cavity on the upstroke. The actuator is placed asymmetrically over the cavity opening, forming narrow and wide slots when viewed from the top. Previous research[1-3] under the current program indicates that several flow fields (free jet, wall jet, vortex flow) are produced by the actuator depending on amplitude, frequency, and slot spacing. Initial computational studies[4], which mimic the experiments, have shown good agreement with the experiments for the vortex flow.

Flow visualization, actuator displacement measurements, and frequency measurements were conducted simultaneously to document the actuator flow field in still-air. The laser-sheet flow visualization system consisted of a 3-watt Argon-Ion laser and a progressive scan video camera. The images were recorded in analog form on tape and also in digital form on computer. The actuator displacements were measured using a fiber-optic displacement sensor. The displacement measurements have an uncertainty of ±4% of the measured value. The non-dimensional scaling was determined from these measurements.

A digital PIV system was used to measure the instantaneous flow field in a plane perpendicular to the actuator plate surface and along the plate width. The flow field measurement was phase locked to eight equally spaced phases (45-degree intervals) of the actuator plate motion. Particle images were recorded using a digital camera (1Kx1K pixels) with a 105mm lens at 1/3 image reduction ratio. Measurement volume spatial resolution was less than 1 mm at the test plane and 32 pixels at the image plane. Ten samples of PIV images were taken at each phase. Ensemble averages were computed to estimate both phase-averaged and over-all averaged velocity fields.

Computational simulation of the actuator generated flows have been developed and applied to several actuator flow modes. The computational simulation uses a time-accurate full Navier-Stokes (NS) solver known as FTNS3D (a full NS version of CFL3D solver). For three-dimensional computations 10 multi-block grids are used and for two-dimensional computations, 6 multi-block grids are used. The grid blocks adjacent to the actuator plate move with the plate motion, and second-order interpolation is used along the block interfaces. Periodic response of the flow has been observed to develop after three cycles of the plate sinusoidal motion.

Accomplishments

In this study, the focus is primarily on the vortex flow regime characterized by a stationary vortex from the wide slot. Figure 1 shows a typical time-averaged visualization for the vortex-induced flow field; the arrow denotes the direction of the vortex. For this case, the vortex spans approximately 50 to 60% of the plate width as observed from the flow visualization. But, the core vortex size, estimated from the velocity profiles, is approximately 30 to 35% of the plate width.
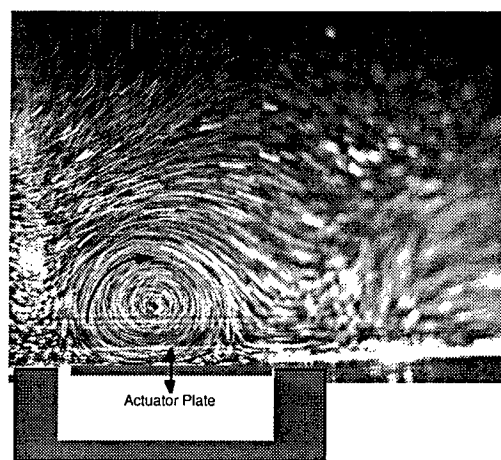

Figure 1: Typical flow visualization of actuator operated in the vortex flow mode

Figure 2 shows the time-averaged streamlines of the computational simulation for the vortex-induced flow field. The time averaging of the flow field was carried out over the fifth cycle of the actuator sinusoidal motion. The repetition rate of the plate motion, f_{rep}, is 190 Hz and the scaled amplitude, S_a, is 0.13. Comparison of the computational results with the time-averaged visualization of Figure 1 shows good agreement.
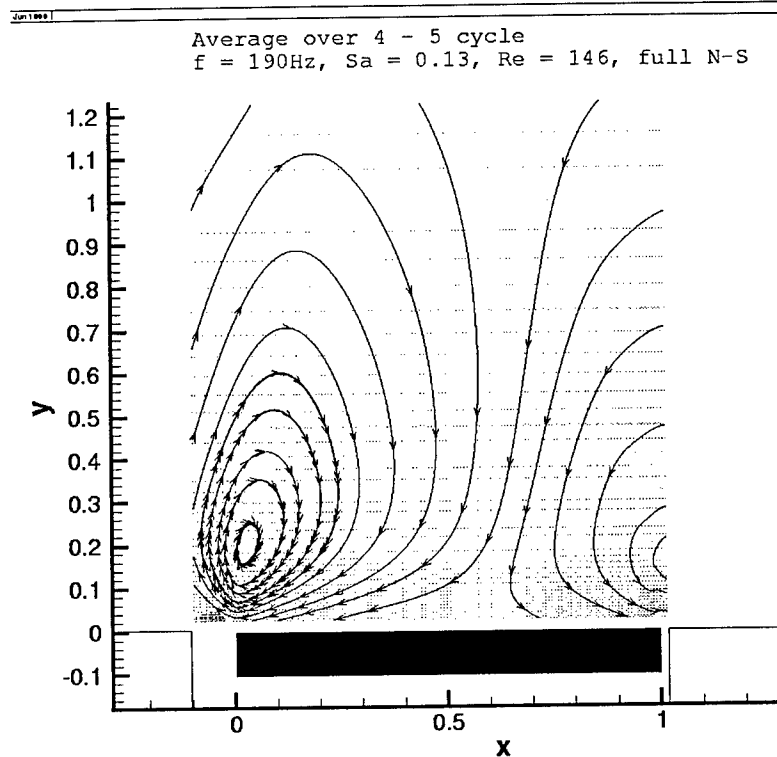
Figure 2: Computation of generated flow of actuator operating in vortex mode

For the present study, it is postulated that some form of asymmetric forcing may lead to a stronger induced vortex (relative to a sine wave forcing) because the vortex generation mechanism relies primarily on the downward stroke of the actuator plate motion. For asymmetric forcing, the duration and form of the positive and negative strokes of the actuator plate differ.

The non-dimensional governing parameters, using asymmetric forcing, can be generalized from the sine wave forcing analysis of Ref. 3. This analysis produces three governing parameters $(Re = \frac{\pi a_d b}{2dTv}$, $S_a = \pi \, a_d/b$, and $g_w = w_w/b)$ assuming 2D incompressible flow, a fixed narrow slot width, and a characteristic velocity equal to the actuator plate peak velocity. Figure 3 shows the non-dimensional design correlation for three flow regimes: wall jet, free jet, and vortex flow. (Note that this data was conducted over an actuator plate width range from 5.56 mm to 18.8 mm and a wide slot range from 0.32 mm to 2.54 mm). Although overlap exists between each region, each flow field has a region that is unique to that particular flow field. Operation of the actuator in this unique region would produce the desired flow of interest; e.g., at $Re \, g_w = 25$, $\sqrt{\frac{Re}{S_a}} \, g_w^2 = 0.5$ and 1 for the vortex flow and wall jet, respectively. For $Re \, g_w = 4$, the free jet exists at $\sqrt{\frac{Re}{S_a}} \, g_w^2 = 0.07$.

For the vortex flow, the non-dimensional range for asymmetric forcing is within the range for sine forcing. This suggests that, although the vortex strength depends on the forcing frequency, the scaling may not dependent on the type of forcing.
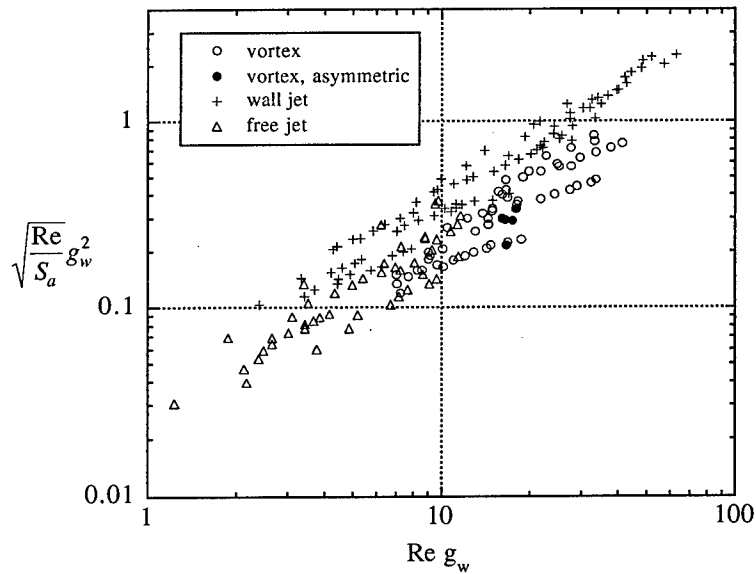
Figure 3: Non-dimensional design correlation

Figures 4 and 5 show the phase-averaged velocity fields for the actuator operating in the vortex mode. Each figure represents the average of 10 samples at a particular phase of the actuator plate oscillation. A vortex structure is measured above the piston for each phase suggesting that the structure is stationary; note that similar results are observed for the additional six phases not presented. This is consistent with the averaged flow visualization pattern observed earlier, and the computation results shown in Figure 2. In addition, an unsteady angled jet flow is pumped from the wide gap indicative of mass ejection from the actuator. Figure 6 shows the averaged flow field over eight phases. A single cell vortex structure is clearly observed, verifying that the vortex is dominated by a stationary mode.
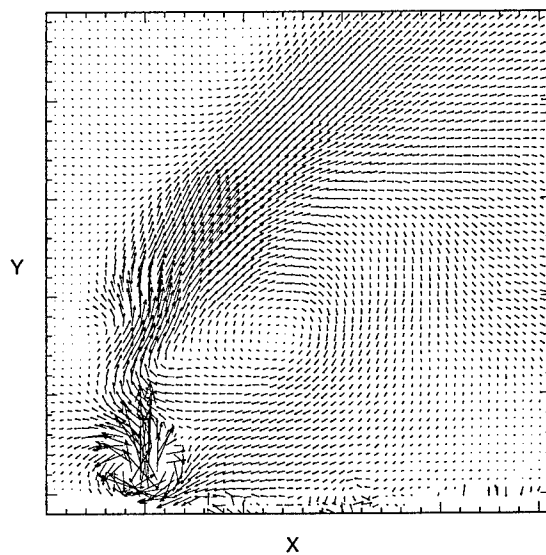

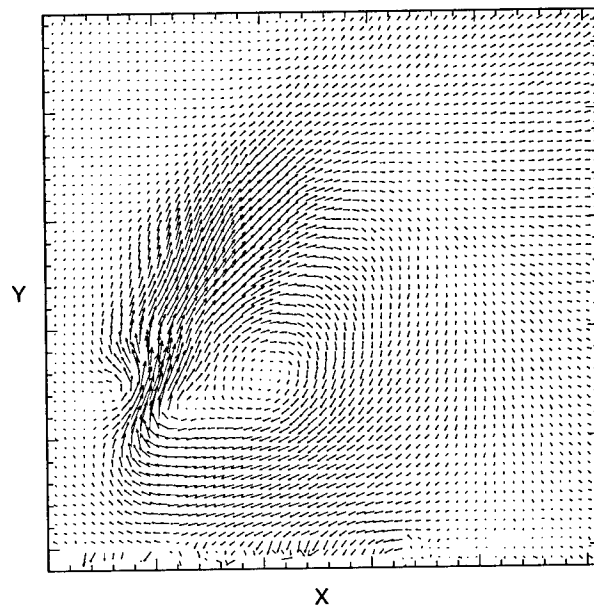Figure 4: Phase-averaged velocity field: Phase 1 (plate into cavity)

286

Figure 5: Phase-averaged velocity field: Phase 3 (plate out of cavity)
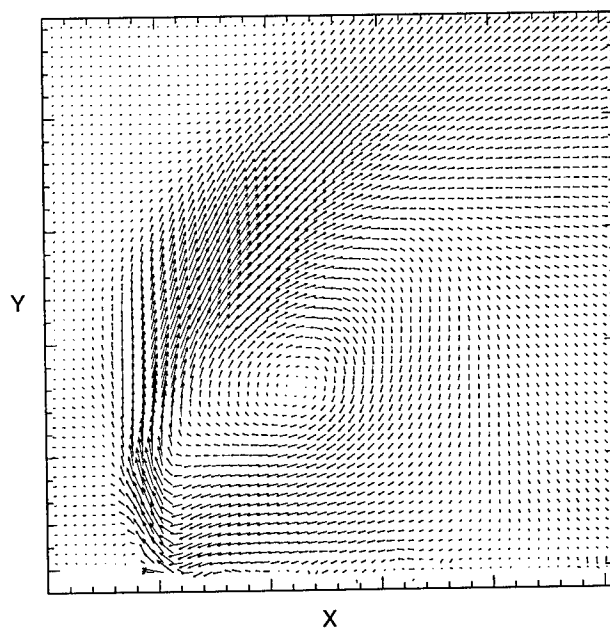

Figure 6: Mean velocity field

Future Work

Future plans are to continue developing and validating the computations with experiment. The actuator flow will be further studied at higher frequencies. Wind tunnel tests using a

single actuator will be conducted in a separated flow to compare the actuator vortex mixing with micro-vortex generators.

Acknowledgment/Disclaimer

Nomenclature

a_d Actuator plate displacement from maximum position out of cavity to maximum position into cavity (mm)

b Actuator plate width (mm)

dT Downward period of actuator plate (s); $dT=1/(2*f_{rep})$ for sine wave plate driver

f_{rep} Actuator plate driver pulse repetition rate (Hz)

g_w Ratio of wide-slot width to (actuator) plate-width, w_w/b

S_a Scale Amplitude= $\pi\, a_d/b$

w_w Wide-slot width (mm)

v Kinematic viscosity (mm^2/s)

References

Lachowicz, J.T., Yao, C.-S., and Wlezien, R.W., "Scaling of an Oscillatory Flow-Control Actuator," 36th Aerospace Sciences Meeting and Exhibit, AIAA 98-0330, Jan. 1998.

Lachowicz, J.T., Yao, C., Joslin, R.D., "Physical Analysis and Scaling of a Jet and Vortex Actuator," 3rd ASME/JSME Joint Fluids Engineering Conference, FEDSM99-6921, July 1999.

Lachowicz, J.T., Yao, C., and Wlezien, R.W., "Flow field Characterization of a Jet and Vortex Actuator," *Experiments in Fluids*, Springer-Verlag, Vol. 26, 1999.

Joslin, R.D., Lachowicz, J.T., and Yao, C.-S., "Simulation of Flow Induced by an Unsteady Fluidic Actuator," ASME Forum on Control of Transitional and Turbulent Flows, FEDSM98-5302, June 1998.